Novel aspects of multiqubit entanglement and qudit computing on an NMR quantum information processor

Thesis

For the award of the degree of

DOCTOR OF PHILOSOPHY

Supervised by:

Dr. Kavita Dorai &
Prof. Arvind

Submitted by:

Shruti Dogra

Indian Institute of Science Education & Research Mohali
Mohali 140 306
India
September 2015

Declaration

The work presented in this thesis has been carried out by me under the guidance of Dr. Kavita Dorai and Prof. Arvind at the Indian Institute of Science Education and Research Mohali.

This work has not been submitted in part or in full for a degree, diploma or a fellowship to any other University or Institute. Whenever contributions of others are involved, every effort has been made to indicate this clearly, with due acknowledgement of collaborative research and discussions. This thesis is a bonafide record of original work done by me and all sources listed within have been detailed in the bibliography.

Shruti Dogra
Place :
Date :

In our capacity as supervisors of the candidate's PhD thesis work, we certify that the above statements by the candidate are true to the best of our knowledge.

Dr. Kavita Dorai
Associate Professor
Department of Physical Sciences
IISER Mohali

Place :
Date :

Dr. Arvind
Professor
Department of Physical Sciences
IISER Mohali

Place :
Date :

Acknowledgements

First of all, I thank my supervisors Dr. Kavita Dorai and Prof. Arvind, who turned out to be much more than a PhD supervisor and guided me through all my ventures. Their consistent encouragement has always been a motivation. Without their unwavering guidance, this thesis would not have been possible. At the same time, I would like to thank Prof. N. Sathyamurthy, Director, IISER Mohali. His plausible arguments and easy approach sorted many problems.

I would like to thank my doctoral committee member Prof. Jasjeet S. Bagla for his useful comments and support throughout the PhD. I am obliged to the faculty of the Department of Physical Sciences of IISER Mohali whose direction and guidance has been very fruitful during the PhD course work and the lab rotations. My sincere thanks to all the faculty members of IISER Mohali for various direct and indirect interactions all through the PhD.

I am happy to be a part of a dynamic research group with numerous research directions. Many thanks to the group meetings and the healthy discussions with the group members. My sincere thanks to the group mates: Navdeep Gogna, Satnam Singh, Amandeep Singh, Rakesh Sharma, Jyotsana Ojha, Amrita Kumari, Matsyendra Nath Shukla, Jaskaran Singh Nirankari, Varinder Singh, Chandan Sharma, Akash Sherawat, Tara George, Vikram Sharma and Akshay Gayakwad. I am obliged to my lab mates and friends Ritabrata Sengupta, Harpreet Singh and Debmalya Das for their critical comments, useful discussions and the team spirit. I would like to thank the graduate students Prashant Mishra, Aditya Jhanjharia, Rajveer Nehra and Abhishek Mishra, who, during their short stay in the lab turned out to be very helping. Many thanks to my friend and group mate Pavithran S Iyer who became very friendly in a small time, and turned out to be very helping, particularly in literature survey. I owe special thanks to my friends George Thomas and Neha Jain for their fruitful suggestions, critical comments, wonderful time, and support that help in making the stay pleasant during the PhD.

I thank Dr. Paramdip S. Chandi for his help at the numerous occasions, Dr. B. S. Joshi (Application Scientist, Bruker India) for his technical support and guidance. I would also like to thank my senior and collaborator Dr. Geetu Narang, for the useful discussions and pleasant time we had.

I would like to thank the whole of the IISER Mohali staff, who put numerous efforts for making an institute run. I am thankful to my fellow students for their various direct and indirect interactions. Special thanks to Mr. Balbir Singh and Mr. Rajesh for various direct and indirect help in the NMR Lab.

Many thanks to my teachers at the school, college and the university levels for their efforts to shape my future.

My sincere gratitude towards my parents who, through all their thick and thin, put my needs at priority and always encouraged to proceed further. Their relentless efforts, sacrifices, patience and consistent faith always inspired me. I would like to thank my sister, Mrs. Jyotsna Dutt Sharma, who has always been there at the back to support me. Her convincing power and the determination provide me the strength. My sincere thanks to my brother-in-law, Mr. Ganesh Dutt Sharma, who in a small time, has become an inspiration for me. I am greatful to the teachings of my grandmother that direct me to choose the right path, perform the duties and the power to dream.

I am obliged to NMR research facility of IISER Mohali housing 400 MHz and 600 MHz Bruker NMR spectrometers. During this thesis, various experiments on 600 MHz are performed using QXI, TXI and BBI probeheads, and on 400 MHz spectrometer using BBFO probehead.

Many thanks to the Library facilities that provide access to various journals and books, IISER Mohali computing facilities for providing the access to various different softwares, basic requirements such as internet facilities and the technical support.

I would like to thank University Grants Commission (UGC) for the financial support during the PhD (Aug. 2010 - Jul. 2015), and IISER Mohali for funding towards participation in EUROMAR 2014, held in Zurich, Switzerland.

Last but not the least, I thank the supreme power, the Almighty that blesses one with a thirst for knowledge and the capabilities to learn.

Shruti Dogra

Abstract

This thesis deals with the study of novel aspects of quantum computational resources, and the experimental implementations of various quantum computing protocols on three-qubit, single-qutrit and hybrid qubit-qudit NMR quantum computers. The study is conducted in two main parts. The first part focuses on different aspects of multipartite entanglement to gain insights about a three-qubit system. GHZ and W-classes are the two inequivalent entanglement classes in a system of three qubits. While three-party correlations in W-class of states can be uniquely and completely determined from its reduced two-party correlations, GHZ class exhibits non-decomposable three-party correlations. An NMR experimental implementation is carried out that supports a recently exposed fact about a three-qubit W-superposition state that belongs to GHZ class but does not possess any non-decomposable three-party correlations. This exercise reveals various hidden aspects of multipartite entanglement in a system of three qubits.

The second part is aimed at the study of contextuality, which is a purely quantum concept and is exhibited by even the indivisible single-qutrit system. The intrinsic quantumness and hence the computational speedup in a single qutrit is attributed to contextuality. This thesis focuses on developing the machinery for a single-qutrit NMR quantum computer using a geometrical representation, followed by a single-qutrit algorithmic implementation exploiting contextuality. Computational protocols on hybrid-qudit systems are also discussed and implemented experimentally. A part of the study is focused on NMR methodology development with an emphasis on the applications of numerically optimized radio-frequency pulses for biomolecular NMR and quantum gate optimizations.

The contents of the present thesis have been divided into seven chapters and an appendix whose brief account is sketched below:

Chapter 1

This chapter describes an introduction to the field of NMR quantum computation and quantum information as well as the motivation behind the present thesis. In addition to the basics of NMR, and quantum computation, recent developments in the field of quantum computation and quantum information are discussed.

Chapter 2

In this chapter, a general pulse sequence to create a five-parameter based, three-qubit generic pure state is proposed and experimentally implemented for various three-qubit states with a non-trivial set of parameters. Experimental evidence is provided in support of a recently proposed idea that three-qubit correlations can be completely and uniquely obtained from a pair of its reduced two-party states (with a few exceptions). The experimental tests are performed for arbitrarily weighted generic-three qubits states, maximally entangled GHZ and W-states, and a recently proposed W-superposition state that is a coherent superposition of W-state and its obverse.

Chapter 3

This chapter describes the geometrical realization and dynamics of a single-qutrit, represented by a pair of points on the Majorana sphere in three-dimensional real space ($\mathcal{R}^3$). This geometrical realization is used to develop an intuitive picture of a single-qutrit magnetization vector. Single-qutrit dynamics is studied under SO(3) and SU(3) transformations, which in the context of Majorana sphere leads to the development of several interesting features. Close analysis of the single-qutrit dynamics on the Majorana sphere leads to the development of NMR pulse sequences implementing single-qutrit quantum gates. Thus using the insights gained via the Majorana representation, basic operations such as the SWAP operations, phase gates and the 3-dimensional analogue of the Hadamard gate are performed. Experimental implementations of these basic computing elements are carried out on spin-1 oriented in a liquid crystal.

Chapter 4

This chapter focuses on exploring single-qutrit contextuality, which is an intrinsic feature providing speed up in quantum computational tasks. Contextuality refers to the context of a measurement, which states that the measurement of an observable may bear different outcomes when measured in different contexts. In this chapter, various theoretical protocols revealing single-qutrit contextuality are studied. An NMR experimental test is proposed and implemented on a single-qutrit NMR quantum information processor that provides evidence in support of the contextual nature of a single-qutrit, using a set of four experiments. The quantum features of the single-qutrit are further exploited by implementing a black-box based algorithm, that determines the parity of a permutation among three objects by a single oracle call whereas its classical counterpart requires two oracle calls. The NMR experiments on a single-qutrit are carried out on a spin-1 oriented in a liquid crystalline matrix.

Chapter 5

This chapter describes the design and implementation of quantum gates for qudit-computing using NMR, and the emulation of qubit-qubit-qutrit (QQT) QFT algorithm on a four-qubit (QQQQ) NMR quantum information processor. The QQQQ system used in this chapter possesses a peculiar coupling pattern giving rise to a spectrum that resembles that of a QQT system. A non-trivial correspondence is described between the QQQQ and the QQT systems. A general QQT tomography protocol is proposed and implemented on the QQQQ emulator to reconstruct the resultant QQT state.

Chapter 6

This chapter deals with NMR methodology development, focused on the design and implementation of GRAPE optimized numerical pulses. These numerical pulses are optimized for the uniform and precise band-selective excitations in SOFAST-HMQC experiments for biomolecular NMR, quantum gate optimizations for qudit QFT implementation on a qubit-qutrit system and in the simulation of low-temperature protein dynamics.

Chapter 7

This chapter contains a brief summary of the main results of the present thesis, their applications as well as their possible future extensions.

Appendix A1

This appendix contains a brief description of the lyotropic liquid crystal sample preparation that provides an anisotropic environment to a spin-1 system. This sample is used to perform qutrit quantum computing using NMR (as described in Chapters 3 and 4).

List of Publications

1. **Shruti Dogra** and Kavita Dorai. Numerically optimized band-selective pulses in SOFAST-HMQC experiments for biomolecular NMR. *J. Mol. Struct.*, 1063, 45-50 (2014).

2. **Shruti Dogra**, Arvind and Kavita Dorai. Determining the parity of a permutation using an experimental NMR qutrit. *Phys. Letts. A*, 378, 3452 (2014).

3. **Shruti Dogra**, Kavita Dorai and Arvind. Experimental construction of generic three-qubit states and their reconstruction from two-party reduced states on an NMR quantum-information processor. *Phys. Rev. A*, 91, 022312 (2015).

4. Debmalya Das, **Shruti Dogra**, Kavita Dorai, and Arvind. Experimental construction of a W superposition state and its equivalence to the Greenberger-Horne-Zeilinger state under local filtration, *Phys. Rev. A*, 92, 022307 (2015).

5. **Shruti Dogra**, Arvind, and Kavita Dorai. Implementation of the quantum Fourier transform on a hybrid qubitâĂŞqutrit NMR quantum emulator, *Int. J. Quantum Inf.*, 13, 7, 1550059 (2015).

6. **Shruti Dogra**, Kavita Dorai, and Arvind. Experimental demonstration of quantum contextuality on an NMR qutrit, arXiv:1511.00241 [quant-ph] (*under review*).

7. **Shruti Dogra**, Kavita Dorai, and Arvind. NMR experimental implementation and Majorana representation of quantum operations on a qutrit, **Manuscript in preparation (2015).**

Contents

List of Figures

List of Tables

LIST OF TABLES

Chapter 1

Introduction

Quantum computation and quantum information is an area of much recent interest, that contains the study and implementations of quantum mechanics-based computational and information processing tasks [1, 2, 3, 4, 5, 6]. Explorations in this field of research began with the idea introduced by Richard Feynman in his talk on "Quantum physics and computer simulations" in 1981 [7]. The talk was inspired by the reversible Fredkin and Toffoli gates, and was focused on the use of quantum particles to derive computational tasks. A quantum information processor can perform some computational tasks more efficiently than its classical counterpart. The computational power is attributed to intrinsically quantum properties of the system such as superposition and entanglement. A quantum computational algorithm is first decomposed in the form of a quantum circuit, that consists of a defined sequence of quantum gates. Quantum gates are unitary operators and are hence reversible. Several quantum algorithms implemented till date include the Deutsch-Jozsa algorithm [8, 9, 10, 11, 12], quantum Fourier transformation [1, 13] which, alongwith phase estimation algorithm [1, 14] is used in factorization algorithms [15]. A search algorithm introduced by L. K. Grover [16] that provides a speedup of O($\sqrt{N}$) as compared to its classical counterpart to search an item in an unsorted dataset of N elements. Quantum computation is also finding applications in quantum cryptography [1, 2] to generate various secure and robust protocols for coding and decoding of the information, for quantum teleportation [1, 2, 3, 17] the property of entanglement is exploited to teleport an unknown state. Several new methods for quantum computing are also arising such as fault tolerant quantum computing [18, 19] which is based on the creation of magic states [20, 21] and the use of Clifford gates [22]. Also an idea of one-way quantum computing [23, 24] is in its infancy that uses cluster or graph states to initialize the system. This is followed by the use of single-qubit gates that implement a one way quantum circuit on the highly entangled cluster state to accomplish the desired computational task.

Theoretical explorations in this field address issues like intrinsic computational resources in a quantum system and the algorithmic developments, while experimental research in the area deals with the search for scalable and physically realizable quantum computational systems, and the experimental implementations of various computational tasks. Several experimental quantum computational systems [4, 25] that are emerging, include trapped ions [26, 27], polarization states of light [25], Nitrogen-vacancy centres [4, 28], ultracold atoms [29] and quantum dots [5, 30].

This thesis uses NMR as the experimental tool to perform quantum information processing tasks. Nuclear spins based NMR quantum computer is one of the first experimental realizations of the quantum information processor [31]. Although quantum computing using NMR is not scalable beyond a certain limit, yet this technique provides a testbed for several quantum algorithmic implementations, molecular simulations and quantum games [5, 6, 32]. The basic criteria for an experimental computational model as provided by David P. DiVincenzo in 2000 [33] include a scalable physical system, the ability to initialize the state, sufficiently long decoherence times, a universal set of quantum gates, and the ability to make measurements.

The technique of Nuclear Magnetic Resonance (NMR) was developed independently by F. Bloch [34] and E. M. Purcell [35] in 1946, for which they were awarded the Nobel prize in 1952. The first method for calculation of the magnetic moments was however proposed by O. Stern and W. Gerlach in 1924 [36], and the elegant idea of resonance was introduced by I. I. Rabi in 1938 [37] in his single-page paper. This technique of NMR found vast applications after R. Ernst developed the concept of Fourier transformation NMR spectroscopy [38], for which he was awarded the Nobel prize in 1991.

NMR is a highly developed and versatile technique that has been flourishing for decades and is finding widespread applications in several areas of physics, chemistry, biology and medicine [6, 39, 40, 41]. New developments are arising in the area of solid state NMR [42], liquid state NMR [43] as well as electron polarization enhanced NMR spectroscopy [44]. Present day NMR spectroscopy is very useful in protein structure determination [40, 43], evaluation of reaction dynamics [45], metabolite studies [46], as well as in the pharma industry [47, 48]. Its use in Magnetic Resonance Imaging (MRI) and functional MRI [41] is a boon to the field of medical diagnostics. NMR is also used in diffusion related studies [49], and NMR studies in the earth's magnetic field using portable NMR spectrometers [50]. Despite all these applications, NMR methodology development is still progressing. There are studies focusing on the relaxation mechanisms of NMR active nuclei [40, 51], decoherence of spin-states [52, 53, 54, 55], pure shift NMR spectroscopy [56], and advent of new higher dimensional NMR experiments [40, 43, 57, 58]. A vast amount of work is going on in the development of fast pulsing NMR experimental techniques such as SOFAST [59, 60, 61], BEST [62], and ASAP [63] based pulse sequences, projection spectroscopy [64], Hadamard spectroscopy [65] and the idea of non-uniform sampling [66].

Out of its numerous applications, NMR quantum computation is a recent one that harnesses the intrinsic quantum properties of the nuclear spins, manipulated by specifically tailored radio frequency pulses (quantum gates) to perform specific computational tasks [1, 5, 67, 68]. The main motivation of the present thesis is to implement various quantum computing protocols on NMR qudits (d-level quantum systems), and to explore their inherent quantumness and their ability to act as computational resources which are responsible for efficiently performing a quantum computational task.

1.1 The phenomenon of NMR

The phenomenon of nuclear magnetic resonance [39, 40, 69, 70] is exhibited by a nucleus with non-zero spin. When a nucleus with non-zero spin is placed in a magnetic field ($\overrightarrow{B}$), it starts precessing about the magnetic field at a characteristic frequency (ω), known as the Larmor precessional frequency. The Hamiltonian of such a system is given by:

$$H = -\overrightarrow{\mu}.\overrightarrow{B} \tag{1.1}$$

where the magnetic moment μ is proportional to the angular momentum I ($\overrightarrow{\mu} = \gamma I$) and γ being the gyromagnetic ratio of the nucleus of interest. Assuming the magnetic field ($\overrightarrow{B}$) to be along the z-axis ($H = -\gamma I_z B_z$), the Larmor frequency $\nu = \frac{\gamma B_z}{2\pi}$. Thus each nucleus type has its own characteristic Larmor frequency. However the nuclei are surrounded by the electronic environment inside the atom, which further exhibits several chemical bonds with various other atoms to form a molecule. This chemical environment leads to shielding of the magnetic field, $B^{eff} = (1-\sigma)B_z$, where σ is the isotropic counterpart of the shielding tensor σ_{ij} $(i, j \in \{x, y, z\})$ at the site of nucleus giving rise to a quantity called the chemical shift. Thus the same nucleus, when placed in different chemical environments, exhibits different values of chemical shifts. A few examples of NMR active nuclei include: ^{1}H, ^{13}C, ^{15}N, ^{19}F, ^{31}P which are the spin-$\frac{1}{2}$ nuclei while ^{2}H, ^{14}N, ^{23}Na, ^{137}Cs have higher values of spin. Nuclei with higher values of spin possess asymmetrical distribution of electric charges, that further gives rise to a quadrupolar moment.

A system of coupled nuclei when placed in a magnetic field exhibit several other inter-spin interactions. The Hamiltonian for a system of coupled spins is given by:

$$H = H_{cs} + H_J + H_Q + H_D \tag{1.2}$$

where the dipolar coupling term H_D and the quadrupolar coupling term H_Q get averaged to zero in liquid state NMR. The only surviving terms are the chemical shift (H_{CS}) and the scalar coupling terms (H_J). The scalar coupling between different nuclei arise due to the mediating electrons. In this thesis, single-qutrit NMR spectroscopy is being used to perform the computational tasks. The experimental tool remains liquid state NMR, however the spin-1 is oriented in a liquid crystal thus providing an anisotropic environment. The anisotropic environment retains the quadrupolar effects of the spin-1. This situation is treated in detail in Chapter 3.

NMR signal

The technique of NMR makes use of the rotating-wave approximation [71] wherein the z-axis of the frame of reference coincides with that of the precessing magnetization vector. T_1 is the spin-lattice relaxation time, which corresponds to the time taken for building up of the magnetization once the magnetic field is switched on, and T_2 is the spin-spin relaxation time that depends upon the decay of the transverse component of the magnetization vector after the implementation of radio-frequency pulse. An explicit treatment of the dynamics of a single spin-$\frac{1}{2}$ is analytically described by the

Bloch equations [69]. A simplified picture of an NMR signal acquisition is described below:

When an NMR active nucleus is kept inside a magnetic field (say along the z-axis), it begins to precess about the direction of the magnetic field. This is then acted upon by an external field in the form of a radio-frequency pulse, through coils lying in the xy-plane. The radio-frequency pulse makes the nucleus flip from its equilibrium position. As soon as this radio-frequency pulse implementation is over, the spin tends to regain its equilibrium position. Due to the corresponding change in the magnetic field, the role of electromagnetic induction comes into play as a result of which a voltage signal is developed. This voltage signal is the free induction delay (FID) in time domain [39] that consists of an oscillating (ω dependent) and a decaying part (T_2 dependent): $f(t) \propto e^{\iota\omega t} \exp^{-t/T_2}$. Fourier transformation of this signal transforms this time-domain signal to the frequency domain spectral line, a Lorentzian. The signal in NMR is acquired in the transverse plane along two perpendicular directions, that captures the information regarding the phase of the line. One of the axes is thus referred to as 'real' and another as the 'imaginary' axis. The NMR spectral line that consists of only the real part is known as the absorptive Lorentzian, while the spectral line that possesses only the imaginary part corresponds to a dispersive Lorentzian signal [39, 40, 70]. Ordinarily, an NMR spectral line is a combination of the absorptive and dispersive Lorentzian functions. One can inter-convert these absorptive and dispersive spectral lines by correcting the phase of the spectrum.

1.2 NMR Quantum Computing

Qubits in NMR are realized by spin-$\frac{1}{2}$ nuclei. A spin-$\frac{1}{2}$ nucleus when placed in a magnetic field has two possible orientations corresponding to spin quantum numbers $\pm\frac{1}{2}$. One can associate the computational basis vectors $|0\rangle$ and $|1\rangle$ with these two spin-states. A single NMR-qubit is governed by the Hamiltonian $H = \nu I_z$, where $\nu = \frac{\gamma B}{2\pi}$ is the Larmor precession frequency and $I_i = \frac{1}{2}\sigma_i$ ($i \in \{x, y, z\}$) is the single-qubit product operator corresponding to the Pauli matrix σ_z. Thus $+\frac{1}{2}\nu$ and $-\frac{1}{2}\nu$ are the energy eigenvalues associated with a single NMR-qubit corresponding to the eigenvectors $|0\rangle$ and $|1\rangle$ respectively. For the case of two-qubits, the Hamiltonian (under

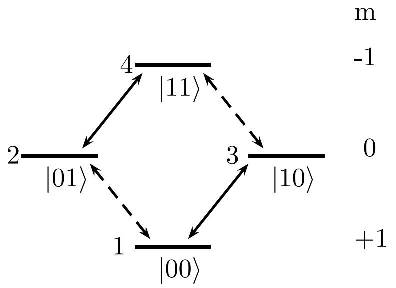

Figure 1.1: Two-qubit energy level diagram where energy levels numbered (1-4) are labelled with computational basis. Single quantum transitions between levels 1-2 and 3-4 correspond to second qubit, and the transitions between levels 1-3 and 2-4 correspond to the first qubit.

secular approximation) of the system assumes the form:

$$H = \nu_1 I_{1z} + \nu_2 I_{2z} + J_{12} I_{1z} I_{2z}. \tag{1.3}$$

The elements of product operators in a system of 'n' qubits are obtained by the tensor products [1] between the Hilbert spaces of individual qubits. For two qubits, $I_{1i} = \frac{1}{2}\sigma_i \otimes I_{2\times 2}$ and $I_{2i} = I_{2\times 2} \otimes \frac{1}{2}\sigma_i$ ($I_{2\times 2}$ is the the 2×2 identity operator). The eigenvectors and eigenvalues for two NMR qubits (Equation (1.3)) are given as: $|00\rangle$: $\frac{1}{2}(\nu_1 + \nu_2 + \frac{1}{2}J_{12})$; $|01\rangle$: $\frac{1}{2}(\nu_1 - \nu_2 - \frac{1}{2}J_{12})$; $|10\rangle$: $\frac{1}{2}(-\nu_1 + \nu_2 - \frac{1}{2}J_{12})$ and $|11\rangle$: $\frac{1}{2}(-\nu_1 - \nu_2 + \frac{1}{2}J_{12})$. Energy level diagram for a two-qubit system is shown in Figure 1.1 where the states numbered (1-4) are shown labeled in the computational basis. Total spin (m) of the two-parties corresponding to each energy level is shown on the right. As per selection rule, $\Delta m = \pm 1$, there are four single quantum transitions that correspond to the spectral lines in NMR. Transitions of the first qubit occur at frequencies $\nu_1 \pm \frac{1}{2}J_{12}$, which are shown as solid line in Figure 1.1. Transitions of the second qubit occur at $\nu_2 \pm \frac{1}{2}J_{12}$ and are shown as dotted lines in Figure 1.1.

1.2.1 Initialization

In quantum computation with liquid state NMR techniques, the sample volume typically lies in the range of 400 - 600 μl. Thus considering the Avogadro number (according to mole concept, 1 mole of a substance contains Avogadro number of particles, which is 6.023×10^{23} [72]), at normal temperature and pressure (NTP: temp.=20 deg.C, pressure=1atm) there are approximately $10^{17} - 10^{18}$ copies of NMR qubits in the sample [39]. At thermal equilibrium, these NMR qubits obey the Boltzmann distribution [1, 73]. Thus one can associate an occupation index or populations to each energy eigenstate of an n-qubit system. The corresponding n-qubit state is therefore a mixed state. However, for many quantum computational purposes, one requires pure states. In NMR, a pure state requires zero temperature, at which the occupancy of the lowest n-qubit energy eigenstate is 1, while all other eigenstates have zero occupation index. However in NMR, the intensity of the transitions between two energy levels are based on the population difference instead of the actual populations of the energy levels. Thus NMR measurements are based on the relative populations and not the actual populations, which provides a base to the concept of a pseudo-pure state.

A pseudo-pure state is a state in which one of the energy levels exhibits a different population against a uniform background of populations. A pseudo-pure state (ρ_n) of an n-qubit system corresponding to pure state $|\psi\rangle\langle\psi|$ is written as:

$$\rho_n = \frac{1-\epsilon}{N} I_{N\times N} + \epsilon|\psi\rangle\langle\psi| \tag{1.4}$$

where $N = 2^n$ is the dimension of the system, ϵ ($\sim 10^{-5}$) is the purity associated with the state ρ_n, and $I_{N\times N}$ is the $N \times N$ identity operator. Second term on the right hand side of Equation (1.4) is the deviation density matrix, which is the pure component of the pseudo-pure state (ρ_n). All the computational tasks are analysed considering only the deviation part of the n-qubit density matrix.

A pseudo-pure state in NMR can be attained by several ways with the same underlying idea of equating the populations of $N - 1$ energy levels, while one energy level is made to attain a different value of the population. Thus the system is initialized in one of the basis states of n-qubit system. Different techniques to create pseudo-pure states in NMR comprise: spatial averaging, temporal averaging and logical labeling. Spatial averaging technique makes use of selective transitions (RF pulses) that perform various unitary operations and gradients, that dephase the unwanted coherences such that the ensemble average over space results into a pseudo-pure state [74]. Temporal averaging technique uses fewer selective pulses performing a set of different experiments, to obtain various different population distributions. The corresponding spectra are then added with different weights to obtain the desired pseudo-pure state [1]. Logical labeling makes use of a larger Hilbert space, wherein the basis states are re-labeled alongwith a set of RF pulses. The re-labeling is done in such a manner that the Hilbert space of interest gives rise to the desired pseudo-pure state [75].

The idea of n-qubit pseudo-pure states is extended to a hybrid-qudit system where the pseudo-pure state assumes the same form as in Equation (1.4), however the total Hilbert space dimension, $N = \Pi_{i=1}^{n} m_i$ with i^{th} (individual) qudit is of dimension 'm_i'. In this thesis, spatial averaging techniques have been used to create pseudo-pure states of three-qubit, single-qutrit, and qubit-qutrit systems.

1.2.2 Quantum gates

Quantum gates are unitary operators which, for a single qubit, can be decomposed as a set of rotations in three-dimensional real space. This set of rotations is experimentally implemented in NMR via radio-frequency pulses of specific energy causing the spin to rotate by a specific angle about the desired axis. The quantum gates can be broadly classified as: single qubit gates and multi-qubit gates. The brief description of these two classifications are given below.

Single-qubit gates

A single-qubit gate acts on one qubit, which in NMR is realized by a set of spin-selective pulses. In addition to an arbitrary rotation operator (which is the most general form of a single-qubit gate), single-qubit gates include Hadamard gate, phase-shift gate, and NOT gate.

- Hadamard gate creates the superposition of the bases states such that $|0\rangle \rightarrow \frac{1}{\sqrt{2}}(|0\rangle + |1\rangle)$ and $|1\rangle \rightarrow \frac{1}{\sqrt{2}}(|0\rangle - |1\rangle)$. An effective Hadamard operation in NMR is implemented by a single spin-selective pulse of 90 degrees about y-axis $(\frac{\pi}{2}_y)$. An explicit form of the Hadamard gates is given as:

$$H = \frac{1}{\sqrt{2}} \begin{pmatrix} 1 & 1 \\ 1 & -1 \end{pmatrix}$$

- A phase-shift gate creates relative phase between the two basis vectors of a single-qubit. This is achieved by a z-rotation $((\phi_z))$ of the single-qubit. The explicit form of the gate is given as:

$$Ph(\phi) = \begin{pmatrix} 1 & 0 \\ 0 & e^{\iota\phi} \end{pmatrix}$$

- A NOT gate flips the populations between the two basis vectors. In NMR this is achieved by a 180 degree pulse about x-axis (π_x). An explicit form of this gate is:

$$NOT = \begin{pmatrix} 0 & 1 \\ 1 & 0 \end{pmatrix}$$

Multi-qubit gates

A controlled-rotation gate (CROT$_{ij}$) is a two-qubit gate in which one of the qubits controls the rotation of other qubit. An ideal controlled rotation gate CR$_{ij}$, where 'i' is control and 'j' is the target qubit is implemented by the sequence [76]: $(\theta)^{j}_{-y}\,(\frac{\pi}{2})^{i,j}_{z}\,\frac{1}{4J_{ij}}\,(\pi)^{i,j}_{y}\frac{1}{4J_{ij}}\,(\pi)^{i,j}_{y}\,(\theta)^{j}_{-y}\,(\pi)^{i,j}_{z}$; where $(\theta)^{i}_{\alpha}$ denotes an rf pulse of flip angle θ and phase α applied on the ith qubit, $(\beta)^{i,j}_{\alpha}$ denotes an rf pulse of flip angle β and phase α applied simultaneously on both the ith and jth qubits, and $\frac{1}{4J_{ij}}$ denotes an evolution period under the coupling Hamiltonian (using standard NMR notation). For $\theta = \frac{\pi}{2}$, and assuming $(i < j)$, the above sequence decomposes to the controlled-NOT (CN$_{12}$) gate, whose explicit matrix form is given as:

$$CN_{12} = \begin{pmatrix} 1 & 0 & 0 & 0 \\ 0 & 1 & 0 & 0 \\ 0 & 0 & 0 & 1 \\ 0 & 0 & 1 & 0 \end{pmatrix}.$$

There also exist simpler sequences implementing a CN$_{12}$ gate such as: $(\frac{\pi}{2})^{2}_{x}\,\frac{1}{2J}\,(\frac{\pi}{2})^{2}_{-y}$, alongwith the development of certain phase differences. These phase differences can be accounted for in the overall pulse-sequence.

This thesis rigorously uses two-qubit controlled rotation gates of various different angles implemented about an arbitrary axis ($\hat{n} = \cos(\phi)\hat{x} + \sin(\phi)\hat{y}$). A specific controlled-phase gate has been used in this thesis that corresponds to the controlled-rotation about z-axis. In addition, in the second chapter of this thesis, certain novel techniques have been introduced that simultaneously implement a three-qubit controlled-controlled-phase gate and a controlled-controlled-rotation gate with a single transition-selective pulse.

1.2.3 Quantum state tomography

Tomography is the process of reconstruction of the complete density matrix of the state of the system via a set of experiments. For an n-qubit system, the dimension of operator space is ($2^n \otimes 2^n$), thus each n-qubit state has 2^{2n} complex coefficients. Under the constraints of Hermiticity ($\rho^\dagger = \rho$) and the normalization of a quantum state ($Tr\,[\rho] = 1$), one is left with ($2^{2n} - 1$) number of independent real variables. Thus complete characterization of an n-qubit state needs the determination of these ($2^{2n}-1$) variables. The operator space basis for n-qubits is constituted by the tensor product between the elements of single-qubit product operators ($I_i = \frac{1}{2}\sigma_i;\ i \in \{x, y, z\}$) and the (2 $\otimes$ 2) Identity operator. Thus a most general n-qubit state is written by linear combination of product operators serving as the bases, alongwith real coefficients. The real coefficients correspond to the expectation values of the respective product-operator elements in the given n-qubit state. Thus quantum state reconstruction is decomposed to the evaluation of the various expectation values.

NMR signal in time domain for a state ρ (n qubits) is given as:

$$S(t) \propto Tr[e^{-\iota Ht}\rho e^{\iota Ht}\Sigma_{k=1}^{n}(I_{kx} + \iota I_{ky})] \tag{1.5}$$

where H is the Hamiltonian of the system 1.2, and I_{kx} (I_{ky}) is the product operator element of the k^{th} spin corresponding to Pauli x (y) operator. The NMR signal of a given state corresponds to the expectation values of the $e^{\iota Ht}I_{kx}e^{-\iota Ht}$ and $e^{\iota Ht}I_{ky}e^{-\iota Ht}$, which after Fourier transformation occur as the intensities of spectral lines at respective resonance frequencies [77, 78]. The static part of the Hamiltonian remains fixed, however the RF part of the Hamiltonian can be modified via various radio-frequency pulses to obtain the complete set of $2^{2n} - 1$ expectation values. Various tomographic protocols have been provided that adopt slightly different ways for state reconstruction [77, 78, 79]. This thesis makes use of the tomography scheme proposed in [78] for state construction for two and three-qubit systems. For qutrit-tomography, and a qubit-qubit-qutrit system the proposed tomography schemes are discussed in Chapters 3 and 5 of the present thesis.

The experimentally reconstructed state is checked for its overlap with the theoretically expected state, which is measured in terms of the fidelity. The fidelity measure used to compute the resemblance of the experimental and theoretical density matrices [13] is defined by:

$$F = \frac{Tr\left(\rho^{\dagger}_{theory}\rho_{expt}\right)}{\sqrt{Tr(\rho^{\dagger}_{theory}\rho_{theory})}\sqrt{Tr(\rho^{\dagger}_{expt}\rho_{expt})}} \tag{1.6}$$

where ρ_{theory} and ρ_{expt} are the theoretically expected and experimentally obtained density matrices respectively. All through this thesis, Equation (1.6) has been used to find the degree of overlap between the theoretically expected and the experimentally obtained states.

1.3 Focus of the thesis

The main motivation of the present thesis is to implement various quantum computing protocols on NMR qudits (d-level quantum systems), and to explore their inherent computational resources which are responsible for efficiently performing a quantum computational task. This study has been carried out in two main parts. The first part of the thesis focuses on various aspects of multiqubit entanglement in a system of three qubits. Entanglement [80, 81] plays a key role in various quantum computational tasks and provides a speedup over their classical counterparts. A system of two-qubits is the smallest system exhibiting entanglement [80, 81]. However the concept of multi-party entanglement requires at least three qubits. In a system of three qubits, there exist two entanglement classes namely: GHZ-class and W-class of states, which are inequivalent under stochastic local operations and classical communication (SLOCC) [80, 81, 82, 83]. Adopting an NMR experimental approach, three-qubit generic pure states are created and the GHZ-class and W-class of entangled states are studied. The purpose of this study is to explore how a multi-party entangled state stores information in the case of three qubits. Also an experimental evidence is provided for the unforeseen entanglement properties in a recently proposed W-superposition state [84] of three qubits which can be obtained from the GHZ state via SLOCC.

The second part of the thesis is focused on quantum computation with higher dimensional systems i.e. qudits (d-level quantum system, $d > 2$) with an emphasis on a qudit with $d = 3$ (qutrit). A qutrit is the smallest indivisible quantum system that provides speedup in quantum computational tasks. There is no role of non-locality in an indivisible system and thus a more profound computational resource is expected to exist. A possible quantum resource is "contextuality" whose idea was first proposed by E. Specker in 1960 [85]. Contextuality [86, 87] refers to the context of a measurement, according to which a measurement of an observable in different contexts may yield different results. The qutrit is the smallest quantum system possessing contextuality. This property makes a qutrit a particularly important system for computation.

To begin with, Majorana representation [88] for a spin-1 is explored for geometrical realization of a qutrit, and to study its dynamics under various quantum operations. In the Majorana representation, a qutrit is represented by '2' points on the Majorana sphere. A geometrical realization of the single-qutrit magnetization vector is also developed in the context of Majorana representation. Ternary quantum gates for qutrit-computing are related to the dynamics of a pair of points representing spin-1 on the 'Majorana sphere'. A close observation of the trajectories of such pairs of points resulting from various logic gates leads to the development of the corresponding NMR pulse sequences. Quantum computational resource in single-qutrit computing, which is attributed to contextuality is studied in detail, and verified experimentally on an NMR qutrit. Further, exploiting the contextuality a single qutrit based quantum algorithm is discussed that provides speedup over its classical counterpart. Moving towards higher dimensional quantum systems, a qudit-specific implementation of the quantum Fourier transform (QFT) is carried out, which is an important step toward the realization of qudit-based quantum computers. The last part of the thesis is focused on NMR methodology development using numerical pulses optimized using GRAPE [89, 90] to carry out different computational tasks for a qudit computer as well as the SO-FAST [57, 59] type of 2D NMR fast pulsing sequences.

1.3.1 Organization of the thesis

This thesis deals with the study of novel aspects of quantum computational resources, and the experimental implementations of various quantum computing protocols on three-qubit, single-qutrit and hybrid qubit-qudit NMR quantum computers. The contents of the present thesis have been divided into seven chapters and an appendix.

Chapter 2 describes the creation of three-qubit generic pure state using NMR and its tomographic reconstruction from its reduced two-party states. Using this general experimental protocol, three-qubit GHZ-state, W-state, and W-superposition states are experimentally constructed and their entanglement properties are studied. This chapter is summarized with an experimental evidence to the unique entanglement properties of the W-superposition state. Chapter 3 focuses on the geometrical and the experimental realization of the structure and dynamics of a single-qutrit . The geometrical picture of a single-qutrit is based on the Majorana representation, which is used to the dynamics of a spin-1 under SO(3) and SU(3) transformations. An intuitive geometrical picture of single-qutrit magnetization vector is also developed in the context of Majorana representation. Chapter 4 discusses single-qutrit contextuality, which is the quantum computational resource inherited by a single indivisible three-level quantum system. Further, exploiting the contextual nature of a qutrit, a single qutrit based quantum algorithm is discussed, that determines the parity of a permutation among three objects. Chapter 5 is focused on the design and implementation of NMR pulse sequences for various single qudit and controlled hybrid qudits gates. This is followed by the implementation of a hybrid quantum Fourier transform on a qubit-qubit-qutrit NMR emulator. Chapter 6 is focused on NMR methodology development using numerically optimized pulses. The usefulness of the numerical pulses is exploited to optimize quantum gates for qudit computing and the implementation of 2D fast pulsing sequences for biomolecular NMR. Chapter 7 consists of the concluding remarks and the possible future extensions of the research directions. Appendix A describes the practicalities involved in the orientation of a single-qutrit in the anisotropic environment of the liquid crystal.

Chapter 2

Generic three-qubit states and their reconstruction from two-party reduced states

2.1 Introduction

A qubit is the smallest possible entity for quantum computation. As one proceeds from one qubit to two qubits, there arises the concept of entanglement, which is an interesting non-local property that makes an $n-$qubit system a useful computational resource [5, 81]. Increasing the number of qubits, does not merely increase the dimension of the system, but also leads to new quantum features. The property of entanglement cannot be associated with a single party, and in the case of two qubits, there is only one unique way in which the two qubits can get entangled with each other. The three-qubit system is the smallest system that possesses multipartite entanglement. Three-qubit states can be classified as separable (those which can be written as a tensor product of constituents), bi-separable (two qubits out of three are entangled) and non-separable states (which cannot be written as the product of constituent qubit states) [91, 92, 93].

In three-qubit systems, there exist two entanglement classes namely the Greenberger-Horne-Zeilinger (GHZ) class and the Werner (W) class of states [94], which are inequivalent under stochastic local operations and classical communication (SLOCC). The entanglement of the GHZ state is fragile under qubit loss while the W-state residual bipartite entanglement is robust against qubit loss. GHZ class of states possess genuine three-party entanglement. Thus upon tracing out one of the parties in a GHZ state, we are left with no more entanglement [80, 81]. On the other hand, the W-class of states consist of both two-party as well as three-party entanglement. Three party entanglement content in a W-class of states can be attributed to its non-zero tangle (quantification of three-party correlations), while the non-zero values of its bipartite concurrence measurements [80, 81] verify the involvement two-party entanglement as well. Thus some of the entanglement in W-class of states is retained even if one of the parties is traced out. Gaining the insights from the entanglement properties of the GHZ and W-class of states, entanglement properties of a $\mathrm{W}\bar{\mathrm{W}}$ state are studied. A $\mathrm{W}\bar{\mathrm{W}}$ state consists of a superposition of the maximally entangled W state and its obverse $\bar{\mathrm{W}}$ (obtained by flipping 0s and 1s in the W state). Both these states (W and $\bar{\mathrm{W}}$) belong to the W-class of states, however a recently unearthed fact states that a $\mathrm{W}\bar{\mathrm{W}}$ state is inter-convertible with the maximally entangled GHZ state under SLOCC, but it stores entanglement very differently [84].

In this chapter, the state space of three qubits is experimentally explored on an NMR quantum information processor. This chapter has three main results: (a) A scheme to create generic states of three qubits is proposed and is implemented on an NMR quantum computer. (b) A curious fact about three-qubit states is demonstrated experimentally, where for almost all pure states, the two-qubit reduced states can be used to reconstruct the full three-qubit state [95, 96, 97]. This method of reconstruction is experimentally demonstrated for generic three-qubit states, W-state, and $\mathrm{W}\bar{\mathrm{W}}$ state by comparing them with their directly tomographed three-qubit states. (c) It is experimentally demonstrated that although the $\mathrm{W}\bar{\mathrm{W}}$ state is inter-convertible with the GHZ state, it stores entanglement very differently. Three-qubit entanglement in the $\mathrm{W}\bar{\mathrm{W}}$ state can be obtained from its reduced two-party states whereas entanglement in the GHZ state is irreducible in terms of two-party correlations. These interesting features of multi-qubit entanglement namely, that two different entangled states belonging to the same SLOCC class can yet have their correlations exhibiting contrasting irreducible properties is demonstrated experimentally.

2.2 Generic state construction

A generic three-qubit state, also termed as a canonical state, was proposed by Acin et al. [83], that exhibits minimal requirements to specify a three-qubit pure state. Every three-qubit state can be obtained from this generic state via local (single qubit) unitary operations. The permutation symmetric canonical (generic) state for three qubits is given by:

$$|\psi\rangle = a_1|000\rangle + a_2|001\rangle + a_3|010\rangle + a_4|100\rangle + a_5 e^{i\phi}|111\rangle; \quad a_i \geq 0; \quad \sum_i a_i^2 = 1 \tag{2.1}$$

where, the coefficients $a_i s$ are positive real numbers. Thus four of the basis vectors of this canonical state have real coefficients while the phase $\phi \in [0, 2\pi]$ gives rise to a complex coefficient of the vector $|111\rangle$. The normalization condition leads to reduction of one parameter and hence the minimal construction of $|\psi\rangle$ state involves five independent non-zero, real parameters (four moduli and one phase).

In this chapter, an experimental construction of three-qubit generic state is discussed using a set of single as well as multi-qubit gates on a three-qubit pseudo-pure state. These gates are one-parameter unitary transformations that can be decomposed elegantly in terms of NMR pulses. The global phase is not detectable in NMR experiments and is thus ignored throughout in gate implementations.

A single-qubit unitary transformation is represented by an operator $U^j_{2\theta}$, which is a separable, non-entangling transformation belonging to the $SU(2)$ group which implements a rotation by an arbitrary angle θ on the j^{th} qubit, leading to a generalized superposition state of the qubit involved. Operator $U^j_{2\theta} = e^{-\iota 2\theta I_{jr}}$ (which rotates the state by an angle 'θ') in NMR, is realized by a qubit-selective pulse on the j^{th} qubit by an angle 2θ about the r^{th} axis.

A two-qubit quantum gate is a unitary transformation in which one of the qubits controls the gate operation. A two-qubit controlled rotation gate (CR$^{2\theta}_{ij}$) implements a rotation by an arbitrary angle θ, on the j^{th} qubit, with the i^{th} qubit as control. The NMR pulse sequence for an ideal controlled rotation implementation on the j^{th} qubit by an angle θ about y-axis is given as ($i < j$): $(\theta)^j_{-y}\,(\frac{\pi}{2})^{i,j}_z\,\frac{1}{4J}\,(\pi)^{i,j}_y\,\frac{1}{4J}\,(\pi)^{i,j}_y\,(\theta)^j_{-y}\,(\pi)^{i,j}_z$. This sequence reduces to the controlled-NOT operation for $\theta = \frac{\pi}{2}$. As can be seen from the above sequence, there are two z-rotations each on the control (i^{th}) and the target (j^{th}) qubits. The implementation of z-cascades increases the experimental time and introduces experimental imperfections. We instead implement a shorter pulse sequence composed of $(\theta)^{j}_{-y}\,\frac{1}{4J}\,(\pi)^{i,j}_{y}\,\frac{1}{4J}\,(\pi)^{i,j}_{y}\,(\theta)^{j}_{-x}$. This sequence creates the desired state along with a relative phase among different spins which can be kept track of or can be eliminated by spin-selective z-rotations. Further decrease in the experimental time is obtained by pairwise avoiding π pulses on i^{th} and j^{th} qubits at the end of J_{ij}-evolution evolution in controlled-rotation (CR_{ij}) and controlled-not gates (CN_{ji}).

A generalized three-qubit controlled-controlled-rotation gate is a three-qubit controlled operation in which two of the qubits act as control and the third one serves as the target. Depending upon the axis of rotation, it can be termed as a controlled-controlled-rotation or a controlled-controlled-rotation phase-shift gate. $\mathrm{CCN}_{12,3}$ implements a controlled-controlled-NOT (Toffoli) gate on the 3rd qubit i.e. it flips the state of qubit 3, if and only if both qubits 1 and 2 are in the $|1\rangle$ state; $\mathrm{Ph}^{\phi}_{12,3}$ is a controlled-controlled-phase shift gate with $1, 2$ as control qubits and 3 being the target qubit. NMR pulse sequence for the implementation of a three-qubit non-separable gate implementation requires the three coupling evolutions to take place. However, the same result can also be obtained effectively by the use of a transition-selective pulse [98, 99].

In this chapter, an explicit sequence of single and multiqubit gates is proposed that lead to the construction of a three-qubit generic pure state starting from a three-qubit pseudo-pure state. The sequence of gates with four real parameters $\alpha, \beta, \gamma, \delta \in [0, \frac{\pi}{2}]$ representing the amplitude parameters $a_1 \cdots a_5$ and the phase $\phi \in [0, 2\pi]$ leading to the construction of a generic three-qubit state is detailed below:

$$
\begin{aligned}
|000\rangle \quad &\xrightarrow{U^{1}_{2\alpha}} \quad \cos\alpha|000\rangle + \sin\alpha|100\rangle \\
&\xrightarrow{\mathrm{CR}^{2\beta}_{12}} \quad \cos\alpha|000\rangle + \sin\alpha\cos\beta|100\rangle + \sin\alpha\sin\beta|110\rangle \\
&\xrightarrow{\mathrm{CN}_{21}} \quad \cos\alpha|000\rangle + \sin\alpha\cos\beta|100\rangle + \sin\alpha\sin\beta|010\rangle \\
&\xrightarrow{\mathrm{CR}^{2\gamma}_{13}} \quad \cos\alpha|000\rangle + \sin\alpha\cos\beta\cos\gamma|100\rangle + \sin\alpha\cos\beta\sin\gamma|101\rangle + \sin\alpha\sin\beta|010\rangle \\
&\xrightarrow{\mathrm{CN}_{31}} \quad \cos\alpha|000\rangle + \sin\alpha\cos\beta\cos\gamma|100\rangle + \sin\alpha\cos\beta\sin\gamma|001\rangle + \sin\alpha\sin\beta|010\rangle \\
&\xrightarrow{\mathrm{CR}^{2\delta}_{12}} \quad \cos\alpha|000\rangle + \sin\alpha\cos\beta\cos\gamma\cos\delta|100\rangle + \sin\alpha\cos\beta\cos\gamma\sin\delta|110\rangle \\
&\qquad\quad + \sin\alpha\cos\beta\sin\gamma|001\rangle + \sin\alpha\sin\beta|010\rangle \\
&\xrightarrow{\mathrm{CCN}_{12,3}} \quad \cos\alpha|000\rangle + \sin\alpha\cos\beta\cos\gamma\cos\delta|100\rangle + \sin\alpha\cos\beta\cos\gamma\sin\delta|111\rangle \\
&\qquad\quad + \sin\alpha\cos\beta\sin\gamma|001\rangle + \sin\alpha\sin\beta|010\rangle
\end{aligned}
$$

$$\begin{aligned}\xrightarrow{\mathrm{Ph}^{\phi}_{12,3}}\quad & \cos\alpha|000\rangle + \sin\alpha\cos\beta\sin\gamma|001\rangle + \sin\alpha\sin\beta|010\rangle \\ & + \sin\alpha\cos\beta\cos\gamma\cos\delta|100\rangle + e^{\iota\phi}\sin\alpha\cos\beta\cos\gamma\sin\delta|111\rangle\end{aligned} \tag{2.2}$$

The system is initialized in a pseudo-pure state $|000\rangle$ which is the lowest energy three-qubit state in the computational basis. A single qubit unitary operator $U^1_{2\alpha}$ on the first qubit by an angle α brings in a superposition of two energy eigenstates. The following controlled rotation gate $CR_{12}(2\beta)$ rotates the second qubit by angle β about $y-$axis with first qubit as control. The resulting state is in superposition of $|000\rangle$, $|100\rangle$, and $|110\rangle$ eigenstates. In the next step, level $|110\rangle$ is transformed to $|010\rangle$ via operator CN_{21}. Further, a sequential implementation of a pair of two-qubit controlled rotation gates $CR_{13}(2\gamma)$ and CN_{31} respectively results into a state containing superposition of four energy levels $|000\rangle$, $|100\rangle$, $|001\rangle$, and $|010\rangle$. This state undergoes a $CR_{12}(2\delta)$ implementation which splits the basis vector $|100\rangle$ into the superposition of $|100\rangle$ and $|110\rangle$. A transition-selective pulse on the transition $|110\rangle$-$|111\rangle$ of the third qubit gives rise to a state with four desired parameters (four moduli) and resembles the generic three-qubit state with real coefficients. A factor of phase ϕ in $|111\rangle$ is introduced by a three-qubit controlled-controlled phase-shift gate $Ph^{\phi}_{12,3}$. The final state obtained is the expected three-qubit generic pure state. The normalization condition is automatically satisfied as the normalization will be preserved under these unitary operations.

Thus a three-qubit generic state with five independent parameters $(\alpha, \beta, \gamma, \delta, \phi)$ is obtained using a sequence of unitary operators. Comparing the three-qubit generic state in Equations (2.1) and (2.2), one can obtain the coefficients:

$$\begin{aligned} a_1 &= \cos\alpha, \\ a_2 &= \sin\alpha\cos\beta\sin\gamma, \\ a_3 &= \sin\alpha\sin\beta, \\ a_4 &= \sin\alpha\cos\beta\cos\gamma\cos\delta, \\ a_5 &= e^{\iota\phi}\sin\alpha\cos\beta\cos\gamma\sin\delta, \end{aligned} \tag{2.3}$$

where $\alpha, \beta, \gamma, \delta \in [0, \frac{\pi}{2}]$ and $\phi \in [0, 2\pi]$. The general scheme to obtain a three-qubit generic pure state, starting from a pseudo-pure state is shown in the quantum circuit in

Figure 2.1(a).

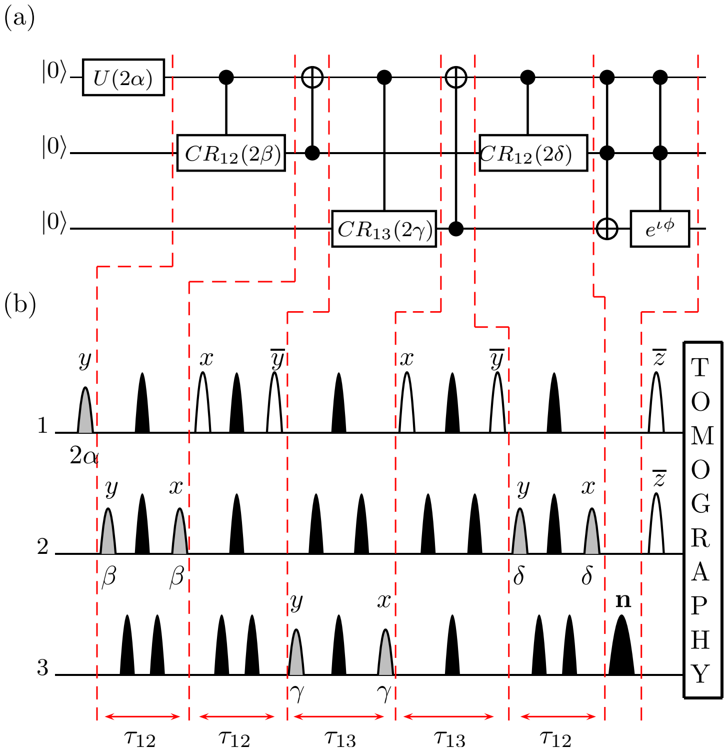

Figure 2.1: (a) Quantum circuit showing the sequence of implementation of the rotation, controlled-rotation, controlled-NOT, controlled-controlled-NOT and controlled-controlled-phase gates required to construct a generic state and (b) NMR pulse sequence to implement a general three-qubit generic state; τ_{ij} is the evolution period under the J_{ij} coupling. The 180^0 pulses are represented by filled (black) and 90^0 pulses are represented by unfilled (white) pulse shapes The other pulses are labeled with their specific flip angles and phases. The last pulse (broad black) on the third qubit is a transition-selective 180^0 pulse on the $|110\rangle$ to $|111\rangle$ transition about an arbitrary axis $\hat{n}$ which is inclined at angle $(\phi + 90)$ with the x-axis. The last two pulses on the first and second qubits are 90^0 z-rotations, to compensate the extra phases acquired (as described in the text).

The NMR pulse sequence to construct the generic three-qubit state starting from the pseudo-pure state $|000\rangle$ is given in Figure 2.1(b). Refocusing pulses are used in the middle of all J-evolution periods to compensate for chemical shift evolution. Pairs of π pulses have been inserted at 1/4 and 3/4 of the J-evolution intervals to eliminate undesirable evolution due to other J-couplings. The 180^0 pulses are represented by filled (black), and 90^0 pulses are represented by unfilled (white) pulse shapes while the other pulses are labeled with their specific flip angles and phases. The two-qubit controlled rotation (CR_{ij}) gates are implemented in NMR using the pulse sequence given in section 2.2. The relative phase gained at the end of each controlled operation is kept track of and is compensated by implementing z-rotations on the spins at the end of the sequence. Three-qubit state that is obtained after the implementation of transition-selective pulse is given as:

$$\begin{aligned}&\cos\alpha|000\rangle + \sin\alpha\cos\beta\sin\gamma|001\rangle + \iota\sin\alpha\sin\beta|010\rangle\\&+\iota\sin\alpha\cos\beta\cos\gamma\cos\delta|100\rangle - e^{\iota\phi}\sin\alpha\cos\beta\cos\gamma\sin\delta|111\rangle\end{aligned} \tag{2.4}$$

This state is close to a generic three-qubit state, despite relative phases between its coefficients. These extra phases are removed by $(-90^0)_z$ pulses on first and second qubits. These compensatory z-rotations eliminate all the unwanted phases acquired in due course of the implementation of this sequence. The last two gates in the circuit, namely the controlled-controlled NOT (Toffoli) gate and the controlled-controlled phase gate were simultaneously implemented using a single transition-selective π pulse, applied about an arbitrary axis of rotation $\hat{n}$ (wide black pulse in Figure 2.1(b)) [98, 99]. A three-qubit controlled-controlled NOT (Toffoli) gate can be experimentally realized by a transition-selective $(\pi)_y$ pulse between energy levels $|110\rangle$ and $|111\rangle$. A transition-selective pulse $(\pi)_{\hat{n}}$ about an arbitrary axis of rotation $\hat{n} = \cos\phi'\hat{x}+\sin\phi'\hat{y}$, on the other hand, introduces an extra phase of $e^{\iota\phi}$ ($\phi' = \phi+\pi/2$). Hence, $(\pi)_{\hat{n}}^{|110\rangle\rightarrow|111\rangle}$ when applied on the basis vector $|110\rangle$, results in the state $e^{\iota\phi}|111\rangle$. This is an ingenious method to reduce the experimental time, and comes in handy in completing the circuit implementation before the decoherence begins to introduce significant distortions.

A desired three-qubit state can be created by choosing different values of the non-local parameters α, β, γ, $\delta \in [0, \frac{\pi}{2}]$ and $\phi \in [0, 2\pi]$. In this chapter, construction of an arbitrary three-qubit generic state, a special $\mathrm{W\bar{W}}$ state (that belongs to the generalized GHZ class of states) as well as the maximally entangled GHZ and W states is performed on a three-qubit NMR quantum computer.

2.3 A three-qubit NMR quantum computer

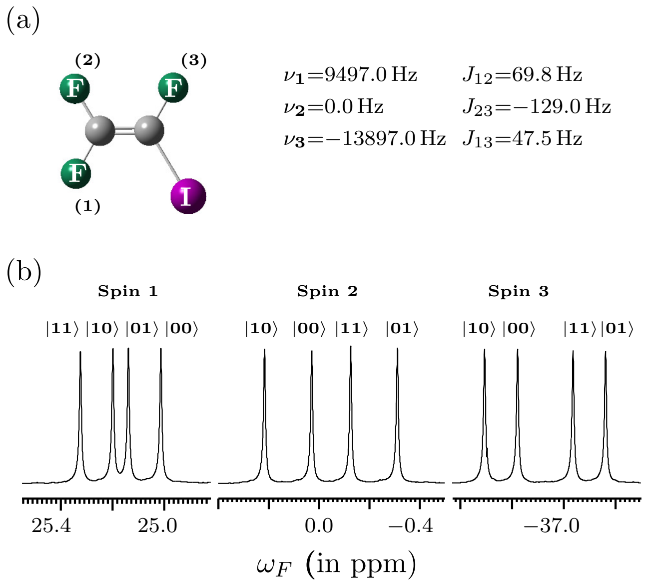

Figure 2.2: (a) Molecular structure and NMR parameters (chemical shifts and J-coupling in Hz) and ^{19}F NMR spectrum of trifluoroiodoethylene. The three fluorine spins correspond to the three-qubit system. (b) The 1D ^{19}F NMR thermal equilibrium spectrum obtained after a $\frac{\pi}{2}$ readout pulse. The NMR transitions of each qubit are labeled by the corresponding logical states of the other two qubits.

The three-qubit system that is used here for NMR quantum information processing is the molecule trifluoroiodoethylene. 1-Iodo-1,2,2-trifluoroethene or trifluoroiodoethylene molecule is obtained by replacing three Hydrogen atoms of the smallest alkene by three fluorine atoms, and the fourth hydrogen atom by another halogen iodine. Trifluoroiodoethylene molecule (purchased from Alfa Aesar) is a small, light-sensitive molecule with a boiling point of around 30^0 C. Three-qubit NMR quantum computer is constructed by dissolving the trifluoroiodoethylene molecule in deuterated acetone, where three qubits are encoded using the ^{19}F nuclei. ^{19}F nucleus is an NMR active nucleus with sensitivity lying quite close to that of ^{1}H, and exists in 100% natural abundance. The gyromagnetic ratio of the ^{19} F nucleus is 40.052 MHz/T and it resonates at a frequency of 376 MHz in a magnetic field of 9.4 T (this value of magnetic field corresponds to a 400 MHz NMR spectrometer).

The Hamiltonian of the three-qubit system in the rotating frame is given by

$$H = \sum_{i=1}^{3} \nu_i I_{iz} + \sum_{i<j,i=1}^{3} J_{ij} I_{iz} I_{jz} \tag{2.5}$$

where I_{iz} is the single-spin Pauli angular momentum operator, ν_i are the Larmor frequencies of the spins and J_{ij} are the spin-spin coupling constants. The coupling constants recorded are $J_{12} = 69.8$ Hz, $J_{23} = -129.0$ Hz, and $J_{13} = 47.5$ Hz. The three qubits here have long enough relaxation times (T_1 and T_2) so that decoherence is not a major issue in this system. The average fluorine longitudinal T_1 relaxation times are of 5.0 seconds and T_2 relaxation times are of 1.0 seconds respectively. The structure of the three-qubit molecule as well as the equilibrium NMR spectrum obtained after a $\pi/2$ readout pulse are shown in Figure 2.2. The resonance lines of each qubit are labeled by the corresponding states of the other two coupled qubits.

2.3.1 NMR pulses

The three fluorine nuclei of trifluoroiodoethylene cover a very large bandwidth of 63 ppm (approximately). Due to problems like RF inhomogeneity and peak power limitations, uniform excitation of such a huge bandwidth is a challenge. A possible solution is the use of shaped pulses that are tailored to excite uniformly the specific frequencies, and to incorporate RF inhomogeneity compensations. All the experiments with this sample of three qubits hence use the shaped pulses for both selective as well as non-selective excitations. The experiments were performed at room temperature on a Bruker Avance III 400 MHz NMR spectrometer equipped with a z-gradient BBFO probe.

Individual qubits are addressed using low power 'Gaussian' shaped selective pulses (from the standard Bruker directory). This spin-selective pulse of duration $265\mu s$ is composed of a total of 1000 points exciting a bandwidth of 8000 Hz. Graphical representations of the amplitude and phase profiles of this pulse are shown in Figure 2.3(A1, A2). The pulses used are robust with good selectivity and uniform spin response in the desired frequency range. The excitation profile of this pulse is uniform in approximately 6000 Hz of the bandwidth with very low-intensity tails extending upto $\pm$10000 Hz offsets as shown in Figure 2.3(A3, A4). In the trifluoroiodoethylene molecule, two

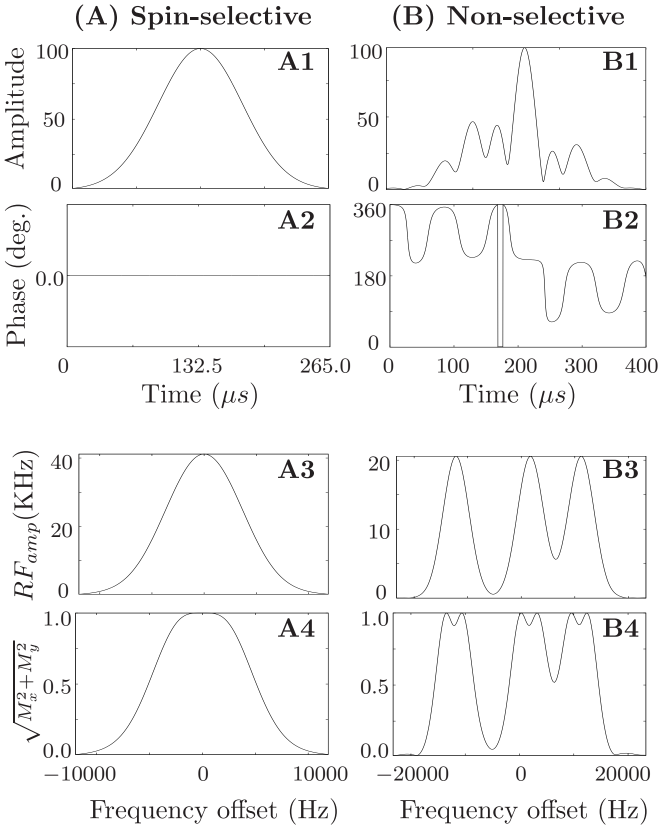

Figure 2.3: Part(A) contains the description of spin-selective radio frequency pulse and part (B) contains the details of the non-selective radio frequency pulse. (A1, A2) contain the normalized amplitude and the phase profiles respectively vs the number of pulse points. This is the pulse profile in time-domain where the pulse points correspond to the digitized duration intervals. Similar pulse profiles for a non-selective rf pulse are shown in (B1, B2) respectively. (A3, B3) show the Fourier transformation of the pulse profiles vs frequency offsets of the spin-selective and the non-selective pulses respectively. The ordinate is the amplitude of the rf pulse in KHz and abscissa is spin offset ranging from -10000 to $+10000$ Hz in (A3) and -20000 to $+20000$ Hz in (B3) with the pulse profiles centered at zero offset values. Parts (A4, B4) contain the amplitude of the excitation profile (for a 90^0) pulse vs spin offset, where M_x and M_y are the $x, y-$components of the magnetization vector. This spin response is simulated using a single spin Bloch model via NMRSIM.

nearest spin offsets are 9497 Hz apart, therefore a spin-selective pulse applied on a single spin has negligible effect on its nearest neighbor, which is also reflected on the frequency scale of the Fourier transformed pulse shape in Figure 2.3(A3).

A non-selective excitation is achieved via simultaneous excitation of all the three spin offsets with three shaped pulses respectively of smaller bandwidths by the same angle and about the same axis. The pictorial views of the amplitude and phase profiles as a function of pulse time are presented in Figure 2.3(B1, B2). Standard 'Gaussian' shaped pulses (of duration 400μs) are frequency modulated to achieve uniform excitation of all the three qubits by exciting three individual bandwidths simultaneously at three different offsets. Excitations of small bandwidths at more than one location reduce the RF inhomogeneity effects, making the pulse robust. Individual 'Gaussian' shaped pulse each of $400\mu s$ duration and consisting of 1500 pulse points, excite a bandwidth of 5000 Hz centered at three spin offsets (9497 Hz, 0 Hz, and -13897 Hz) respectively. Fourier transformation of the frequency modulated pulse shape depicts the three resonances being excited simultaneously and uniformly (Figure 2.3(B3)). An example of spin-response as a result of non-selective excitation by 90^0 flip angle is shown in Figure 2.3(B4). This spin response is simulated via NMRSIM software provided along with Topspin 2.1 assuming a single spin Bloch model. The graph shows (Figure 2.3(B4)) a nearly hat shaped amplitude of the excitation profile, obtained around the respective spin offsets.

2.3.2 Pseudo-pure state

As described in Chapter 1, at thermal equilibrium, nuclear spins exist in mixed ensembles, which is not suitable for quantum computation. The state of the system is hence initialized in a pseudo-pure state. Pseudopure state used in this chapter is one of the basis states of a three-qubit system, $|000\rangle$ whose density operator is given by,

$$\rho_{000} = \frac{1-\epsilon}{8} I_8 + \epsilon |000\rangle\langle 000|, \tag{2.6}$$

with a thermal polarization $\epsilon \approx 10^{-5}$ and I_8 being an 8×8 identity matrix. The pseudo-pure state $|000\rangle$ is obtained in NMR by the spatial averaging technique [74]. Starting with thermal equilibrium density operator, NMR pulse sequence for the creation of pseudo-pure state is shown in Figure2.4. The scheme for three-qubit generic state creation in this chapter is implemented on this pseudo-pure state ($|000\rangle$). The three qubits are represented by three channels numbered as $(1, 2, 3)$ and the fourth channel in Figure 2.4 is for the gradient implementation. All the pulses are shaped pulses, such

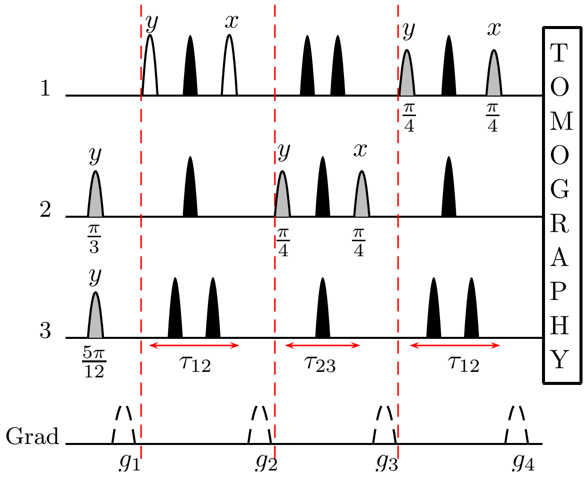

Figure 2.4: NMR pulse sequence to create a three-qubit pseudo-pure state $|000\rangle$. The 180^0 pulses are represented by filled and 90^0 pulses are represented by unfilled pulse shapes. The other pulses are labeled with their specific flip angles and phases. Gradient pulse shapes are shown as dotted curves.

that the filled black shapes correspond to 180^0 and the white pulse shapes correspond to 90^0 flip angles. Gray shaded pulses are of varied angles as specified along with the pulse phase. Gradients are represented as the wide dotted curves with gradient strength g_i, being used to dephase the transverse components of the magnetic field. This in turn averages out the coherences at desired stages. The experimentally created pseudo-pure state $|000\rangle$ was tomographed with a fidelity of 0.99 (discussed in subsection 2.3.3).

2.3.3 Tomography

All experimentally generated states were completely characterized by performing NMR quantum state tomography [100]. In this chapter, the three-qubit tomography scheme used is based on the protocol proposed by Leskowitz et al. [78]. According to this scheme [78], a three-qubit state is completely reconstructed with a set of 7 operations defined by $\{\mathrm{III}, \mathrm{XXX}, \mathrm{IIY}, \mathrm{XYX}, \mathrm{YII}, \mathrm{XXY}, \mathrm{IYY}\}$. Here $X(Y)$ denotes a single spin operator, and I is the identity operator. These operators can be implemented by applying the corresponding spin-selective $\pi/2$ pulses. Motivated by this tomographic protocol, here an expanded set of 11 operations is used to determine all the 63 variables for a system of three qubits. The new set of tomography operations is given by:

$$\{\mathrm{III}, \mathrm{IIX}, \mathrm{IXI}, \mathrm{XII}, \mathrm{IIY}, \mathrm{IYI}, \mathrm{YII}, \mathrm{YYI}, \mathrm{IXX}, \mathrm{XXX}, \mathrm{YYY}\}.$$

This set of operators is more convenient to implement on a system with rapidly dephasing, widely spaced qubits. This set of experimentally accessible measurements is found sufficient to completely characterize the experimental density matrix with good fidelity. The measure of the fidelity of the experimentally reconstructed density matrices [13] is obtained using Equation (1.6).

2.4 NMR implementation of generic state scheme

2.4.1 Generic state implementation

The general scheme to create generic three-qubit states (section 2.2), is demonstrated on a trifluoroiodoethylene molecule. NMR implementation of the general scheme is carried out to create a state in which all the terms in the generic state expression given in Equation (2.2) are involved in a nontrivial way. Chosen values of five experimental parameters are: $\alpha = 45^0, \beta = 55^0, \gamma = 60^0, \delta = 58^0$ and $\phi = 125^0$. This set of parameters leads to the creation of the generic state:

$$0.707|000\rangle + 0.351|001\rangle + 0.579|010\rangle + 0.107|100\rangle + 0.172e^{i(125^0)}|111\rangle \qquad (2.7)$$

The three-qubit state thus created has three single quantum coherences with transition label $|00\rangle$ (as per Figure 2.2) corresponding to each of the three spins. NMR spectrum of generic three-qubit state acquired without any detection pulse is shown in Figure 2.5 First order NMR spectrum of the generic state (with parameters: $\alpha = 45^0, \beta = 55^0, \gamma = 60^0, \delta = 58^0$ and $\phi = 125^0$) obtained without any detection pulse is shown in Figure 2.5. The NMR spectrum is expected to have only one non-zero single quantum coherence corresponding to transition label $|00\rangle$ on each spin. The expected single quantum coherences of first, second, and third spins in the generic state assume values 0.07, 0.41, and 0.25 respectively. Intensities of respective spectral lines as shown in the spectrum Figure 2.5 lie quite close to the theoretically expected ones for the second and third qubits. The coherence of the first qubit is expected to have very low intensity (0.07) that makes the spurious spectral lines look relatively prominent. The state thus

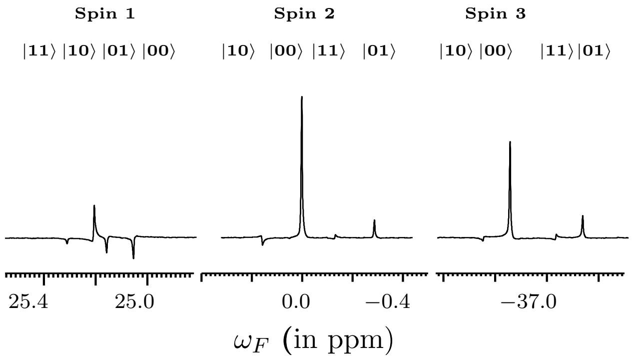

Figure 2.5: First order NMR spectrum of the generic three-qubit state. This state is created with parameters: $\alpha = 45^0, \beta = 55^0, \gamma = 60^0, \delta = 58^0$ and $\phi = 125^0$.

created is tomographed to completely reconstruct the final state density operator. The tomograph corresponding to this state is shown in Figure 2.6, wherein the experimentally tomographed state (Figure 2.6(b)) is compared with the theoretically expected state (Figure 2.6(a)). The fidelity of the experimentally tomographed state in this case is 0.92.

Let us consider another example of a three-qubit state construction which can be obtained from generic three-qubit state by a non-selective $z-$rotation by 180^0 on all the three qubits. The parameters for the generic state ($|\psi_g\rangle$) construction are chosen as: $\alpha = 45^0$, $\beta = 25.66^0$, $\gamma = 28.71^0$, $\delta = 71.57^0$ and $\phi = 0$. The three-qubit state thus obtained upon the implementation of local unitary operators $(\pi)_z^{1,2,3}$ is given as:

$$0.707|000\rangle + 0.306|001\rangle + 0.306|010\rangle + 0.177|100\rangle + 0.530|111\rangle \qquad (2.8)$$

This state can however be obtained by a simpler sequence of operations. The corresponding set of quantum gates implementations are explicitly worked and shown in the set of Equations (2.9). The sequence begins with the implementation of a single qubit quantum gate on the pseudo-pure state ($|000\rangle$) creating superposition of basis vectors $|000\rangle$ and $|100\rangle$. This is followed by two sequential controlled-rotation gate implementations instead of the pairwise implementations of $CR_{i,j}$ and $CN_{j,i}$ (as described in Equation (2.2)). This step makes the present scheme more feasible to implement, however it restricts the set of three-qubit states. This scheme creates a subset of the three-qubit generic states. Next is the implementation of two controlled-NOT gates, at the end of which the desired three-qubit generic state is obtained. Also, there is no

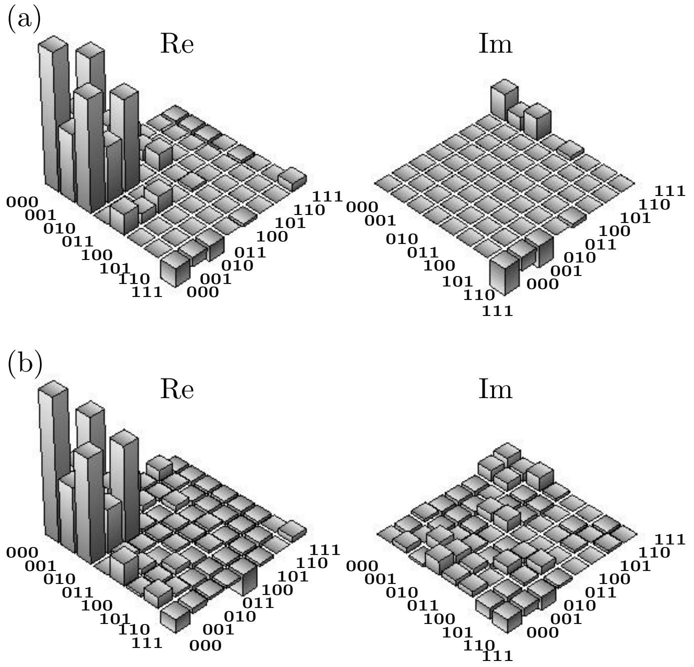

Figure 2.6: The real (Re) and imaginary (Im) parts of the (a) theoretical and (b) experimental density matrices for the three-qubit generic state, reconstructed using full state tomography. The values of the parameters are $\alpha = 45^0, \beta = 55^0, \gamma = 60^0, \delta = 58^0, \phi = 125^0$. The rows and columns encode the computational basis in binary order, from $|000\rangle$ to $|111\rangle$. The experimentally tomographed state has a fidelity of 0.92.

three-qubit controlled gate involved in the present sequence. The step by step implementation of quantum gates is given as:

$$\begin{aligned}
|000\rangle \quad & \xrightarrow{U^1_{2\alpha'}} \quad \cos\alpha'|000\rangle + \sin\alpha'|100\rangle \\
& \xrightarrow{\mathrm{CR}^{2\beta'}_{12}} \quad \cos\alpha'|000\rangle + \sin\alpha'\cos\beta'|100\rangle + \sin\alpha'\sin\beta'|110\rangle \\
& \xrightarrow{\mathrm{CR}^{2\gamma'}_{13}} \quad \cos\alpha'|000\rangle + \sin\alpha'\cos\beta'\cos\gamma'|100\rangle + \\
& \qquad \sin\alpha'\cos\beta'\sin\gamma'|101\rangle + \sin\alpha'\sin\beta'\cos\gamma' \\
& \qquad |110\rangle + \sin\alpha'\sin\beta'\sin\gamma'|111\rangle \\
& \xrightarrow{\mathrm{CN}_{31}} \quad \cos\alpha'|000\rangle + \sin\alpha'\cos\beta'\cos\gamma'|100\rangle + \\
& \qquad \sin\alpha'\cos\beta'\sin\gamma'|001\rangle + \sin\alpha'\sin\beta'\cos\gamma'|110\rangle + \\
& \qquad \sin\alpha'\sin\beta'\sin\gamma'|011\rangle
\end{aligned}$$

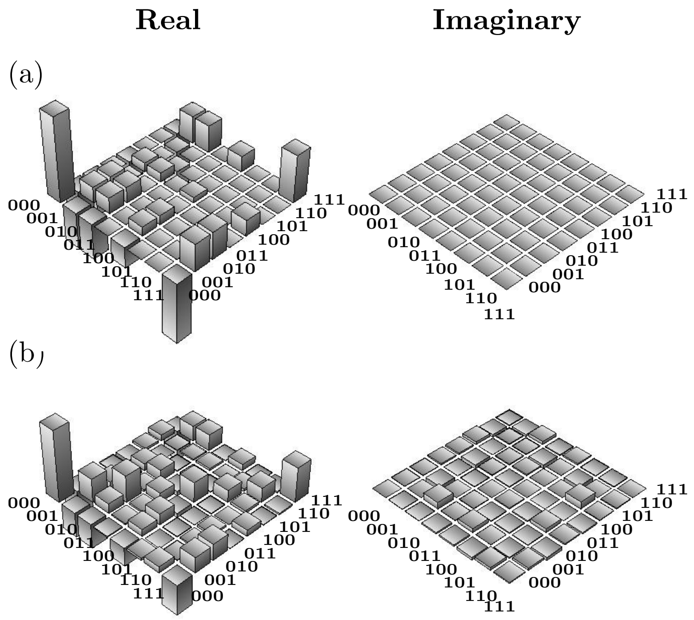

Figure 2.7: The real (Re) and imaginary (Im) parts of the (a) theoretical and (b) experimental density matrices for the three-qubit generic state, reconstructed using full state tomography. The values of the parameters are $\alpha = 45^0, \beta = 25.66^0, \gamma = 28.71^0, \delta = 71.57^0, \phi = 0^0$. The rows and columns encode the computational basis in binary order, from $|000\rangle$ to $|111\rangle$. The experimentally tomographed state has a fidelity of 0.92.

$$\begin{aligned} \xrightarrow{\mathrm{CN}_{21}} \quad & \cos\alpha'|000\rangle + \sin\alpha'\cos\beta'\cos\gamma'|100\rangle + \\ & \sin\alpha'\cos\beta'\sin\gamma'|001\rangle + \sin\alpha'\sin\beta'\cos\gamma'|010\rangle + \\ & \sin\alpha'\sin\beta'\sin\gamma'|111\rangle \end{aligned} \tag{2.9}$$

Three-qubit state (2.8) is constructed by choosing the values of parameters: $\alpha' = 45^0$, $\beta' = \gamma' = \delta' = 60^0$ and $\phi' = 0^0$. The state is constructed experimentally with a fidelity of 0.92. Theoretically expected and experimentally obtained states are shown in Figure 2.7.

2.4.2 GHZ state implementation

Generalized GHZ states are the three-qubit entangled states equivalent to the form, $a_1|000\rangle + e^{\iota\phi}a_2|111\rangle$. A maximally entangled GHZ state has all the three qubits entangled with each other, however there is no residual two-party entanglement if one of the parties is traced out. For a maximally entangled GHZ state, the value of three tangle [80, 81] is found out to be 1 and the measure of entanglement [80, 81] between the individual parties (concurrence) is found out to be zero. Thus there exist only three-party non local correlations in a maximally entangled GHZ state.

A set of GHZ states can be obtained from the three- qubit generic state given in Equation (2.1), corresponding to the parameter values $\alpha = \alpha, \beta = \gamma = 0, \delta = \pi/2, \phi = 0$. The resulting state is thus of the form, $\cos\alpha|000\rangle + \sin\alpha|111\rangle$. Since $\beta = \gamma = 0$, this renders the controlled rotation operators $CR_{12}(2\beta)$ and $CR_{12}(2\gamma)$ redundant. The scheme to create a three-qubit generic state (Figure 2.1(a)) is hence reduced for preparation of a GHZ state. The effective quantum circuit to create a GHZ state is shown in Figure 2.8(a). Starting with the pseudo-pure state $|000\rangle$, first quantum gate implementation results into the superposition of the bases states $|000\rangle$ and $|100\rangle$. Following multi-qubit controlled gates: CR_{12} and $CCN_{12,3}$ convert the basis state $|100\rangle$ to $|111\rangle$, however basis state $|000\rangle$ remains unaffected. Thus one obtains a three-qubit GHZ state. The same effect however can be achieved via a simpler sequence consisting of a single-qubit rotation followed by two two-qubit controlled-NOT gates. This simplified quantum circuit to create a GHZ state is shown in Figure 2.8(b), A step by step detailed implementation of quantum circuit (Figure 2.8(b)) to create a GHZ state is described in the following set of equations. An arbitrarily weighted GHZ kind of entangled state can be prepared from the initial pseudo-pure state $|000\rangle$ by the sequence of operations

$$\begin{aligned} |000\rangle &\xrightarrow{U^1_{2\alpha}} \cos\alpha|000\rangle + \sin\alpha|100\rangle \\ &\xrightarrow{\mathrm{CN}_{12}} \cos\alpha|000\rangle + \sin\alpha|110\rangle \\ &\xrightarrow{\mathrm{CN}_{13}} \cos\alpha|000\rangle + \sin\alpha|111\rangle \end{aligned} \tag{2.10}$$

For $\alpha = \pi/4$, the above sequence leads to a maximally entangled GHZ state:

$$|\psi_{\mathrm{GHZ}}\rangle = \frac{1}{\sqrt{2}}(|000\rangle + |111\rangle) \tag{2.11}$$

The NMR pulse sequence to create an arbitrary GHZ-like entangled state beginning from the pseudo-pure state $|000\rangle$ and ignoring overall phase factors is given in Figure 2.8(c). The CN_{12} and CN_{13} in the circuit are controlled-NOT gates with qubit 1 as the control and qubit 2 (3) as the target. Since the target qubits are different in both these cases, these gates commute and can be applied in parallel, leading to a reduction

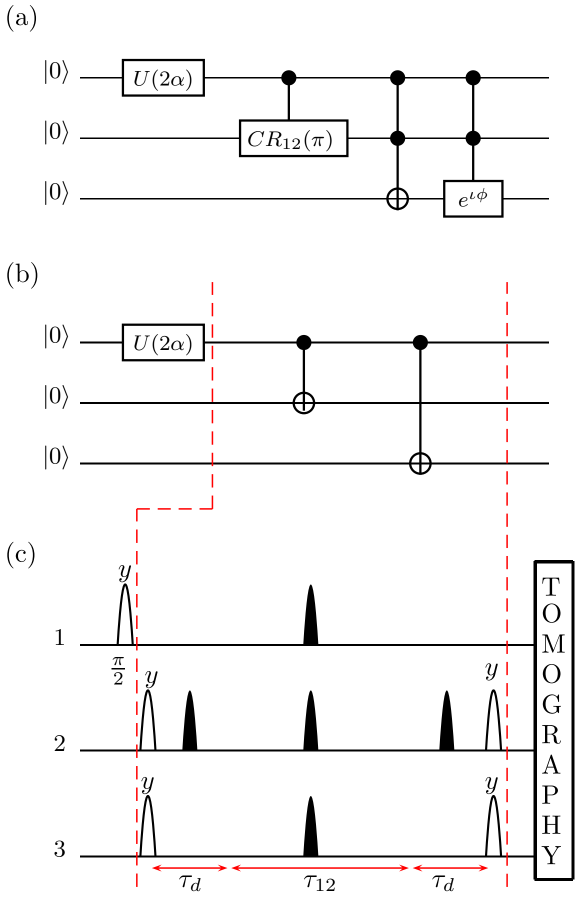

Figure 2.8: (a) Quantum circuit to implement a generalized GHZ state, derived from the general circuit for generic state construction given in Figure 2.1(a). (b) Simplified circuit for experimental implementation of the GHZ state. (c) NMR pulse sequence corresponding to the circuit in (b). The $\tau_d = \frac{\tau_{13}-\tau_{12}}{2}$ period is tailored such that the system evolves solely under the J_{13} coupling term.

in experimental time. For our system $\tau_{13} > \tau_{12}$, where $\tau_{ij} = \frac{1}{2J_{ij}}$ denotes the evolution period under the J_{ij} coupling term. Hence, during the period τ_{12}, both qubits 2 and 3 evolve under the the J-couplings J_{12} and J_{13} (Figure 2.8(c)). The evolution in the intervals $\tau_d = \dfrac{\tau_{13} - \tau_{12}}{2}$ is solely governed by the J_{13} coupling term, and by the end of the evolution period, the system evolves under J_{12} and J_{13} couplings for durations $\frac{1}{2J_{12}}$ and $\frac{1}{2J_{13}}$ respectively.

This NMR pulse sequence is implemented on a trifluoroiodoethylene molecule and a maximally entangled GHZ state is created. The density operator for a GHZ state con-

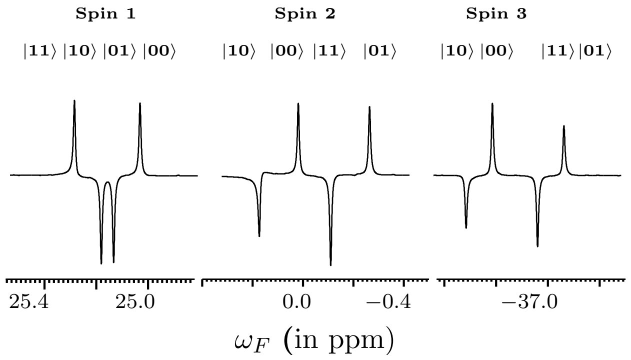

Figure 2.9: First order NMR spectrum of the three-qubit GHZ state is shown, as obtained by 90^0 spin-selective detection pulses on each of these qubits separately.

sists of elements at the diagonal (populations) and at positions $|000\rangle\langle 111|$ ($|111\rangle\langle 000|$), which correspond to the triple quantum coherences. Both populations as well as the higher order coherences are not captured in an NMR spectrum, therefore NMR spectrum after GHZ state implementation does not contain any transition. NMR spectrum for GHZ state obtained by implementing a 90^0_y spin-selective detection pulse is shown in Figure 2.9. The state generated experimentally (Figure 2.10(b)) was tomographed and lies very close to the theoretically expected state (Figure 2.10(a)) with a computed fidelity of 0.97.

2.4.3 W-state implementation

Generalized W-states form another class of entangled three-qubit states which are inequivalent to GHZ states under local operations. For a maximally entangled W-state, the value of 3-tangle is found out to be $\frac{2}{3}$ and the concurrence among the reduced single parties is calculated [80, 81] as $\frac{1}{3}$. Thus, these measures of entanglement conclude the existence of both two party as well as three-party non local correlations in a maximally entangled three-qubit W-state.

Generalized W-states are a special case of the generic state given in Equation (2.1) corresponding to the parameter values $\alpha = \pi/2, \beta, \gamma \in [0, \pi/2], \delta = 0, \phi = 0$. This set of parameters leads to the state $|\psi\rangle = \cos\gamma\cos\beta|100\rangle + \sin\gamma\cos\beta|001\rangle + \sin\beta|010\rangle$. The general quantum circuit for generic state construction Figure 2.1(a), here reduces to the special form shown in Figure 2.11(a). A sequential action of the quantum gates

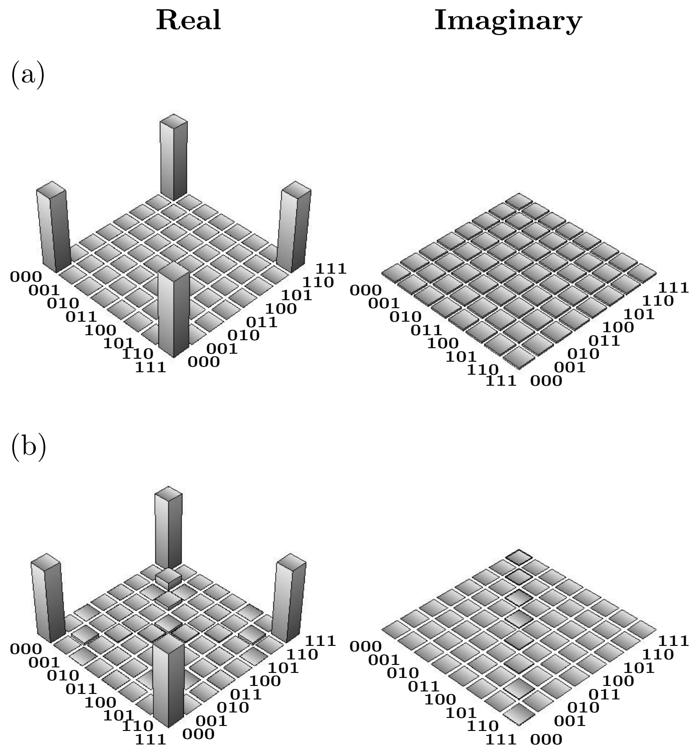

Figure 2.10: The real (Re) and imaginary (Im) parts of the (a) theoretical and (b) experimental density matrices for the GHZ state, reconstructed using full state tomography. The rows and columns encode the computational basis in binary order, from $|000\rangle$ to $|111\rangle$. The experimentally tomographed state has a fidelity of 0.97.

on a three- qubit pseudo-pure state $|000\rangle$ leads to:

$$
\begin{aligned}
|000\rangle &\xrightarrow{U_\pi^1} |100\rangle \\
&\xrightarrow{\mathrm{CR}_{12}^{2\beta}} \cos\beta|100\rangle + \sin\beta|110\rangle \\
&\xrightarrow{\mathrm{CN}_{21}} \cos\beta|100\rangle + \sin\beta|010\rangle \\
&\xrightarrow{\mathrm{CR}_{13}^{2\gamma}} \cos\gamma\cos\beta|100\rangle + \sin\gamma\cos\beta|101\rangle + \sin\beta|010\rangle \\
&\xrightarrow{\mathrm{CN}_{31}} \cos\gamma\cos\beta|100\rangle + \sin\gamma\cos\beta|001\rangle + \sin\beta|010\rangle
\end{aligned}
\tag{2.12}
$$

The first gate is a single qubit unitary operator that leads to basis vector $|100\rangle$. The next gate in the sequence is a controlled rotation gate ($CR_{12}(2\beta)$), which implements a rotation by angle β on the target qubit whenever the control qubit is in state $|1\rangle$. This gate is followed by the implementation of CN_{21} operation, such that at the end of this step, the resultant state is a linear combination of $|100\rangle$ and $|010\rangle$. The next pair of gates $CR_{13}(2\gamma)$ and CN_{31}, implemented in the given order leads to the basis vector $|001\rangle$. The resultant state consists of the linear combination of vectors $|001\rangle$, $|010\rangle$, and $|100\rangle$ with weights as functions of angles β and γ.

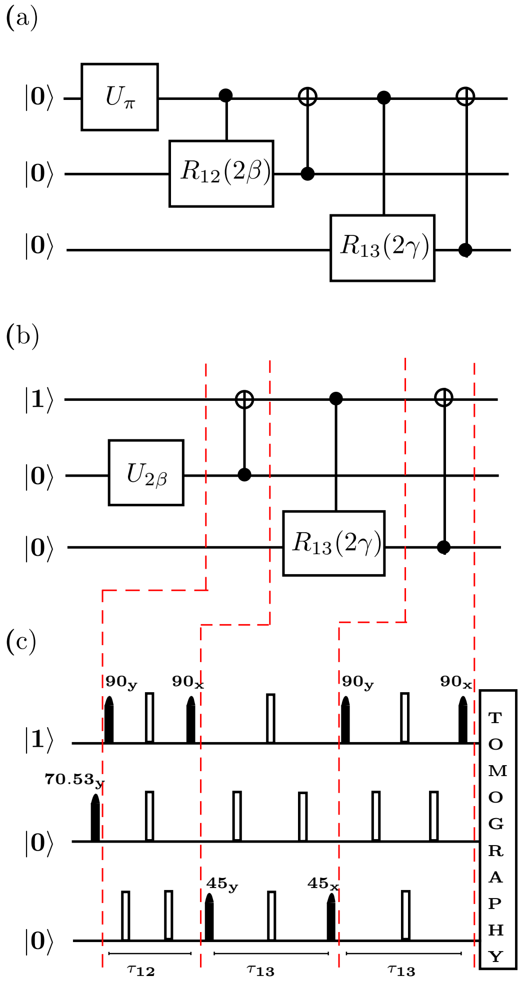

Figure 2.11: (a) Quantum circuit to implement the W-state, derived from the general circuit for generic state construction given in Figure 2.1(a). (b) Simplified circuit for experimental implementation of the W-state. (c) NMR pulse sequence to experimentally implement the W-state, starting from the initial pseudo-pure state $|100\rangle$. The first pulse on the second qubit implements a $U^2_{2\beta}$ rotation, with $2\beta = 2\sin^{-1}(1/\sqrt{3}) \equiv 70.53^0$.

There is a simplified scheme for the W-state creation as shown in Figure 2.11(b).

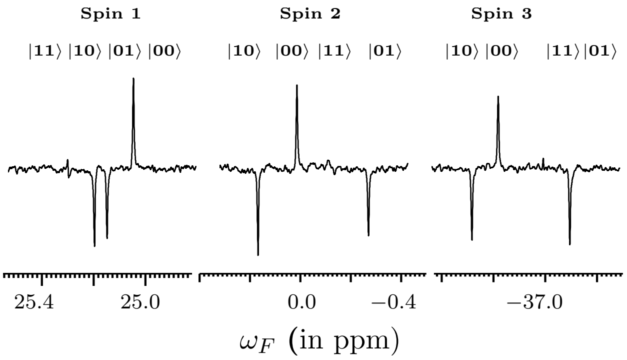

Figure 2.12: NMR spectrum of three-qubit maximally entangled W-state is shown. Spectrum of each of these spins is acquired separately by spin-selective 90^0 excitation pulse.

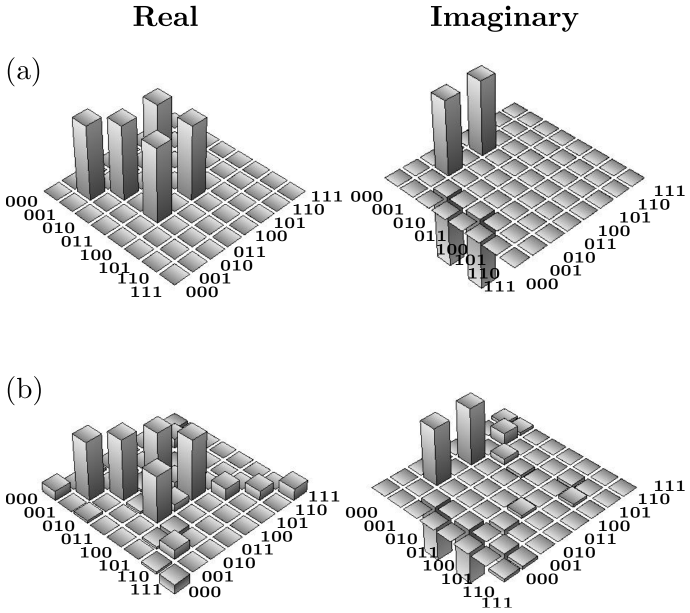

Figure 2.13: The real (Re) and imaginary (Im) parts of the (a) theoretical and (b) experimental density matrices for the W state, reconstructed using full state tomography. The rows and columns encode the computational basis in binary order, from $|000\rangle$ to $|111\rangle$. The experimentally tomographed state has a fidelity of 0.96.

As per this scheme, the first single qubit unitary gate on first qubit is dropped and the implementation is carried out on a different initial state ($|100\rangle$). The next gate is a $CR_{12}(2\beta)$ according to the general scheme (Figure 2.11(a)), where the first qubit acts as the control qubit. The present case always has the control qubit in state $|1\rangle$, thus one can avoid implementing this two-qubit controlled gate (Equation (2.12)). Instead a much simpler and faster $U^2_{2\beta}$ gate on the second qubit is implemented, which in this case yields the same result. The modified circuit is shown in Figure 2.11(b). For $2\beta = 2\sin^{-1}(1/\sqrt{3})$ and $\gamma = 45^0$, the circuit leads to implementation of the standard W-state (upto a phase factor):

$$|\psi_{\mathrm{W}}\rangle = \frac{1}{\sqrt{3}}(i|001\rangle + |010\rangle + |100\rangle) \tag{2.13}$$

One can get rid of the extra phase factor by a single-qubit $z-$rotation on the third qubit. The NMR pulse sequence for the creation of an arbitrary W-like entangled state beginning from the pseudo-pure state $|100\rangle$ and ignoring overall phase factors, is given in Figs. 2.11(c).

NMR implementation of the maximally entangled W-state is carried out on a pseudo-pure state $|100\rangle$, which is obtained with a fidelity of 0.99. Each of the three-qubits are acted upon by the spin-selective 90^0_y pulses, and the corresponding NMR spectra are acquired separately. From each of these three experiments, spectral lines of the those spins are chosen on which direct detection pulse was being applied. These spectral lines of individual spins are then collated together and shown in Figure 2.12. Due to absence of single-quantum coherences, w-state NMR spectrum without any detection pulse does not possess any spectral line. The maximally entangled W-state is created and the complete quantum state tomography is performed. The experimentally reconstructed density matrix (Figure 2.13(b)) matches well with the theoretically expected values (Figure 2.13(a)), with a computed state fidelity of 0.96.

2.4.4 W$\bar{\text{W}}$-state implementation

The $\mathrm{W\bar{W}}$-state is an interesting three-qubit state which belongs to the generalized GHZ class of entangled states. This state can be obtained from a maximally entangled GHZ state via SLOCC (Stochastic Local Operation and Classical Communication) [80, 81, 82, 83]. Stochastic local operations involve non-unitary single qubit operations with probabilistic outcomes. Though the state belongs to the GHZ class of states, yet it possesses entanglement features in contrast to that of the GHZ states.

This state can be represented as a permutation symmetric superposition of the W state and its obverse $\bar{\mathrm{W}} = 1/\sqrt{3}\,(|011\rangle + |101\rangle + |110\rangle)$ [84, 101]. The $\bar{\mathrm{W}}$ state also belongs to the generalized W class of states and can be obtained from the maximally entangled W-state by single-qubit $(180^0)_y^{1,2,3}$ rotations of all the three qubits. An explicit representation of $\mathrm{W\bar{W}}$ state is given by:

$$\begin{aligned}|\mathrm{W\bar{W}}\rangle &= \frac{1}{\sqrt{2}}\left(|\mathrm{W}\rangle + |\mathrm{\bar{W}}\rangle\right)\\ &= \frac{1}{\sqrt{6}}\left(|001\rangle + |010\rangle + |011\rangle + |100\rangle + |101\rangle + |110\rangle\right)\end{aligned} \tag{2.14}$$

The $\mathrm{W\bar{W}}$ state is unitarily equivalent to the generic three-qubit state (Equation (2.2)), with a set of parameters : $\alpha = 90^0, \beta = 16.78^0, \gamma = 17.55^0, \delta = 71.57^0, \phi = 180^0$. The corresponding three-qubit generic pure state is given as:

$$|\psi\rangle = \frac{1}{2\sqrt{3}}(|001\rangle + |010\rangle + |100\rangle) - \frac{\sqrt{3}}{2}|111\rangle \tag{2.15}$$

The implementation of single-qubit Hadamard operators $(U(\frac{\pi}{2})_y)$ on all the three qubits of the above state, gives rise to the required $|\mathrm{W\bar{W}}\rangle$ state.

Here a slightly different and more convenient approach to create this novel W-superposition state is adopted. The sequence of gates to construct a $\mathrm{W\bar{W}}$ state, starting from the initial pseudo-pure state $|000\rangle$ is given as:

$$\begin{aligned}|000\rangle &\overset{U^1(-\frac{\pi}{3})_y}{\longrightarrow} \frac{1}{2}\left(\sqrt{3}|000\rangle - |100\rangle\right)\\ &\overset{\mathrm{CROT}_{12}\left(2cos^{-1}(1/\sqrt{3})\right)_y}{\longrightarrow} \frac{1}{2}\left(\sqrt{3}|000\rangle - \frac{1}{\sqrt{3}}|100\rangle - \sqrt{\frac{2}{3}}|110\rangle\right)\\ &\overset{\mathrm{CROT}_{21}(-\frac{\pi}{2})_y}{\longrightarrow} \frac{1}{2}\left(\sqrt{3}|000\rangle - \frac{1}{\sqrt{3}}(|100\rangle + |110\rangle + |010\rangle)\right)\\ &\overset{\mathrm{CNOT}_{13}}{\longrightarrow} \frac{1}{2}\left(\sqrt{3}|000\rangle - \frac{1}{\sqrt{3}}(|101\rangle + |111\rangle + |010\rangle)\right)\\ &\overset{\mathrm{CNOT}_{23}}{\longrightarrow} \frac{1}{2}\left(\sqrt{3}|000\rangle - \frac{1}{\sqrt{3}}(|101\rangle + |110\rangle + |011\rangle)\right)\\ &\overset{U^{1,2,3}(\frac{\pi}{2})_y}{\longrightarrow} \frac{1}{\sqrt{6}}\left(|001\rangle + |010\rangle + |011\rangle + |100\rangle + |101\rangle + |110\rangle\right)\end{aligned} \tag{2.16}$$

The quantum circuit to construct the $\mathrm{W\bar{W}}$ state on a three-qubit system is given in Figure 2.14(a). The NMR pulse sequence to create the $\mathrm{W\bar{W}}$ state, starting from the

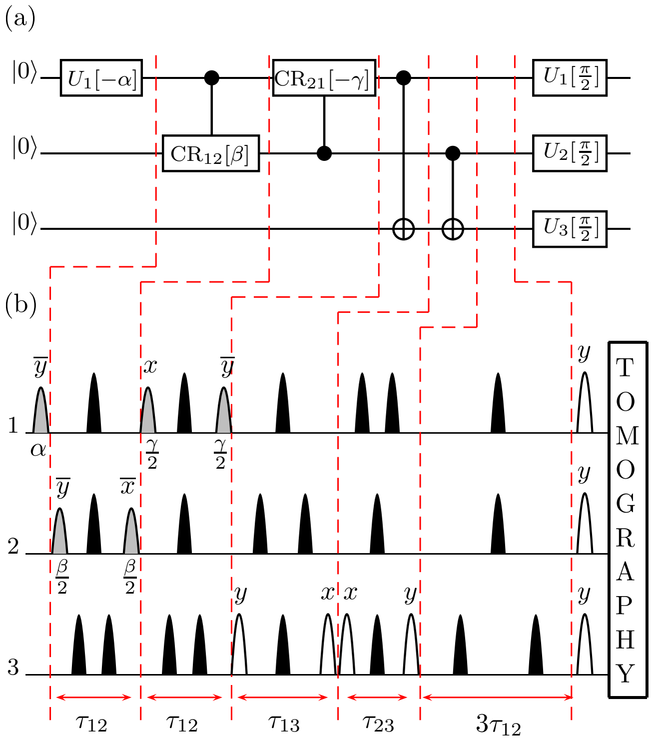

Figure 2.14: (a) Quantum circuit showing sequence of gates required to construct the W$\bar{\mathrm{W}}$ state, starting from the pseudo-pure state $|000\rangle$. (b) NMR pulse sequence to create a W$\bar{\mathrm{W}}$ state. All the pulses are low-power selective pulses represented by shaped blocks. Filled black shapes are π refocusing pulses, unfilled shapes correspond to pulses of $\frac{\pi}{2}$ flip angle and the gray shaded shapes are labeled with their specific flip angles and phases. Vertical dotted red lines show the correspondence between the quantum circuit and the experimental pulse sequence. All pulses are of phase x unless otherwise labeled. The values of the rf pulse flip angles used are $\alpha = \frac{\pi}{3}, \beta = 2\cos^{-1}(\frac{1}{\sqrt{3}}), \gamma = \frac{\pi}{2}$ and The last $3\tau_{12}$ period is used to compensate the extra phase acquired (as described in the text).

pseudo-pure state $|000\rangle$ is given in Figure 2.14(b). After the evolution interval τ_{23} and the $[\frac{\pi}{2}]_y$ on the third qubit (corresponding to a CN_{23} gate), the state obtained is $\frac{\sqrt{3}}{2}|000\rangle - \frac{1}{2\sqrt{3}}(\iota|101\rangle + |110\rangle + \iota|011\rangle)$. There is an undesirable extra relative phase of ‘ι’ that has accumulated between two of the basis vectors. This undesired extra phase factor is compensated for during the evolution interval $3\tau_{12}$. The implementation of the last module (simultaneous $[\frac{\pi}{2}]_y$ pulses on all the three qubits) results in the desired W$\bar{\mathrm{W}}$ state with no extra relative phase. The NMR spectrum of the W$\bar{\mathrm{W}}$ state thus obtained is shown in Figure 2.15.

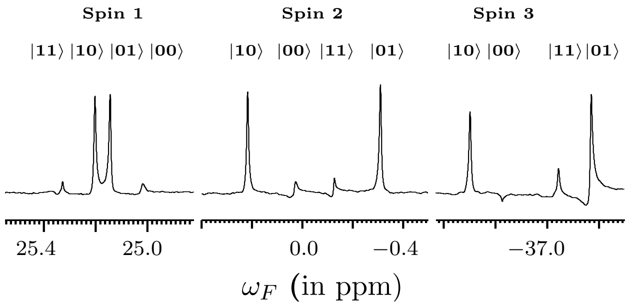

Figure 2.15: The 1D ^{19}F NMR spectrum corresponding to the creation of the $\mathrm{W\bar{W}}$ state. The NMR transitions of each qubit are labeled by the corresponding logical states of the other two qubits.

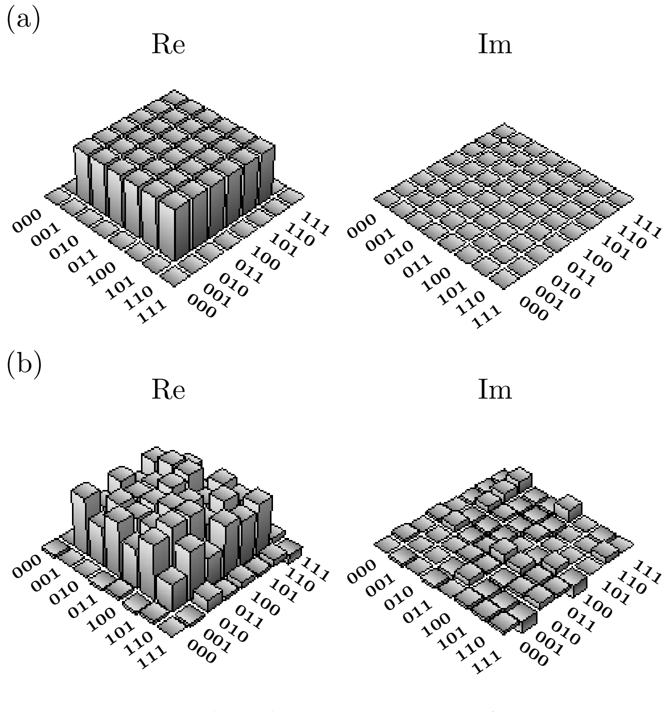

Figure 2.16: The real (Re) and imaginary (Im) parts of the (a) theoretically expected and (b) experimentally density matrices for the $\mathrm{W\bar{W}}$ state reconstructed using full state tomography. The rows and columns of the bar graphs depict the computational basis of the three qubits in binary order from $|000\rangle$ to $|111\rangle$. The experimentally tomographed state has a fidelity of 0.94.

As shown in Figure 2.15, each spin multiplet has two resonance peaks (as compared to four resonance peaks for the thermal equilibrium state). The expected NMR spectral pattern of an ideal $\mathrm{W\bar{W}}$ state should contain resonance peaks of equal magnitude and phase, and deviations from ideal spectral peak intensities and phases in the experimentally obtained spectrum, can be attributed to imperfections in the rf pulse calibrations and to relaxation during the selective pulse durations.

Complete quantum state tomography of the three-qubit $\mathrm{W\bar{W}}$ state is performed using a set of eleven operators as described in Section 2.3.3. The tomograph of the experimentally constructed $\mathrm{W\bar{W}}$ state is shown in Figure 2.16. The experimentally tomographed state was compared with the theoretically expected state and the density matrices match well, within experimental error, with a computed state fidelity of 0.94 (the fidelity was computed from Equation (1.6)).

2.5 Three-qubit state reconstruction from two-party reduced states

This part of the chapter is focused on a salient feature of three-qubit pure states, according to which, three-party non-local correlations can be decomposed as two-party correlations. In other words, a three-qubit pure state can be completely reconstructed from its reduced two party marginals [95]. However, there are certain exceptional states that do not obey the above statement, namely states of the type: $a|000\rangle + be^{\iota\phi}|111\rangle$. It has been shown in [95] that only two, two-party reduced states, are sufficient to completely reconstruct a three-party pure state. This property has also been generalized for N-qubit pure states, according to which N-party pure states can be completely constructed from its reduced N-1 party maginals [102]. There have also been attempts to find out the upper limit over the knowledge of the quantum system required to completely reconstruct the N-party pure state. In [102], it has been proposed that knowledge of somewhere between $0.189N$ to $0.667N$ number of N-1 party reduced states are sufficient to obtain the N-party pure state completely and uniquely. Sufficient information required to obtain the higher order correlations requires the specification of a fraction of N-1 party reduced states. Another bound over the minimum number of parties required is presented in [103]. According to this, a little over $\frac{N}{2}$ number of N-1 party reduced states are sufficient to obtain the N-party pure state.

The present chapter deals with the three-party scenario and follows the ideas proposed in [95]. The non-local correlations of various three-qubit entangled states, are probed, to gain insights into how information is stored in multipartite entangled states. In a related work [96], an explicit solution has been provided to completely characterize almost all generic three-qubit pure states, based only on pairwise two-qubit detectors.

Consider a three-qubit pure state $\rho_{ABC} = |\psi_{ABC}\rangle \langle\psi_{ABC}|$, with ρ_{AB}, ρ_{BC}, ρ_{AC} being its two-party reduced states. The two-party reduced state ρ_{AB} is obtained from the three-qubit pure state ρ_{ABC} by tracing out the qubit 'C', i.e. $\rho_{AB} = Tr_C(\rho_{ABC})$. Similarly $\rho_{BC} = Tr_A(\rho_{ABC})$ and $\rho_{AC} = Tr_B(\rho_{ABC})$. ρ_{ABC} is a pure state, however its reduced two-party marginals may be mixed or pure depending upon whether the three-party state is entangled or not. The single-qubit reduced states ρ_A, ρ_B and ρ_C can be further obtained from the two-party reduced states in a similar way. Since ρ_{ABC} is pure, ρ_A and ρ_{BC} share the same set of eigen values, and can be written as

$$\begin{aligned} \rho_A &= \sum_i p_A^i |i\rangle \langle i| \\ \rho_{BC} &= \sum_i p_A^i |i;BC\rangle \langle i;BC| \end{aligned} \tag{2.17}$$

where $\{|i\rangle\}$ are the eigenvectors of ρ_A with eigenvalues $\{p_A^i\}$, and $\{|i;BC\rangle\}$ are the eigenvectors of ρ_{BC} with eigenvalues $\{p_A^i\}$. The three-qubit states compatible with ρ_A and ρ_{BC} are

$$|\psi_{ABC};\alpha\rangle = \sum_i e^{\iota\alpha_i}\sqrt{p_A^i}\,|i\rangle \otimes |i;BC\rangle \tag{2.18}$$

Using a similar argument, the set of three-qubit pure states obtained from ρ_{AB} and ρ_C is given by

$$|\psi_{ABC};\gamma\rangle = \sum_k e^{\iota\gamma_k}\sqrt{p_c^k}\,|k;AB\rangle \otimes |k\rangle \tag{2.19}$$

where $\{|k\rangle\}$ are the eigenvectors of ρ_C with eigenvalues $\{p_c^k\}$ and $\{|k;AB\rangle\}$ are the corresponding eigenvectors of ρ_{AB}. Since the pure state $|\psi_{ABC}\rangle$ is compatible with both ρ_{AB} and ρ_{BC}, one can determine the values of α_i and γ_k such that,

$$|\psi_{ABC};\alpha\rangle = |\psi_{ABC};\gamma\rangle\,. \tag{2.20}$$

The state thus created has been proved to be unique [96]. Almost all three-qubit pure states can be completely and uniquely determined from any two of their corresponding two-party reduced states. The set (ρ_{AB}, ρ_{AC}) or the equivalent sets (ρ_{AB}, ρ_{BC}) or (ρ_{BC}, ρ_{AC}) can be used to reconstruct ρ_{ABC}.

Example 1

We now give an example to construct a three-qubit maximally entangled W state, $|\psi\rangle_{ABC} = \frac{1}{\sqrt{3}}\left(|001\rangle + |010\rangle + |100\rangle\right)$. A pair of its reduced two-qubit states are given as:

$$\rho_{AB} = \frac{1}{3}\begin{pmatrix} 1 & 0 & 0 & 0 \\ 0 & 1 & 1 & 0 \\ 0 & 1 & 1 & 0 \\ 0 & 0 & 0 & 0 \end{pmatrix}, \qquad \rho_{BC} = \frac{1}{3}\begin{pmatrix} 1 & 0 & 0 & 0 \\ 0 & 1 & 1 & 0 \\ 0 & 1 & 1 & 0 \\ 0 & 0 & 0 & 0 \end{pmatrix}. \tag{2.21}$$

Each of these reduced states have eigenvectors $|\psi_1\rangle = \frac{1}{\sqrt{2}}\begin{pmatrix} 0 & 1 & 1 & 0 \end{pmatrix}^\dagger$ and $|\psi_2\rangle = \begin{pmatrix} 1 & 0 & 0 & 0 \end{pmatrix}^\dagger$ with non-zero eigenvalues $\frac{2}{3}$ and $\frac{1}{3}$ respectively. These eigenvalues are same as the eigenvalues of single party reduced states ρ_C and ρ_A respectively. The other two eigenvalues of the state ρ_{AB} (ρ_{BC}) are zero, as the strength of a correlation is always determined by the smaller party. The three-party states constructed using ρ_{AB} and ρ_C is given as:

$$|\psi_{ABC};\phi_1\rangle = e^{\iota\phi_{11}}\sqrt{\frac{2}{3}}\frac{1}{\sqrt{2}}\begin{pmatrix} 0 \\ 1 \\ 1 \\ 0 \end{pmatrix} \otimes \begin{pmatrix} 1 \\ 0 \end{pmatrix} + e^{\iota\phi_{12}}\frac{1}{\sqrt{3}}\begin{pmatrix} 1 \\ 0 \\ 0 \\ 0 \end{pmatrix} \otimes \begin{pmatrix} 0 \\ 1 \end{pmatrix} \tag{2.22}$$

Similarly, the three-qubit state obtained through ρ_A and ρ_{BC} is given by:

$$|\psi_{ABC};\phi_2\rangle = e^{\iota\phi_{21}}\sqrt{\frac{2}{3}}\begin{pmatrix} 1 \\ 0 \end{pmatrix} \otimes \frac{1}{\sqrt{2}}\begin{pmatrix} 0 \\ 1 \\ 1 \\ 0 \end{pmatrix} + e^{\iota\phi_{22}}\frac{1}{\sqrt{3}}\begin{pmatrix} 0 \\ 1 \end{pmatrix} \otimes \begin{pmatrix} 1 \\ 0 \\ 0 \\ 0 \end{pmatrix} \tag{2.23}$$

We have $|\psi_{ABC};\phi_1\rangle = |\psi_{ABC};\phi_2\rangle$ to be satisfied, which in turn determines the angles $\phi_{11}, \phi_{12}, \phi_{21}, \phi_{22}$. As can be seen clearly, the three-party states found in both the cases are similar upto relative phase factors. The simplest solution corresponds to the angles, $\phi_{11} = \phi_{12} = \phi_{21} = \phi_{22} = 0$. The three-qubit state thus obtained is given as

$$\frac{1}{\sqrt{3}}\begin{pmatrix} 0 & 1 & 1 & 0 & 1 & 0 & 0 & 0 \end{pmatrix}^\dagger. \tag{2.24}$$

Thus the maximally entangled W-state is completely constructed.

Example 2

We give an example to construct a state belonging to the GHZ class, $|\psi\rangle_{ABC} = \frac{1}{\sqrt{2}}\left(|000\rangle + e^{\iota\phi}|111\rangle\right)$. This state has got all the three two-party reduced states, possessing exactly same form of the density operators. The three two-party reduced states are given as:

$$\rho_{AB} = \rho_{BC} = \rho_{AC} = \frac{1}{2}\begin{pmatrix} 1 & 0 & 0 & 0 \\ 0 & 0 & 0 & 0 \\ 0 & 0 & 0 & 0 \\ 0 & 0 & 0 & 1 \end{pmatrix} \tag{2.25}$$

As can be clearly seen, the information about the phase factor ϕ is not retained in the reduced two-party states. Thus three qubit correlations can not be found completely from the two-party reduced states in this case.

These two examples correspond to two locally inequivalent maximally entangled three-qubit states. The three-qubit correlations in case of example 1 are shown to be found using only two two-party reduced states. However, the three-qubit correlations in a GHZ state cannot be determined from the two two-party reduced states.

2.5.1 Experimental reconstruction of the three-qubit pure states

Corresponding to any three-qubit (pseudo) pure state constructed on a three-qubit NMR quantum computer, partial quantum state tomography is performed to find the two-party reduced density operators ρ_{AB}, ρ_{BC} and ρ_{AC}. Using a tomography scheme by Leskowitz et al. [78], two qubit density operator is completely determined by a set of four operations {II, IX, IY, XX}. In this case of partial tomography of the two-party sub-systems of a three-qubit system, the extra qubit is always acted upon by an Identity operator. The explicit set of tomography operations performed to experimentally reconstruct all three two-party reduced states include: {III, IXI, IYI, XXI} to reconstruct ρ_{AB}; {III, IIX, IIY, IXX} to reconstruct ρ_{BC} and {III, IIX, IIY, XIX} to reconstruct ρ_{AC}. Any two reduced party states can be chosen to completely construct a three-qubit state. The three-party state ρ_{ABC} is reconstructed here using the (ρ_{AB}, ρ_{BC}) set of two-party reduced states. The reconstructed three-qubit state is compared with that of three-qubit state obtained via complete quantum state tomography.

2.5.1.1 Generic state reconstruction

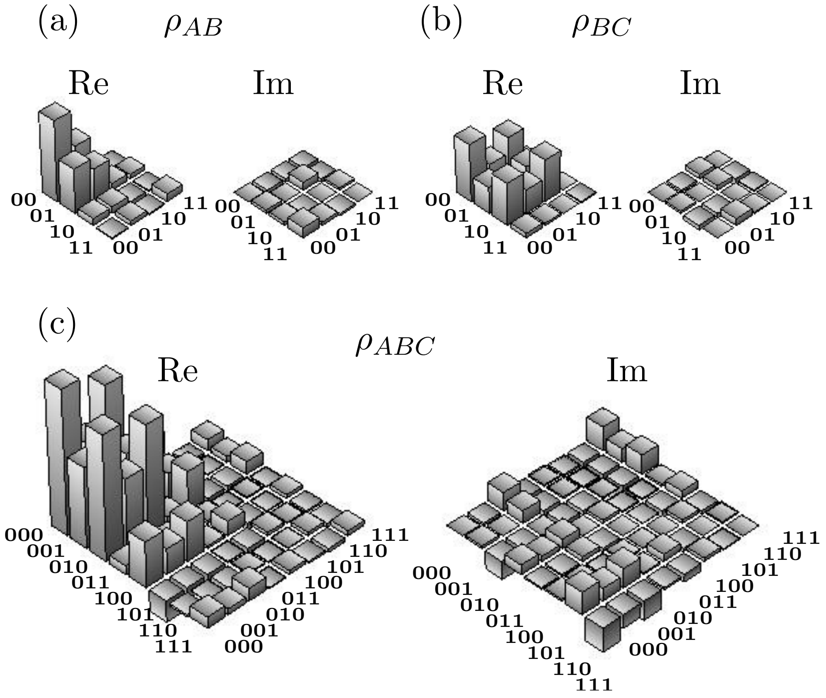

Figure 2.17: The real (Re) and imaginary (Im) parts of the density matrix for the generic state: (a) The two-qubit reduced density matrix ρ_{AB}. (b) The two-qubit reduced density matrix ρ_{BC}. (c) The entire three-qubit density matrix ρ_{ABC}, reconstructed from the corresponding two-qubit reduced density matrices. The parameter set includes $\alpha = 45^0, \beta = 55^0, \gamma = 60^0, \delta = 58^0, \phi = 125^0$. The rows and columns encode the computational basis in binary order, from $|00\rangle$ to $|11\rangle$ for two qubits and from $|000\rangle$ to $|111\rangle$ for three qubits. The tomographed state has a fidelity of 0.90.

An arbitrarily weighted generic three-qubit state is experimentally reconstructed from its reduced two two-party states. The set of parameters chosen for generic state construction being: $\alpha = 45^0, \beta = 55^0, \gamma = 60^0, \delta = 58^0, \phi = 125^0$. Partial quantum state tomography is performed that experimentally reconstructs the following two-party reduced density operators,

$$\rho_{AB} = \begin{pmatrix} 0.54 & -0.18 & -0.14 - 0.04i & 0.07 - 0.02i \\ -0.18 & 0.15 & -0.02 - 0.02i & 0.01 + 0.01i \\ -0.14 + 0.04i & -0.02 + 0.02i & 0.09 & -0.02 + 0.02i \\ 0.07 + 0.02i & 0.01 - 0.01i & -0.02 - 0.02i & 0.22 \end{pmatrix} \tag{2.26}$$

$$\rho_{BC} = \begin{pmatrix} 0.56 & -0.2+0.01i & -0.17+0.02i & 0.02+0.04i \\ -0.2-0.01i & 0.14 & 0.11+0.05i & 0.02 \\ -0.17-0.02i & 0.11-0.05i & 0.14 & 0.-0.01i \\ 0.02-0.04i & 0.02 & 0.+0.01i & 0.16 \end{pmatrix} \tag{2.27}$$

As per the protocol described in Section 2.5, the three-qubit density operator is completely constructed. Three-qubit density matrix (ρ_{ABC}) for the generic state is explicitly given in Equation 2.28.

Density operators ρ_{AB}, ρ_{BC} as well as the three-qubit reconstructed state ρ_{ABC} are shown graphically in Figure 2.17. The two-party reduced states were able to reconstruct this three-qubit state with a fidelity of 0.90, which compares well with the full reconstruction of the entire three-qubit state given in Figure 2.6(b).

$$\rho_{ABC} = \begin{pmatrix} 0.52 & -0.24 & -0.23 & -0.08 & -0.22 & -0.01 & & -0.26 \\ & +0.07i & +0.02i & +0.05i & -0.03i & +0.08i & +0.02i & -0.06i \\ & & & & & & & \\ -0.24 & 0.12 & 0.11 & 0.04 & 0.10 & 0.01 & & 0.11 \\ 0.07i & & +0.02i & -0.01i & +0.04i & -0.04i & -0.01i & +0.06i \\ & & & & & & & \\ -0.23 & 0.11 & 0.10 & 0.03 & 0.10 & 0.01 & & 0.11 \\ 0.02i & -0.02i & & -0.02i & +0.02i & -0.04i & -0.01i & +0.04i \\ & & & & & & & \\ -0.08 & 0.04 & 0.03 & 0.02 & 0.03 & 0.01 & 0 & 0.03 \\ -0.05i & +0.01i & +0.02i & & +0.02i & -0.01i & & +0.03i \\ & & & & & & & \\ -0.22 & 0.10 & 0.10 & 0.03 & 0.09 & 0 & & 0.11 \\ 0.03i & -0.04i & -0.02i & -0.02i & & -0.03i & -0.01i & +0.01i \\ & & & & & & & \\ -0.01 & 0.01 & 0.01 & 0.01 & 0 & 0.01 & 0 & -0.01i \\ -0.08i & +0.04i & +0.04i & +0.01i & +0.03i & & & 0.04i \\ & & & & & & & \\ -0.02i & +0.01i & +0.01i & & +0.01i & & & +0.01i \\ & & & & & & & \\ -0.26 & 0.11 & 0.11 & 0.03 & 0.11 & -0.01 & 0 & 0.14 \\ 0.06i & -0.06i & -0.04i & -0.03i & -0.01i & -0.04i & -0.01i & \end{pmatrix} \tag{2.28}$$

2.5.1.2 W-state reconstruction

Another demonstration of this theoretical proposition (as described earlier), is provided by the three-qubit W-state. Partial tomography of the two party parts of the W-state gives rise to the following density operators,

$$\rho_{AB} = \begin{pmatrix} 0.36 & 0 & 0 & 0.-0.01i \\ 0 & 0.21 & 0.2+0.05i & -0.01 \\ 0 & 0.2-0.05i & 0.21 & 0.01 \\ 0.+0.01i & -0.01 & 0.01 & 0.22 \end{pmatrix} \tag{2.29}$$

$$\rho_{BC} = \begin{pmatrix} 0.34 & -0.01 & 0.+0.01i & 0 \\ -0.01 & 0.3 & 0.+0.24i & 0.02 \\ -0.01 & 0.-0.24i & 0.2 & 0 \\ 0 & 0.02 & 0 & 0.16 \end{pmatrix} \tag{2.30}$$

These experimental tomographed density matrices were then used to reconstruct the three-qubit W-state density matrix ρ_{ABC} given by:

$$\rho_{ABC} = \begin{pmatrix}
0 & \begin{matrix}-0.01\\-0.02i\end{matrix} & \begin{matrix}0.02\\-0.01i\end{matrix} & 0 & 0.02 & 0 & 0 & 0 \\
\begin{matrix}-0.01\\+0.02i\end{matrix} & 0.36 & \begin{matrix}\\+0.29i\end{matrix} & 0.02 & \begin{matrix}-0.1\\+0.37i\end{matrix} & \begin{matrix}-0.01\\+0.01i\end{matrix} & \begin{matrix}-0.02\\-0.02i\end{matrix} & 0 \\
\begin{matrix}0.02\\+0.01i\end{matrix} & \begin{matrix}\\-0.29i\end{matrix} & 0.23 & \begin{matrix}\\-0.02i\end{matrix} & \begin{matrix}0.30\\+0.08i\end{matrix} & 0.01 & \begin{matrix}-0.01\\+0.01i\end{matrix} & 0 \\
0 & \begin{matrix}0.02\\+0.02i\end{matrix} & \begin{matrix}\\+0.02i\end{matrix} & 0 & \begin{matrix}-0.01\\0.02i\end{matrix} & 0 & 0 & 0 \\
0.02 & \begin{matrix}-0.10\\-0.37i\end{matrix} & \begin{matrix}0.30\\-0.08i\end{matrix} & \begin{matrix}-0.01\\-0.02i\end{matrix} & 0.40 & 0.02 & \begin{matrix}-0.01\\+0.02i\end{matrix} & 0 \\
0 & \begin{matrix}-0.01\\-0.01i\end{matrix} & 0.01 & 0 & 0.02 & 0 & 0 & 0 \\
0 & \begin{matrix}-0.02\\+0.02i\end{matrix} & \begin{matrix}-0.01\\-0.01i\end{matrix} & 0 & \begin{matrix}-0.01\\-0.02i\end{matrix} & 0 & 0 & 0 \\
0 & 0 & 0 & 0 & 0 & 0 & 0 & 0
\end{pmatrix} \tag{2.31}$$

The reconstructed density matrix for the W-state is shown in Figure 2.18, computed from two sets of the corresponding two-qubit reduced density matrices. The tomographed state has a fidelity of 0.97, which matches well with the fidelity of the original three-qubit density matrix of the W-state (Figure 2.13(b)).

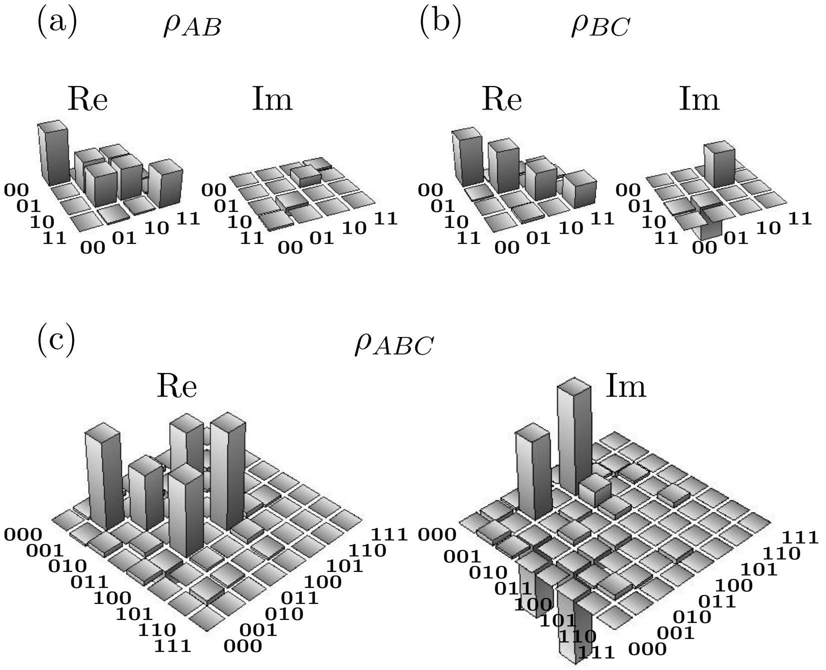

Figure 2.18: The real (Re) and imaginary (Im) parts of the density matrix for the W-state: (a) The two-qubit reduced density matrix ρ_{AB}. (b) The two-qubit reduced density matrix ρ_{BC}. (c) The entire three-qubit density matrix ρ_{ABC}, reconstructed from the corresponding two-qubit reduced density matrices. The rows and columns encode the computational basis in binary order, from $|00\rangle$ to $|11\rangle$ for two qubits and from $|000\rangle$ to $|111\rangle$ for three qubits. The tomographed state has a fidelity of 0.97.

2.6 Reconstruction of three-qubit W$\bar{\text{W}}$-state from its reduced parties

An discussed earlier, an interesting feature of three-qubit pure states, according to which there is no more information content in a three-qubit state than its two two-party reduced states, has a few exceptions. The exceptional states are the generalized GHZ states ($a|000\rangle + be^{\iota\phi}|111\rangle$), in which the information about relative phase between the basis vectors is inaccessible through the two-party reduced marginals. Thus we can not obtain the three-qubit GHZ state reconstruction using its reduced two party marginals. Yet there is an interesting fact, which states that a W$\bar{\mathrm{W}}$ state which is obtainable from GHZ state via SLOCC can be reconstructed from its reduced two party marginals.

Consider a three-qubit generic state $|\psi_{ABC}\rangle = \frac{1}{2\sqrt{3}}(|001\rangle + |010\rangle + |100\rangle - 3|111\rangle)$, from where a W$\bar{\mathrm{W}}$-state is constructed by implementing a $U^{1,2,3}(\frac{\pi}{2})_y$ operator. Two reduced two-qubit states of $|\psi_{ABC}\rangle$ are given as:

$$\rho_{AB} = \frac{1}{12}\begin{pmatrix} 1 & 0 & 0 & -3 \\ 0 & 1 & 1 & 0 \\ 0 & 1 & 1 & 0 \\ -3 & 0 & 0 & 9 \end{pmatrix}, \tag{2.32}$$

$$\rho_{BC} = \frac{1}{12}\begin{pmatrix} 1 & 0 & 0 & -3 \\ 0 & 1 & 1 & 0 \\ 0 & 1 & 1 & 0 \\ -3 & 0 & 0 & 9 \end{pmatrix} \tag{2.33}$$

Both ρ_{AB} and ρ_{BC} have eigenvectors:

$$\begin{aligned} |\psi_1\rangle &= \frac{1}{\sqrt{10}}\begin{pmatrix} 1 & 0 & 0 & -3 \end{pmatrix}^\dagger \\ \text{and} \qquad |\psi_2\rangle &= \frac{1}{\sqrt{2}}\begin{pmatrix} 0 & 1 & 1 & 0 \end{pmatrix}^\dagger \end{aligned} \tag{2.34}$$

with non-zero eigenvalues $\frac{5}{6}$ and $\frac{1}{6}$ respectively. These eigenvalues are as the same for two single party reduced states ρ_C and ρ_A. The other two eigenvalues of the state $\rho_{AB}(\rho_{BC})$ are zero, as the strength of a correlation is always determined by the smaller party. The three-party states constructed using ρ_{AB} and ρ_C is given as:

$$|\psi_{ABC};\phi_1\rangle = e^{\iota\phi_{11}}\sqrt{\frac{1}{12}}\begin{pmatrix} 0 \\ 1 \\ 1 \\ 0 \end{pmatrix} \otimes \begin{pmatrix} 1 \\ 0 \end{pmatrix} + e^{\iota\phi_{12}}\frac{1}{\sqrt{12}}\begin{pmatrix} 1 \\ 0 \\ 0 \\ -3 \end{pmatrix} \otimes \begin{pmatrix} 0 \\ 1 \end{pmatrix} \tag{2.35}$$

Similarly, the three-qubit state obtained through ρ_A and ρ_{BC} are given as

$$|\psi_{ABC};\phi_2\rangle = e^{\iota\phi_{21}}\sqrt{\frac{1}{12}}\begin{pmatrix}1\\0\end{pmatrix}\otimes\begin{pmatrix}0\\1\\1\\0\end{pmatrix}+e^{\iota\phi_{22}}\frac{1}{\sqrt{12}}\begin{pmatrix}0\\1\end{pmatrix}\otimes\begin{pmatrix}1\\0\\0\\-3\end{pmatrix} \tag{2.36}$$

We have, $|\psi_{ABC};\phi_1\rangle = |\psi_{ABC};\phi_2\rangle$ to be satisfied, which in turn determines the angles $\phi_{11}, \phi_{12}, \phi_{21}, \phi_{22}$. As can be seen clearly, the three-party states found in both the cases are similar upto relative phase factors. The simplest solution corresponds to the angles, $\phi_{11} = \phi_{12} = \phi_{21} = \phi_{22} = 0$. The three-qubit state thus obtained is given as

$$\frac{1}{\sqrt{12}}\begin{pmatrix}0 & 1 & 1 & 0 & 1 & 0 & 0 & -3\end{pmatrix}^{\dagger}. \tag{2.37}$$

Thus this special three-qubit state is able to construct the three-party state from its reduced two party states. This generic state gives rise to the $\mathrm{W\bar{W}}$-state under local unitary operators (Section 2.4.4). Therefore, it can be concluded that three-qubit $\mathrm{W\bar{W}}$-state has no irreducible three-party correlations.

2.6.1 Experimental reconstruction of $\mathrm{W\bar{W}}$-state

Experimentally constructed $\mathrm{W\bar{W}}$-state is obtained by quantum state tomography of its reduced two-party states. The reduced density operators ρ_{AB} and ρ_{BC} are partially tomographed to experimentally obtain 4×4 dimensional reduced parties given as:

$$\rho_{AB} = \begin{pmatrix} 0.19 & 0.18-0.02i & 0.17 & 0.02-0.06i \\ 0.18+0.02i & 0.34 & 0.35+0.07i & 0.18-0.03i \\ 0.17 & 0.35-0.07i & 0.31 & 0.16+0.02i \\ 0.02+0.06i & 0.18+0.03i & 0.16-0.02i & 0.16 \end{pmatrix} \tag{2.38}$$

$$\rho_{BC} = \begin{pmatrix} 0.13 & 0.13 & 0.18-0.02i & 0.01 \\ 0.13 & 0.31 & 0.29-0.08i & 0.19 \\ 0.18+0.02i & 0.29+0.08i & 0.38 & 0.18-0.01i \\ 0.01 & 0.19 & 0.18+0.01i & 0.19 \end{pmatrix} \tag{2.39}$$

As per method described in the previous section, three-party state (ρ_{ABC}) is completely characterized using ρ_{AB} and ρ_{BC} from Equations (2.38) and (2.39) respectively. The three-party state thus reconstructed is given as:

$$\rho_{ABC} = \begin{pmatrix} 0 & 0.01-0.01i & 0.01-0.01i & 0.01-0.01i & 0.01-0.01i & 0.01 & 0.01-0.01i & 0 \\ 0.01+0.01i & 0.19 & 0.16-0.01i & 0.19-0.01i & 0.15-0.02i & +0.02i+0.02i & 0.21-0.06i & 0.01 \\ 0.01+0.01i & 0.16+0.01i & 0.14 & 0.16 & 0.13-0.01i & 0.12+0.02i & 0.18-0.04i & 0 \\ 0.01+0.01i & 0.19+0.01i & 0.16 & 0.19 & 0.15-0.01i & 0.14+0.02i & 0.21-0.05i & 0.01 \\ 0.01+0.01i & 0.15+0.02i & 0.13+0.01i & 0.15+0.01i & 0.13 & 0.11+0.03i & 0.17-0.03i & 0 \\ 0.01 & 0.14-0.02i & 0.12-0.02i & 0.14-0.02i & 0.11-0.03i & 0.1 & 0.14-0.06i & 0 \\ 0.01+0.01i & 0.21+0.06i & 0.18+0.04i & 0.21+0.05i & 0.17+0.03i & 0.14+0.06i & 0.24 & 0.01 \\ 0 & 0.01 & 0 & 0.01 & 0 & 0 & 0.01 & 0 \end{pmatrix} \tag{2.40}$$

The graphical representation of the reconstructed density matrix (Equation (2.40)) for the W$\bar{\text{W}}$ state, using two sets of the corresponding two-qubit reduced density matrices (ρ_{AB}, ρ_{BC}) is given in Figure 2.19. The two-party reduced states were able to reconstruct the three-party W$\bar{\text{W}}$ state with a fidelity of 0.92, which matches well with the full reconstruction of the entire three-qubit state given in Figure 2.16(b). This experiment provides an evidence for the reconstruction of non-local three party correlations existing in W$\bar{\text{W}}$ state from its reduced two-party states, which is in contrast with the entanglement features of the GHZ class of states.

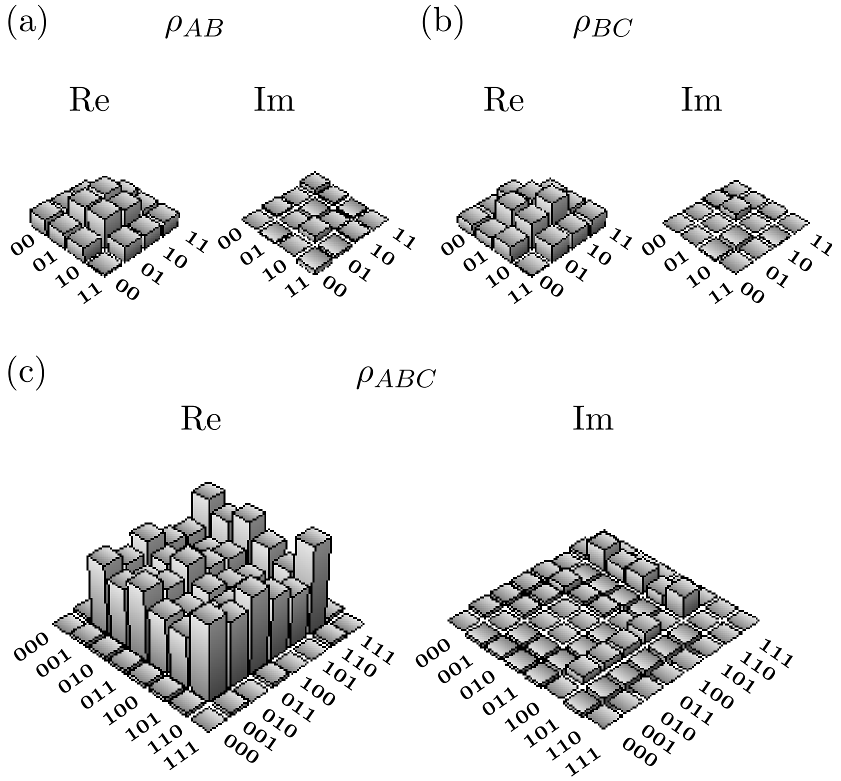

Figure 2.19: The real (Re) and imaginary (Im) parts of the tomographed density matrix for the state $\mathrm{W\bar{W}}$ state. (a) The two-qubit reduced density matrix ρ_{AB}. (b) The two-qubit reduced density matrix ρ_{BC}. (c) The entire three-qubit density matrix ρ_{ABC}, reconstructed from the corresponding two-qubit reduced density matrices. The rows and columns in the bar graphs encode the computational basis of the qubits, from $|00\rangle$ to $|11\rangle$ for two qubits and from $|000\rangle$ to $|111\rangle$ for three qubits. The fidelity between the three-qubit state (ρ_{ABC}) reconstructed from the two-qubit density matrices and the three-qubit state obtained by complete three-qubit state tomography is found to be 0.92.

2.7 Conclusions

An NMR-based scheme is proposed and implemented to construct a generic three-qubit state from which any general pure state of three-qubits (including separable, biseparable and maximally entangled states) can be constructed, up to local unitaries. Full tomographic reconstruction of the experimentally generated states showed good fidelity of preparation and we have achieved a high degree of control over the state space of three-qubit quantum systems. Generating generic three-qubit states with a nontrivial phase parameter was an experimental challenge and we achieved it by crafting a special pulse scheme. It has been previously shown that in a system of three qubits, almost no irreducible three-party correlations exist (exceptions belong to GHZ class of states) and that all information about such quantum states is completely contained in the three two-party correlations. We have demonstrated this important result experimentally in a system of three qubits. The three-qubit density operator ρ_{ABC} is obtained by complete quantum state tomography and compared with the same three-qubit state reconstructed from tomographs of the two-party reduced density operators given by ρ_{AB}, ρ_{BC} and ρ_{AC}. This part of the work has been published in *Phys. Rev. A*, **91**, 022312 (2015).

The $\mathrm{W\bar{W}}$ state which belongs to GHZ class of states is experimentally implemented. This state is able to construct the complete three-qubit density matrix from a set of two-party reduced density operators (ρ_{AB}, ρ_{BC}). Thus, although the $\mathrm{W\bar{W}}$ state belongs to the same entanglement class as the GHZ state, the two states store information about multi-party correlations in completely different ways. Experimental demonstration of an interesting feature of multi-qubit entanglement is shown, namely, that two different entangled states belonging to the same SLOCC class can yet have their correlations exhibiting contrasting irreducible properties. This part of the work has been published in *Phys. Rev. A*, **92**, 022307 (2015).

Chapter 3

Single qutrit dynamics using Majorana geometrical representation

Nuclei with higher spins possess quadrupolar moments due to the lack of symmetry in the distribution of electric charges [39, 42]. A spin-$\frac{1}{2}$ is analogous to a magnetic dipole which starts precessing at its natural frequency when kept in a magnetic field. A spin-$\frac{1}{2}$ (qubit) is a two-level quantum system whose dynamics can be completely determined from its Bloch sphere representation in three-dimensional real coordinate space ($\mathcal{R}^3$). However the geometry of quantum systems become very complicated with increasing dimension [104]. Thus even for a single spin-1, it is interesting to explore the feasible geometrical models that can characterize its structure and dynamics. This motivates the present chapter to obtain an intuitive geometrical realization of the spin-1 (qutrit) magnetization vector and to study the dynamics of a qutrit.

The Bloch sphere representation of a qubit provides a geometrical picture of a single-qubit, in which a state of a qubit in two-dimensional Hilbert space is mapped onto a sphere in the three-dimensional real coordinate space($\mathcal{R}^3$). This mapping ensures that every single-qubit pure state lies on the surface and mixed state in the interior of the Bloch sphere [1, 104]. This picture provides a geometrical representation for the spin-1/2 magnetization vector. Extensions of such a physical picture to higher spin systems are non-trivial.

A single-qutrit pure state is associated with a three-dimensional complex vector space and thus its geometrical realization in the three-dimensional real space is not possible. This chapter describes the geometrical representation of a qutrit, in which the pure state of a single-qutrit is represented by two points on a 2-sphere. There have been various proposals for the geometrical representations of higher level quantum systems [105, 106, 107, 108, 109, 110]. For instance, a three-level quantum system has been shown to occupy an octant in eight-dimensional real space [105], another piece of work deals in the generalization of the Bloch sphere for three-dimensional Hilbert space [106, 108], and mapping N-qubit pure states onto a polynomial which is further used to geometrically represent multi-qubit pure states [111, 112].

In a seminal paper by Ettore Majorana in 1932, a geometrical representation was proposed, according to which, a pure state of a spin 's' is represented by '$2s$' points on the surface of a unit sphere [88]. Henceforth, in this thesis, this unit sphere is referred to as 'Majorana sphere'. Though the paper [88] was originally aimed at atoms oriented in a magnetic field and the calculation of probability of spin flips, the Majorana representation for spin$-s$ systems found widespread applications such as determining geometric phase of spins [113, 114], representing N spinors by N points on the Majorana sphere [101], geometrical representation and dynamics of multi-qubit entangled states [101, 115], statistics of chaotic quantum dynamical systems [116] and characterizing polarized light [117]. In the context of Majorana representation of polarized light, the direction of propagation of light is along the bisector (or its reverse) of the angle enclosed between both the points at the center of the sphere [117]. In this chapter, the Majorana representation is adopted for geometrical realization of a single-qutrit consisting of two points on the surface of a unit sphere, and to observe their dynamics under SO(3) and SU(3) transformations, and for representing NMR pulses in an intuitive way.

In qudit ($d-$level quantum system) based quantum computing schemes [118, 119, 120, 121, 122, 123, 124, 125], a single qutrit system ($d = 3$) is of particular importance. This is the smallest system with inherent quantum properties such as contextuality [85, 86, 87]. Qudits in NMR can be modeled by naturally existing nuclei with spin $> 1/2$ or can be carved out of two or more than two dipolar coupled spin-1/2 nuclei. In the context of NMR based quantum computing, decomposition of quantum gates for qutrits is not well understood unlike for qubits [5, 67]. The decomposition of quantum gates for a qutrit are proposed and their experimental implementations are carried out on an NMR quantum information processor, in this chapter.

In this chapter, the Majorana representation is used to explore the dynamics of a single qutrit, discuss its various properties and draw a parallel with the ternary quantum gates. The state of a qutrit is written in parametric form, also known as the ‘canonical state’. This is the minimal representation of a state of a qutrit, which when subject to SO(3) transformations alone, can span the complete state space of a qutrit. In the context of Majorana representation, this state is composed of two points lying symmetrically about the $z-$axis in the plane $x = 0$. A most general pure state of a qutrit is also defined that should ideally be composed of four parameters. This state can be obtained from the canonical state via a set of three SO(3) transformations.

The magnetization of a pure ensemble of single qutrit states is discussed. The corresponding magnetization vector is given a physical interpretation in the context of Majorana representation. Further, the states of single-qutrit systems are broadly classified as pointing and non-pointing states.

As the state of a qutrit evolves under the effect of different quantum operations, the points representing the state move on the surface of the Majorana sphere. SO(3) transformations correspond to the rotations in a three-dimensional real space, under which the relative separation of two points representing a qutrit on the Majorana sphere is invariant. Such operators are experimentally realized in NMR via spin-selective pulses (which in the present case of a single-qutrit, is a non-selective pulse). The dynamics of a pair of points on the Majorana sphere is also observed under SU(3) transformations generated by a complete set of eight Λ-matrices [105]. These transformations are realized experimentally in NMR via transition-selective pulses. Observation of the trajectories of the pair of Majorana points under SO(3) and SU(3) draw a correspondence between the rotation operators and basic quantum gates. Various quantum gates for a qutrit include swap gates, controlled phase shift gates and a three-dimensional analogue of the Hadamard gate are realized. NMR experimental implementation of these ternary quantum gates is followed by a complete quantum state tomography of the single-qutrit system. A spin-1 deuterium nucleus of the deutrated-chloroform molecule serves as a single-qutrit system. In order to obtain a well resolved pair of single-quantum transitions in deuterium NMR spectrum, the chloroform-D molecule is embedded in an anisotropic environment provided by a lyotropic liquid crystal. Simultaneous excitation of both the transitions correspond to the spin-selective excitations (or non-selective as there is only one spin here), and the excitation of one transition at a time corresponds to the transition-selective pulse.

3.1 Majorana representation

Consider the state of a spin 's' in $2s+1$ dimensional Hilbert space ('s' can have both integral as well as half integral values),

$$|\Psi\rangle = \sum_{j=-s}^{+s} C_j|j\rangle = C_{-s}|{-s}\rangle + \cdots + C_0|0\rangle + \cdots + C_{+s}|{+s}\rangle \tag{3.1}$$

where $|j\rangle s$ are the orthonormal basis vectors and $C_j s$ are their respective complex coefficients. Majorana introduced a polynomial of degree $2s$,

$$a_0\zeta^{2s} + a_1\zeta^{2s-1} + \ldots \cdots + a_{2s} = 0, \tag{3.2}$$

where

$$a_r = (-1)^r \frac{C_{s-r}}{\sqrt{(2s-r)!r!}}. \tag{3.3}$$

This polynomial has '$2s$' complex roots, which are plotted on the xy-plane (complex plane with purely real roots lying on the $x-$axis and the imaginary ones on the $y-$axis). Inverse stereographic projection of each of these roots with respect to the south pole of the unit sphere, gives rise to '$2s$' points on the surface of a unit sphere. These '$2s$' points comprise the Majorana representation of a spin s. In case of a single-qutrit (spin-1 system), $|\Psi\rangle = C_{-1}|{-1}\rangle + C_0|0\rangle + C_{+1}|{+1}\rangle$ and the corresponding Majorana polynomial is a quadratic equation given by

$$\begin{aligned} & a_0\zeta^2 + a_1\zeta + a_2 = 0, \\ & a_0 = \frac{C_{+1}}{\sqrt{2}}, \quad a_1 = -C_0, \quad = \frac{C_{-1}}{\sqrt{2}}. \end{aligned} \tag{3.4}$$

The roots of this equation are plotted in the plane $z = 0$, which are represented by points ($P_1'(x_1', y_1', 0)$ and $P_2'(x_2', y_2', 0)$) in Figure 3.1(a). Their respective inverse stereographic projections, lead to two points on the unit sphere that is centered at $O(0,0,0)$. In Figure 3.1(a), the stereographic projections are shown by dashed lines passing through south pole of the unit sphere ($S(0,0,-1)$) and the respective roots shown as two black dots in the plane $z = 0$. These two dashed lines intersect the unit sphere at two points ($P_1(x_1, y_1, z_1)$ and $P_2(x_2, y_2, z_2)$) shown in red and blue colors respectively. Thus a qutrit is represented by 2 points on the surface of a unit sphere in Majorana representation. A few examples of the Majorana representation of a set of single-qutrit basis vectors are given below:

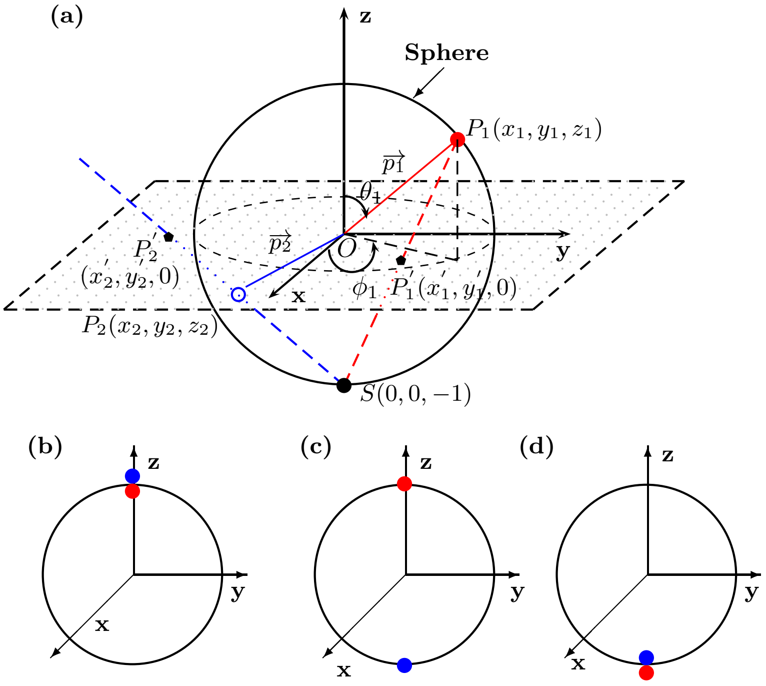

Figure 3.1: Majorana representation of a qutrit represented by two points P_1 and P_2, connected with the center of the sphere by lines shown in red and blue colors respectively. θ_1, ϕ_1 are the polar and azimuthal angles respectively corresponding to point P_1 (similarly there are spherical polar coordinates θ_2, ϕ_2 for point P_2). (a) Roots of the Majorana polynomial are shown in the plane $z = 0$ by points P_1' and P_2', whose inverse stereographic projection give rise to the Majorana representation. Three examples are shown corresponding to the Majorana representation of single-qutrit basis vectors (b) $|+1\rangle$, (c) $|0\rangle$ and (d) $|-1\rangle$.

- $$|\psi\rangle = |+1\rangle = \begin{pmatrix} 1 \\ 0 \\ 0 \end{pmatrix} \tag{3.5}$$

This leads to $a_0 = \frac{1}{\sqrt{2}}$, $a_1 = 0$, $a_2 = 0$, and thus both the roots of the polynomial in Equation (3.4) are found to be ‘0’,whose coordinates in the prescribed xy plane are (0,0). Inverse stereographic projection w.r.t south pole, intersects the Majorana sphere at the north pole of the sphere. Thus the Majorana representation of the eigenvector of Pauli z-operator, Σ_z (in three dimensions) with eigenvalue +1, consists of both the points at the north pole of the sphere, whose

(x, y, z) coordinates in three-dimensional real space ($\mathcal{R}^3$) are given as $(0, 0, 1)$, $(0, 0, 1)$. This is pictorially shown in Figure 3.1(b).

-
$$|\psi\rangle = |0\rangle = \begin{pmatrix} 0 \\ 1 \\ 0 \end{pmatrix} \tag{3.6}$$

  This leads to $a_0 = 0$, $a_1 = -1$, $a_2 = 0$, the Majorana polynomial

$$\epsilon\zeta^2 - 1\zeta = 0, \qquad \epsilon \to 0, \tag{3.7}$$

  gives rise to two roots '0' and '∞', with coordinates in the xy plane (0,0) and (∞,0) respectively. Inverse stereographic projection of these two points w.r.t south pole, intersect the Majorana sphere at the north pole and the south pole respectively of the sphere. Thus the Majorana representation of the eigenvector of Pauli z-operator, Σ_z (in three dimensions) with eigenvalue 0, consists of two points: $(0, 0, 1)$, $(0, 0, -1)$. This is pictorially shown in Figure 3.1(c).

-
$$|\psi\rangle = |-1\rangle = \begin{pmatrix} 0 \\ 0 \\ 1 \end{pmatrix} \tag{3.8}$$

  This leads to $a_0 = 0$, $a_1 = 0$, $a_2 = \frac{1}{\sqrt{2}}$, the Majorana polynomial

$$\epsilon\zeta^2 + \frac{1}{\sqrt{2}} = 0, \qquad \epsilon \to 0, \tag{3.9}$$

  gives rise to two roots '$\pm\iota\infty$', with coordinates in the xy plane ($\iota\infty$,0) and ($-\iota\infty$,0). Inverse stereographic projection w.r.t south pole, does not intersect the unit sphere anywhere else, other than the south pole of the sphere. Thus the Majorana representation of the eigenvector of Pauli z-operator, Σ_z (in three dimensions) with eigenvalue -1, consists of both the points at the south pole of the sphere, whose (x,y,z) coordinates in three-dimensional real space ($\mathcal{R}^3$) are given as $(0, 0, -1)$, $(0, 0, -1)$. This is pictorially shown in Figure 3.1(d).

General state of a three-level system and its Majorana representation

As per Majorana representation of a qutrit, every pure state of a qutrit can be represented geometrically by a pair of points on a unit sphere. Conversely, given two arbitrary points on a unit sphere, there always exists a pure quantum state of a qutrit corresponding to the given pair of points.
Let us consider two points $P_1(\theta_1, \phi_1)$ and $P_2(\theta_2, \phi_2)$ chosen arbitrarily on the unit sphere such that $\theta_i \in [0, \pi]$, $\phi_i \in [0, 2\pi]$. As shown in Figure 3.1(a), x, y, z coordinates of these points are written as:
$P_1(\sin\theta_1 \cos\phi_1, \sin\theta_1 \sin\phi_1, \cos\theta_1)$ and $P_2(\sin\theta_2 \cos\phi_2, \sin\theta_2 \sin\phi_2, \cos\theta_2)$.

Each of these points (P_1, P_2), when connected with the south pole of the sphere, $S(0, 0, -1)$ by a line, intersects the plane $z = 0$ at points $P_1^{'}(x_1^{'}, y_1^{'}, 0)$ and $P_2^{'}(x_2^{'}, y_2^{'}, 0)$ respectively. Figure 3.1(a) shows the dotted plane $z = 0$ with dashed black boundaries. A dashed blue line starting from the point $S(0, 0, -1)$, and after passing through point $P_2(x_2, y_2, z_2)$ (which lies on the rear portion of the sphere and hence is represented by a blue ring) is shown to intersect the plane $z = 0$ at point $P_2^{'}(x_2^{'}, y_2^{'}, 0)$ (when produced). The point $P_1(x_1, y_1, z_1)$, shown in red, when connected via a red dashed line with the south pole of the sphere, intersects the plane $z = 0$ at point $P_1^{'}(x_1^{'}, y_1^{'}, 0)$ shown as a black dot (Figure 3.1(a)). The coordinates of the points of intersection being $x_i^{'} = (\sin\theta_i \cos\phi_i)/(1 + \cos\theta_i)$, $y_i^{'} = (\sin\theta_i \sin\phi_i)/(1 + \cos\theta_i)$, $z_i^{'} = 0$. As per Majorana representation, these points ($P_i^{'}$, $i = 1, 2$) correspond to the graphical representation of the roots of the Majorana polynomial. Thus two roots of the second degree Majorana polynomial for a qutrit are $e^{\iota\phi_i} \tan\frac{\theta_i}{2}$, $i = 1, 2$. Finding the coefficients of the quadratic Majorana polynomial, state of the qutrit in 3-dimensional Hilbert space is found out to be

$$|\psi_g\rangle = \Gamma \begin{pmatrix} \sqrt{2}\cos\frac{\theta_1}{2}\cos\frac{\theta_2}{2} \\ e^{\iota\phi_1}\sin\frac{\theta_1}{2}\cos\frac{\theta_2}{2} + e^{\iota\phi_2}\cos\frac{\theta_1}{2}\sin\frac{\theta_2}{2} \\ \sqrt{2}e^{\iota(\phi_1+\phi_2)}\sin\frac{\theta_1}{2}\sin\frac{\theta_2}{2} \end{pmatrix} \tag{3.10}$$

where $\Gamma = \sqrt{2}/\left(\sqrt{3 + \cos\theta_1\cos\theta_2 + \sin\theta_1\sin\theta_2\cos(\phi_1 - \phi_2)}\right)$.

This state is the most general single-qutrit state whose Majorana representation is given by points P_1 and P_2. Assuming values of $\theta_i \in [0, \pi]$ and $\phi_i \in [0, 2\pi]$, state $|\psi_g\rangle$ spans the complete qutrit Hilbert space. For example, taking $\theta_1 = \phi_1 = \theta_2 = \phi_2 = 0$, points P_1, P_2 are found to lie at north pole of the unit sphere and $|\psi_g\rangle$ is found out to be $|+1\rangle$, which is as expected. Similarly $\theta_1 = 0, \phi_1 = 0, \theta_2 = \pi, \phi_2 = 0$ and $\theta_1 = \pi, \phi_1 = 0, \theta_2 = \pi, \phi_2 = 0$ result in states $|0\rangle$ and $|-1\rangle$ respectively.

3.1.1 Rotations on the Majorana sphere

Rotations of the pair of points, representing a qutrit on the Majorana sphere, can be achieved by the group of rotations in three-dimensional real space ($\mathcal{R}^3$). Consider a single-qutrit state, $|\psi_{initial}\rangle$ whose Majorana representation is given as points $P_1(x_1, y_1, z_1)$ and $P_2(x_2, y_2, z_2)$ (Figure 3.1(a)). Joining each of these points with the center of the sphere ($O(0,0,0)$), one obtains unit vectors $\overrightarrow{OP_1}$ and $\overrightarrow{OP_2}$, which are being represented as $\overrightarrow{p_1}$ and $\overrightarrow{p_2}$ respectively in Figure 3.1(a). Rotation of these vectors in three-dimensional coordinate space ($\mathcal{R}^3$) is governed by the rotation operators, $R_i(\xi_i)$ with $i \in \{x, y, z\}$ (giving rotation about $i-$axis by angle ξ_i):

$$R_x(\xi_x) = \begin{pmatrix} 1 & 0 & 0 \\ 0 & \cos(\xi_x) & \sin(\xi_x) \\ 0 & -\sin(\xi_x) & \cos(\xi_x) \end{pmatrix},$$

$$R_y(\xi_y) = \begin{pmatrix} \cos(\xi_y) & 0 & -\sin(\xi_y) \\ 0 & 1 & 0 \\ \sin(\xi_y) & 0 & \cos(\xi_y) \end{pmatrix},$$

$$R_z(\xi_z) = \begin{pmatrix} \cos(\xi_z) & \sin(\xi_z) & 0 \\ -\sin(\xi_z) & \cos(\xi_z) & 0 \\ 0 & 0 & 1 \end{pmatrix}. \tag{3.11}$$

These are the SO(3) group of transformations, under whose action, the pair of points move like a rigid object on the Majorana sphere, which in turn rotate the corresponding single-qutrit state. In order to gain further insights into the Majorana representation of a qutrit, it is interesting to find out the corresponding operations in the Hilbert space of a single qutrit.

The operator space of a single-qutrit is completely spanned by eight elements of the SU(3) group [126]. This set of elements of course span the much smaller single-qutrit state space. However, a set of three-dimensional analogue of the Pauli matrices which is a subgroup of the SU(3) transformations consist of only three elements. These three elements act as generators for the SO(3) transformations. Explicitly, SO(3) transformations in $3-$dimensional Hilbert space are generated by the three-dimensional analogue of the Pauli matrices,

$$\Sigma_x = \frac{1}{\sqrt{2}} \begin{pmatrix} 0 & 1 & 0 \\ 1 & 0 & 1 \\ 0 & 1 & 0 \end{pmatrix}, \Sigma_y = \frac{1}{\sqrt{2}} \begin{pmatrix} 0 & -\iota & 0 \\ \iota & 0 & -\iota \\ 0 & \iota & 0 \end{pmatrix}, \Sigma_z = \begin{pmatrix} 1 & 0 & 0 \\ 0 & 0 & 0 \\ 0 & 0 & -1 \end{pmatrix}. \tag{3.12}$$

These Hermitian operators generate unitary transformations defined as:

$$U_i(\xi) = e^{\iota \xi \Sigma_i} = \Delta + (\cos\xi - 1)\ \Sigma_i^2 + \iota \sin\xi\ \Sigma_i \tag{3.13}$$

where Δ is the 3×3 identity matrix.

These transformations span only a part of the Hilbert space of a qutrit, but possess some interesting features. When $U_i(\xi)$ acts on a single-qutrit state $|\psi\rangle$ in the $3-$dimensional Hilbert space, it leads to the rotation of the two points representing a qutrit on the Majorana sphere by angle ξ about i-axis. Explicit matrices for the unitary transformations generated by $\Sigma_x, \Sigma_y, \Sigma_z$ are respectively given as:

$$U_x(\xi_x) = \frac{1}{\sqrt{2}} \begin{pmatrix} \sqrt{2}\cos^2(\frac{\xi_x}{2}) & \iota\sin(\xi_x) & -\sqrt{2}\sin^2(\frac{\xi_x}{2}) \\ \iota\sin(\xi_x) & \sqrt{2}\cos(\xi_x) & \iota\sin(\xi_x) \\ -\sqrt{2}\sin^2(\frac{\xi_x}{2}) & \iota\sin(\xi_x) & \sqrt{2}\cos^2(\frac{\xi_x}{2}) \end{pmatrix},$$

$$U_y(\xi_y) = \frac{1}{\sqrt{2}} \begin{pmatrix} \sqrt{2}\cos^2(\frac{\xi_y}{2}) & \sin(\xi_y) & -\sqrt{2}\sin^2(\frac{\xi_y}{2}) \\ -\sin(\xi_y) & \sqrt{2}\cos(\xi_y) & \sin(\xi_y) \\ -\sqrt{2}\sin^2(\frac{\xi_y}{2}) & -\sin(\xi_y) & \sqrt{2}\cos^2(\frac{\xi_y}{2}) \end{pmatrix},$$

$$U_z(\xi_z) = \begin{pmatrix} e^{\iota\xi_z} & 0 & 0 \\ 0 & 1 & 0 \\ 0 & 0 & e^{-\iota\xi_z} \end{pmatrix}. \tag{3.14}$$

The correspondence between the action of $R_i(\xi_i)$ on the Majorana representation in $\mathcal{R}^3$ and that of $U_i(\xi_i)$ in three-dimensional Hilbert space can be revealed using the following procedure:

- Consider a state of qutrit $|\psi_{initial}\rangle$, and its Majorana representation $P_1(x_1, y_1, z_1)$ and $P_2(x_2, y_2, z_2)$.

- Implement a unitary transformation $U_i(\xi_i)$ in the three-dimensional Hilbert space, such that $|\psi_{final}\rangle = U_i(\xi_i)|\psi_{initial}\rangle$. Majorana representation of the final state being $Q_1(x_1^{'}, y_1^{'}, z_1^{'})$ and $Q_2(x_2^{'}, y_2^{'}, z_2^{'})$.

- On the other hand, consider rotation of vectors $\overrightarrow{p_1}$ and $\overrightarrow{p_2}$ under the operator $R_i(\xi_i)$ on the Majorana sphere. This results in vectors $\overrightarrow{q_1} = R_i(\xi_i)\overrightarrow{p_1}$ and $\overrightarrow{q_2} = R_i(\xi_2)\overrightarrow{p_1}$. It is found that vectors $\overrightarrow{q_1}$ and $\overrightarrow{q_2}$ intersect the Majorana sphere at points $Q_1(x_1^{'}, y_1^{'}, z_1^{'})$ and $Q_2(x_2^{'}, y_2^{'}, z_2^{'})$ respectively. These points are exactly same as that of the Majorana representation of $|\psi_{final}\rangle$.

This step by step procedure is demonstrated explicitly for a general single-qutrit state under the effect of a unitary transformation. Let us consider a general single-qutrit state ($|\psi_g\rangle$) as the initial state:

$$|\psi_{initial}\rangle = \Gamma \begin{pmatrix} \sqrt{2}\cos\frac{\theta_1}{2}\cos\frac{\theta_2}{2} \\ e^{\iota\phi_1}\sin\frac{\theta_1}{2}\cos\frac{\theta_2}{2} + e^{\iota\phi_2}\cos\frac{\theta_1}{2}\sin\frac{\theta_2}{2} \\ \sqrt{2}e^{\iota(\phi_1+\phi_2)}\sin\frac{\theta_1}{2}\sin\frac{\theta_2}{2} \end{pmatrix} \tag{3.15}$$

where $\Gamma = \sqrt{2}/\left(\sqrt{3 + \cos\theta_1\cos\theta_2 + \sin\theta_1\sin\theta_2\cos(\phi_1 - \phi_2)}\right)$.
The Majorana representation of this state is given by two points (Section 3.1):
$P_1(\sin\theta_1\cos\phi_1, \sin\theta_1\sin\phi_1, \cos\theta_1)$ and $P_2(\sin\theta_2\cos\phi_2, \sin\theta_2\sin\phi_2, \cos\theta_2)$.

Considering an operator $U_z(\xi_z = \phi_1)$, under whose action, the general single-qutrit state gives rise to the final state,

$$|\psi_{final}\rangle = U_z(\phi_1)|\psi_{initial}\rangle = \Gamma \begin{pmatrix} \sqrt{2}\cos\frac{\theta_1}{2}\cos\frac{\theta_2}{2} \\ \sin\frac{\theta_1}{2}\cos\frac{\theta_2}{2} + e^{\iota(\phi_2-\phi_1)}\cos\frac{\theta_1}{2}\sin\frac{\theta_2}{2} \\ \sqrt{2}e^{\iota(\phi_2-\phi_1)}\sin\frac{\theta_1}{2}\sin\frac{\theta_2}{2} \end{pmatrix} \tag{3.16}$$

where $\Gamma = \sqrt{2}/\left(\sqrt{3 + \cos\theta_1\cos\theta_2 + \sin\theta_1\sin\theta_2\cos(\phi_1 - \phi_2)}\right)$.
Majorana representation of state $|\psi_{final}\rangle$ is found to be the points: $Q_1\left(\sin\theta_1, 0, \cos\theta_1\right)$

and $Q_2\,(\sin\theta_2\cos(\phi_2-\phi_1),\sin\theta_2\sin(\phi_2-\phi_1),\cos\theta_2)$.
On the other hand, re-considering points (P_1, P_2), constituting the Majorana representation of state $|\psi_{initial}\rangle$, and its corresponding unit vectors ($\overrightarrow{p_1},\overrightarrow{p_2}$) (Figure 3.1(a)). Let us rotate each of these unit vectors about $z-$axis by angle (ϕ_1) in the clockwise direction. The resulting vectors: $\overrightarrow{q_1}=R_z(\phi_1)\overrightarrow{p_1}$ and $\overrightarrow{q_2}=R_z(\phi_1)\overrightarrow{p_2}$ intersect the unit sphere at points Q_1' and Q_2' respectively. These points are found out to be: $Q_1'\,(\sin\theta_1,0,\cos\theta_1)$ and $Q_2'\,(\sin\theta_2\cos(\phi_2-\phi_1),\sin\theta_2\sin(\phi_2-\phi_1),\cos\theta_2)$, which are exactly same as points Q_1 and Q_2 respectively. Thus a most general single-qutrit state when acted upon by operator $U_z(\xi_z)$ in $\mathcal{H}^3$, its corresponding Majorana representation undergoes the rotation in $\mathcal{R}^3$ by same angle (ξ_z) about $z-$axis. This argument holds for an arbitrary single-qutrit SO(3) transformation. This has been numerically tested with randomly chosen single-qutrit states under the effect of arbitrarily chosen SO(3) transformation operators.

Thus, it can be concluded that there is a one-one correspondence between the action of $U_i(\xi_i)$ in Hilbert space ($\mathcal{H}^3$) and $R_i(\xi_i)$ in $\mathcal{R}^3$ for a single-qutrit. In general, $U_i(\xi_i)$ transformations in Hilbert space of a qutrit, induce rotations of the corresponding 'Majorana points' like a rigid object on the 'Majorana sphere'.

3.1.2 Canonical state of a three-level system

SO(3) group of transformations rotate the two points (representing a qutrit on the Majorana sphere) together like a rigid body rotation in three-dimensional coordinate space. Interestingly, these transformations rotate a single-qutrit as a whole, and are thus experimentally implemented in NMR by non-selective radio frequency pulses. This makes it more interesting to explore the SO(3) subgroup of SU(3) operations for a three-level quantum system. A pair of Majorana points representing a qutrit and its rotations in $\mathcal{R}^3$ corresponding to the SO(3) transformations in a single-qutrit Hilbert space, are used as a probe to explore many interesting properties of a qutrit. In three-dimensional Hilbert space ($\mathcal{H}^3$) a pure state of a single-qutrit is represented using three complex parameters or one can say six real parameters. One of these complex parameters can be made purely real by taking out the global phase, thus reducing the total number of real parameters to five. Normalization further reduces the number of parameters giving rise to a total of four independent real parameters to define a pure state of a qutrit. The Majorana representation of a single-qutrit does not take into account the global phase, thus a given pair of points on the Majorana sphere represent infinitely many single-qutrit states that are equivalent to each other upto a global phase. In other words, one can omit the global phase of a single-qutrit state in the context of Majorana representation. Thus, the discussion here is confined only to the four independent real parameters that characterize a single-qutrit pure state.

A basic question arises: Is there a state of a three-level quantum system from which each and every state in three-dimensional Hilbert space of a qutrit can be obtained by SO(3) operators? The answer to this is of course 'no'; however one can define a set of parametric states. Such a set of single-qutrit states are termed here as 'canonical states'. A 'canonical state' of a single-qutrit can be represented as:

$$|\psi_c\rangle = \begin{pmatrix} \sin\alpha \\ 0 \\ \cos\alpha \end{pmatrix}, \qquad \alpha \in [0, \pi/2]. \tag{3.17}$$

Here Majorana representation is used in order to analyze that, while $\alpha \in [0, \pi/2]$; canonical state, $|\psi_c\rangle\,(\alpha)$ is able to span the complete 3-dimensional Hilbert space under the action of SO(3) transformations. Majorana representation of $|\psi_c\rangle$ is composed of two points, $P_1(0, y_c, z_c)$ and $P_2(0, -y_c, z_c)$ where

$$\begin{aligned} x_c &= 0, \\ y_c &= \frac{\sqrt{2\sin 2\alpha}}{\sin\alpha + \cos\alpha}, \\ z_c &= \frac{\sin\alpha - \cos\alpha}{\sin\alpha + \cos\alpha}. \end{aligned} \tag{3.18}$$

These points lie on the great circle in the plane $x = 0$, such that they have same value of $z-$ coordinates and equal and opposite values of the projection on $y-$axis as shown in Figure 3.2. Angle enclosed between the points P_1 and P_2 at the center of sphere is given as: $\eta = 2\sin^{-1} y_c$. As α varies from $0 \leq \alpha \leq \frac{\pi}{2}$, η assumes values $0 \leq \eta \leq 2\pi$, thus the two points P_1 and P_2 lie all along the great circle in the plane $x = 0$ as shown in Figure 3.2.

Re-considering the Majorana representation of $|\psi_c\rangle$ (3.2), $OO^{'}$ is the perpendicular bisector of line joining the points P_1, P_2 as well as that of the angle η. Under the action of $U_i(\xi_i)$ transformation on a canonical state (fixing the value of α), corresponding $OO^{'}$ in the Majorana representation rotates like an ordinary vector in the coordinate space.

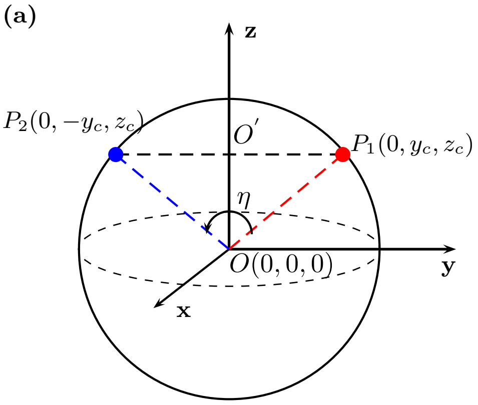

Figure 3.2: Majorana representation of canonical state, $|\psi_c\rangle$ shown as two points P_1 and P_2 in red and blue colors respectively. Dotted lines joining P_1 and P_2 with center $O(0,0,0)$, enclose angle η at the center of the sphere.

In general, a set of three rotations in $\mathcal{R}^3$ (example: Euler rotations) can help a vector to assume all the possible orientations on a sphere in three-dimensional real space. Thus a fixed value of the vector $\overrightarrow{OO'}$ can span the surface of a sphere with radius $|\overrightarrow{OO'}|$ in a three-dimensional real space under $R_i(\xi_i)$. Also, the bisector OO' attains values ranging from -1 to 1, as α assumes the values: $0 \leq \alpha \leq \frac{\pi}{2}$, which provides another degree of freedom. Therefore the bisector of the pair of Majorana points (representing a canonical state) assume infinitely many orientations on the Majorana sphere and exhibit the magnitude of the bisector in the range $[0,1]$. One degree of freedom (α) of the canonical state, and the three degrees of freedom obtained from three SO(3) transformations, are capable to provide a most general pure state of a qutrit as discussed in Section 3.1.

3.1.3 A set of SO(3) operators that links the general qutrit state with the qutrit canonical state

In this section, a set of three SO(3) operators are explicitly obtained with specific angles and rotation axes, under whose action, general and canonical states of a single-qutrit can be inter-converted. As discussed in section 3.1.1 there exists one to one correspondence between the action of operators $U_i(\xi_i)$ in three-dimensional Hilbert space ($\mathcal{H}^3$) and $R_i(\xi_i)$ in the three-dimensional space real coordinate space ($\mathcal{R}^3$). The

Majorana representation of the states ($|\psi_g\rangle$, $|\psi_c\rangle$) is used to find a set of rotation matrices, $R_i(\xi_i)s$.

Considering two arbitrary points $P_i(x_i, y_i, z_i)$ ($i = 1, 2$) representing the state of a qutrit on the Majorana sphere. These two points are rotated separately by same angle and about the same axes on the Majorana sphere. As per Majorana representation, pair of points representing a canonical state lie along the circumference of the great circle in the plane $x = 0$. Therefore points $P_i(x_i, y_i, z_i)$ ($i = 1, 2$) are first brought to the plane $x = 0$. This is achieved by β angle rotation about $y-$axis which is then followed by γ angle rotation about $z-$axis. The values of angles β and γ are found in such a way that $x-$components of vectors $R_z(\gamma)R_y(\beta)\overrightarrow{OP_i} = 0$ ($i = 1, 2$). The equations obtained in this case help in determining the values of β and γ. The state resulted previously is then rotated about $x-$axis by angle 'δ' with constraints that the y-coordinates of the final points are of equal and opposite values or z-coordinates of both the points are equal. Thus one can arrive at the configuration of points as per definition of that of the canonical state (ψ_c). The angles found explicitly, are given as:

$$\begin{aligned}
\beta &= \tan^{-1}\frac{\cos\phi_1\tan\theta_1 - \cos\phi_2\tan\theta_2}{\sin\phi_1\tan\theta_1 - \sin\phi_2\tan\theta_2} \\
\gamma &= \cos^{-1}\pm\sqrt{\frac{\cos^2\theta_1 - \cos^2\theta_2}{\sin^2\theta_2\sin^2(\beta+\phi_2) - \sin^2\theta_1\sin^2(\beta+\phi_1)}} \\
\delta &= \tan^{-1}\frac{\cos\gamma(\sin\theta_1\sin(\beta+\phi_1) + \sin\theta_2\sin(\beta+\phi_2)}{\cos\theta_1 + \cos\theta_2}
\end{aligned} \tag{3.19}$$

Corresponding operations in the Hilbert space leads us to the canonical state, starting from the general qutrit state (or vice versa)

$$|\psi_c\rangle = U_x(\delta)U_z(\gamma)U_y(\beta)|\psi_g\rangle. \tag{3.20}$$

Thus, the single parameter family of canonical states ($|\psi_c\rangle_\alpha$) alongwith the angles β, γ, and δ completely span three-dimensional Hilbert space.

3.1.4 SU(3) transformations

SU(3) is a special unitary group whose elements can completely span the operator space of a qutrit. A set of eight Λ matrices that are the generators of the SU(3) group, are the Gell Mann matrices [126] which are also used in particle physics. A set of eight Λ matrices and their properties [105, 126] given as:

$$\Lambda_1 = \begin{pmatrix} 0 & 1 & 0 \\ 1 & 0 & 0 \\ 0 & 0 & 0 \end{pmatrix}, \Lambda_2 = \begin{pmatrix} 0 & -\iota & 0 \\ \iota & 0 & 0 \\ 0 & 0 & 0 \end{pmatrix}, \Lambda_3 = \begin{pmatrix} 1 & 0 & 0 \\ 0 & -1 & 0 \\ 0 & 0 & 0 \end{pmatrix},$$

$$\Lambda_4 = \begin{pmatrix} 0 & 0 & 1 \\ 0 & 0 & 0 \\ 1 & 0 & 0 \end{pmatrix}, \Lambda_5 = \begin{pmatrix} 0 & 0 & -\iota \\ 0 & 0 & 0 \\ \iota & 0 & 0 \end{pmatrix}, \Lambda_6 = \begin{pmatrix} 0 & 0 & 0 \\ 0 & 0 & 1 \\ 0 & 1 & 0 \end{pmatrix},$$

$$\Lambda_7 = \begin{pmatrix} 0 & 0 & 0 \\ 0 & 0 & -\iota \\ 0 & \iota & 0 \end{pmatrix}, \quad \Lambda_8 = \frac{1}{\sqrt{3}} \begin{pmatrix} 1 & 0 & 0 \\ 0 & 1 & 0 \\ 0 & 0 & -2 \end{pmatrix}. \tag{3.21}$$

Such that the commutator,

$$[\Lambda_a, \Lambda_b] = 2\iota f_{abc}\Lambda_c \quad \text{where} \quad a, b, c \in \{1, 2 \ldots 8\} \tag{3.22}$$

The non-vanishing components of f_{abc} are:

$$\begin{aligned} & f_{123} = 1,\ f_{458} = f_{678} = \frac{\sqrt{3}}{2} \\ \text{and} \qquad & f_{147} = f_{246} = f_{257} = f_{345} = f_{516} = f_{637} = \frac{1}{2} \end{aligned} \tag{3.23}$$

The anti-commutator,

$$\{\Lambda_a, \Lambda_b\} = \frac{4}{3}\delta_{ab} + 2d_{abc}\Lambda_c. \tag{3.24}$$

Where the non-zero components of completely symmetric tensor d_{abc} are given as:

$$\begin{aligned} & d_{118} = d_{228} = d_{338} = -d_{888} = \frac{1}{\sqrt{3}}, \\ & d_{448} = d_{558} = d_{668} = d_{778} = -\frac{1}{2\sqrt{3}}, \\ \text{and} \qquad & d_{146} = d_{157} = -d_{247} = d_{256} = d_{344} = d_{355} = -d_{366} = -d_{377} = \frac{1}{2}. \end{aligned} \tag{3.25}$$

Also $\mathrm{Tr}\left(\Lambda_a\Lambda_b\right) = 2\delta_{ab}$, thus it follows that: $f_{abc} = -\frac{1}{4}\iota\mathrm{Tr}\left(\Lambda_a\left[\Lambda_b,\Lambda_c\right]\right)$, and $d_{abc} = \frac{1}{4}\mathrm{Tr}\left(\Lambda_a\{\Lambda_b,\Lambda_c\}\right)$.

The transformations that these matrices generate ($U_{\Lambda_i} = e^{\iota\theta\Lambda_i}$) target a two-level subspace of the three-level quantum system. These operations can be experimentally implemented via transition-selective pulses in NMR. A transition-selective pulse in NMR is governed by the single transition operators [40], generating transformations:

$$e^{\iota\xi I_k^{rs}} = I - I^{rs} + \cos\frac{\xi}{2}\,I^{rs} + 2\iota\sin\frac{\xi}{2}\,I_k^{rs}, \tag{3.26}$$

which is a unitary operator exciting transition between levels r, s about k^{th} axis by angle ξ. I_k^{rs} is the product operator element corresponding to the (r, s) subspace ($r, s \in \{1, 2, 3\}$: correspond to the three labels of the spin-1 energy levels, and $|i\rangle$, $|j\rangle$ are the single-qutrit basis vectors) and $k \in \{x, y, z\}$. The explicit form of the matrix elements of these transition-selective operators [40] is given as:

$$\begin{aligned}
\langle i|I_x^{rs}|j\rangle &= \frac{1}{2}(\delta_{ir}\delta_{js}+\delta_{is}\delta_{jr})\\
\langle i|I_y^{rs}|j\rangle &= \frac{\iota}{2}(-\delta_{ir}\delta_{js}+\delta_{is}\delta_{jr})\\
\langle i|I_z^{rs}|j\rangle &= \frac{1}{2}(\delta_{ir}\delta_{jr}-\delta_{is}\delta_{js})\\
\langle i|I^{rs}|j\rangle &= \frac{1}{2}(\delta_{ir}\delta_{jr}+\delta_{is}\delta_{js})
\end{aligned} \tag{3.27}$$

Using simple algebra, one can easily arrive at:

$$I_x^{12} = \frac{1}{2}\Lambda_1, \qquad I_y^{12} = \frac{1}{2}\Lambda_2, \qquad I_z^{12} = \frac{1}{2}\Lambda_3 \tag{3.28}$$

$$I_x^{23} = \frac{1}{2}\Lambda_6, \qquad I_y^{23} = \frac{1}{2}\Lambda_7, \qquad I_z^{23} = \frac{1}{2}\left(\sqrt{3}\Lambda_8 - \Lambda_3\right) \tag{3.29}$$

$$I_x^{13} = \frac{1}{2}\Lambda_4, \qquad I_y^{13} = \frac{1}{2}\Lambda_5, \qquad I_z^{13} = \frac{1}{2}\left(\sqrt{3}\Lambda_8 + \Lambda_3\right) \tag{3.30}$$

Equations (3.28), (3.29),and (3.30) depict the direct link between single-transition operators in NMR and the Gell Mann matrices. Correspondence shown in Equation (3.30) corresponds to the subspace of levels 1 and 3 of a qutrit. However, there is double quantum associated with this type of transition, thus it can not be implemented by a single transition. Correspondence shown in Equations (3.28) and (3.29) represents the subspace containing levels (1,2) and levels (2,3) respectively.

3.2 Spin-1 Magnetization vector

In this part of the present chapter, a physical picture of the single-qutrit magnetization vector is introduced with the help of Majorana representation. Although a qutrit is a higher dimensional object and is not realizable in $\mathcal{R}^3$, yet the magnetization associated with a single-qutrit pure state is a vector in real three-dimensional space.

As per the analysis described in the previous section, any general single-qutrit state can be brought to the canonical state via a set of three SO(3) transformations. Reconsidering the canonical pure state of a single-qutrit,

$$|\psi\rangle = \begin{pmatrix} \sin\alpha \\ 0 \\ \cos\alpha \end{pmatrix}, \qquad \alpha \in [0, \pi/2]. \tag{3.31}$$

Expectation values of the three-dimensional analogue of the Pauli operators (Σ_i) in state $\rho = |\psi\rangle\langle\psi|$ correspond to the components of the spin-1 magnetization vector along i^{th} axes. Thus spin-1 magnetization vector is written as:

$$\overrightarrow{M} = \langle\Sigma_x\rangle\hat{x} + \langle\Sigma_y\rangle\hat{y} + \langle\Sigma_z\rangle\hat{z}. \tag{3.32}$$

The expectation values in the given state are obtained as:

$$\begin{aligned} \langle\Sigma_x\rangle &= 0, \\ \langle\Sigma_y\rangle &= 0, \\ \langle\Sigma_z\rangle &= -\cos(2\alpha). \end{aligned} \tag{3.33}$$

Thus, the magnitude of the magnetization vector,

$$|\overrightarrow{M}| = |\cos(2\alpha)|. \tag{3.34}$$

Special cases :

- At $\alpha = \frac{\pi}{2}$, $|\overrightarrow{M}| = 1$,
- At $\alpha = \frac{\pi}{4}$, $|\overrightarrow{M}| = 0$,
- At $\alpha = 0$, $|\overrightarrow{M}| = 1$.

Thus the magnitude of the magnetization vector obtained, is as expected for the three eigenstates of Σ_z. The magnitude of the magnetization vector remains unaltered under the effect of SO(3) transformations. SO(3) rotations cause rotations of spin as a whole without effecting the content of the magnetization (magnitude of the magnetization vector). This can be easily proved as shown in the following subsection.

3.2.1 Invariance of the magnitude of magnetization vector under SO(3) transformations

Consider an arbitrary single-qutrit state $|\psi\rangle$ in $\mathcal{H}^3$. Expectation values of the Pauli matrices can be defined as:

$$\begin{aligned} \langle\Sigma_x\rangle &= \text{Tr}\langle\psi|\Sigma_x|\psi\rangle \\ \langle\Sigma_y\rangle &= \text{Tr}\langle\psi|\Sigma_y|\psi\rangle \\ \langle\Sigma_z\rangle &= \text{Tr}\langle\psi|\Sigma_z|\psi\rangle, \end{aligned} \tag{3.35}$$

and the magnitude of the magnetization vector is given as:

$$|\overrightarrow{M}| = |\sqrt{\langle\Sigma_x\rangle^2 + \langle\Sigma_y\rangle^2 + \langle\Sigma_z\rangle^2}|. \tag{3.36}$$

Consider the evolution of the state $|\psi\rangle$ under SO(3) transformations (U) generated by Σ_y (say) by an arbitrary angle θ. The final state is given as: $|\psi\rangle_f$=exp$(-\iota\theta\Sigma_y)|\psi\rangle$. Re-considering the expectation values of the Pauli spin operators in state $|\psi\rangle'$,

$$\begin{aligned} \langle\Sigma_x\rangle_f &= \text{Tr}\langle\psi|U^\dagger\Sigma_x U|\psi\rangle \\ &= \text{Tr}\langle\psi|(\cos(\theta)\Sigma_x - \sin(\theta)\Sigma_z)|\psi\rangle \\ &= \cos(\theta)\text{Tr}\langle\psi|\Sigma_x|\psi\rangle - \sin(\theta)\text{Tr}\langle\psi|\Sigma_z|\psi\rangle \\ &= \cos(\theta)\langle\Sigma_x\rangle - \sin(\theta)\langle\Sigma_z\rangle \\ \langle\Sigma_y\rangle_f &= \text{Tr}\langle\psi|\Sigma_y|\psi\rangle \\ &= \langle\Sigma_y\rangle \\ \langle\Sigma_z\rangle_f &= \text{Tr}\langle\psi|\Sigma_z|\psi\rangle \\ &= \text{Tr}\langle\psi|(\cos(\theta)\Sigma_z + \sin(\theta)\Sigma_y)|\psi\rangle \\ &= \cos(\theta)\text{Tr}\langle\psi|\Sigma_z|\psi\rangle + \sin(\theta)\text{Tr}\langle\psi|\Sigma_y|\psi\rangle \\ &= \cos(\theta)\langle\Sigma_z\rangle + \sin(\theta)\langle\Sigma_y\rangle \end{aligned} \tag{3.37}$$

The magnitude of the magnetization vector for state $|\psi\rangle'$ is thus obtained as:

$$\begin{aligned}|\overrightarrow{M}_f| &= |\sqrt{\langle\Sigma_x\rangle_f^2+\langle\Sigma_y\rangle_f^2+\langle\Sigma_z\rangle_f^2}| \\ &= |\sqrt{(\cos(\theta)\langle\Sigma_x\rangle-\sin(\theta)\langle\Sigma_z\rangle)^2+\langle\Sigma_y\rangle^2+(\cos(\theta)\langle\Sigma_z\rangle+\sin(\theta)\langle\Sigma_y\rangle)^2}| \\ &= |\sqrt{\langle\Sigma_x\rangle^2+\langle\Sigma_y\rangle^2+\langle\Sigma_z\rangle^2}| = |\overrightarrow{M}| \qquad (3.38)\end{aligned}$$

This verifies that the magnitude of magnetization of a qutrit in an arbitrary state $|\psi\rangle$ remains unaltered under SO(3) transformation generated by Σ_x operator. Similar is the situation with that of transformations generated by Σ_y and Σ_z by arbitrary angles. This leads us to the known fact that $|\overrightarrow{M}|$ is rotationally invariant.

Summarizing the properties of single-qutrit magnetization

- Projections of the magnetization vector of a given single-qutrit state on the x,y,z-axes in $\Re^3$ correspond to $\langle\Sigma_x\rangle$, $\langle\Sigma_y\rangle$ and $\langle\Sigma_z\rangle$ respectively.

- $|\overrightarrow{M}|$ is rotationally invariant, thus for a fixed value of α, one can obtain infinitely many single-qutrit states with same value of the magnetization.

- As α varies between [0,$\frac{\pi}{2}$], $|\overrightarrow{M}|$ assumes a continuous set of values ranging from [0,1].

3.2.2 Majorana representation of the magnetization vector

Re-considering the single-qutrit canonical state and its Majorana representation. In the context of Majorana representation, as per Figure 3.2, the length 'l_b' of the perpendicular bisector OO' can be given as $\cos(\frac{\eta}{2}) = z_c$.

$$\begin{aligned}l_b &= \frac{\sin\alpha-\cos\alpha}{\sin\alpha+\cos\alpha} \\ &= \frac{-1}{\cos 2\alpha}+\frac{\sqrt{1-\cos^2(2\alpha)}}{\cos 2\alpha} \\ l_b+\frac{1}{\cos 2\alpha} &= \frac{\sqrt{1-\cos^2(2\alpha)}}{\cos 2\alpha}\end{aligned}$$

Squaring both sides,

$$\begin{aligned} l_b^2 + \frac{1}{\cos^2(2\alpha)} + \frac{2l_b}{\cos(2\alpha)} &= \frac{1-\cos^2(2\alpha)}{\cos^2(2\alpha)} \\ -\cos(2\alpha) &= \frac{2l_b}{(l_b^2+1)} \end{aligned} \tag{3.39}$$

L.H.S. of Equation (3.39) is $\langle\psi_c|\Sigma_z|\psi_c\rangle$. Also, as seen in the previous section, $\langle\psi_c|\Sigma_x|\psi_c\rangle = 0$ and $\langle\psi_c|\Sigma_y|\psi_c\rangle = 0$. The magnitude of the magnetization vector of a single-qutrit in state $|\psi_c\rangle$ is given as:

$$\begin{aligned} |\overrightarrow{M}| &= |\langle\psi_c|\Sigma_z|\psi_c\rangle| \\ &= |-\cos(2\alpha)| \\ &= \frac{2|l_b|}{(l_b^2+1)} \end{aligned} \tag{3.40}$$

Therefore one can conclude that R.H.S. of Equation (3.39) is the magnitude of the magnetization vector of a qutrit in state $|\psi_c\rangle$. Thus, in the context of Majorana representation, $|\overrightarrow{M}|$ can be obtained from length 'l_b' of the bisector OO' (Figure 3.2). Again

$$|\overrightarrow{M}| = |\cos(2\alpha)| = \frac{2|l_b|}{(l_b^2+1)} \tag{3.41}$$

Under SO(3) transformations on the Majorana sphere in $\mathcal{R}^3$, the points representing a qutrit move like a rigid object on the unit sphere. Therefore the quantity 'l_b' is invariant under SO(3) transformations and so is the quantity $\frac{2|l_b|}{(l_b^2+1)}$.

Re-considering the Majorana representation of the canonical state of a single-qutrit (Figure 3.2), as angle α varies from 0 to $\frac{\pi}{4}$, the length of the bisector (l_b) varies from '1' to '0', and further changes from '0' to '1' with α varying from $\frac{\pi}{4}$ to $\frac{\pi}{2}$. Correspondingly the magnitude of the magnetization vector ($|\overrightarrow{M}|$) also varies from '1' to '0', and then from '0' to '1'. Thus the magnitude of the magnetization vector ($|\overrightarrow{M}|$) in a pure ensemble of a single-qutrit can assume values in the range [0,1]. On the contrary, the pure ensemble of a qubit always possesses unit magnitude of the magnetization vector associated with it. Further, for a fixed value of angle α, the length (l_b) and hence $|\overrightarrow{M}|$ assume a fixed value in the range [0,1]. As discussed earlier, length of the bisector (l_b) and hence the magnitude of the magnetization vector are rotationally invariant, thus under the effect of SO(3) transformations, one can obtain infinitely many single-qutrit

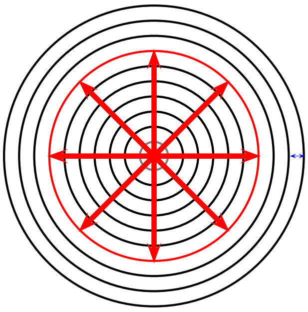

Figure 3.3: This is a cross-section of the Majorana sphere. Circles of different radii correspond to the surfaces of constant magnetization in a single qutrit. Red arrows pointing towards different directions are few of the infinitely many magnetization vectors with constant surface of magnetization shown in red.

states with same value of $|\overrightarrow{M}|$. Therefore under the effect of a set of three SO(3) transformations (Section 3.1.3), one obtains single qutrit states lying all over the Majorana sphere, and the corresponding bisector (and so is the magnetization vector) traversing a sphere with radius l_b ($|\overrightarrow{M}|$). Thus one can say that in case of a single spin-1, there exist concentric spheres of constant magnetization (corresponding to given value of α). Thus corresponding to a given value of the length of the bisector, one can assume concentric spheres with continuously varying radii, whose surfaces are the surfaces of constant magnetization. The radii of these spheres are equal to $|\overrightarrow{M}|$, that vary in the range [0,1]. Circular cross-section of the Majorana sphere depicting the magnetization vector is shown in Figure 3.3 where an example with $|\overrightarrow{M}| = \frac{1}{\sqrt{2}}$ is shown as a red circle inside the cross-section of a unit sphere.

3.2.3 Pointing and non-pointing states

Depending on whether a specific direction can be assigned to the qutrit state or not, these states can be classified as ‘pointing’ or ‘non-pointing’. A single-qutrit state that has a direction of orientation and also possesses a non-zero magnetization is termed as a pointing state, while the states with zero magnetization and with no directional orientation are termed as non-pointing states. In the context of Majorana representation, non-pointing states are diametrically opposite points on the unit sphere, such that the bisector of the angle enclosed at the center of the sphere vanishes. On the other hand, pointing states have non-zero magnetization. Under SO(3) transformations, pointing states remain always pointing while the non-pointing states remain non-pointing.

Here are a few examples: Reconsidering the Majorana representation of $|+1\rangle(|-1\rangle)$, it is interesting to see that this state points along $+z(-z)$ direction. On the other hand $|0\rangle$ has diametrically opposite points in the Majorana representation and is a non-pointing state.

In general, an eigenstate of Σ_i with eigenvalue $+1$ points along the $+i$ direction and an eigenstate of Σ_i with eigenvalue -1 points in the $-i$ direction. States with zero eigenvalue can be supposed to have a zero magnetization and thus do not have any preferred direction of orientation.

3.3 Quantum computing with a single-qutrit

The quantum operations on a single-qutrit can be utilized to perform computing on a single-qutrit system.

3.3.1 NMR qutrit

The simplest way to realize a qutrit in NMR is to use a nucleus with spin-1. Three energy eigenstates of a spin-1 are mapped on to the three energy levels of a qutrit labeled as ($|+1\rangle$, $|0\rangle$ and $|-1\rangle$). There exist two single quantum transitions governed by a set of Λ matrices (as described in Chapter-3). A qutrit in NMR can be obtained by using a spin-1 nucleus. A spin-1 nucleus possesses electric quadrupole moment which upon interaction with the electric field gradients give rise to a quadrupolar coupling term in the Hamiltonian. NMR Hamiltonian of a spin-1 (with gyromagnetic ratio = γ) in the presence of a static magnetic field ($B_0 = -\omega_0/\gamma$) [39, 42] is given as:

$$H = -\omega_0 I_z + \frac{eQV_{zz}}{4I(2I-1)}(3I_z^2 - I^2) \tag{3.42}$$

where ω_0 is the Larmor precession frequency, Q is the quadrupolar moment and V_{zz} is the average value of the uniaxial electric field gradient component over the molecular motion. The second term on the R.H.S. of the Hamiltonian(H) in Equation (3.42) is the quadrupolar coupling term, whose average vanishes in an isotropic medium, as provided by liquid state NMR. Thus, only the Zeeman interaction term survives which leads to equally separated three energy levels of a spin-1 resulting in two degenerate transitions. The resulting overlapped pair of spectral lines in frequency space can no longer be addressed separately. This renders the spin-1 nucleus useless for quantum computation using liquid state NMR techniques.

This problem can be resolved by providing an anisotropic environment for the spin-1 molecule so that the quadrupolar coupling does not average to zero. This is achieved by inserting the molecule in a liquid crystalline matrix. Liquid crystals exist in liquid phase and exhibit properties of crystals. The molecular components of a liquid crystal have a preferred direction of orientation and thus exhibit anisotropy like a crystal (Appendix 1). Anisotropic molecular orientation with respect to the strong magnetic field, gives rise to a finite quadrupolar coupling term in the Hamiltonian which is now given by

$$H = -\omega_0 I_z + \Lambda(3I_z^2 - I^2) \tag{3.43}$$

where $\Lambda = e^2qQS/4$ is the effective value of the quadrupolar coupling, $eq = V_{zz}$ denotes the field gradient parameter, and S is the order parameter of the liquid crystal. Depending upon the order parameter of the liquid crystal, a non-zero quadrupolar coupling value also termed as the effective quadrupolar coupling is obtained. This effective quadrupolar coupling term is responsible for the splitting between the previously degenerate transitions and hence gives rise to the two lines in the NMR spectrum.

3.3.2 Experimental single qutrit system

Quadrupolar nuclei have fast relaxation rates, which are further enhanced by the anisotropic interactions. Therefore a careful choice of spin-1 nucleus and the liquid crystal is important. Deuterium nucleus is a spin-1 system with least value of the quadrupolar moment and sufficiently long spin relaxation times. The spin-1 system used in this study is a deuterated chloroform molecule oriented in a lyotropic liquid crystal, where the deuterium nucleus serves as the single qutrit. The lyotropic liquid crystal is composed of 25.6% of Potassium Laurate, 68.16% of H_2O and 6.24% of Decanol, and 50 μl of Chloroform-D is added to 500 μl of liquid crystal. The deuterium NMR spectrum of oriented Chloroform-D was acquired at different temperatures (Appendix 1). This system possesses a liquid crystalline phase for a wide range of temperature. Spin-lattice and spin-spin relaxation times, and the effective quadrupolar moment of the ^{2}D nucleus were observed for a wide range of temperatures. Qutrit computing demands individual transitions to be addressed separately, thus a sufficiently large relative separation between the spectral lines is required. There is an interplay between the large effective quadrupolar moment with increased anisotropy (here at lower temperatures) and the slower relaxation rates at lesser anisotropy (here at higher temperatures). An optimal temperature of 277 K was found at which T_1 and T_2 relaxation times are approximately 170 ms and 50 ms respectively. The relative separation of the single quantum transitions is of 936 Hz.

Figure 3.4 shows the energy level diagram of the three-level system along with the relative populations in the presence of a magnetic field B_0. The energy levels are numbered as $\{1, 2, 3\}$ corresponding to the qutrit eigenstates $|+1\rangle, |0\rangle, |-1\rangle$ respectively, and the single quantum transitions are labeled with arrows. Figure 3.4(c) shows the deuterium NMR spectrum of oriented Chloroform-D; the spectral lines corresponding to transitions 1-2 and 2-3 are labeled as Line 1 and Line 2 respectively.

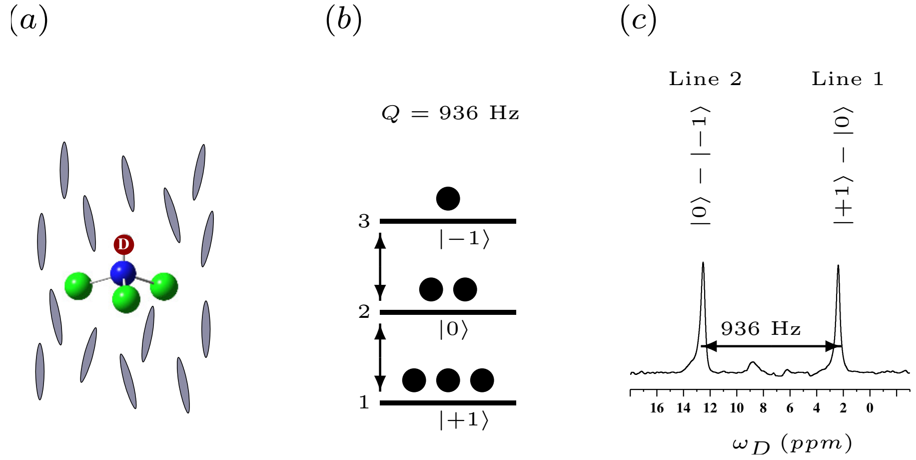

Figure 3.4: A single spin 1 (Deuterium nucleus) in anisotropic environment acting as a single qutrit. (a) Schematic of Chloroform-D molecule oriented in a liquid crystal exhibiting nematic phase, (b) Energy level diagram of a single qutrit with energy levels numbered from 1-3 and labeled with the respective basis vectors. Relative occupation of the energy levels is shown by black circles. (c) Deuterium NMR spectrum of Chloroform-D with both the spectral lines labeled with the corresponding transitions. The spectrum is acquired at 278 K. ν is the chemical shift of Deuterium and Q is the effective quadrupolar splitting at a given temperature.

Experimental details

All the experiments were performed on a 600 MHz Avance III NMR spectrometer equipped with a QXI probe, with the deuterium nucleus resonating at 91.108 MHz. The deuterium relaxation times T_1 and T_2 were of the order of 170 ms and 50 ms respectively. All the transition-selective pulses used in this work are 4ms long 'Gaussian' shaped pulses and the non-selective ones are 'Sinc' shaped pulses with a duration of 0.5ms.

3.3.3 Initialization

For the purpose of NMR quantum computation, one needs to initialize the quantum system in a pseudo-pure state. A pseudo-pure state is obtained by a different population in one of the energy levels over a uniform background in an ensemble of $\sim 10^{18}$ spins. Thus at thermal equilibrium, a single-qubit system already exists in a pseudo-pure state, however this is not the case with a qutrit. A qutrit has three energy eigenstates and therefore, three possible pseudo-pure states : $|+1\rangle$, $|0\rangle$, $|-1\rangle$. These states are obtained from the thermal equilibrium state using transition-selective pulses followed by gradient pulse that dephases the coherences. Pulse sequences for the preparation of all three pseudo-pure states is shown in Figure 3.5.

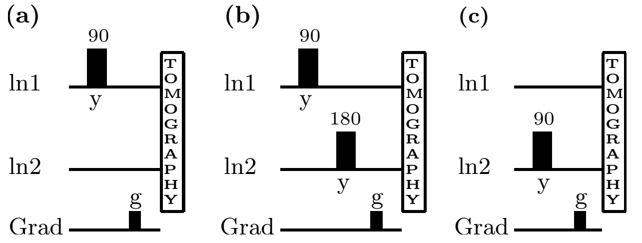

Figure 3.5: Pseudopure state preparation scheme, resulting into states : (a) $|-1\rangle$, (b) $|0\rangle$ and (c) $|+1\rangle$. Channels ln1 and ln2 correspond to transitions 1-2 and 2-3 respectively. The gradient pulse of strength g is shown in the third channel.

3.3.4 Tomography of a single-qutrit

The final readout of the experimental state is carried out by quantum state tomography. Generators of SU(3) operators (Λ matrices) alongwith a 3×3 identity matrix form a complete set of orthonormal bases in the operator space of qutrit and are identified as a basis for tomography of a qutrit. The state of the qutrit in general is $\rho = \frac{1}{2}\sum_{i=1}^{8} c_i\Lambda_i$ where $c_i s$ are real numbers, explicit form of the qutrit state is given as

$$\rho = \frac{1}{2}\begin{pmatrix} c_3 + \frac{c_8}{\sqrt{3}} & c_1 - \iota c_2 & c_4 - \iota c_5 \\ c_1 + \iota c_2 & -c_3 + \frac{c_8}{\sqrt{3}} & c_6 - \iota c_7 \\ c_4 + \iota c_5 & c_6 + \iota c_7 & \frac{-2c_8}{\sqrt{3}} \end{pmatrix}. \tag{3.44}$$

State reconstruction requires all eight expectation values $c_i s$ to be determined which requires a minimum of four operations as given below alongwith their corresponding NMR pulse sequences.

- Identity : No operation
- $U_{\Lambda_1}(\frac{3\pi}{2}) : I_x^{1-2}(-\pi)$
- kill coherences, $U_{\Lambda_1}(\frac{\pi}{4}) : Grad_z, I_y^{1-2}(\frac{\pi}{2})$
- kill coherences, $U_{\Lambda_7}(\frac{\pi}{4}) : Grad_z, I_y^{2-3}(\frac{\pi}{2})$

Single-qutrit NMR spectrum consists of two lines which are single quantum coherences ρ_{12} and ρ_{23}. First experiment gives the values of (c_1, c_2, c_6, c_7), second experiment interchanges the intensities of single and double quantum terms providing the values of (c_4, c_5) and last two experiments give the diagonal elements and hence the values of (c_3, c_8). Calculating all these values from the intensities of spectral lines, the experimental density matrix (ρ_e) can be constructed. Equation (1.6) is used to measure the overlap between the theoretically expected and experimentally constructed density matrices.

The pulse sequence shown in Figure 3.5 is implemented experimentally on thermal equilibrium state of a qutrit. The initial and final state density operators are then tomographed using the set of four operators. Experimentally reconstructed single-qutrit states are shown in Figure 3.6. Pseudo-pure states $|+1\rangle$, $|0\rangle$ and $|-1\rangle$ are obtained with the fidelities (Equation (1.6)) 0.99, 0.97 and 0.99 respectively.

3.3.5 Experimental implementation of Λ matrices

There are two single quantum transitions exhibited by a three-level quantum system, each one of these transitions belong to a two-level subspace. The transition-

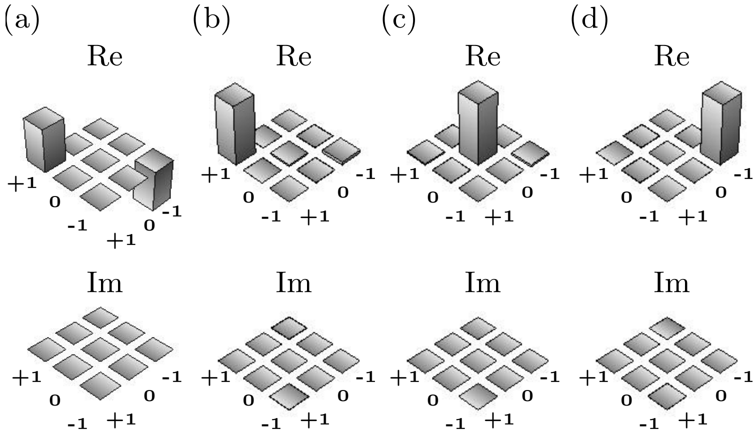

Figure 3.6: Real (Re) and imaginary (Im) parts of the experimentally constructed single-qutrit density matrices are shown for (1) thermal equilibrium state, and the pseudo-pure states: (b) $|+1\rangle$, (c) $|0\rangle$, and (d) $|-1\rangle$. These pseudo-pure states are created using pulse sequences given in Figure 3.5. The pseudo-pure states $|+1\rangle$, $|0\rangle$, and $|-1\rangle$ are found to have fidelities of 0.99, 0.97 and 0.99 respectively.

selective pulses in NMR are governed by transition-selective operators as described earlier (Equation (3.27)). Trajectory of the Majorana points representing a qutrit is traced under the effect of SU(3) transformations, which results into the motion of only one point at a time. Their experimental realization in NMR is achieved by addressing the transitions selectively. U_{Λ_1}, U_{Λ_2} implementations require a selective excitation of the transition between energy levels 1, 2 (Equation (3.28)) and for U_{Λ_6}, U_{Λ_7} (Equation (3.29)) a transition-selective radio frequency pulse between energy levels 2, 3. U_{Λ_4}, U_{Λ_5} (Equation (3.30)) implementation require double quantum excitation which is achieved using a set of three transition-selective pulses [98]. U_{Λ_3} and U_{Λ_8} correspond to the $z-$rotations and therefore implemented using $z-$cascades. NMR Pulse sequences for the $U_{\Lambda_i}(\theta)$ implementations are shown in Figure 3.7 .

Coherence transfer operations

Experimental implementation of the pulse sequences described in Figure 3.7 is carried out on a single-qutrit using NMR. As mentioned earlier, for $\theta = 180^0$, $U_{\Lambda_1}(U_{\Lambda_2})$, given in Figure 3.7(a) effectively acts as swap$_{12}$ gate. However a complete swap$_{12}$ operation is achieved by the sequence : $(180)_y^{ln2}(180)_y(180)_{-y}^{ln2}$. Similarly $\theta = 180^0$ in Fig-

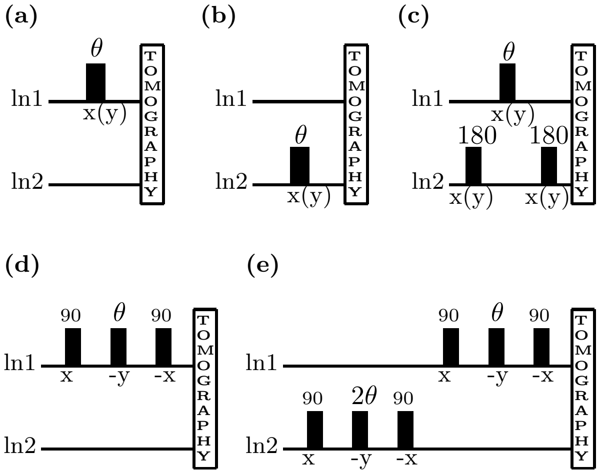

Figure 3.7: NMR pulse sequence for the implementation of (a) $U_{\Lambda_1}(U_{\Lambda_2})$ giving rotation $\frac{\theta}{2}$, using transition-selective pulses. $\theta = \pi$ swaps the populations between energy levels 1 and 2 of a single spin 1, (b) $U_{\Lambda_6}(U_{\Lambda_7})$ giving rotation $\frac{\theta}{2}$, using transition selective pulses. $\theta = \pi$ swaps the populations between energy levels 2 and 3, (c) $U_{\Lambda_4}(U_{\Lambda_5})$ giving rotation $\frac{\theta}{2}$, using a single spin selective pulse. $\theta = \pi$ swaps the populations between energy levels 1 and 3. Pulse sequences for the implementation of (d) U_{Λ_3} and (e) U_{Λ_8} matrices giving rise to the relative phase shifts. All the black rectangular pulses are the shaped pulses with angle of rotation mentioned at the top and the axis of rotation is mentioned at the bottom. ln1 and ln2 stand for the transitions between levels 1-2 and 2-3 respectively.

ure 3.7(b) effectively leads to swap$_{23}$ gate and that in part (c) gives rise to swap$_{13}$ gate. Swap$_{13}$ gate is also implemented by a non-selective 180^0 pulse. The sequence for ideal swap$_{23}$ operator being : $(180)^{ln1}_{-y}(180)_y(180)^{ln1}_y$. These operators are implemented on an ensemble of qutrits at thermal equilibrium and resulting states are completely reconstructed using tomography protocols. The NMR experimental implementations of swap gates are discussed in the next section.

Phase shift operations

Experimental implementation of the pulse sequences described in Figure 3.7(d,e) implement the unitary transformations generated by Λ_3 and Λ_8 operators. These operations give rise to relative phases between the coherences. However, the diagonal states remain unaffected under these unitary operations. These transformations are thus the phase-shift gates, that are important from quantum computation point of view. The details of the this sequence implementation and the results obtained are given in Section 3.3.6.

3.3.6 Quantum Gates

Like qubits, quantum computation with qutrits uses single-qutrit and two-qutrit controlled quantum operators as quantum gates.

Chrestenson gate

Chrestenson gate is the qutrit analog of the two-dimensional Hadamard gate. It is a single-qutrit gate that creates uniform superpositions of the energy levels alongwith relative phases between the basis vectors. Chrestenson gate for single-qutrit is written as:

$$Ch = \frac{1}{\sqrt{3}} \begin{pmatrix} 1 & 1 & 1 \\ 1 & e^{\frac{2\iota\pi}{3}} & e^{\frac{4\iota\pi}{3}} \\ 1 & e^{\frac{4\iota\pi}{3}} & e^{\frac{2\iota\pi}{3}} \end{pmatrix} \tag{3.45}$$

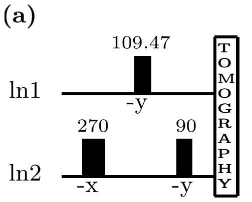

Figure 3.8: Pulse sequence for Chrestenson gate implementation, where two channels correspond to two transitions of a single-qutrit (Figure 3.4). Pulse angles and axes are mentioned alongwith all the pulses.

Considering the action of Chrestenson gate on the non-pointing state $|0\rangle$ leads to the state $\frac{1}{\sqrt{3}}\left(|+1\rangle + e^{\frac{2\pi\iota}{3}}|0\rangle + e^{\frac{4\pi\iota}{3}}|-1\rangle\right)$, which is a pointing state. Chrestenson gate can not be obtained solely under SO(3) transformations. Therefore, the decomposition of this gate requires a set of SU(3) operators which inturn require transition-selective pulses for NMR experimental implementation. Non-trivial sequence of RF pulses for the Chrestenson gate implementation in NMR is proposed, which is given in Figure 3.8

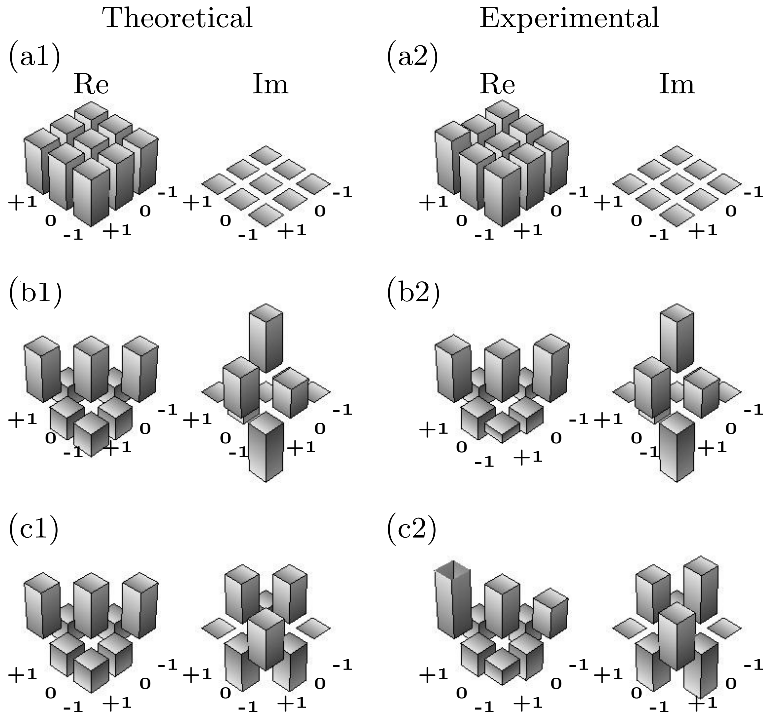

Figure 3.9: Real and imaginary parts of the theoretically expected (a_1, b_1, c_1) and experimentally obtained (a_2, b_2, c_2) tomographs of the resultant single-qutrit state after chrestenson gate implementation on different initial states. The initial states corresponding to different parts are: (a_1, a_2) $|+1\rangle$, (b_1, b_2) $|0\rangle$, and (c_1, c_2) $|-1\rangle$.

This pulse sequence is applied on all three qutrit bases states and the final state is completely tomographed. Final state density matrices are shown in Figure 3.9. As seen from the Figure 3.9, theoretically expected and experimentally obtained single-qutrit states match well after the Chrestenson gate implementation. The exact overlap between the theoretically expected and experimentally obtained states (Equation (1.6)) is found out to be 0.99, 0.98, 0.98 corresponding to initial states $|+1\rangle$, $|0\rangle$, $|-1\rangle$ respectively.

Swap gates

Qutrit is a three-level system, therefore there are three possible swap operations between levels 1-2, 2-3 and 1-3. This is achieved by using transition-selective pulses. Exact pulse sequences for NMR implementation of swap$_{12}$, swap$_{23}$ and swap$_{13}$ are shown in Figure3.10. However for $\theta = \pi$, swap gates can effectively be conducted by the unitary operators U_{Λ_j} as described in earlier sections. The explicit matrices for swap$_{12}$, swap$_{23}$ and swap$_{13}$ are written as

$$\begin{pmatrix} 0 & 1 & 0 \\ 1 & 0 & 0 \\ 0 & 0 & 1 \end{pmatrix}, \quad \begin{pmatrix} 1 & 0 & 0 \\ 0 & 0 & 1 \\ 0 & 1 & 0 \end{pmatrix}, \quad \begin{pmatrix} 0 & 0 & 1 \\ 0 & 1 & 0 \\ 1 & 0 & 0 \end{pmatrix} \tag{3.46}$$

respectively.

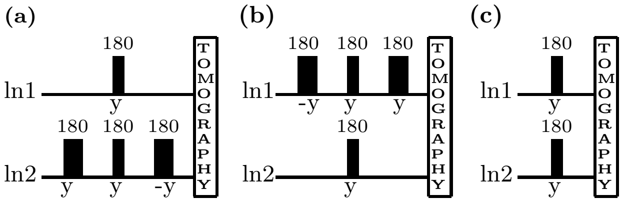

Figure 3.10: Pulse sequence for implementation of swap operations. (a) swap12, (b) swap23 and (c) swap13. Transition selective pulses are shown by thick rectangles while thin rectangles are the non-selective pulses.

All three swap gates are implemented experimentally on the thermal equilibrium state. Complete quantum state tomography of the initial state as well as the states obtained after swap operations is performed. The fidelities corresponding to swap$_{12}$, swap$_{23}$, and swap$_{13}$ implementations are 0.99, 0.99, 0.99 respectively. The tomographs of the initial and final states are shown in Figure 3.11.

Phase gates

Phase shift gates in qutrits introduce relative phases between the base vectors of the same qutrit. These gates are primarily $z-$rotations. These gates are described in earlier sections, obtained by $U_{\Lambda_3}(\theta)$ and $U_{\Lambda_8}(\theta)$ implementations. Explicit matrix forms of $U_{\Lambda_3}(\theta)$ and $U_{\Lambda_8}(\theta)$ are:

$$U_{\Lambda_3} = \begin{pmatrix} e^{\iota\theta} & 0 & 0 \\ 0 & e^{-\iota\theta} & 0 \\ 0 & 0 & 1 \end{pmatrix}, \quad U_{\Lambda_8} = \begin{pmatrix} 1 & 0 & 0 \\ 0 & 1 & 0 \\ 0 & 0 & e^{\iota\sqrt{3}\theta} \end{pmatrix} \tag{3.47}$$

These gates are implemented with various values of θ on a single-qutrit using NMR. The initial state (ρ_i^{exp}) is created by a non-selective 90^0 pulse on thermal equilibrium

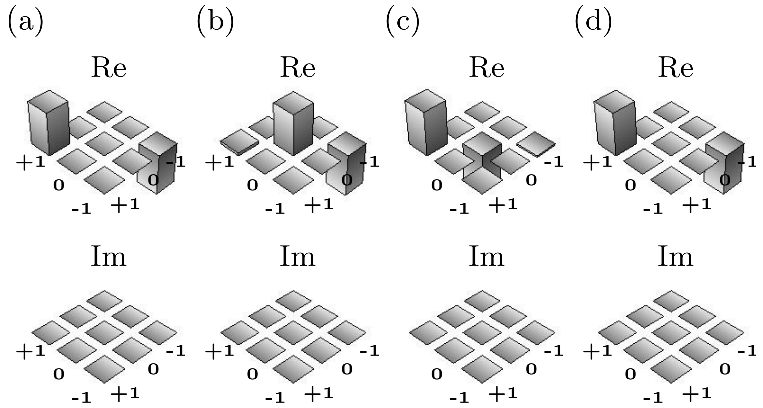

Figure 3.11: Real and imaginary parts of the (a) Initial state (thermal equilibrium) and the states resulting after the implementation of (b) swap$_{12}$, (c) swap$_{23}$, and (d) swap$_{13}$ operators. The states resulting after experimental implementation of swap$_{12}$, swap$_{23}$, and swap$_{13}$ gates have fidelities of 0.99, 0.99 and 0.98 respectively.

state, so that one begins with in-phase values of the single quantum coherences. Action of $U_{\Lambda_3}(\theta)$ builds a relative phase difference of $\frac{3\theta}{2}$ between the two single quantum coherences. This relative phase is the phase difference between the spectral lines in a single-qutrit NMR spectrum obtained by $U_{\Lambda_3}(\theta)$ implementation on ρ_i^{exp}. Second column of the Table 3.1 shows the values of angles implemented (θ) as given in Figure 3.7(d), columns 3 and 4 contain the values of the theoretically expected (θ_{th}) and experimentally obtained (θ_{exp}) values of the phase difference respectively.
A $U_{\Lambda_8}(\theta)$ builds a relative phase difference of $\sqrt{3}\theta$ between the two single quantum coherences. Relative phase in the spectral lines of the first order single-qutrit spectrum under $U_{\Lambda_8}(\theta)$ implementation (θ_{exp})is shown in column 6 of the Table 3.1, column 5 contains the theoretically expected values of phase difference (θ_{th}) between the two single quantum coherences.

NMR spectra showing single quantum coherences for different values of θ are shown in Figure 3.12. Two spectral lines correspond to the two transitions. The initial state is a coherent state with equally intense, inphase spectral lines. Thus while implementing the phase shift gates, recorded spectrum at each step depict the relative phase being acquired between the coherences. The spectra are phase corrected in such a manner that one of the transitions (one on left) remains in-phase in all the spectra making the visual appearance of phase difference more prominent between the spec-

Table 3.1: Phase differences between the two single quantum transitions obtained corresponding to different values of θ under Λ_3 and Λ_8 implementations. Columns 3 and 4 contain the theoretically expected and experimentally obtained values of the phase difference obtained in Λ_3 implementations, and columns 5,6 contain the theoretically expected and experimentally obtained values of the phase difference obtained as a result of Λ_8 implementations.

		U_{Λ_3}		U_{Λ_8}	
	θ	θ_{th}	θ_{exp}	θ_{th}	θ_{exp}
1	0	0	0	0	0
2	30	45	39.95	$30\sqrt{3}$	47
3	45	67.5	62.4	$45\sqrt{3}$	70
4	60	90	84.2	$60\sqrt{3}$	110
5	90	135	139.05	$90\sqrt{3}$	168
6	120	180	203.3	$120\sqrt{3}$	220

tral lines (different spectra correspond to different values of θ). The exact values of the phase differences obtained experimentally are given in Table 3.1. In each of these spectra, zeroth order phase correction is performed in order to make one of the transitions a purely absorptive Lorentzian. Here the transition on the left (between levels 2,3 as per Figure 3.4) is used for this purpose. The interest here lies in finding out the relative phase difference between the two spectral lines. Now that transition on left corresponds to a real number, the phase of the complex single quantum term is reflected by the peak on the right hand side (between levels 1,2 as per Figure 3.4). The values of this phase difference are measured corresponding to different values of θ for both Λ_3 and Λ_8 implementations. In the context of Majorana representation, under the effect of transformations generated by Λ matrices, only one point moves at a time on the surface of the unit sphere. In case of phase gates, the trajectory of the point falls in the plane z =constant.

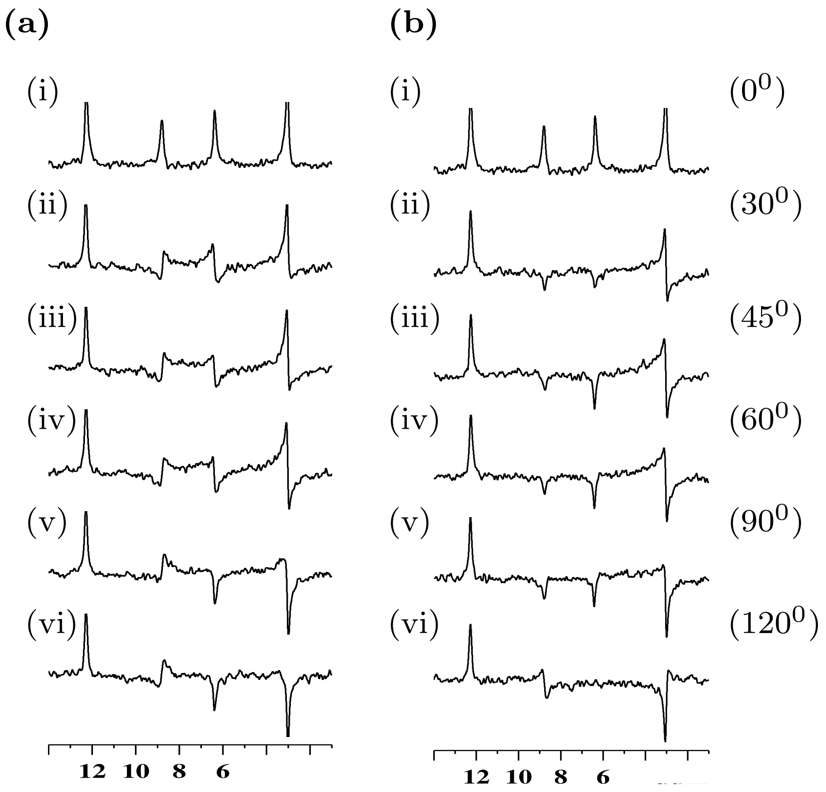

Figure 3.12: Spectra acquired with different values of θ corresponding to pulse sequences given in Figure 3.7(d,e). (a) The spectra acquired after Λ_3 implementations corresponding to θ=0^0, 30^0, 45^0, 90^0, 120^0 respectively. (b) Spectra acquired as a result of Λ_8 implementations for different values of θ.

3.4 Concluding Remarks

In this chapter, a geometrical representation of higher spin systems is studied and various aspects related to a spin-1 (qutrit) are explored. A qutrit is represented by two points on a unit sphere as per Majorana representation. In this chapter two main directions are followed: the first one focuses on the geometrical picture of a single-qutrit magnetization vector. Various features of the single-qutrit magnetization vector are studied in context of Majorana representation. It is shown geometrically that the magnitude of a single-qutrit magnetization vector assumes values in the range [0,1], with three eigenvectors of Σ_z; $|\pm 1\rangle$ and $|0\rangle$ possessing values 1 and 0 respectively. This is further utilized in the geometrical interpretation of pointing and non-pointing states. The second direction is focused on performing quantum computing with a qutrit. The decomposition of some single qutrit quantum gates in terms of the radio-frequency pulses was not known (example: three dimensional analogue of the Hadamard gate) unlike qubits. Close observations of the dynamics of points representing a qutrit on the Majorana sphere under the action of various quantum gates are used to obtain the rf pulse decompositions. Basic single-qutrit gates: swap gates, phase gates, Chrestenson gate are implemented on a single-qutrit NMR quantum information processor. A protocol for quantum state tomography is also proposed and implemented. This chapter provides new insights into the intrinsic features of a qutrit with the help of Majorana representation as well as introduces various NMR quantum computing protocols for a single qutrit.

Chapter 4

Exploring contextuality and determining the parity of a permutation using an NMR qutrit

Quantum information processors exploit the intrinsic quantumness of quantum systems to perform computational tasks more efficiently than their classical counterparts [1, 5]. A single qubit is the basic building block for quantum computation, however there are no known single-qubit based quantum features that do not have a classical description. Multi-qubit systems on the other hand, exhibit properties such as entanglement which does not have a classical analogue. In fact, the polarization states of a classical beam of light provide a classical system with exactly the same properties as that of a single qubit. Therefore, by manipulating the polarization states of a classical beam of light via half-wave and quarter-wave plates, one can efficiently simulate a single qubit [127, 128]. Thus one requires at least two qubits in order to perform a useful computational task. Any quantum computational task is written as an algorithm exploiting quantum properties possessed by the system of interest. Proposals of new quantum algorithms to obtain advantage over the corresponding classical algorithms began with introduction of Deutsch's algorithm [8, 129] and were further modified to exploit entanglement as a resource [9]. Scaling issues in algorithmic implementations and achieving computational speedup without entanglement has been discussed in [10, 68, 130]. Though a single qubit is not capable of providing a quantum advantage in the computation, multi-qubit systems possess intrinsic quantumness that is capable of speeding up the computational task. Various multi-qubit quantum algorithms [15] have been proposed that show an advantage over their classical counterparts.

However a single qutrit (unlike a qubit) possesses intrinsic quantumness. Another notable fact regarding a qutrit is that, it is an indivisible system and hence the property of entanglement cannot be associated with a single qutrit. The quantumness of a qutrit and hence its utility as a computational resource may be attributed to 'contextuality' [85, 86, 87, 131].

Contextuality refers to the context of measurement. According to non-contextual hidden variable theories, one can pre-assign the values to measurement outcomes of observables even before the measurement is actually performed [132]. In other words, one can say that that the measurement outcome is pre-determined and is independent of the other observables being co-measured. However it was proposed by E. Specker in 1960 [85] that there exists a context among the measurement outcomes which is attributed to the lack of joint probability distributions of more than two observables. This is called the context of a measurement. More specifically, let us consider observables A, B and C such that A commutes with both B and C, while $[B, C] \neq 0$; measurement of A, B together and measurement of A alongwith C may lead to different measurement results of A. Thus contextuality refers to the context in which a measurement of an observable takes place.

This chapter explores and exploits the intrinsic quantum features of a single-qutrit, to which the computational speedup in qutrit-computing is attributed. A detailed analysis for the verification of single-qutrit contextuality is carried out for two different sets of observables composed of thirteen and nine elements respectively. On the basis of a set of nine measurements, an experimental test is designed and implemented on a single-qutrit based NMR quantum information processor to reveal the single-qutrit contextuality. This involves recasting the original inequality in terms of observables which can be actually measured in an NMR experiment. Further exploiting the quantum features of a qutrit, the implementation of a qutrit-based quantum algorithm is carried out on a single-qutrit NMR quantum computer. The algorithm is implemented experimentally to determine the parity of a permutation of three objects.

4.1 Single-qutrit contextuality

First test for contextuality was proposed by S. Kochen and E. P. Specker in 1967 [133], in which they used a set of 117 rays to reveal the contextuality of a single-qutrit. A ray here corresponds to the direction of the axis of measurement. The modification to the procedure in terms of the number of observables was introduced by Peres in 1991 using 33 rays [134]. Since then, there have been various proposals to bring down the number of observables that show the contextual nature of a qutrit. A pentagram inequality known as KCBS inequality [135] was proposed in 2008, that makes use of a set of only five measurements to reveal the contextuality of a single-qutrit. However this is a state-dependent inequality. In case of a three-level system, a minimal set of measurements for the state independent contextuality test is proposed by S. Yu and C. H. Oh [87], which requires a set of 13 observables. Later Cabello et al [131] proved this to be the minimum number of observables to reveal the contextuality in a three level system. There came another proposal by Kurzynski et al in 2012 [86] in which authors suggest a set of nine observables that prove the contextuality of almost all the states of a single-qutrit. Experimental implementations of these contextuality tests have been performed by different groups using the photonic qutrits [136, 137]. An experimental test based on solid-state NMR techniques has also been designed to verify the contextuality in quantum systems [138]. This experimental scheme is based on one clean qubit in NMR, and is shown to demonstrate the contextual nature of a system of two qubits [138]. In this chapter, the experimental protocol involves the recasting of the original inequality in terms of observables which can be actually measured in an NMR experiment.

Following subsections discuss the state-independent single-qutrit contextuality test for two different sets of measurements.

4.1.1 State-independent test with 13 observables

A state independent test for the single-qutrit contextuality was proposed by S. Yu and C. H. Oh in 2012 that can verify the contextuality in all the states of a qutrit. This set of 13 observables are obtained from a set of 13 rays that correspond to 26 points on the surface of a magic cube [87]. A ray $r = (r_a,\, r_b,\, r_c)$ has one to one correspondence with a normalized single-qutrit pure state ($|\psi_r\rangle$), such that $|\psi_r\rangle = r_a|+1\rangle + r_b|0\rangle +$

$r_c|-1\rangle$, where $\{|+1\rangle, |0\rangle, |-1\rangle\}$ represent the set of single-qutrit basis vectors. The set of rays is given as:

$$\begin{aligned} h_0 &= (1,1,1), \quad & y_1^{\pm} = (0,1,\pm 1), \quad & z_1 = (1,0,0), \\ h_1 &= (-1,1,1), \quad & y_2^{\pm} = (\pm 1,0,1), \quad & z_2 = (0,1,0), \\ h_2 &= (1,-1,1), \quad & y_3^{\pm} = (0,\pm 1,1), \quad & z_3 = (0,0,1), \\ h_3 &= (1,1,-1). & & \end{aligned} \tag{4.1}$$

The orthogonality relations satisfied by theses rays is shown in Figure 4.1. The vertices of the graph represent the rays (or equivalently the corresponding projectors in three-dimensional Hilbert space of a qutrit), and the edges of the graph depict the orthogonality relations, such that two connected vertices of the graph are orthogonal. Global unitary transformations of this set of rays also obey the same orthogonality relations as per Figure 4.1. One can assign measurement outcomes to each of these 13 projectors as proposed by Kochen and Specker, in accordance with the non-contextual hidden variable theories [133]. The Kochen-Specker value assignment is done in such a manner that (a) one can assign only dichotomic values (0 and 1) to these projectors, and (b) no two connected vertices can be assigned the value '1' simultaneously because they represent orthogonal projectors. Following this value assignment, one can find that only one of the projectors belonging to $\{h_0, h_1, h_2, h_3\}$ can be assigned the value '1'. As can be seen from the graph in Figure 4.1, each of the vertices occupied by vectors h_i ($i \in \{0,1,2,3\}$) is connected to three other vertices occupied by $y_n^{\pm}$ ($n \in \{1,2,3\}$). Explicitly, the observables corresponding to projectors h_0,h_1,h_2,h_3 share context with the sets of projectors $\{y_1^-, y_2^-, y_3^-\}$, $\{y_1^-, y_2^+, y_3^+\}$, $\{y_1^+, y_2^-, y_3^+\}$, and $\{y_1^+, y_2^+, y_3^-\}$ respectively. If one choses,

$$\langle h_i \rangle = \langle h_j \rangle = 1, \qquad i \neq j, \ (i,j \in \{0,1,2,3\}), \tag{4.2}$$

the projectors to which they are directly attached will attain the expectation value 'zero' (as the connected vertices correspond to orthogonal projectors). There are six possible combinations of h_is to which one can assign the same value '1'. It is interesting to see that whichever combination one may choose, it always ends up in a scenario where two pairs of $y_n^{\pm}$ and $y_m^{\pm}$ ($m,n \in \{0,1,2,3\}$; $m \neq n$) exhibit value 'zero'. Each of the $y_n^{\pm}$ also shares context with z_n, and the three of these are mutually orthogonal.

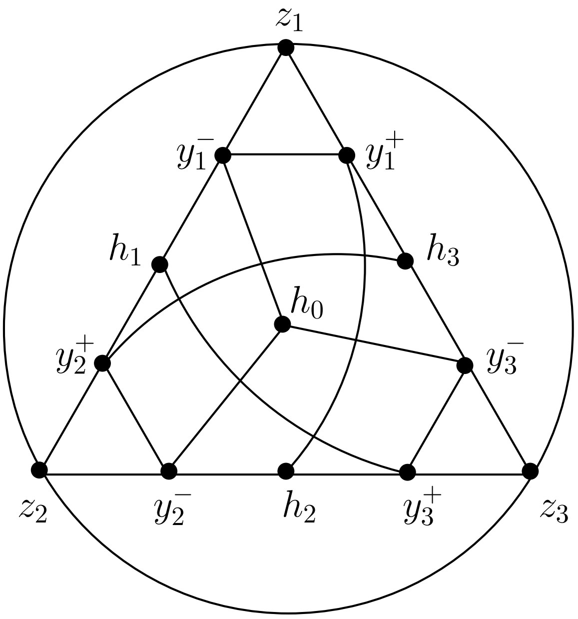

Figure 4.1: An orthogonality graph (G) showing the 13 projectors as the vertices and the edges depicting the orthogonality relations between various vertices.

Correspondingly, there arise following situation:

$$\langle z_m \rangle = \langle z_n \rangle = 1; \qquad m \neq n,\ (m, n \in \{1, 2, 3\}). \tag{4.3}$$

Which is not possible, as the three z_ms are mutually orthogonal and thus only one of these can exhibit the expectation value '1'. Therefore the initial assumption (Equation 4.2) is not appropriate. Thus it is concluded that,

$$\sum_{i=0}^{3} \langle h_i \rangle_G \leq 1. \tag{4.4}$$

Equation (4.4) is supposed to be obeyed by any non-contextual single qutrit state. However using simple algebra, one can arrive at:

$$\sum_{i=0}^{3} |h_i\rangle\langle h_i| = \frac{4}{3} I \tag{4.5}$$

where I is the 3×3 identity operator. Thus quantum mechanically for any state of a single-qutrit,

$$\sum_{i=0}^{3} \langle h_i \rangle_Q = \frac{4}{3}. \tag{4.6}$$

Therefore according to quantum mechanics, supplemented by non-contextual hidden variable theories, any state of a single-qutrit violates the contextuality inequality given in Equation (4.4).

This is an elegant and simple test for a state independent single-qutrit contextuality [87]. An experimental implementation of this test has been performed using a single photonic qutrit [137]. One can look for other experimental schemes for testing the single-qutrit contextuality. In the given set of thirteen projectors, all the projectors add up to give rise to identity operator alongwith a 'multiple' (number). The resultant expectation value obtained from the inequality (Equation 4.6) that determines the contextual nature of the set of 13 operators is thus embedded in the 'multiple'. The identity operator can not be measured in NMR [1, 39], thus experimental implementation of such a scheme on an NMR quantum information processor is not possible.

4.1.2 State-independent test with nine observables

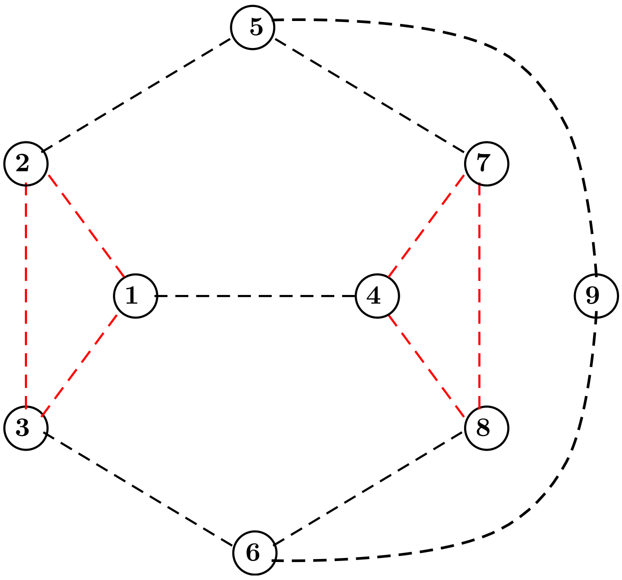

Figure 4.2: An orthogonality graph(G) showing the nine projectors as the vertices and the edges ($E(G)$) depicting the orthogonality relations between various vertices.

Let us consider another state-independent test for single-qutrit contextuality proposed by kurzynski et al. [86]. This consists of nine measurements that can reveal the contextuality of all single qutrit states other than the maximally mixed state represented by identity. The set of nine projectors are represented as $\Pi_i = |\psi_i\rangle\langle\psi_i|$, $i \in \{1, 9\}$, where a set of vectors ψ_is obey certain orthogonality relations shown in the adjoining graph G. Vertices in the orthogonality graph G are occupied by the vectors ψ_is and the edges connect the vertices occupied by mutually orthogonal vectors. As per non-contextual hidden variable theory, one can consider the pre-assignment of the dichotomous measurement outcomes $(0, 1)$ to each of the projection operator Π_i. The projection operators obey the orthogonality relations depicted in Graph G, due to which no two connected vertices in Graph G can be assigned the value '1' simultaneously. Thus, sum total of the maximum value of the measurement outcomes that can be obtained from Graph G is '3'. This set of projective measurements over an ensemble of single qutrit states yields the following inequality

$$\sum_{i=1}^{9} \langle \Pi_i \rangle \leq 3. \tag{4.7}$$

Inequality in Equation (4.7) is violated by any contextual single-qutrit state. There is no unique set of nine measurements that test the contextual nature of each and every single-qutrit state. However, corresponding to every single-qutrit state (except maximally mixed state) one can always find such a set of nine measurements ($\Pi_i = |\psi_i\rangle\langle\psi_i|$) that reveal its contextuality. One such example set is given as:

$$\begin{aligned}
|\psi_1\rangle &= (1,\, 0,\, 0)^\dagger\,, & |\psi_6\rangle &= \frac{1}{\sqrt{3}}\left(1,\, \sqrt{2},\, 0\right)^\dagger, \\
|\psi_2\rangle &= (0,\, 1,\, 0)^\dagger\,, & |\psi_7\rangle &= \frac{1}{2}\left(\sqrt{2},\, 1,\, 1\right)^\dagger, \\
|\psi_3\rangle &= (0,\, 0,\, 1)^\dagger\,, & |\psi_8\rangle &= \frac{1}{2}\left(\sqrt{2},\, -1,\, -1\right)^\dagger, \\
|\psi_4\rangle &= \frac{1}{\sqrt{2}}(0,\, 1,\, -1)^\dagger\,, & |\psi_9\rangle &= \frac{1}{2}\left(\sqrt{2},\, -1,\, 1\right)^\dagger, \\
|\psi_5\rangle &= \frac{1}{\sqrt{3}}\left(1,\, 0,\, -\sqrt{2}\right)^\dagger.
\end{aligned} \tag{4.8}$$

The orthogonality relation between these projectors is evident from the construction, and is consistent with that of graph G (Figure 4.2).

Introducing the dichotomous observables, $A_i = I - 2\Pi_i$ (assuming values ± 1) associated with the projection operators ($\Pi_i = |\psi_i\rangle\langle\psi_i|$). The projectors of the graph G

connected via an edge correspond to the mutually compatible observables. The edges of the graph can be termed as context. Let us consider an edge corresponding to the observables A_i and A_j. Measurement outcomes of A_i and A_j are mutually exclusive and thus can be measured simultaneously. But at the same time, $A_i(A_j)$ occurs in more than one contexts. Pre-assignment of the measurement outcomes to each of these observables, on the basis of a non-contextual hidden variable theory doesnot consider the joint probability distributions of all those operators which are being co-measured. Considering the non-contextual pre-assignments (as before) Equation (4.7) is reformulated in terms of the contexts, represented as the correlations between the compatible observables (A_iA_j). We have

$$\begin{aligned} A_i &= I - 2\Pi_i, \\ \sum_{i=1}^{9}\langle A_i\rangle &= 9\langle I\rangle - 2\sum_{i=1}^{9}\langle \Pi_i\rangle, \\ \Rightarrow \qquad \sum_{i=1}^{9}\langle A_i\rangle &\geq 3. \end{aligned} \tag{4.9}$$

Considering the measurement-contexts that are shown in Figure 4.2 as thirteen edges,

$$\begin{aligned} A_iA_j &= (I-2\Pi_i)(I-2\Pi_j) = I - 2\Pi_i - 2\Pi_j, \qquad (\because \Pi_i\Pi_j = 0) \\ \sum_{i,j_{(i<j)}\in E(G)} \langle A_iA_j\rangle &= \sum_{i,j\in E(G)} \frac{1}{2}\langle I - 2\Pi_i - 2\Pi_j\rangle, \end{aligned} \tag{4.10}$$

where $E(G)$ are the edges of graph G. There are a total of 13 edges and each combination is occurring twice, therefore first term on the R.H.S. of Equation (4.10) gives number 13 ($\because Tr[\rho] = 1$). Each one of the vertices numbered from $1-8$ in Figure 4.2 are connected to three other vertices while 9^{th} vertex is connected to only two vertices. Therefore second term on the R.H.S. of Equation (4.10), $\frac{1}{2}\sum_{i,j\in E(G)}\langle 2\Pi_i\rangle$ can be replaced by $3\sum_{i=1}^{9}\langle\Pi_i\rangle - \langle\Pi_9\rangle$ and so is the third term. Equation(4.10) is now written as (for $i < j$)

$$
\begin{aligned}
\sum_{i,j \in E(G)} \langle A_i A_j \rangle &= 13\langle I \rangle - 6\sum_{i=1}^{9} \langle \Pi_i \rangle + 2\langle \Pi_9 \rangle, \\
&= 14\langle I \rangle - 6\sum_{i=1}^{9} \langle \Pi_i \rangle - (\langle I \rangle - 2\langle \Pi_9 \rangle) \\
&= 14\langle I \rangle - 6\sum_{i=1}^{9} \langle \Pi_i \rangle - \langle A_9 \rangle \\
\sum_{i,j \in E(G)} \langle A_i A_j \rangle + \langle A_9 \rangle &= 14 - 6\sum_{i=1}^{9} \langle \Pi_i \rangle \qquad (4.11)
\end{aligned}
$$

It is known from Equation (4.7) $\sum_{i=1}^{9} \langle \Pi_i \rangle \leq 3$, second term on the R.H.S. ≤ -18. The above equation takes the form

$$
\sum_{i,j \in E(G)} \langle A_i A_j \rangle + \langle A_9 \rangle \geq -4 \qquad (4.12)
$$

The inequality in Equation (4.12) is to be satisfied by the context independent single qutrit states.

Equations 4.7 and 4.12 represent single-qutrit contextuality inequalities in terms of the set of nine measurements and the measurement contexts respectively. Violation of these inequalities is a test for the contextual nature of a single-qutrit state, corresponding to a given set of nine measurements. An experimental test corresponding to this scheme is designed and implemented on a single-qutrit NMR quantum information processor in the next section.

4.2 Experimental test for single-qutrit contextuality

An experimental test to verify single-qutrit contextuality is designed for NMR quantum information processor. The measurements and the measurement contexts are thus redefined in terms of the observables in NMR. This section focuses on the reformulation of the contextuality inequality in terms of traceless Λ matrices (Section 3.1.4).

4.2.1 Contextuality relations in terms of traceless observables

Considering the observables corresponding to the given set of nine projection operators, $A_i = I - 2|\psi_i\rangle\langle\psi_i|$. These observables are written as a combination of a set of eight Lambda (Λ) matrices and the 3×3 Identity operator. One can obtain the single qutrit contextuality inequality in terms of traceless observables, independently for equations (4.9),(4.12),(4.7) respectively. Explicit form the decompositions of these nine ($A_i s$) observables are given in terms of Λ matrices:

$$\begin{aligned}
A_1 &= -\Lambda_3 - \frac{1}{\sqrt{3}}\Lambda_8 + \frac{1}{3}I \\
A_2 &= \Lambda_3 - \frac{1}{\sqrt{3}}\Lambda_8 + \frac{1}{3}I \\
A_3 &= \frac{2}{\sqrt{3}}\Lambda_8 + \frac{1}{3}I \\
A_4 &= \frac{1}{2\sqrt{3}}\left(\sqrt{3}\Lambda_3 + 2\sqrt{3}\Lambda_6 + \Lambda_8\right) + \frac{1}{3}I \\
A_5 &= \frac{1}{3}\left(-\Lambda_3 + 2\sqrt{2}\Lambda_4 + \sqrt{3}\Lambda_8\right) + \frac{1}{3}I \\
A_6 &= \frac{1}{3}\left(-2\sqrt{2}\Lambda_1 + \Lambda_3 - \sqrt{3}\Lambda_8\right) + \frac{1}{3}I \\
A_7 &= \frac{1}{4\sqrt{3}}\left(-2\sqrt{6}\Lambda_1 - \sqrt{3}\Lambda_3 - 2\sqrt{6}\Lambda_4 - 2\sqrt{3}\Lambda_6 - \Lambda_8\right) + \frac{1}{3}I \\
A_8 &= \frac{1}{4\sqrt{3}}\left(2\sqrt{6}\Lambda_1 - \sqrt{3}\Lambda_3 + 2\sqrt{6}\Lambda_4 - 2\sqrt{3}\Lambda_6 - \Lambda_8\right) + \frac{1}{3}I \\
A_9 &= \frac{1}{4\sqrt{3}}\left(2\sqrt{6}\Lambda_1 - \sqrt{3}\Lambda_3 - 2\sqrt{6}\Lambda_4 + 2\sqrt{3}\Lambda_6 - \Lambda_8\right) + \frac{1}{3}I
\end{aligned} \tag{4.13}$$

Using the decompositions given above, the L.H.S. of Equation (4.9) becomes:

$$\sum_{i=1}^{9}\langle A_i\rangle = \frac{1}{12}\langle -2\sqrt{2}\Lambda_1 - 3\Lambda_3 + 2\sqrt{2}\Lambda_4 + 6\Lambda_6 - \sqrt{3}\Lambda_8\rangle + 3\langle I\rangle \tag{4.14}$$

Substituting above expression in the inequality in Equation (4.9), ($Tr[\rho] = 1$) results into:

$$\langle -2\sqrt{2}\Lambda_1 - 3\Lambda_3 + 2\sqrt{2}\Lambda_4 + 6\Lambda_6 - \sqrt{3}\Lambda_8\rangle \geq 0 \tag{4.15}$$

This is an inequality composed of 3×3 traceless observables, that is to be obeyed by any non-contextual single qutrit state. For any contextual single qutrit state, left hand side of Equation (4.15) bears a negative value, and thus violates the inequality.

Let us reconsider the contextuality inequality as derived from the correlations between the compatible observables. Following set of equations contain the explicit form of the correlations (A_iA_j) in terms of Λ-matrices and 3×3 identity operator.

$$\begin{aligned}
A_1A_2 &= -\frac{2}{\sqrt{3}}\Lambda_8 - \frac{1}{3}I \\
A_1A_3 &= \frac{1}{2\sqrt{3}}\left(2\Lambda_8 - 2\sqrt{3}\Lambda_3\right) - \frac{1}{3}I \\
A_1A_4 &= \frac{1}{2\sqrt{3}}\left(-\sqrt{3}\Lambda_3 + 2\sqrt{3}\Lambda_6 - \Lambda_8\right) - \frac{1}{3}I \\
A_2A_3 &= \frac{1}{2\sqrt{3}}\left(2\sqrt{3}\Lambda_3 + 2\Lambda_8\right) - \frac{1}{3}I \\
A_2A_5 &= \frac{2}{3}\left(\Lambda_3 + \sqrt{2}\Lambda_4\right) - \frac{1}{3}I \\
A_3A_6 &= \frac{1}{3\sqrt{2}}\left(-\Lambda_1 + \sqrt{2}\Lambda_3 + \sqrt{6}\Lambda_8\right) - \frac{1}{3}I \\
A_4A_7 &= \frac{1}{12}\left(-6\sqrt{2}\Lambda_1 + 3\Lambda_3 - 6\sqrt{2}\Lambda_4 + 6\Lambda_6 + \sqrt{3}\Lambda_8\right) - \frac{1}{3}I \\
A_4A_8 &= \frac{1}{12}\left(6\sqrt{2}\Lambda_1 + 3\Lambda_3 + 6\sqrt{2}\Lambda_4 + 6\Lambda_6 + \sqrt{3}\Lambda_8\right) - \frac{1}{3}I \\
A_5A_7 &= \frac{1}{12}\left(-6\sqrt{2}\Lambda_1 - 7\Lambda_3 + 2\sqrt{2}\Lambda_4 - 6\Lambda_6 + 3\sqrt{3}\Lambda_8\right) - \frac{1}{3}I \\
A_5A_9 &= \frac{1}{12}\left(6\sqrt{2}\Lambda_1 - 7\Lambda_3 + 2\sqrt{2}\Lambda_4 + 6\Lambda_6 + 3\sqrt{3}\Lambda_8\right) - \frac{1}{3}I \\
A_6A_8 &= \frac{1}{12}\left(-2\sqrt{2}\Lambda_1 + \Lambda_3 + 6\sqrt{2}\Lambda_4 - 6\Lambda_6 - 5\sqrt{3}\Lambda_8\right) - \frac{1}{3}I \\
A_6A_9 &= \frac{1}{12}\left(-2\sqrt{2}\Lambda_1 + \Lambda_3 - 6\sqrt{2}\Lambda_4 + 6\Lambda_6 - 5\sqrt{3}\Lambda_8\right) - \frac{1}{3}I \\
A_7A_8 &= \frac{1}{2\sqrt{3}}\left(-\sqrt{3}\Lambda_3 - 2\sqrt{3}\Lambda_6 - \Lambda_8\right) - \frac{1}{3}I
\end{aligned} \tag{4.16}$$

Using the description of the correlations given above, the L.H.S. of Equation (4.12) is found out to be

$$\sum_{i,j\in E(G)} \langle A_iA_j\rangle + \langle A_9\rangle = \frac{1}{4}\langle -2\sqrt{2}\Lambda_1 - 3\Lambda_3 + 2\sqrt{2}\Lambda_4 + 6\Lambda_6 - \sqrt{3}\Lambda_8\rangle - 4I. \tag{4.17}$$

Substituting it in Equation (4.12), one obtains

$$\frac{1}{4}\langle -2\sqrt{2}\Lambda_1 - 3\Lambda_3 + 2\sqrt{2}\Lambda_4 + 6\Lambda_6 - \sqrt{3}\Lambda_8\rangle - 4\langle I\rangle \geq -4.$$

Finally, the inequality assumes the form,

$$\langle -2\sqrt{2}\Lambda_1 - 3\Lambda_3 + 2\sqrt{2}\Lambda_4 + 6\Lambda_6 - \sqrt{3}\Lambda_8 \rangle \geq 0 \tag{4.18}$$

Also, the contextuality inequality as obtained from Equation (4.7), by substituting the values of $\Pi_i = \frac{1}{2}(I - A_i)$ is given as:

$$\langle -2\sqrt{2}\Lambda_1 - 3\Lambda_3 + 2\sqrt{2}\Lambda_4 + 6\Lambda_6 - \sqrt{3}\Lambda_8 \rangle \geq 0 \tag{4.19}$$

From Equations (4.15), (4.18) and (4.19), it is concluded that a non-contextual single qutrit state obeys,

$$\langle -2\sqrt{2}\Lambda_1 - 3\Lambda_3 + 2\sqrt{2}\Lambda_4 + 6\Lambda_6 - \sqrt{3}\Lambda_8 \rangle \geq 0. \tag{4.20}$$

The above inequality consists of the expectation values of the Λ matrices that can be determined experimentally in an NMR experiment. All three equivalent forms of the contextuality inequalities in Equations (4.7), (4.9) and (4.12) lead to inequalities in Equations (4.19), (4.15) and (4.18) respectively. All these inequalities in terms of traceless observables are same (with a constant factor) as shown in Equation (4.20). Corresponding to any set of nine projectors as per graph G, one can always find such contextuality inequality.

It is to be noted that this inequality corresponds to the set of nine vectors given in Equation (4.8). A global unitary transformation of this set of vectors transforms the L.H.S. of Equation (4.20) as well by same unitary operator.

4.3 NMR Experimental verification of contextuality

An experimental determination of the expectation values of Λ matrices is carried out to evaluate the L.H.S. of the contextuality inequality given in Equation (4.20). For a single-qutrit at thermal equilibrium ($\rho = \Sigma_z$; where Σ_z is the three-dimensional analogue of the Pauli matrix [71]), the value of the L.H.S. of Equation (4.20) is '-2'. Thus it is a contextual single-qutrit state. As depicted in [86], the set of single-qutrit measurements corresponding to Equation (4.8) can reveal the contextuality of the diagonal states. This test is performed for various initial states. Each of these single-qutrit states are prepared from thermal equilibrium state and the contextuality test is performed on it. However, in order to ascertain the control over the system, each of these initial states are allowed to evolve for certain time τ. During this free evolution of a qutrit, the state of the qutrit decoheres and tend to achieve the state of thermal equilibrium. The experimental contextuality tests are performed at various intervals of time. This turned out to be a useful exercise to observe the (weighted) sum total of the expectation values of various Λ matrices, that approach the value of '-2' corresponding to thermal equilibrium. The experimental scheme and other technical issues are addressed in the following sections.

4.3.1 The NMR qutrit

A single-qutrit is a three-level quantum system that gives rise to two degenerate single quantum transitions in liquid state NMR experiments. A naturally existing single-qutrit is a spin-1 nucleus whose quadrupolar moment gets averaged to zero in the isotropic environment, and the single-qutrit NMR spectrum thus results into one overlapped line. However in the presence of an anisotropic medium to surrounding spin-1, an effective quadrupolar coupling comes into picture and the spectral lines corresponding to the two single-quantum transitions get separated in the frequency space. The details of single qutrit NMR are discussed in Chapters 3 and 4 of this thesis. NMR qutrit used here is a spin-1 deuterium nucleus (^{2}H) nucleus of deutrated Chloroform molecule oriented in a lyotropic liquid crystal. Energy level diagram depicting thermal equilibrium population distribution and the single quantum transitions are shown in Figure 4.3 alongwith first order NMR spectrum of a qutrit at 277 K. (The molecule is shown in Figure 3.4 of chapter 3 of this thesis.) Transitions between levels $1-2$ and $2-3$ (Figure 4.3(a)) are shown as spectral lines labelled 'Line 1' and 'Line 2' respectively in Figure 4.3(b).

4.3.2 Experimental scheme

The set of eight Λ matrices form a basis in the space of operators in the qutrit Hilbert space and therefore the state ρ_0 is given by:

$$\rho_0 = \sum_{i=1}^{8} \langle \Lambda_i \rangle \Lambda_i, \tag{4.21}$$

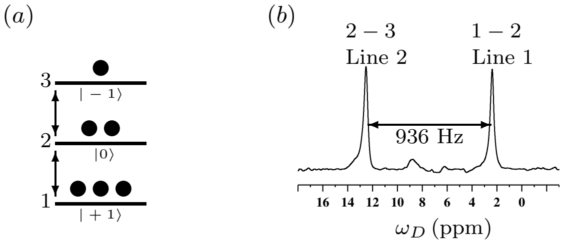

Figure 4.3: (a) Single-qutrit energy level diagram depicting the thermal equilibrium population distribution of the eigen vectors labelled as $\{1, 2, 3\}$. (b) Deuterium NMR spectrum of oriented deutrated chloroform molecule at 277 K. The spectral lines are labelled as Line 1 and Line 2. At 277 K the anisotropic liquid crystalline environment is shown to exhibit the effective quadrupolar splitting of 936 Hz.

where $\langle\Lambda_i\rangle$ is the expectation value of Λ_i in the state ρ_0. The explicit form of the single-qutrit density matrix is given by (Section 3.3.4):

$$\rho = \frac{1}{2}\begin{pmatrix} \langle\Lambda_3\rangle + \frac{1}{\sqrt{3}}\langle\Lambda_8\rangle & \langle\Lambda_1\rangle - \iota\langle\Lambda_2\rangle & \langle\Lambda_4\rangle - \iota\langle\Lambda_5\rangle \\ \langle\Lambda_1\rangle + \iota\langle\Lambda_2\rangle & -\langle\Lambda_3\rangle + \frac{1}{\sqrt{3}}\langle\Lambda_8\rangle & \langle\Lambda_6\rangle - \iota\langle\Lambda_7\rangle \\ \langle\Lambda_4\rangle + \iota\langle\Lambda_5\rangle & \langle\Lambda_6\rangle + \iota\langle\Lambda_7\rangle & -\frac{2}{\sqrt{3}}\langle\Lambda_8\rangle \end{pmatrix} \tag{4.22}$$

As discussed in Section 1.2.3, the NMR spectrum depicts the single-quantum coherences, such that the absorptive part of the spectral line corresponds to the real part, whereas the dispersive part corresponds to the imaginary part of the single-quantum coherence term. A single-qutrit density matrix has two single-quantum coherences occurring as elements $\rho_0(1,2)$ and $\rho_0(2,3)$ of the density matrix ρ_0. These terms have direct correspondence with the NMR spectral lines resulting from transitions between energy levels $1-2$ and $2-3$ (Figure 4.3) respectively. From Equation (4.22), we have

$$\begin{aligned} \rho_0(1,2) &= \frac{1}{2}(\langle\Lambda_1\rangle - \iota\langle\Lambda_2\rangle), \\ \rho_0(2,3) &= \frac{1}{2}(\langle\Lambda_6\rangle - \iota\langle\Lambda_7\rangle). \end{aligned} \tag{4.23}$$

Thus the expectation value corresponding to state ρ_0: $\langle\Lambda_1\rangle_{\rho_0} = \mathfrak{Re}\{\mathbf{I}(\text{Line 1})\}$, is determined from the intensity ($\mathbf{I}$) of the real part ($\mathfrak{Re}$) of the first spectral line (Line 1), and $\langle\Lambda_2\rangle_{\rho_0} = -\mathfrak{Im}\{\mathbf{I}(\text{Line 1})\}$ corresponds to imaginary part ($\mathfrak{Im}$). Similarly, from second spectral line (Line2), one obtains, $\langle\Lambda_6\rangle_{\rho_0} = \mathfrak{Re}\{\mathbf{I}(\text{Line 2})\}$ and $\langle\Lambda_7\rangle_{\rho_0} = -\mathfrak{Im}\{\mathbf{I}(\text{Line 2})\}$.

A set of four NMR experiments evaluate the L.H.S. of the Equation (4.20). The experiments consist of transition-selective pulses (θ_j^{r-s}) of angle θ about j^{th} axis on transition between levels $r-s$, and the non-unitary z-gradient implementations. The set of experiments are designed in such a manner that the directly inaccessible expectation values of the density matrix (ρ_0) appear at the sites of single-quanta in the final state density matrix (ρ_k) of the k^{th} experiment. The idea of finding the expectation values is similar to that of the process used in tomography (Section 1.2.3), however in this case one does not need to construct the complete single-qutrit density matrix. The aim is to evaluate the (weighted) sum of the expectation values of the observables in the L.H.S. of Equation (4.20), that contains only five expectation values of the given state corresponding to the five Λ matrices with only real elements. The expectation values of various Λ matrices are obtained (as discussed) in form of real ($\mathfrak{Re}$) and imaginary ($\mathfrak{Im}$) parts of the spectral line intensities (**I**(Line 1) and **I**(Line 2)) in the NMR spectrum of state ρ_k. This set of experiments is used to determine $\langle\Lambda_1\rangle_{\rho_0}$, $\langle\Lambda_3\rangle_{\rho_0}$, $\langle\Lambda_4\rangle_{\rho_0}$, $\langle\Lambda_6\rangle_{\rho_0}$ and $\langle\Lambda_8\rangle_{\rho_0}$. The details of the experiments are given as:

- Exp-1: No operation
  Result: $\langle\Lambda_1\rangle_{\rho_0} = \mathfrak{Re}\{\mathbf{I}(\text{Line 1})\}_{exp1}$ and
  $\langle\Lambda_6\rangle_{\rho_0} = \mathfrak{Re}\{\mathbf{I}(\text{Line 2})\}_{exp1}$

- Exp-2: $(\pi_y)^{1-2}$; final state = ρ_1
  Result: $\langle\Lambda_4\rangle_{\rho_0} = \mathfrak{Re}\{\mathbf{I}(\text{Line 2})\}_{exp2}$

- Exp-3: Grad$_z$ $(\frac{\pi}{2}_y)^{1-2}$; final state = ρ_2
  Result: $\langle\Lambda_3\rangle_{\rho_0} = \mathfrak{Re}\{\mathbf{I}(\text{Line 1})\}_{exp3}$

- Exp-4: Grad$_z$ $(\frac{\pi}{2}_y)^{2-3}$; final state = ρ_3
  Result: $\frac{1}{2}(\langle\Lambda_3\rangle_{\rho_0} - \sqrt{3}\langle\Lambda_8\rangle_{\rho_0}) = -\mathfrak{Im}\{\mathbf{I}(\text{Line 2})_{exp4}\}$
  or $\langle\Lambda_8\rangle_{\rho_0} = \frac{1}{\sqrt{3}}\left[2\mathfrak{Im}\{\mathbf{I}(\text{Line 2})\}_{exp4} + \mathfrak{Re}\{\mathbf{I}(\text{Line 1})\}_{exp3}\right]$

The expectation values thus obtained experimentally are substituted into the L.H.S. of Equation (4.20), to test single-qutrit contextuality. This set of experiments are shown diagrammatically in Figure 4.4, where set of four experiments are shown as four independent modules (numbered from (i)-(iv)). All the pulses used are the transition-selective pulses that are shown separately corresponding to the horizontal lines labelled 'ln1' and 'ln2'. RF pulses shown along 'ln1' correspond to the frequency offset of Line 1 (Figure 4.3), while 'ln2' correspond to that of Line 2. Gradient channel is shown as a third horizontal line, labelled 'Grad', implementing gradients of strength g_i along $z-$axis. A meter in each experimental module is a symbol, depicting the measurement of the corresponding line intensity. This set of measurements are made on various single-qutrit states that are explicitly discussed in the next section.

All the experiments in this chapter were performed at 277 K on a 600 MHz Avance III NMR spectrometer equipped with a QXI probe, with the deuterium nucleus resonating at 91.108 MHz. All the pulses used are the soft radio frequency pulses. All the transition-selective pulses are 'Gauss' shaped pulses of duration 4000 μs composed of a total of 1000 points exciting a bandwidth of 400 Hz (approximately). The non-selective pulses are 'Sinc' shaped pulses of duration 500 μs composed of a total of 1000 points exciting a bandwidth of 3000 Hz. The offset for this rf pulse is kept in the larmor frequency of the experimental qutrit. The soft pulses used are from the standard Bruker directory and are robust with good selectivity and uniform spin response in the desired frequency range. The gradient pulses are of 'Sine' shape applied for a duration of 800 μs followed by a gradient recovery of 2000 μs.

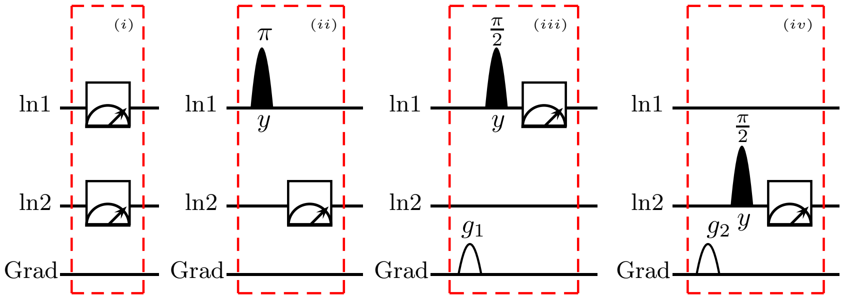

Figure 4.4: NMR pulse sequences for a single qutrit contextuality measurements where a single qutrit state is prepared which is followed by various blocks finding the desired expectation values. Block (i) gives $\langle\Lambda_2\rangle$ and $\langle\Lambda_6\rangle$, (ii) $\langle\Lambda_4\rangle$, (iii) $\langle\Lambda_3\rangle$ and (iv) $\langle\Lambda_8\rangle$. 'ln1' and 'ln2' correspond to the two single quantum transitions of a qutrit and 'Grad' is the gradient channel.Pulse angles are shown at the top and the axes of rotation at the bottom of each pulse.

4.3.3 Experiment and analysis

The experiments are performed on three single-qutrit pseudo-pure states and a Σ_x state. The contextuality tests are performed at various intervals for all these states, and are plotted. The plots are shown in Figure 4.5.

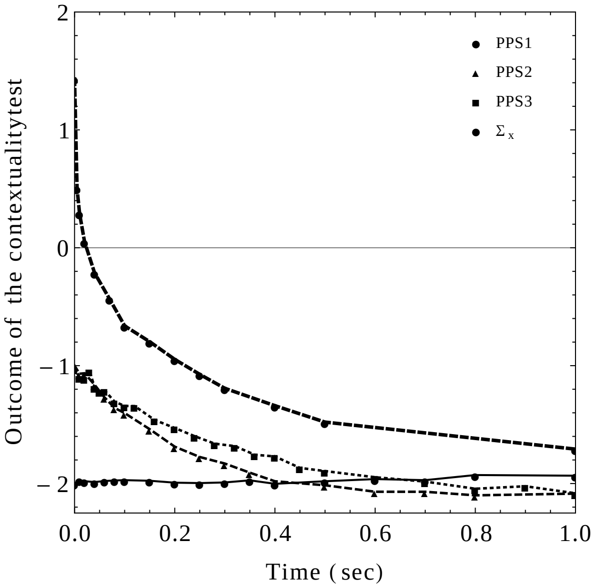

Figure 4.5: Plot showing the values obtained (from L.H.S. of Equation (4.20)) as a result of contextuality test for four different initial states at different intervals of time. Thin solid line starting from -2 along the vertical axis correspond to state 'PPS1', dashed line with triangular point markers represent 'PPS2', dotted line with squares represent 'PPS3' and the thick dashed line correspond to the state Σ_x. The contextuality test is performed at various time points, which are represented by the point markers, while the connecting lines are not of much significance.

PPS1

$$\text{PPS1} = |+1\rangle = \frac{1}{6}\begin{pmatrix} 2 & 0 & 0 \\ 0 & -1 & 0 \\ 0 & 0 & -1 \end{pmatrix} \tag{4.24}$$

This state is prepared by the sequence: $\left(\frac{\pi}{2}\right)_y^{(2-3)}$, Grad$_z$. Equation (4.20) is found to have value -2 in this state, thus PPS1 is contextual. As this state evolves, it tends towards thermal equilibrium, however the contextuality-value remains -2 all through this time. This is shown as a thick black curve in Figure 4.5.

PPS2

$$\mathrm{PPS2} = |0\rangle = \frac{1}{6}\begin{pmatrix} 1 & 0 & 0 \\ 0 & -2 & 0 \\ 0 & 0 & 1 \end{pmatrix} \tag{4.25}$$

This state is prepared by the sequence: $\left(\frac{\pi}{2}\right)_y^{(2-3)}$, Grad$_z$, $(\pi)_y^{(1-2)}$. Equation (4.20) is found to have value -1 in this state, thus PPS2 is contextual. As this state evolves, it tends towards thermal equilibrium, which reflects in the dotted curve in Figure 4.5

PPS3

$$\mathrm{PPS3} = |-1\rangle = \frac{1}{6}\begin{pmatrix} 1 & 0 & 0 \\ 0 & 1 & 0 \\ 0 & 0 & -2 \end{pmatrix} \tag{4.26}$$

This state is prepared by the sequence: $\left(\frac{\pi}{2}\right)_y^{(1-2)}$, Grad$_z$. Equation (4.20) is found to have value -1 in this state, thus PPS3 is contextual, and its changing contextuality-value with time, depicts the decoherence of the state. This is shown as dotted curve in Figure 4.5

Σ_x

$$\Sigma_x = \frac{1}{3\sqrt{2}}\begin{pmatrix} 0 & 1 & 0 \\ 1 & 0 & 1 \\ 0 & 1 & 0 \end{pmatrix} \tag{4.27}$$

This state is obtained by a $\left(\frac{\pi}{2}\right)_y$ non-selective pulse on the thermal equilibrium state. It is clear from its explicit matrix representation, this state does not have any diagonal term. The contextuality value for this state comes out to be $+1.06$. Thus this state is non-contextual corresponding to the set of vectors in Equation (4.8). However as time advances, this state tends to approach thermal equilibrium, which is seen in the plot (Figure 4.5).

The contextuality test for all the diagonal states of a single-qutrit can be performed in a single shot measurement. If a state is prepared in a diagonal form, $\langle\Lambda_1\rangle = \langle\Lambda_4\rangle = \langle\Lambda_6\rangle = 0$. Therefore for testing contextuality, one needs to find only the non-vanishing expectation values $\langle\Lambda_3\rangle$ and $\langle\Lambda_8\rangle$. Thus contextuality inequality 4.20 in this case is reduced to

$$\langle -3\Lambda_3 - \sqrt{3}\Lambda_8\rangle \geq 0. \tag{4.28}$$

Consider an NMR experimental test consisting of sequential implementation of two unitary operators $\Lambda_6(\frac{\pi}{4})\Lambda_2(\frac{\pi}{4})$ on the diagonal state ρ_d; one obtains,

$$\rho_f = \exp\left(\iota\frac{\pi}{4}\Lambda_6\right)\exp\left(\iota\frac{\pi}{4}\Lambda_2\right)\rho_d\exp\left(-\iota\frac{\pi}{4}\Lambda_2\right)\exp\left(-\iota\frac{\pi}{4}\Lambda_6\right) \tag{4.29}$$

The line intensity $\mathbf{I}(\text{Line } 1)$ in the NMR spectrum of state ρ_f is given by:

$$\frac{1}{4}(-3\langle\Lambda_3\rangle_{\rho^0} - \sqrt{3}\langle\Lambda_8\rangle_{\rho^0}) \tag{4.30}$$

Comparing Equations (4.29) and (4.30), the contextuality inequality decomposes to finding of the line intensity in the NMR spectrum of single-qutrit state ρ^f. This new inequality is given as:

$$\mathfrak{Re}\{\mathbf{I}(\text{Line } 1)\}_f \leq 0 \tag{4.31}$$

The violation of above inequality is a test for single-qutrit contextuality.

The NMR experimental evidence in support of the contextual nature of a qutrit is further exploited to harness the intrinsic quantumness of a qutrit. Next section deals with NMR experimental implementation of a single-qutrit based algorithm to determine the parity of a permutation.

4.4 Parity Determining Algorithm

Recently a qutrit-based black-box algorithm has been proposed to evaluate the parity of permutation of three objects [139]. The classical counterpart of this algorithm needs to query the black-box at least twice before returning the answer. However, this qutrit-based quantum algorithm can accomplish the task in only one oracle call.

Consider a set of three objects $\{1, 2, 3\}$, that can arrange themselves in six possible ways. These six different arrangements can be achieved through various exchange operations. These exchange operations may or may not retain the cyclic order of the three objects in the resulting arrangements. Whenever the resultant state retains the cyclic order under the exchange operations the parity of the permutation is said to be even, and if the cyclic order is destroyed, the permutation is said to be of odd parity. In other words, the parity of the permutation is termed as **even** or **odd**, depending on whether the number of exchange operations performed is **even** or **odd**. The computational task to be performed is to find the parity of a given permutation.

Considering the permutation as a function $f(x)$ where $x \in \{1, 2, 3\}$, is a set of three objects arranged in a specific manner. In order to solve this problem classically, one needs to query at least twice. In classical approach, one can ask questions of the type that after the permutation operation which specific object is at a particular position in set x. Of course identification of a single object occupying a particular position can not determine the parity of the permutation performed. Thus one needs to inquire about the occupancy of one more position, knowledge of these two pieces of information are enough to determine the parity of a permutation. Therefore the classical algorithm accesses the black-box twice before concluding the result. However the task is shown to be accomplished in a single step using the quantum counterpart of the algorithm.

As per quatum approach the three objects in the set $x \in \{1, 2, 3\}$ correspond to spin-1 eigen states of a single-qutrit labeled by its spin quantum number $|m\rangle$ where $m = 1, 0, -1$. The action of permutations ($f(x)$) on these states are the bijective maps $f : \{1, 0, -1\} \longrightarrow \{1, 0, -1\}$. The six possible maps can be written down using Cauchy's notation [140]. The three even maps and the corresponding unitary transformations are given by:

$$
\begin{aligned}
f_1 &= \begin{pmatrix} 1 & 0 & -1 \\ 1 & 0 & -1 \end{pmatrix}; \quad U_1 = \begin{pmatrix} 1 & 0 & 0 \\ 0 & 1 & 0 \\ 0 & 0 & 1 \end{pmatrix} \\
f_2 &= \begin{pmatrix} 1 & 0 & -1 \\ 0 & -1 & 1 \end{pmatrix}; \quad U_2 = \begin{pmatrix} 0 & 1 & 0 \\ 0 & 0 & 1 \\ 1 & 0 & 0 \end{pmatrix} \\
f_3 &= \begin{pmatrix} 1 & 0 & -1 \\ -1 & 1 & 0 \end{pmatrix}; \quad U_3 = \begin{pmatrix} 0 & 0 & 1 \\ 1 & 0 & 0 \\ 0 & 1 & 0 \end{pmatrix}
\end{aligned}
\tag{4.32}
$$

while the three odd maps and the corresponding unitary transformations are given by:

$$\begin{aligned}
f_4 &= \begin{pmatrix} 1 & 0 & -1 \\ 0 & 1 & -1 \end{pmatrix}; \qquad U_4 = \begin{pmatrix} 0 & 1 & 0 \\ 1 & 0 & 0 \\ 0 & 0 & 1 \end{pmatrix} \\
f_5 &= \begin{pmatrix} 1 & 0 & -1 \\ 1 & -1 & 0 \end{pmatrix}; \qquad U_5 = \begin{pmatrix} 1 & 0 & 0 \\ 0 & 0 & 1 \\ 0 & 1 & 0 \end{pmatrix} \\
f_6 &= \begin{pmatrix} 1 & 0 & -1 \\ -1 & 0 & 1 \end{pmatrix}; \qquad U_6 = \begin{pmatrix} 0 & 0 & 1 \\ 0 & 1 & 0 \\ 1 & 0 & 0 \end{pmatrix}
\end{aligned} \tag{4.33}$$

A unitary transformation 'U' is a part of the black box which is the quantum oracle and performs a given permutation on the input state of the qutrit. A direct run of the oracle on the eigen states of the qutrit is as good as a classical parity determining algorithm and therefore is of no use. However, a quantum advantage is achieved if one begins with a superposition state obtained by Fourier transforming the eigen states, using the unitary transformation,

$$F = \frac{1}{\sqrt{3}} \begin{pmatrix} 1 & 1 & 1 \\ 1 & e^{\frac{2\pi\iota}{3}} & e^{\frac{-2\pi\iota}{3}} \\ 1 & e^{\frac{-2\pi\iota}{3}} & e^{\frac{2\pi\iota}{3}} \end{pmatrix} \tag{4.34}$$

The various steps in the implementation of the algorithm are: (1) The system is first initialized in one of the eigenstates (consider the state $|\psi_i\rangle = |-1\rangle$). (2) Initial state $|\psi_i\rangle$ is then Fourier transformed resulting into the state $F|\psi_i\rangle = \frac{1}{\sqrt{3}}(|+1\rangle + e^{\frac{-2\pi\iota}{3}}|0\rangle + e^{\frac{2\pi\iota}{3}}|-1\rangle)$. Thus a linear superposition of the eigenbases is obtained. This step is the soul of this algorithm and plays a major role in the computational speedup. (3) The Fourier transformed state is then allowed to go through the black box. A black box is an oracle call i.e. an operation where the unitary operator U_f (corresponding to the function f_k) is applied to the superposition state created by the quantum Fourier transformation. Under even permutations (Equation (4.32)) resultant states are $\frac{1}{\sqrt{3}}(|+1\rangle + e^{-2\pi\iota/3}|0\rangle + e^{2\pi\iota/3}|-1\rangle)$, $\frac{1}{\sqrt{3}}(+e^{-2\pi\iota/3}|+1\rangle + e^{2\pi\iota/3}|0\rangle + |-1\rangle)$ and $\frac{1}{\sqrt{3}}(+e^{2\pi\iota/3}|+1\rangle + |0\rangle + e^{-2\pi\iota/3}|-1\rangle)$ respectively.

When this state undergoes odd permutations (Equation (4.33)) the following states are obtained: $\frac{1}{\sqrt{3}}(e^{-2\pi\iota/3}|+1\rangle + |0\rangle + e^{2\pi\iota/3}|-1\rangle)$, $\frac{1}{\sqrt{3}}(|+1\rangle + e^{2\pi\iota/3}|0\rangle + e^{-2\pi\iota/3}|-1\rangle)$ and $\frac{1}{\sqrt{3}}(e^{2\pi\iota/3}|+1\rangle + e^{-2\pi\iota/3}|0\rangle + |-1\rangle)$ respectively. (4) The output state is then subjected to an inverse Fourier transformation which brings the state back to one of the eigen states of the qutrit (up to a phase factor). Even permutations followed by the inverse Fourier transformation return the qutrit eigenstate $|-1\rangle$ with a global phase while output states corresponding to odd permutations give rise to eigenstate $|0\rangle$ with a global phase. The final state for the case of an even function is orthogonal to the final state for the case of an odd function and are thus distinguishable by a measurement on a single copy. The result of such a measurement in the $\{|1\rangle, |0\rangle, |-1\rangle\}$ basis will thus reveal the parity of the corresponding permutation. The quantum circuit for determining the parity of a permutation of three objects is shown in Fig. 4.6. The circuit consists of the Fourier (F) and inverse (F^{-1}) gates, sandwiching the black box operations. Six possible black box operations are the permutations in accordance with Equations (4.32,4.33). These permutations are achieved via a set of single qutrit swap gates, that swap two levels of a single qutrit, interchanging the corresponding populations as well as coherences.

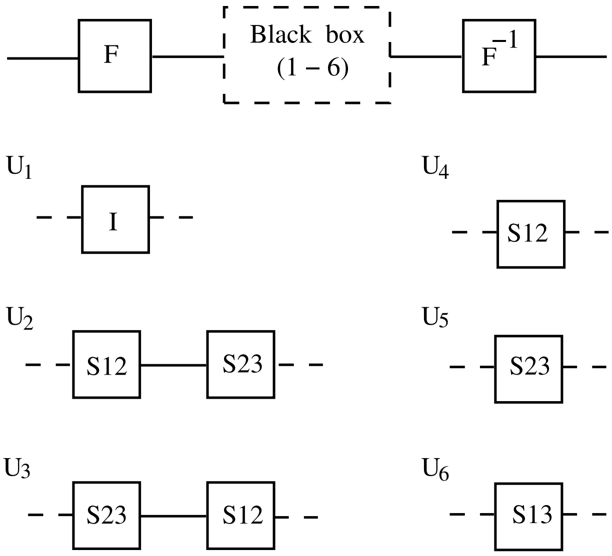

Figure 4.6: Quantum circuit to determine the parity of a permutation of three objects in a single step. Quantum gates F and F^{-1} represent the Fourier transformation and inverse Fourier transformation respectively. Black box is shown as a dotted rectangle and all the permutation operations are elaborated in lower part of the diagram. 'I' is the identity operator, while '$S12$', '$S23$' and '$S13$' are SWAP operators describing a swap between levels $1-2$, $2-3$ and $1-3$ of a single qutrit respectively. The initial state is the pure state of a single qutrit, $|-1\rangle$.

4.4.1 Experimental implementation of the Parity Algorithm

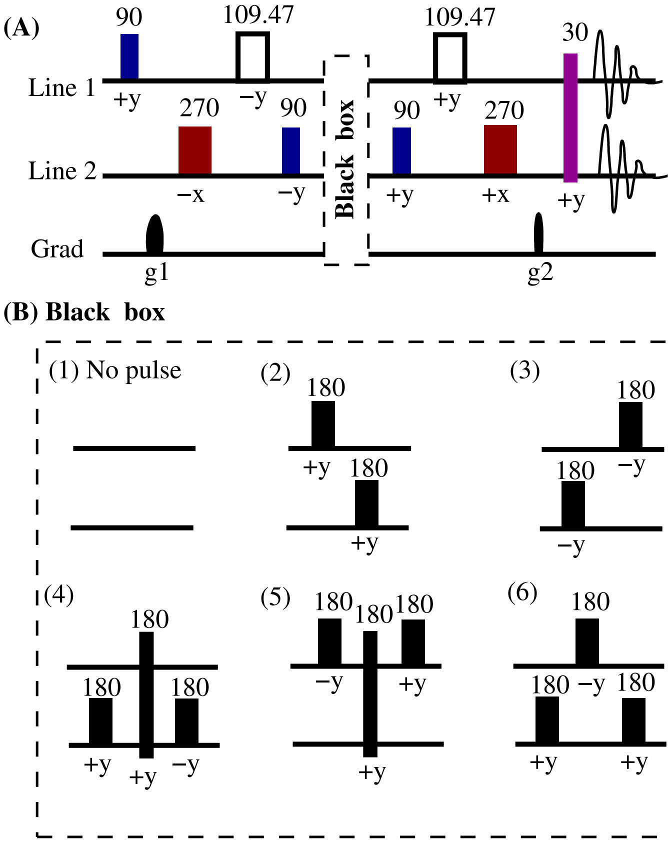

Figure 4.7: (a) Pulse sequence for the implementation of the parity algorithm on a single qutrit. Channels labeled as 'Line 1' and 'Line 2' correspond to the two NMR transitions of a qutrit. Pseudo-pure state $|-1\rangle$ is created at end of gradient g1. The next three pulses perform the Fourier transformation. (b) The black box carries out the six possible permutations corresponding to the three even and three odd functions. The two channels inside the black box correspond to the two NMR transitions of a single qutrit. A 30^0 non-selective detection pulse preceded by a clean up gradient g2 is applied to evaluate the final result of the computation. All the 90^0 pulses are shown in blue, 270^0 in red and 180^0 in black. Non-selective pulses are shown as a common rectangle for both the transitions. Pulse angles and the axes of rotations are shown corresponding to each pulse. All the pulses are shaped pulses.

The algorithm determining parity of a permutation in a set of three objects is experimentally implemented on a single qutrit NMR quantum information processor (Figure 3.4). Single qutrit quantum gates that constitute the quantum circuit given in Figure 4.6 are decomposed in the form of radio-frequency pulses to be implemented in NMR. The corresponding NMR pulse sequence is shown in Figure 4.7. As seen in part (A) of Figure 4.7, there are three channels, the channel labeled with 'Line 1' corresponds to transition between the energy eigenstates $|{+1}\rangle - |0\rangle$ and the one with 'Line 2' corresponds to transition between the energy eigenstates $|0\rangle - |-1\rangle$. Third channel is the gradient channel that implements a z-gradient pulse of prescribed strength for a given duration. Gradient is a non-unitary operation and thus cannot be a part of the quantum gates. First gradient (g_1) is a part of the pseudo-pure state preparation and the second gradient (g_2) is a clean up gradient which is a part of the detection operation. Since all the resulting states are not supposed to possess any coherences, this gradient pulse precedes the non-selective detection pulse to obtain a cleaner final state.

The system is initialized in a pseudo pure state $|-1\rangle$. First 90^0_y pulse on 'Line 1' (Figure 4.7) equates the populations of levels 1 and 2 of the qutrit (Figure 4.3). The coherence created by this pulse is dephased by the implementation of gradient g_1, and a different population in level 3 is obtained over a uniform background of the populations. Thus desired pseudo pure state is created at the end of gradient g_1. This is followed by the implementation of Fourier transformation, which creates the superposition of all the bases states alongwith relative phases. Creation of superposition of the bases states before performing the permutation operation is the key step in this algorithm. Fourier transformation operation is achieved with the help of three non-trivial transition selective pulses $(270)^{\text{Line 2}}_{-x}\,(109.47)^{\text{Line 1}}_{-y}\,(90)^{\text{Line 2}}_{-y}$. This Fourier transformed state is allowed to undergo the permutation operations applied by the black box. Experimental radio frequency pulses for the black box operations are shown in part (B) of Figure 4.7. The pulse sequences for the black box operations are shown explicitly corresponding to each permutation. Permutations inside the black box are the swap operations being implemented by 180^0 selective pulses with axes of rotations mentioned at the bottom of each pulse. The two channels correspond to 'Line 1' and 'Line 2' respectively. There are no gradient pulses, so gradient channel has been omitted in this part of the pulse sequence. The pulses shown on one of the channels are the transition-selective pulses, while those shown as a common rectangle on both the channels are the spin-selective (non-selective in this case) pulses. The state after the permutation operation undergoes inverse Fourier transformation which is applied by a set of three transition-selective pulses. Fourier (or its inverse) transformation implementation is the most crucial part of the pulse sequence. Cancelation of the Fourier and inverse Fourier transformations, despite experimental imperfections is important for a precise implementation of the algorithm. Finally the detection of the resultant state is carried out by a non-selective 30^0 detection pulse preceded by a cleanup gradient g_2.

4.4.2 Experimental analysis

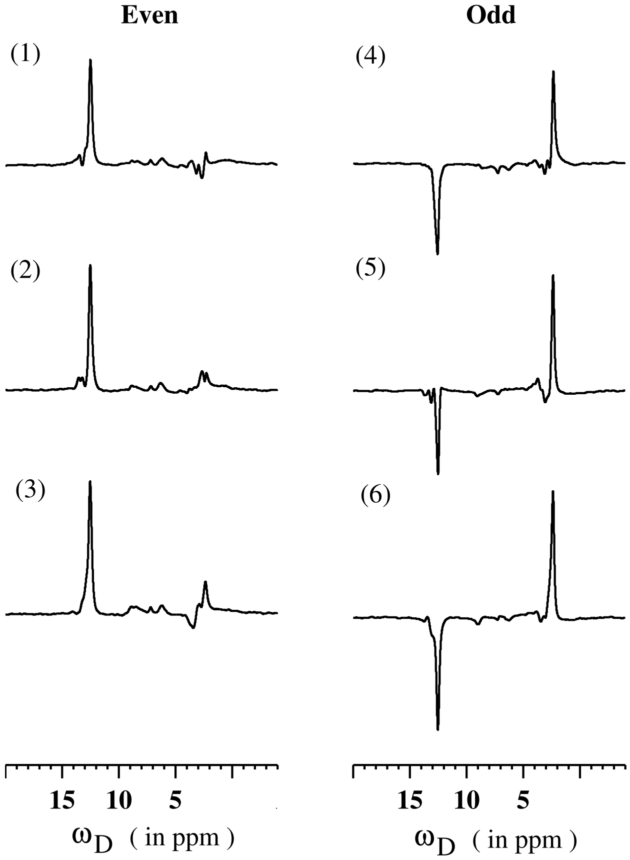

Figure 4.8: The NMR spectra after implementing the parity determining algorithm on a single qutrit. Spectra (numbered 1 to 6) correspond to the six possible permutations. All the spectra were obtained by applying a 30^0 non-selective detection pulse on both the transitions. Spectra 1,2,3 correspond to the state $|-1\rangle$ (resulting from an even permutation) and spectra 4,5,6 correspond to state $|0\rangle$ (resulting from an odd permutation).

NMR spectrum of the resultant states obtained by the implementation of the given pulse sequence corresponding to all six permutations are shown in Figure 4.8. Labels (1)-(6) of the spectra correspond to the respective black box operations (Figs. 4.6, 4.7). As discussed earlier (section 4.4), resultant states in case of even parity of permutations are $e^{\iota\phi}|-1\rangle$, and the ones resulting from the odd parity of permutations are $e^{\iota\phi}|0\rangle$. The global phase of a quantum state is of no significance and can be ignored. The final state NMR spectra are thus phase corrected to eliminate the global phase effects. The two types of parities of permutations result into the respective orthogonal eigenstates of a single qutrit which can be distinguished from each other through spectral signature resulting from the implementation of a non-selective small angle detection pulse As observed from Figure 4.8, the NMR spectra corresponding to even and odd parities of the permutation operations are easily identified. The characteristic spectra of the spin-1 eigenstates obtained by a small angle detection pulse, is a single step measurement of the determination of a parity of permutation in a single qutrit.

Tomography

The experimental output states are checked for the quantitative measurement of the state fidelities. Figure 4.9 shows the experimental tomographed density matrices after implementation of the parity-determining algorithm. Quantum state tomography of a single qutrit is performed by a set of four experiments, using 'Gaussian' shaped transition-selective pulses and z-gradients (g_z). The detailed description of the tomographic protocol has been provided in Section 3.3.4 of Chapter 3. The fidelity measure used to compute the resemblance of the experimental and theoretical density matrices is obtained by the expression given in Equation (1.6). As seen from Figure 4.9, the state tomography is able to reconstruct the density matrix well. The computed fidelities of the resultant states for the six possible permutations with respect to the theoretically expected states are found out to be (1) 0.98, (2) 0.95, (3) 0.98, (4) 0.95, (5) 0.93 and (6) 0.92 respectively. Last three transition selective pulses correspond to inverse Fourier transformation and the expected final state possesses only the populations and no coherence. During last 12 ms of the pulse sequence duration, coherences are being pumped back to the populations. In case of operation (6) of the black box (Figure 4.7), before applying the last pulse ($(270^0)_x^{\text{Line 2}}$), there exists only one single quantum coherence term at position 2,3 of the density matrix. As the final state density

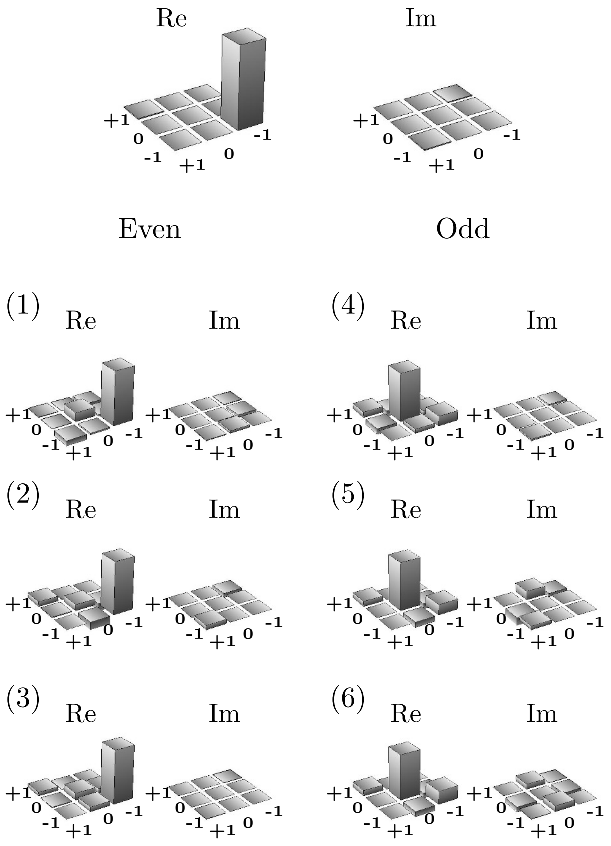

Figure 4.9: Top tomograph shows the real (left) and imaginary (right) parts of the experimental density matrix of the input state ($|-1\rangle$) used in the parity determining algorithm. The real (left) and imaginary (right) parts of the final state density matrices corresponding to the six possible permutations are shown below (numbered from 1 to 6). The state fidelities for the six possible permutations are computed to be (1) 0.98, (2) 0.95, (3) 0.98, (4) 0.95, (5) 0.93 and (6) 0.92 respectively.

matrix in this case has non-zero ρ_{23} element, the last pulse could not have transferred whole of this coherence to the diagonal position which is clear from the tomography. In addition significant values of other population elements can be seen. Fidelities are quantified in all the cases and this particular case is found to have lesser fidelity than that of other operations numbered (1)-(5). As shown in Figure 4.9, tomographs labeled (1), (2), and (3) correspond to the state $|-1\rangle$ (resulting from an even permutation) while tomographs labeled (4), (5), and (6) correspond to the state $|0\rangle$ (resulting from an odd permutation). The results of this chapter are described in *Phys. Lett. A*, **378**, 3452

(2014).

4.5 Concluding Remarks

In this chapter, single-qutrit state-independent contextuality tests are explored for a set of 13 and 9 observables respectively. NMR experimental test is proposed to reveal the single- qutrit contextuality with a set of four experiments. This protocol is successfully implemented on a single-qutrit NMR quantum information processor for various different states. A single-shot contextuality test is also devised for diagonal states of a single-qutrit. Experimental test for the verification of contextuality in a single-qutrit is an important step towards the understanding of the quantumness of this indivisible quantum system.

An NMR experimental implementation of a single qutrit algorithm is also presented, which shows a speed up over its classical counterpart. Interestingly, the dynamics of a single qubit can always be efficiently simulated classically, and therefore does not lead to a computational advantage for any quantum algorithm. A single qutrit on the other hand, possesses contextuality, and can be used for quantum computation. This toy algorithm paves the way for a new direction for computation with higher dimensional spin systems.

Chapter 5

Implementation of the quantum Fourier transform on a hybrid qubit-qutrit NMR quantum emulator

Fourier transformation is a linear transform with several applications to physical problems [141]. The subject began in eighteenth century with the representation of certain functions as a trigonometric series and providing a solution to the problem of a vibrating string. A broader view to such solutions using the expansion of a function in the form of an infinite series, was provided by Jean-Baptiste Joseph Fourier in 1822 by providing analytical solutions to the problem of propagation of heat through solids [142]. Representation of a piecewise continuous function which is periodic in a given interval, as a sum of sine and cosine functions, is known as a Fourier series. Further generalization is obtained by assuming the function to be periodic in a period of infinite extent, thus introducing the concept of the Fourier integral [143]:

$$\begin{aligned} f(t) &= \int_{-\infty}^{\infty} \left[\int_{-\infty}^{\infty} f(t) e^{2\pi \iota s t} dt \right] e^{-2\pi \iota s t} ds \\ \text{or} \qquad f(t) &= \int_{-\infty}^{\infty} F(s) e^{-2\pi \iota s t} ds \\ \text{and} \qquad F(s) &= \int_{-\infty}^{\infty} f(t) e^{2\pi \iota s t} dt. \end{aligned} \tag{5.1}$$

where $f(t)$ (function in $t-$space) and $F(s)$ (function in $s-$space) are Fourier transforms of each other. This generalized method of transforming the given function in terms of more suitable variables is widely used in the context of transformations between time-frequency domains and for transformations between position-momentum space [1, 141]. For discretized functions, the integral in Equation (5.1) is replaced by a summation and the resulting expression is termed as a discrete Fourier transformation (DFT),

$$F_s = \frac{1}{\sqrt{N}} \sum_{t=0}^{N-1} \exp\left(\frac{2\pi\iota st}{N}\right) f_t. \tag{5.2}$$

The advent of discrete Fourier transform is particularly important in case of numerical computing, which requires the function to be digitized in order to perform any operations.

Quantum Fourier transformation (QFT) is a special form of the discrete Fourier transform, which is applied to the states of quantum systems and plays an important role in quantum computation. Consider a 'd' level quantum system (qudit) in a set of basis vectors $|x\rangle$. The QFT transforms the basis vectors to another set of basis vectors represented as $|y\rangle$. The action of the QFT on the basis vectors of a hybrid qudit system is given by [144, 145]:

$$\text{QFT}\,|x\rangle = \frac{1}{\sqrt{D}} \sum_{k=0}^{D-1} \exp\left(\frac{2\pi\iota xy}{D}\right) |y\rangle \tag{5.3}$$

where the states $|y\rangle$ have the same form as $|x\rangle$, and $D = \prod_{j=1}^{N} d_j$ is the dimension of $N-$qudit system. The coefficients of the vectors get discrete Fourier transformed. The QFT operator can be explicitly written as a matrix which exhibits a specific pattern in its elements. This matrix creates a linear superposition of the input basis vectors.

QFT is a key ingredient of several quantum algorithms such as factorization [15], quantum phase estimation [146] and the hidden subgroup problem [147]. QFT has been experimentally implemented by several groups on different physical systems [13, 148, 149, 150, 151]. A hybrid-qudit QFT implementation is hence an important step towards the realization of qudit-based quantum computers. Decompositions of the QFT for qudit systems have been worked out by several groups [14, 145, 152, 153]. In this chapter the quantum computing protocols for hybrid qudit systems (a system of coupled qudits of different dimensions) is discussed on a qubit-qubit-qutrit based NMR quantum information processor.

Qudits in NMR are not trivial to realize. Quantum computation with naturally existing NMR qudits demands the manipulation of coupled quadrupolar nuclei under radio frequency fields. Small decoherence times of the quadrupolar nuclei make it difficult to perform computational tasks efficiently. Also in the isotropic environment of liquid state NMR techniques, effective quadrupolar moments average to zero due to which several aspects of the quadrupolar nuclei remain hidden which hinders the quantum computational tasks. However providing anisotropic medium to these qudits further decrease their decoherence times due to which the state of the system decoheres much faster. Faster decoherence rates become unafordable for certain computational tasks, thus adding inefficacy to computing with hybrid-qudit systems. Qudits are also realized in NMR by orienting magnetically equivalent qubits in an anisotropic environment. Magnetically equivalent nuclei exhibit dipolar coupling in the anisotropic environment due to which the otherwise degenerate transitions get separated out in the frequency space. An analogy is drawn between this splitting obtained in the magnetically equivalent nuclei and that of the effective quadrupolar splitting [39, 42] of quadrupolar nuclei. Thus a set of magnetically equivalent qubits mimic qudits in NMR. In this chapter a slightly different way to realize coupled NMR qudits is adopted. A naturally existing system of four qubits with specific degenerate transitions is used, that gives rise to a spectrum resembling that of a qubit-qubit-qutrit system. In this chapter, the experimental implementation of the hybrid qudit QFT on an NMR quantum emulator is described, using four qubits to emulate a single qutrit coupled to two qubits.

5.1 QFT Decompositions

The state of a system of N hybrid qudits each of a different dimension d_p ($p = 1 \cdots N$) can be written in terms of an orthonormal basis of product states

$$\begin{aligned} |x\rangle &= |x_0\rangle \otimes |x_1\rangle \otimes \cdots \otimes |x_{N-1}\rangle \\ &\equiv |x_0 \cdots x_j \cdots x_k \cdots x_{N-1}\rangle \end{aligned} \tag{5.4}$$

where $x_j \in \{0, 1, \ldots d_p\}$. For $d_p = d = 2$, this reduces to an N qubit state, with $x = \sum_{j=0}^{N-1} x_{N-1-j} 2^{N-1-j}$, and $x_j \in \{0, 1\}$ being binary integers. However, x does not retain this simple form for hybrid qudits with $d_p > 2$.

5.1.1 Qudit Gates

The quantum Fourier transform (QFT) of a qudit is a unitary transformation possessing a quantum circuit decomposition [154] in terms of single-qudit and two-qudit quantum gates. A set of hybrid quantum gates have been designed to act on qudits of different dimensions, including the hybrid SUM, SWAP, Toffoli and Fredkin gates [144, 155].

The Fourier gate (F_p) is a single-qudit gate that creates a superposition of all basis states of the qudit with equal amplitudes, with its action on the p^{th} qudit in an N-qudit system given by [144, 145]:

$$\begin{aligned} F_p|x_j\rangle &= \frac{1}{\sqrt{d}}\sum_{y_k=0}^{d-1}\exp\left(\frac{2\pi\iota x_j y_k}{d}\right)|y_k\rangle \\ & \quad x_j, y_k \in [0,1,2,\ldots(d-1)] \end{aligned} \tag{5.5}$$

For $d = 2$ (qubit) and $d = 3$ (qutrit) the Fourier gate reduces to the Hadamard gate (H) and the Chrestenson gate (Ch) respectively:

$$\begin{aligned} H &= \frac{1}{\sqrt{2}}\begin{pmatrix} 1 & 1 \\ 1 & -1 \end{pmatrix} \\ Ch &= \frac{1}{\sqrt{3}}\begin{pmatrix} 1 & 1 & 1 \\ 1 & e^{\frac{2\pi\iota}{3}} & e^{\frac{4\pi\iota}{3}} \\ 1 & e^{\frac{4\pi\iota}{3}} & e^{\frac{2\pi\iota}{3}} \end{pmatrix} \end{aligned} \tag{5.6}$$

For a system of N "hybrid" qudits, each of different dimensions $d_1, d_2, \cdots d_N$, the action of a two-qudit hybrid controlled-rotation gate $R^H_{j,k}$ (with j being the control qudit and k the target qudit) is given by [144, 155]:

$$\begin{aligned} & R^H_{j,k}|x_0\cdots x_j\cdots x_k\cdots x_{N-1}\rangle = \\ & \qquad \exp\left(\frac{-2\pi\iota x_j x_k}{\prod_{p=j}^{k} d_p}\right)|x_0\cdots x_j\cdots x_k\cdots x_{N-1}\rangle \end{aligned} \tag{5.7}$$

where d_p is the dimension of the p^{th} qudit; $k > j$ has been assumed here, in order to explicitly define the action of the gate on the N-qudit basis state, however interchanging j and k does not alter the gate operation. For $d_p = d = 2$, the hybrid two-qudit controlled-rotation gate reduces to the standard two-qubit controlled-rotation gate $R_{j,k}$.

5.1.2 Hybrid Qudit QFT

A system of hybrid qudits is composed of coupled qudits of different dimensions. The circuit for implementing the QFT on N hybrid qudits can be decomposed as a set of single-qudit Fourier gates interspersed with two-qudit controlled-rotation gates: $F_1 R^H_{1,2} R^H_{1,3} \cdots R^H_{1,N} F_2 R^H_{2,3} \cdots F_{N-1} R^H_{N-1,N} F_N$. For N qudits each of a different dimension d_j, the total dimension of the Hilbert space is $D = \prod_{j=1}^{N} d_j$, and it has to be kept in mind while implementing hybrid controlled-rotation gates that the dimensions of the control and target qudits may be different. After the implementation of the QFT using the above decomposition, the bit values of the resultant state appear in the reverse order. A sequence reversal can be achieved by applying a series of multi-valued permutation gates [156].

5.2 An ideal QQT emulator

A QQT system consists of a qutrit coupled to two qubits. This section characterizes a four qubit (QQQQ) system that emulates a QQT system. Considering a QQT system governed by the Hamiltonian [39, 42]

$$\begin{aligned} H^{\mathrm{QQT}} = \omega_1 I_{1z} + \omega_2 I_{2z} + \Omega_3 S_{3z} + D_Q(3S_{3z}^2 - S^2) + J_{12} I_{1z} I_{2z} \\ + J'_{23} I_{2z} S_{3z} + J'_{13} I_{1z} S_{3z} \end{aligned} \tag{5.8}$$

where 1, 2 and 3 label the qubits and the qutrit respectively, $I_{iz}(S_{iz})$ is the z-component of the magnetization vector of the i^{th} qubit(qutrit), $S_3^2 = \sum_j S_{3j}^2$, $j = x, y, z$ is the total magnetization of the qutrit, and $\omega_1, \omega_2, \Omega_3$ denote their Larmor frequencies i.e. the free precession of the qubits(qutrit) in a static magnetic field. D_Q represents the effective quadrupolar splitting of the qutrit levels. J_{ij}s denote the scalar coupling strengths between i^{th} and j^{th} qubits, and J'_{ij} represents an interaction term involving the qutrit.

Comparing the QQT system that belongs to $2 \times 2 \times 3$ dimensional Hilbert space with a system of four coupled qubits (QQQQ) that spans $2 \times 2 \times 2 \times 2$ dimensional Hilbert space. The Hamiltonian of a four-qubit QQQQ system is given by

$$\begin{aligned} H^{\mathrm{QQQQ}} = \omega_1 I_{1z} + \omega_2 I_{2z} + \omega_3 I_{3z} + \omega_4 I_{4z} + J_{12} I_{1z} I_{2z} + J_{13} I_{1z} I_{3z} \\ + J_{14} I_{1z} I_{4z} + J_{23} I_{2z} I_{3z} + J_{24} I_{2z} I_{4z} + J_{34} I_{3z} I_{4z} \end{aligned} \tag{5.9}$$

Assuming a model four qubit system in which two of the qubits are magnetically inequivalent and are not coupled to each other, however each of them is coupled to rest of the spins with same coupling strength. Under these conditions, $J_{13} = J_{14} = J^{'}_{13}$, $J_{23} = J_{24} = J^{'}_{23}$ and $J_{34} = 0$). Spins 3 and 4 of the four-qubit system are used to mimic a qutrit, such that the qutrit subspace containing levels 1,2 is emulated by the third qubit and the qutrit subspace with levels 2,3 is emulated by the fourth qubit. Comparing Equations (5.8) and (5.9), chemical shifts of third and fourth qubits are denoted as $\omega_3 = \Omega_3 + D_Q$ and $\omega_4 = \Omega_3 - D_Q$. The Hamiltonian of the four-qubit QQQQ system thus reduces to

$$\begin{aligned} H^{\mathrm{QQQQ}} = \omega_1 I_{1z} + \omega_2 I_{2z} + (\Omega_3 + D_Q) I_{3z} + (\Omega_3 - D_Q) I_{4z} + J_{12} I_{1z} I_{2z} \\ + J^{'}_{23} I_{2z}(I_{3z} + I_{4z}) + J^{'}_{13} I_{1z}(I_{3z} + I_{4z}) \end{aligned} \tag{5.10}$$

where all the terms have their usual meaning. Comparing the QQT and the QQQQ emulator Hamiltonians, it is found that free evolution of the qutrit (Equation (5.8)) under the effect of its own chemical shift and quadrupolar effects is equivalent to the chemical shift evolutions of qubits 3 and 4 (Equation (5.10)) at frequencies $\Omega_3 + D_Q$ and $\Omega_3 - D_Q$ respectively.

A four qubit system with such a configuration, gives rise to degenerate transitions in the NMR spectrum. Each of the qubits 1 and 2, have two pairs of degenerate transitions, thus accounting for six transitions each, while qubits 3 and 4 together possess a total of eight degenerate pairs of transitions. The spectrum thus resembles the first order NMR spectrum of a QQT system (wherein each qubit multiplet contains six transitions and the qutrit multiplet contains eight transitions). However the pattern of intensities in the four qubit QQT-emulator differs from that of an actual QQT system. Each qubit in the QQT system gives rise to six spectral lines of equal intensities while in a four qubit QQT-emulator, the two lines of each multiplet (belonging to qubits 1 and 2) are of double the intensity. Figure 5.1 shows the energy level diagram of the four-qubit QQT emulator (energy levels numbered from 1-16) and an actual QQT system (energy levels numbered from 1-12). The energy levels are labeled in the computational bases consisting of $\{|0\rangle, |1\rangle\}$ for a qubit and $\{|0'\rangle, |1'\rangle, |2'\rangle\}$ for a qutrit. All the single-quantum transitions belonging to qubits 1 and 2 in Figure 5.1(a) are shown in blue and brown colors respectively, and those corresponding to the third and fourth qubits are shown in purple. Figure 5.1(b) exhibits the corresponding single quantum transitions of the QQT system.

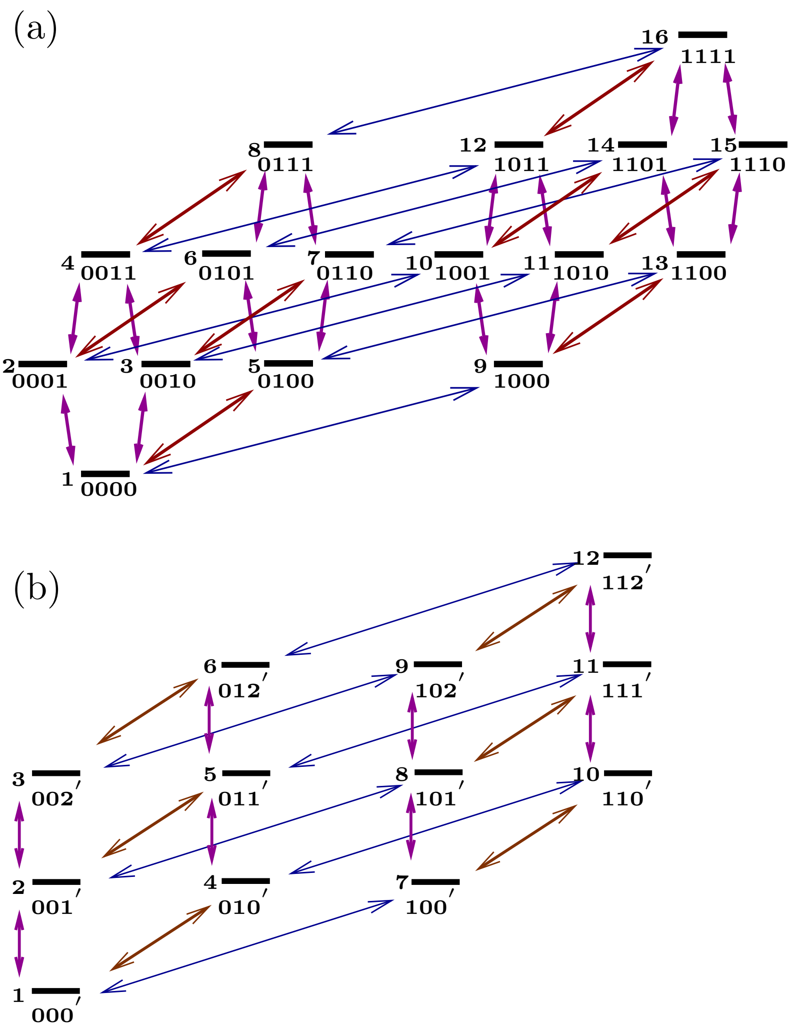

Figure 5.1: Energy eigenstates labeled in the computational basis and the possible single quantum transitions are shown for a QQQQ and a QQT system. (a) A QQQQ system showing 16 energy levels corresponding to four coupled spin-$1/2$ particles. Each energy level is labeled by the spin state 0, 1. There are 32 single quantum transitions. Transitions belonging to spins 1 and 2 are shown in blue and brown respectively while transitions belonging to spins 3 and 4 are shown in purple. (b) A hybrid QQT system showing 12 energy levels and 20 transitions with energy levels labeled in the computational basis; $0^{'}$, $1^{'}$ and $2^{'}$ correspond to the qutrit spin states $+1$, 0 and -1 respectively. Each qubit undergoes six single spin flips shown in blue (spin 1) and brown (spin 2) respectively. Qutrit transitions are shown in purple.

5.3 NMR Implementation

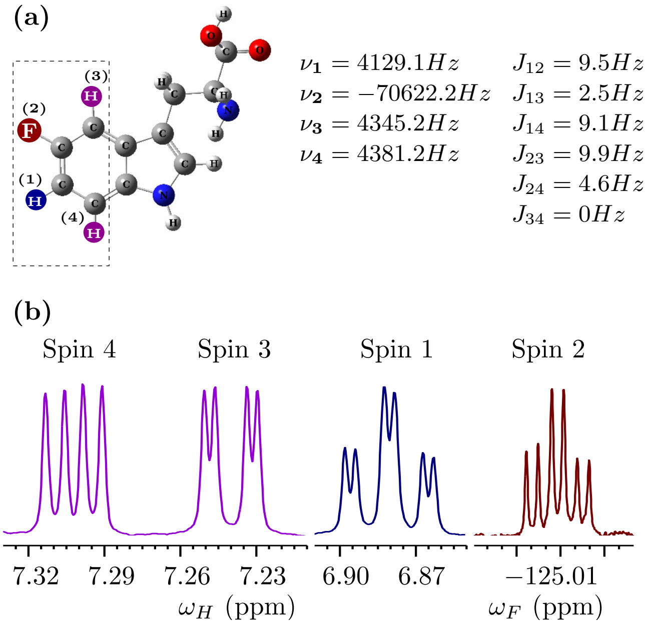

Figure 5.2: (a) Molecular structure of 5-Fluorotryptophan acting as a QQT emulator The qubits of interest (three ^{1}H nuclei and one ^{19}F nucleus) are shown inside the dotted rectangular block and numbered from 1-4. Qubits numbered 3 and 4 shown in same color, together mimic a qutrit. The chemical shift values (in ppm) and indirect coupling constants (in Hz) are tabulated alongside. (b) NMR spectrum of the thermal state of 5-Fluorotryptophan. The ^{1}H and ^{19}F spectra are shown on the same scale. Colors of the spectral lines correspond to the spin color given in the molecular structure. The spins resonate at the frequencies ω_1, ω_2 and ω_3, with J_{ij} corresponding to the scalar coupling constant between spins i, j.

A four-qubit system satisfying all the constraints described in section 5.2 is not straightforward to achieve. However in NMR, one can re-interpret the actual values of coupling strengths in terms of the effective coupling strengths by tailoring the coupling-evolution intervals. We use a 5-Fluorotryptophan molecule to emulate the QQT system. Tryptophan is an amino acid consisting of an aromatic ring with four hydrogen atoms, one of which is replaced by a ^{19}F. These three ^{1}H nuclei and one ^{19}F represent a system of four qubits. However, two ^{1}H nuclei which are at para positions with respect to each other, have vanishing coupling strength, due to which this fluorinated amino acid exhibits degeneracy in certain resonance frequencies. The number of resolved resonance frequencies in this molecule is exactly same as that of required for a QQT system. Besides, a peculiar coupling pattern makes 5-Fluorotryptophan a system which is very close to a QQT emulator.

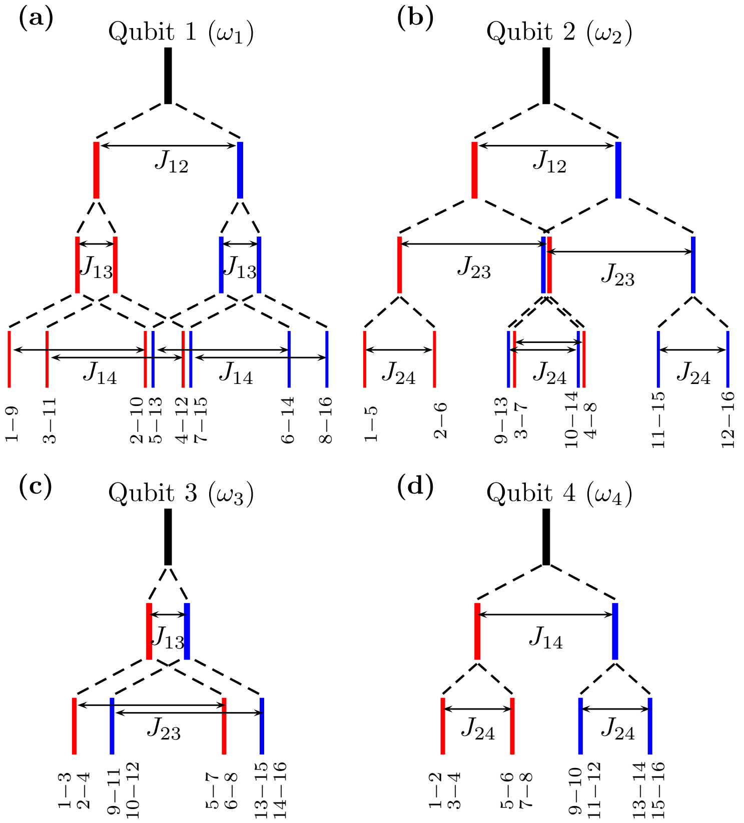

Figure 5.3: The multiplet pattern of the NMR spectral lines corresponding to each of the four qubits under the effect of the magnetic field manipulations at local scales. Part (a) represents the splitting pattern of first qubit due to scalar coupling constants J_{12}, J_{13}, J_{14}, (b) second qubit due to J_{12}, J_{23}, J_{24}, (c) third qubit due to J_{12}, J_{23} and (d) fourth qubit under the effect of J_{14}, J_{24} of the four-qubit NMR emulator. The ratio of coupling constants $J_{12} : J_{13} : J_{14}$, $J_{12} : J_{23} : J_{24}$, $J_{13} : J_{23}$ and $J_{14} : J_{24}$ is the same as in the 5-Fluorotryptophan molecule. The line thickness is proportional to the spectral line intensity. Labels below each line refer to the corresponding transition as marked in Figure 5.1(a).

The molecular structure and NMR parameters of QQQQ emulator are depicted in Figure 5.2(a) and the thermal equilibrium 1D NMR spectrum is shown in Figure 5.2(b). The T_1 and T_2 relaxation times for all four qubits range between 1.17 - 3.96 s and 0.82

- 2.28 s respectively. The coupling pattern of 5-Fluorotryptophan is not in accordance with the constraints of the ideal QQT emulator. However this point is resolved by considering the effective $J-$ values and not the actual ones (while implementing the required gates). The multiplet patterns of all the four qubits of 5-Fluorotryptophan are shown in Figure 5.3, leading to a spectrum resembling a QQT system. For an ideal QQT emulator, the lines of the i^{th} qubit occurring at $\omega_i \pm J_{i3} \mp J_{i4}$ overlap with each other, while in the 5-Fluorotryptophan molecule, $J_{i3} \neq J_{i4} (i \in [1,2])$ and the lines occurring at $\omega_i \pm J_{i3} \mp J_{i4}$ are separated by $2 \mid J_{i3} - J_{i4} \mid$. Labels below each spectral line refer to the corresponding transitions as per Figure 5.1(a). Each multiplet is centered around its chemical shift value (black lines representing $\omega_1, \omega_2, \omega_3$ and ω_4 respectively), which is further split by scalar coupling interaction. The ratio of coupling constants $J_{12} : J_{13} : J_{14}$, $J_{12} : J_{23} : J_{24}$, $J_{13} : J_{23}$ and $J_{14} : J_{24}$ is the same as in the 5-Fluorotryptophan molecule. The line thickness is proportional to the spectral line intensity. The mapping between the transitions (labeled Q1, Q2, T) of the QQT system and the four-qubit QQT emulator (labeled q1, q2, q3, q4) is given in Table 5.1.

Table 5.1: Mapping between the transition frequencies of a QQT system (labeled Q1, Q2 and T) and a four-qubit QQQQ system (labeled q1, q2, q3, q4) which acts as QQT emulator.

Q1	q1	Q2	q2	T	q3, q4
1-7	1-9	1-4	1-5	1-2	1-3, 2-4
2-8	2-10, 3-11	2-5	2-6, 3-7	2-3	1-2, 3-4
3-9	4-12	3-6	4-8	4-5	5-7, 6-8
4-10	5-13	7-10	9-13	5-6	5-6,7-8
5-11	6-14, 7-15	8-11	10-14, 11-15	7-8	9-11, 10-12
6-12	8-16	9-12	12-16	8-9	9-10, 11-12
–	–	–	–	10-11	13-15, 14-16
–	–	–	–	11-12	13-14, 15-16

5.3.1 Experimental implementation of the QFT

Experimental implementation of the hybrid QFT on a QQT emulator was carried out on a 5-Fluorotryptophan molecule dissolved in D_2O. The experiments were performed on a 600 MHz Avance III NMR spectrometer equipped with a triple resonance QXI probehead . The corresponding ^{19}F nuclei resonates at 564 MHz.

Hybrid qudit gates are interpreted in the form of radio frequency pulses for their NMR experimental implementation. The hybrid QFT for a QQT system is implemented by the sequence of gates:

$$QFT^{hyb} = H_1 R_{12} R^H_{13} H_2 R^H_{23} Ch_3. \tag{5.11}$$

The explicit forms of these gates are given in Equations 5.6, 5.7. The sequential implementation of these gates as applied from left to right results in the desired quantum Fourier transformation operator. The NMR pulse sequences for the hybrid QFT gate implementations are given in Table 5.2.

Table 5.2: NMR pulse sequences implementing the hybrid qudit QFT operations. Second and third columns contain the sequence of rotations that implement the quantum gates given in first column. Spins in QQT system are labeled as (Q_1, Q_2, T), while defining a single spin operation.

Gate	QQT system	Four qubit QQT emulator
H_1	$\left(\frac{\pi}{2}\right)^{Q_1}_y$	$\left(\frac{\pi}{2}\right)^{1}_y$
R_{12}	$\frac{1}{2J_{12}}\left(\frac{\pi}{2}\right)^{Q_1,Q_2}_z$	$\frac{1}{2J_{12}}\left(\frac{\pi}{2}\right)^{1,2}_z$
R^H_{13}	$\left(\frac{\pi}{3}\right)^{Q_1}_z\left(\frac{\pi}{6}\right)^{T}_z\frac{1}{6J'_{13}}$	$\left(\frac{\pi}{3}\right)^{1}_z\left(\frac{\pi}{6}\right)^{3,4}_z\frac{1}{6J_{13}}\frac{1}{6J_{14}}$
H_2	$\left(\frac{\pi}{2}\right)^{Q_2}_y$	$\left(\frac{\pi}{2}\right)^{2}_y$
R'_{23}	$\left(\frac{2\pi}{3}\right)^{Q_2}_z\left(\frac{\pi}{3}\right)^{T}_z\frac{1}{3J'_{23}}$	$\left(\frac{2\pi}{3}\right)^{2}_z\left(\frac{\pi}{3}\right)^{3,4}_z\frac{1}{3J_{23}}\frac{1}{3J_{24}}$
Ch_3	$\left(\frac{\pi}{2}\right)^{T}_y$	$\left(\frac{\pi}{2}\right)^{3,4}_y$

As shown in the Table 5.2, the pulse sequences for the hybrid gates implementation is contained in column2. Column3 contains the respective pulse sequences corresponding to the hybrid QFT implementation on a four-qubit QQT emulator. The operations on the qutrit of the QQT system can be translated to operations on qubits 3,4 of the

QQQQ system (QQT emulator). The NMR pulse sequence for the experimental implementation of a hybrid qudit QFT on the four-qubit QQT NMR emulator is shown in Figure 6.2. A hybrid controlled-rotation gate $R^H_{j,k}$ (where 'j' is the control-qubit and 'k' is the target qutrit) can be realized by a z-rotation of the qutrit state by an angle $\frac{2\pi x_j x_k}{\prod_{m=j}^{k} d_m}$ ($j \in [0,1]$, $k \in [0,1,2]$). For the two qubits mimicking a qutrit, this controlled-rotation can be obtained by rotating both the qubits by the same angle with respect to the control qubit. Chemical shift offsets are chosen such that spins 1 and 2 always remain on resonance.

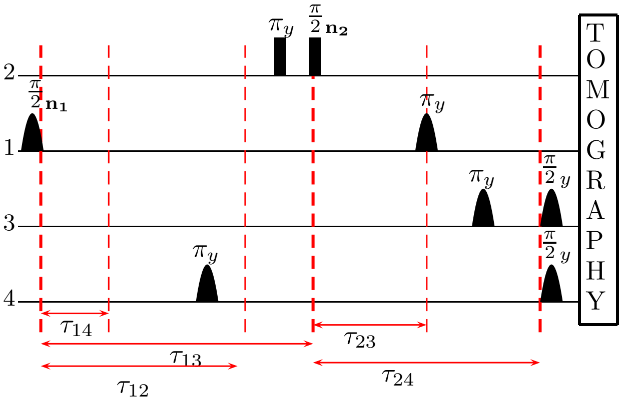

Figure 5.4: NMR pulse sequence for a hybrid qubit-qubit-qutrit QFT implementation on a four-qubit QQT emulator. Flip angles and axes of rotation are displayed over each pulse. Rotation axes $\mathbf{n_1}$ and $\mathbf{n_2}$ are aligned at angles $\theta_1 = \frac{\pi}{2} + \frac{5\pi}{6}$ and $\theta_2 = \frac{\pi}{2} + \frac{2\pi}{3}$ with respect to the x-axis. The shaped pulses represent selective pulses while black rectangles represent non-selective pulses; τ_{ij}s represent time intervals of evolution under the scalar couplings J_{ij}.

The motive of this hybrid QFT implementation is to observe the periodicity of the transformation matrix, as reflected in the final state of the system of interest. The full periodic pattern is seen if one begins with all possible pseudo-pure states of the hybrid qudit system. As an example, if one begins with the QQT state $|000\rangle$ in the computational basis, the resultant state is a coherent superposition of all the basis vectors. For any other initial state, the resultant state is a superposition of all the basis vectors alongwith certain phase differences that are responsible for the pattern. The action of the QFT in extracting state periodicity can be equally well demonstrated on an initial thermal equilibrium state as on a pseudo-pure state and hence the QFT on a thermal equilibrium state [13] is demonstrated in this chapter. Beginning with the thermal equilibrium density operator, the first $\left(\frac{\pi}{2}\right)^{1}_{\mathbf{n_1}}$ pulse implements a Hadamard gate on the first qubit. The axis of rotation $\mathbf{n_1} = \cos\theta_1\hat{x} + \sin\theta_1\hat{y}$ (aligned at an angle of $\theta_1 = \frac{\pi}{2} + \frac{5\pi}{6}$ with the x-axis) was chosen to obtain a $z-$rotation of the first qubit by an angle $\frac{5\pi}{6}$, thereby circumventing the high time cost involved in implementing $z-$rotations. At this point in the pulse sequence, the qubits 2, 3 and 4 do not have any coherence, and thus single spin $z-$rotations are redundant in their case. The first evolution period incorporates the controlled-rotation gates $R_{1,2}$ and $R^{H}_{1,3}$ for a time $\tau_{ij} = \frac{\theta_{ij}}{\pi J_{ij}}$ (θ_{ij} is the desired rotation angle). The evolutions under the scalar coupling J_{12} by an angle $\frac{\pi}{2}$, under the scalar coupling J_{13} by an angle $\frac{\pi}{6}$, and under the scalar coupling J_{14} by an angle $\frac{\pi}{6}$ are achieved simultaneously during the first evolution period. Refocusing pulses are introduced at appropriate points to obtain the desired rotation angles. The next module of the hybrid QFT begins with a $\left(\frac{\pi}{2}\right)^{2}_{\mathbf{n_2}}$ pulse that implements a Hadamard gate along with producing an effective $z-$rotation of $\frac{2\pi}{3}$ on the second qubit (the axis $\mathbf{n_2}$ is chosen to make an angle of $\theta_2 = \frac{\pi}{2} + \frac{2\pi}{3}$ with the x-axis). This is followed by an evolution under the couplings J_{23} and J_{24} during the second evolution interval. The effect of evolution on the first spin is refocused by a pulse in the middle of the evolution period. The final Hadamard gate on the third and fourth qubits is performed by a $\left(\frac{\pi}{2}\right)^{3,4}_{y}$ pulse (which effectively mimics a single-qutrit Fourier gate). All pulses on qubit 1 are Gaussian pulses of 13 ms duration and the simultaneous excitation of qubits 3 and 4 is achieved using a 7 ms shaped pulse (*Seduce.100*). Qubit 2 corresponds to ^{19}F, which is being modulated by a different channel, thus all the pulses of second qubit are hard pulses. Since qubits 3 and 4 are only 36 Hz apart it is difficult to individually address them in an experiment, and hence the controlled-rotation gates on these two qubits have been implemented without applying individual refocusing pulses on them. This leads to certain deviations from the expected pattern of the final QFT state.

5.3.2 Tomographic reconstruction

It is known that an arbitrary quantum state of a $d-$level quantum system requires the specification of $d^2 - 1$ independent variables to be described completely as described in Section 1.2.3. In NMR quantum computation, one obtains single quantum coherences in the form of first-order NMR spectrum. Thus the method of quantum state tomography (QST) involves the projection of the information contained in the populations and higher order coherences onto the single quanta through various experiments. Single quantum terms of the density operator are complex numbers which correspond to the respective spectral lines of the NMR spectrum. A purely absorptive spectral line correspond to a purely real number while a dispersive spectral line correspond to a purely imaginary number representing single quantum term. An arbitrary phase of the spectral line contains both absorptive as well as dispersive parts and thus represents a complex number. These real and imaginary parts of the complex number corresponding to a single quantum term are obtained by measuring the intensities of the spectral line without any phase correction and with a zero order phase change of (-90^0) respectively. However, in this very system of four qubits, the baseline becomes quite distorted at the end of the desired gate implementation. This leads to a genuine problem of finding the spectral intensities. The solution to this problem is obtained by considering the complex numbers in polar coordinates. Thus the task consists of finding the total intensity of the line and its phase difference with respect to a purely absorptive line. Total intensity of a line is proportional to the number of spins responding to a particular gate operation. This is obtained by making the line purely absorptive by zero order phase correction before measuring its intensity. The intensities of all the spectral lines are obtained in this way, thus reducing the errors due to baseline imperfections. The information regarding the phase is retained by measuring the angular twist provided, while making the spectral line purely absorptive. Thus one obtains 'r' in the form of normalized total intensity of a spectral and the phase 'θ' as the phase difference between the actual line and the corresponding purely absorptive line, resulting in a complex number '$re^{\iota\theta}$' corresponding to each spectral line.

QQT tomography scheme

Partial tomography of the QQQQ system was performed in order to reconstruct the desired QQT density matrix. First, a set of operators were designed to reconstruct the full QQT density operator in $d \times d$ dimensional Liouville space (in this case $d = 2 \otimes 2 \otimes 3$). This set of operators was then extended to the analogous set of tomography operations in a 16×16 dimensional operator space of the four-qubit NMR emulator.

The complete characterization of a 12×12 dimensional QQT density operator requires the determination of 143 variables. The 11 diagonal elements (populations) are obtained by applying an appropriate z-gradient to kill off-diagonal elements, followed by spin-selective rotations to project the diagonal elements onto experimentally measurable parts of the density matrix. The remaining 132 elements are obtained by a set of 19 operators: III′, YII′, XII′, IYI′, IXI′, IIY′, IYY′, IXY′, YIY′, XIX′, XXI′, YYI′, XYI′, YXI′, XYY′, XXY′, YXX′, YYX′ and IIλ'-**Grad**$_z$-IIΥ', where I is the identity operator, X(Y) refers to a single spin operator and primed operators correspond to qutrit operations. These operators can be implemented by applying the corresponding spin-selective $\frac{\pi}{2}$ pulses (or a no-operation for the identity operator). The last tomography experiment consists of a z gradient pulse sandwiched between two y pulses represented by λ and Υ applied on the qutrit, of flip angles $(-\frac{\pi}{2})$ and $(\frac{\pi}{4})$ respectively. The tomography scheme is designed to have only the spin-selective rotations, thus for qutrit subspace of the QQT system, three dimensional analogue of the Pauli matrices are used as generators of rotations. The explicit tomography protocol and the QQT state reconstruction are described in Tables 5.3 and 5.4.

Table 5.3: A set of experiments performing partial tomography of a qubit-qubit-qutrit system alongwith their respective pulse sequences for NMR experimental implementations are shown. The pulse sequences compose of the angular twists with subscript referring to the axis of rotation and the superscript corresponding to the spin number.

S.No.	Experiment	Pulse sequence	S.No.	Experiment	Pulse sequence
1	III′	No operation	11	XXI′	$(\frac{\pi}{2})^1_x\,(\frac{\pi}{2})^2_x$
2	YII′	$(\frac{\pi}{2})^1_y$	12	YYI′	$(\frac{\pi}{2})^1_y\,(\frac{\pi}{2})^2_y$
3	XII′	$(\frac{\pi}{2})^1_x$	13	XYI′	$(\frac{\pi}{2})^1_x\,(\frac{\pi}{2})^2_y$
4	IYI′	$(\frac{\pi}{2})^2_y$	14	YXI′	$(\frac{\pi}{2})^1_y\,(\frac{\pi}{2})^2_x$
5	IXI′	$(\frac{\pi}{2})^2_x$	15	XYY′	$(\frac{\pi}{2})^1_x\,(\frac{\pi}{2})^2_y\,(\frac{\pi}{2})^3_y$
6	IIY′	$(\frac{\pi}{2})^3_y$	16	XXY′	$(\frac{\pi}{2})^1_x\,(\frac{\pi}{2})^2_x\,(\frac{\pi}{2})^3_y$
7	IYY′	$(\frac{\pi}{2})^2_y\,(\frac{\pi}{2})^3_y$	17	YXX′	$(\frac{\pi}{2})^1_y\,(\frac{\pi}{2})^2_x\,(\frac{\pi}{2})^3_x$
8	IXY′	$(\frac{\pi}{2})^2_x\,(\frac{\pi}{2})^3_y$	18	YYX′	$(\frac{\pi}{2})^1_y\,(\frac{\pi}{2})^2_y\,(\frac{\pi}{2})^3_x$
9	YIY′	$(\frac{\pi}{2})^1_y\,(\frac{\pi}{2})^3_y$	19	IIλ'-Grad$_z$-IIΥ'	$-(\frac{\pi}{2})^3_y\,G_z\,(\frac{\pi}{4})^3_y$
10	XIX′	$(\frac{\pi}{2})^1_x\ \frac{\pi}{2}{}^3_x$			

Table 5.4: Terms of the QQT density matrix obtained from various experiments.

This table contains the description of various terms as obtained from the given set of experiments for QQT tomography. Second column contains the elements of the QQT density operator written as $\rho_{r,c}$ (r is the row number and c is the column number), third column contains the list of QQT experiments used to determine the respective elements (as per column 2) and last column contains the number of variables (η) found by the corresponding combination of experiments.

	Elements of ρ^{QQT}	Experiment (as per Table 5.3)	η
1	$\rho_{1,2}$; $\rho_{1,4}$; $\rho_{1,7}$; $\rho_{2,3}$; $\rho_{2,5}$; $\rho_{2,8}$; $\rho_{3,6}$; $\rho_{3,9}$; $\rho_{4,5}$; $\rho_{4,10}$; $\rho_{5,6}$; $\rho_{5,11}$; $\rho_{6,12}$; $\rho_{7,8}$; $\rho_{7,10}$; $\rho_{8,9}$; $\rho_{8,11}$; $\rho_{9,12}$; $\rho_{10,11}$; $\rho_{11,12}$	Exp-1	40
2	$\rho_{1,8}$; $\rho_{1,10}$; $\rho_{2,7}$; $\rho_{2,9}$; $\rho_{2,11}$; $\rho_{3,8}$; $\rho_{3,12}$; $\rho_{4,7}$; $\rho_{4,11}$; $\rho_{5,8}$; $\rho_{5,10}$; $\rho_{5,12}$; $\rho_{6,9}$; $\rho_{6,11}$	Exp-2, Exp-3	28
3	$\rho_{1,5}$; $\rho_{2,4}$; $\rho_{2,6}$; $\rho_{3,5}$; $\rho_{7,11}$; $\rho_{8,10}$; $\rho_{h,12}$; $\rho_{9,11}$	Exp-4, Exp-5	16
4	$\rho_{1,3}$; $\rho_{4,6}$; $\rho_{7,9}$; $\rho_{10,12}$	Exp-6, Exp-19	8
5	$\rho_{1,9}$; $\rho_{3,7}$; $\rho_{4,12}$; $\rho_{6,10}$	Exp-9, Exp-10	8
6	$\rho_{1,11}$; $\rho_{2,10}$; $\rho_{4,8}$; $\rho_{5,7}$	Exp-11, Exp-12, Exp-13, Exp-14	8
7	$\rho_{2,12}$; $\rho_{3,11}$; $\rho_{5,9}$; $\rho_{6,8}$	Exp-11, Exp-12, Exp-13, Exp-14	8
8	$\rho_{1,6}$; $\rho_{3,4}$; $\rho_{7,12}$; $\rho_{9,10}$	Exp-7, Exp-8	8
9	$\rho_{1,12}$; $\rho_{3,10}$; $\rho_{4,9}$; $\rho_{6,7}$	Exp-15, Exp-16, Exp-17, Exp-18	8

The set of experiments described in Table 5.3 transfer various elements of the QQT density operator at the positions of single quanta, that are directly observable in the respective first order NMR spectra. The detailed description of the subsets of experiments determining various elements is given in Table 5.4. Once all the variables are obtained complete QQT density operator is constructed.

Correspondence between the QQT and QQQQ density matrices

In this chapter a QQT state was reconstructed after Quantum Fourier Transform on the thermal equilibrium state, thus there are no diagonal elements. The first-order NMR spectrum of the four qubit system (actual QQT emulator) matches with that of the QQT system, and the above set of experiments project all the information of the state on these single quantum lines alone. Thus as per mapping between the spectral lines of QQT system and four-qubit QQT emulator described in Table 5.1 and Figure 5.3, the intensities of the spectral lines of QQT system are obtained. An analysis is conducted explicitly to present the correspondence between the spectral lines of QQT system and that of the QQT emulator. There are some unwanted degenerate transitions (as in the actual emulator $J_{i3} \neq J_{i4}$ and thus lines at $\omega_i \pm J_{i3} \mp J_{i4}$ are not degenerate) in qubits 1 and 2 of the actual QQT emulator which is circumvented by using the constraint that lines at $\omega_i \pm J_{i3} \mp J_{i4}$ are of equal intensity. This assumption fits for the final QFT density matrix as well as for the various tomography pulses. Therefore mapping all the 20 lines of the NMR spectrum of the actual QQT emulator onto those of the expected lines of a QQT system, one obtains various elements of the QQT density matrix. Thus using the information gained from single quantum terms of the QQQQ system at the end of various tomography experiments, a 12×12 QQT density matrix is reconstructed.

Considering the intensities of spectral lines corresponding to a QQQQ system being designated as ‘Int(s,t)’, where ‘s’ and ‘t’ are the labels of the energy levels as per Figure 5.1. Single quantum line intensities (Int) of QQT system are obtained from the linear combinations of single quantum line intensities of QQQQ system. The detailed list is given below, where intensities of the transitions on left hand side correspond to the QQT system and those on the right hand side correspond to the QQQQ system.

Spin-1 (qubit)

1. Int(1-7) = Int(1-9)
2. Int(2-8) = Int(3-11)
3. Int(3-9) = Int(4-12) + Int(7-15) - Int(6-14); (assumption: Int(6-14) = Int(7-15))
4. Int(4-10) = Int(2-10) + Int(5-13) - Int(3-11); (assumption: Int(2-10) = Int(3-11))
5. Int(5-11) = Int(6-14)
6. Int(6-12) = Int(8-16)

Spin-2 (qubit)

1. Int(1-4) = Int(1-5)
2. Int(2-5) = Int(2-6)
3. Int(3-6) = Int(4-8) + Int(10-14) - Int(11-15); (assumption: Int(10-14) = Int(11-15))
4. Int(7-10) = Int(3-7) + Int(9-13) - Int(2-6); (assumption: Int(2-6) = Int(3-7))
5. Int(8-11) = Int(11-15)
6. Int(9-12) = Int(12-16)

Spins-3 & **4 (qutrit)**

1. Int(1-2) = Int(1-3) + Int(2-4)
2. Int(2-3) = Int(1-2) + Int(3-4)
3. Int(4-5) = Int(5-7) + Int(6-8)
4. Int(5-6) = Int(5-6) + Int(7-8)
5. Int(7-8) = Int(9-11) + Int(10-12)
6. Int(8-9) = Int(9-10) + Int(11-12)
7. Int(10-11) = Int(13-15) + Int(14-16)
8. Int(11-12) = Int(13-14) + Int(15-16)

Intensities of NMR spectral lines of a QQT system are obtained in this manner for all the tomography experiments. Various terms of the QQT density operators are obtained from the set of experiments depicted in Table 5.4, thus final QQT density operator is constructed from a given QQQQ system. It is to be noted that the assumptions described while quantitative analysis of the line intensities are taken care of while determining the tomography protocol.

A theoretical QQT density operator (ρ^{QQT}) obtained after QFT implementation on the thermal equilibrium state is shown in Figure 5.5(a). A QQT density operator is simulated corresponding to QFT implementation on the QQQQ system using hybrid qudit gates. During these gate implementations, qubits 3 and 4 are assumed to emulate a qutrit. The final QQT state is reconstructed using the tomography protocol described in previous action. The real and imaginary parts of the resultant density operator ($\rho^{emulator}$) are shown in Figure 5.5(b).

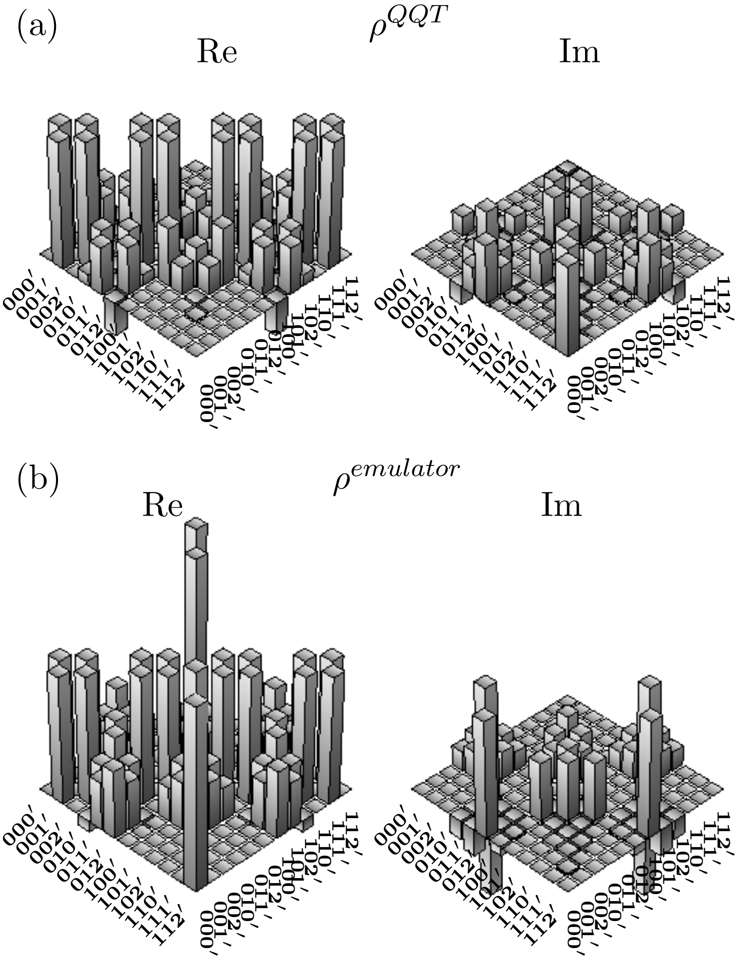

Figure 5.5: Real and imaginary parts of (a) ideal QQT density operator after QFT implementation and (b) QQT density operator simulated by drawing mapping between the spectral lines of QQQQ and QQT systems.

In order to determine the pattern contained after the QFT implementation, it is more convenient to visualize the complex state of the system in polar form. Matrices corresponding to the amplitude and phase parts of the polar form of ρ^{QQT} and $\rho^{emulator}$ are separately analyzed. Comparison of the density matrices showing amplitudes show a complete overlap. The phase differences as shown are found to follow a specific pattern. Thus in the simulated density operator also the pattern is retained in a way. The final state density operators (written in polar form, with the phase given in degrees) of the QQT system (ρ_{amp}^{QQT}, ρ_{ph}^{QQT}) and the 12×12 dimensional reconstructed state of the NMR emulator ($\rho_{amp}^{emulator}$, $\rho_{ph}^{emulator}$), after applying a hybrid QFT on a thermal equilibrium initial state, are detailed below:

$$\rho_{amp}^{QQT} = \begin{pmatrix} 0. & 0.71 & 0. & 0.12 & 0.31 & 0.38 & 0. & 0. & 0. & 0. & 0. & 0.5 \\ 0.71 & 0. & 0.71 & 0.31 & 0.25 & 0.31 & 0. & 0. & 0. & 0. & 0.5 & 0. \\ 0. & 0.71 & 0. & 0.38 & 0.31 & 0.12 & 0. & 0. & 0. & 0.5 & 0. & 0. \\ 0.12 & 0.31 & 0.38 & 0. & 0.71 & 0. & 0.38 & 0.31 & 0.12 & 0. & 0. & 0. \\ 0.31 & 0.25 & 0.31 & 0.71 & 0. & 0.71 & 0.31 & 0.25 & 0.31 & 0. & 0. & 0. \\ 0.38 & 0.31 & 0.12 & 0. & 0.71 & 0. & 0.12 & 0.31 & 0.38 & 0. & 0. & 0. \\ 0. & 0. & 0. & 0.38 & 0.31 & 0.12 & 0. & 0.71 & 0. & 0.12 & 0.31 & 0.38 \\ 0. & 0. & 0. & 0.31 & 0.25 & 0.31 & 0.71 & 0. & 0.71 & 0.31 & 0.25 & 0.31 \\ 0. & 0. & 0. & 0.12 & 0.31 & 0.38 & 0. & 0.71 & 0. & 0.38 & 0.31 & 0.12 \\ 0. & 0. & 0.5 & 0. & 0. & 0. & 0.12 & 0.31 & 0.38 & 0. & 0.71 & 0. \\ 0. & 0.5 & 0. & 0. & 0. & 0. & 0.31 & 0.25 & 0.31 & 0.71 & 0. & 0.71 \\ 0.5 & 0. & 0. & 0. & 0. & 0. & 0.38 & 0.31 & 0.12 & 0. & 0.71 & 0. \end{pmatrix} \tag{5.12}$$

$$\rho_{amp}^{emulator} = \begin{pmatrix} 0. & 0.71 & 0. & 0.12 & 0.31 & 0.75 & 0. & 0. & 0. & 0. & 0. & 1. \\ 0.71 & 0. & 0.71 & 0.31 & 0.12 & 0.31 & 0. & 0. & 0. & 0. & 0. & 0. \\ 0. & 0.71 & 0. & 0.75 & 0.31 & 0.12 & 0. & 0. & 0. & 1. & 0. & 0. \\ 0.12 & 0.31 & 0.75 & 0. & 0.71 & 0. & 0.38 & 0.31 & 0.25 & 0. & 0. & 0. \\ 0.31 & 0.12 & 0.31 & 0.71 & 0. & 0.71 & 0.31 & 0.38 & 0.31 & 0. & 0. & 0. \\ 0.75 & 0.31 & 0.12 & 0. & 0.71 & 0. & 0.25 & 0.31 & 0.38 & 0. & 0. & 0. \\ 0. & 0. & 0. & 0.38 & 0.31 & 0.25 & 0. & 0.71 & 0. & 0.12 & 0.31 & 0.75 \\ 0. & 0. & 0. & 0.31 & 0.38 & 0.31 & 0.71 & 0. & 0.71 & 0.31 & 0.12 & 0.31 \\ 0. & 0. & 0. & 0.25 & 0.31 & 0.38 & 0. & 0.71 & 0. & 0.75 & 0.31 & 0.12 \\ 0. & 0. & 1. & 0. & 0. & 0. & 0.12 & 0.31 & 0.75 & 0. & 0.71 & 0. \\ 0. & 0. & 0. & 0. & 0. & 0. & 0.31 & 0.12 & 0.31 & 0.71 & 0. & 0.71 \\ 1. & 0. & 0. & 0. & 0. & 0. & 0.75 & 0.31 & 0.12 & 0. & 0.71 & 0. \end{pmatrix} \tag{5.13}$$

$$\rho_{ph}^{QQT} =$$

$$\begin{pmatrix}
0. & 0. & 0. & -60. & 30. & 120. & 0. & 0. & 0. & 0. & 0. & 90. \\
0. & 0. & 0. & 30. & 120. & 30. & 0. & 0. & 0. & 0. & 90. & 0. \\
0. & 0. & 0. & 120. & 30. & -60. & 0. & 0. & 0. & 90. & 0. & 0. \\
60. & -30. & -120. & 0. & 0. & 0. & 30. & -60. & -150. & 0. & 0. & 0. \\
-30. & -120. & -30. & 0. & 0. & 0. & -60. & 30. & -60. & 0. & 0. & 0. \\
-120. & -30. & 60. & 0. & 0. & 0. & -150. & -60. & 30. & 0. & 0. & 0. \\
0. & 0. & 0. & -30. & 60. & 150. & 0. & 0. & 0. & -60. & 30. & 120. \\
0. & 0. & 0. & 60. & -30. & 60. & 0. & 0. & 0. & 30. & 120. & 30. \\
0. & 0. & 0. & 150. & 60. & -30. & 0. & 0. & 0. & 120. & 30. & -60. \\
0. & 0. & -90. & 0. & 0. & 0. & 60. & -30. & -120. & 0. & 0. & 0. \\
0. & -90. & 0. & 0. & 0. & 0. & -30. & -120. & -30. & 0. & 0. & 0. \\
-90. & 0. & 0. & 0. & 0. & 0. & -120. & -30. & 60. & 0. & 0. & 0.
\end{pmatrix} \tag{5.14}$$

$$\rho_{ph}^{emulator} =$$

$$\begin{pmatrix}
0. & 0. & 0. & -120. & -30. & 60. & 0. & 0. & 0. & 0. & 0. & 0. \\
0. & 0. & 0. & -30. & -120. & -30. & 0. & 0. & 0. & 0. & 0. & 0. \\
0. & 0. & 0. & 60. & -30. & -120. & 0. & 0. & 0. & 0. & 0. & 0. \\
120. & 30. & -60. & 0. & 0. & 0. & 60. & -30. & -120. & 0. & 0. & 0. \\
30. & 120. & 30. & 0. & 0. & 0. & -30. & 60. & -30. & 0. & 0. & 0. \\
-60. & 30. & 120. & 0. & 0. & 0. & -120. & -30. & 60. & 0. & 0. & 0. \\
0. & 0. & 0. & -60. & 30. & 120. & 0. & 0. & 0. & -120. & -30. & 60. \\
0. & 0. & 0. & 30. & -60. & 30. & 0. & 0. & 0. & -30. & -120. & -30. \\
0. & 0. & 0. & 120. & 30. & -60. & 0. & 0. & 0. & 60. & -30. & -120. \\
0. & 0. & 0. & 0. & 0. & 0. & 120. & 30. & -60. & 0. & 0. & 0. \\
0. & 0. & 0. & 0. & 0. & 0. & 30. & 120. & 30. & 0. & 0. & 0. \\
0. & 0. & 0. & 0. & 0. & 0. & -60. & 30. & 120. & 0. & 0. & 0.
\end{pmatrix} \tag{5.15}$$

Close observation of the polar form of the theoretical and the simulated QQT density operators reveal the pattern created by the QFT operation on the thermal equilibrium state. Theoretical and the simulated density operators differ only along the counter-diagonal elements of the 3×3 block matrices.

5.3.3 Tomographic analysis of the QFT implementation

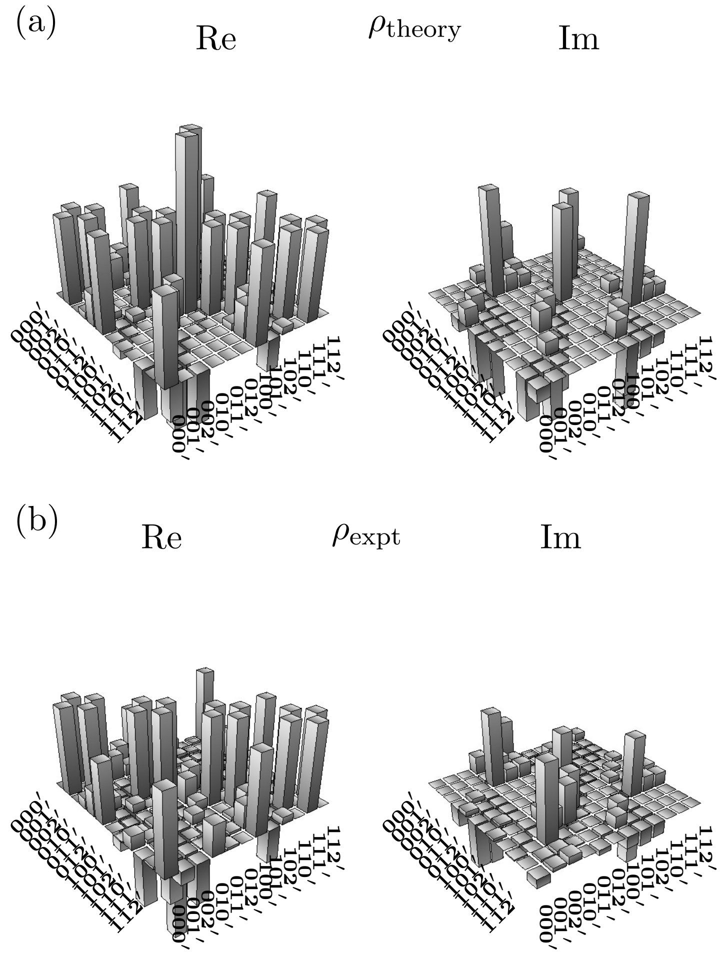

Figure 5.6: Tomographs of the real and imaginary parts of the (a) theoretically expected (ρ_{theory}) and (b) experimentally obtained (ρ_{expt}) final density operator obtained after applying a hybrid QFT on the thermal equilibrium state of the four-qubit QQQQ system used as a QQT emulator. The rows and columns are labeled by the multi-valued logic states ($|000'\rangle$ to $|112'\rangle$) of a QQT system.

A corresponding set of 19 operations can be used to determine the off-diagonal elements of the four-qubit QQQQ system: IIII, YIII, XIII, IYII, IXII, IIYY, IYYY, IXYY, YIYY, XIXX, XXII, YYII, XYII, YXII, XYYY, XXYY, YXXX, YYXX and II$\lambda\lambda$-**Grad**$_z$-II$\Upsilon\Upsilon$. The last tomography experiment on the QQQQ system consists of a z gradient pulse sandwiched between two y pulses represented by λ and Υ, applied simultaneously on qubits 3 and 4 of flip angles $(-\frac{\pi}{2})$ and $(\frac{\pi}{4})$ respectively.

The theoretically expected and experimentally obtained tomographs of the real and imaginary parts of the density matrices obtained after applying a hybrid QFT on the four-qubit QQT NMR emulator are given in Figure 5.6. The theoretically expected state considered here corresponds to the one without refocusing pulse implementations in qubits 3 and 4. On visual inspection, one can see that the general pattern of the weights in the density matrices is quite similar, indicating the success of the QFT implementation. Quantitatively, the fidelity of the reconstructed state was computed using the measure given in Equation (1.6). The fidelity of the experimentally reconstructed density matrix was computed to be 0.83. The loss in fidelity of the experimentally reconstructed state can be attributed to several experimental factors, namely, rf pulse imperfections, imperfect refocusing of chemical shift evolution of unwanted coherences during the evolution intervals and rf field inhomogeneity.

5.4 Concluding remarks

In this chapter, a unique way is adopted for the physical realization of a qudit system suitable for quantum computation. Here a four-spin system is used, which due to its degeneracies cannot be treated as a potential QQQQ system. However its peculiar coupling pattern makes it suitable for qudit computing. Thus the degeneracy in transitions of this four qubit system is used to emulate a qubit-qubit-qutrit system. Further the techniques of computing with NMR qudits is developed. QFT is one of the key quantum circuits in several quantum algorithms and it is hence important to look for decompositions of the QFT specifically designed for qudits and hybrid qubit-qudit systems. Qubit-qubit-qutrit QFT is implemented experimentally on the four qubit system emulating a hybrid system of two qubits coupled to a qutrit. A tomography protocol for the reconstruction of a hybrid qubit-qubit-qutrit is proposed which is another mandatory step in order to perform a hybrid qudit computation. A correspondence is drawn between the tomography protocols of a QQQQ system and a QQT system for the complete characterization of the emulator used. These non-trivial results are a few steps towards the advancement of the area of qudit quantum computing on an NMR quantum information processor. It is expected that these experiments will pave the way for the implementation of full-fledged qudit-based quantum computing proposals.

Chapter 6

Applications of numerically optimized pulses in NMR

Nuclear Magnetic Resonance is a versatile technique that demands increasing precision as its applications increase. Optimal control theory in the context of NMR is a field of much recent interest, which deals in obtaining a good control over the experimental systems [157]. Optimal control theory-based NMR experimental implementations facilitate nearly perfect coherence transfer amplitudes [158, 159], a precise uniform excitation of spins [160], quantum gate implementations with a single rf pulse [5, 32, 161], and the compensation of decoherence among spins [162]. This chapter describes a few applications of numerically optimized pulses in NMR.

The experimental regime in NMR provides much flexibility in various operations, and control over the system of nuclear spins. One can design a desired set of radio frequency pulses and delays in a specific order, and implement it on a system of NMR-active nuclear spins [163]. Pulse parameters like pulse duration, pulse power, and bandwidth depend upon each other, pulse duration and bandwidth are inversely proportional to each other, while pulse power depends upon the angle of excitation. Thus introducing the interplay between the pulse duration, pulse power and the bandwidth even single transitions can be addressed precisely. However, during the actual pulse implementations, experimental imperfections come into the picture leading to signal distortion. Numerically optimized pulses are designed taking into consideration these hurdles. Such numerical pulses that compensate the experimental imperfections, prove to be very useful, and have various applications. Numerically optimized pulses specifically tailor the radio frequency profiles for a specific flip angle, uniformly exciting a desired set of resonances. Gradient Ascent Pulse Engineering (GRAPE) [89] provides an efficient way to generate a numerical pulse corresponding to state-to-state transfer or operator optimization. In this chapter, the use of these pulses optimized via the SIMPSON software program [90], is exploited for various purposes such as qudit computing in NMR, betterment of 2D fast pulsing SOFAST type of sequences for biomolecular NMR and the simulation of low temperature protein dynamics.

6.0.1 Numerical optimization using GRAPE

GRAPE [89] is an efficient algorithm for optimal pulse design. It is based on the evolution of the state of the system under the effect of an RF field as per the Liouville Von Neumann equation

$$\frac{\partial \rho}{\partial t} = -\iota[H(t), \rho(t)] \tag{6.1}$$

The Hamiltonian of the system, $H_t = H_0 + H_{rf}$ consists of a static part (H_0) (specifying the system) and an RF part (H_{rf}) which is optimized iteratively using gradient ascent methods. The RF part of the Hamiltonian is divided into 'N' steps each of width 'Δt', such that $T = N\Delta t$ is the total duration of the pulse. Corresponding to the j^{th} time step,

$$H_{rf}(j) = \sum_{k=1}^{m} u_k(j) H_k \tag{6.2}$$

where $u_k(j)$ is the amplitude of the control Hamiltonian (H_k) at j^{th} time step corresponding to the k^{th} spin type (e.g. ^{13}C, ^{1}H etc.). Assuming the amplitudes (RF strength) to be constant in each time step, the vector $u_k(t)$ begins with a guess profile. The state of the system is acted upon by $U_j = Exp[-\iota \Delta t H_t(j)]$ corresponding to the j^{th} time step leading to a numerically attained final state

$$\rho_n = U_n U_{n-1} \ldots\ldots U_1 \rho_0 U_1^{\dagger} \ldots\ldots U_{n-1}^{\dagger} U_n^{\dagger} \tag{6.3}$$

At the end of each iteration, the fidelity $\phi = Tr(\rho_{th}^{\dagger} \rho_n)$ is calculated between the theoretically expected (ρ_{th}) and the numerically achieved final density matrix. The control amplitudes are updated as per the gradient ascent method in order to maximize the fidelity. The entire protocol is iterated until the desired fidelity is achieved. The control amplitudes at different time steps together form the pulse profile. In this chapter numerical pulses are optimized to implement a quantum gate and for band-selective excitation using GRAPE. It is to be noted that the pulse profile obtained using GRAPE is not unique; there can exist more than one GRAPE optimized pulse shape of the same duration, exciting the same bandwidth and simulating the same operation.

6.1 Numerically optimized pulses for QFT on a hybrid qubit-qutrit system

In order to re-implement hybrid QFT on coupled qudits as described in Chapter 5, let us consider a hybrid qubit-qutrit system. The Hamiltonian of a such a system (Equation (5.8)) in the presence of a strong magnetic field $\overrightarrow{B} = B_0\hat{z}$ is:

$$H = \omega_1 I_z + \omega_2 S_z + 2\pi J_{1,2} I_z S_z + Q(3S^2 - S_z.S_z), \tag{6.4}$$

where ω_1 and ω_2 are the resonance frequency offsets of the qubit and the qutrit respectively, J_{12} is the scalar coupling strength, and Q is the effective quadrupolar moment of the qutrit. I_k and S_K ($k \in x, y, z$) are the elements of angular momentum operators corresponding to the qubit and the qutrit respectively. Explicitly, one can write $I_k = \frac{1}{2}\sigma_k \otimes I_{3\times3}$ and $S_k = I_{2\times2} \otimes \Sigma_k$ respectively, where σ_k is the Pauli matrix for a two-level quantum system and Σ_k is the three-dimensional analogue of the Pauli matrix. $I_{2\times2}$ and $I_{3\times3}$ are the identity operators in two and three dimensions respectively. The resultant Hamiltonian thus represents a six-level quantum. The six-dimensional Hilbert space has six energy levels (labeled from 1-6 in Figure 6.1(b)). Corresponding to an ensemble of spins at thermal equilibrium, relative occupation indices are shown in Figure 6.1(b) above each energy eigenstate where $r = \frac{\gamma_C}{\gamma_D} \approx 1.63$ is the ratio of the gyromagnetic ratios of qubit (γ_C) and qutrit (γ_D). $[|0'\rangle, |1'\rangle, |2'\rangle]$ represent the set of orthonormal basis vectors for a qutrit, such that the angular momenta associated with the spin states $|0'\rangle = +1$, $|1'\rangle = 0$ and $|2'\rangle = -1$. The computational basis of the qubit is $[0, 1]$ with spin states $|0\rangle = +\frac{1}{2}$ and $|1\rangle = -\frac{1}{2}$. There are seven single-quantum transitions (obeying the selection rule $\Delta m = \pm 1$) as shown in Figure 6.1(b). Out of these transitions, three correspond to qubit flips and four to that of qutrit flips. The qutrit has two degenerate pairs of transitions when experiments are performed in an isotropic medium, like the liquid state NMR environment. As explained in Chapters 3, 4 as well as Appendix A of the present thesis, the quadrupolar coupling strength

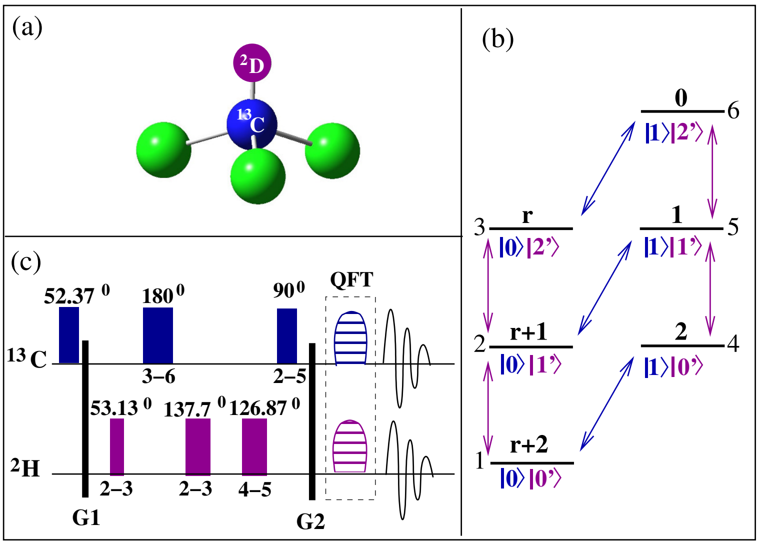

Figure 6.1: (a) Molecular structure of Chloroform-D: ^{13}C (spin $1/2$) is the qubit while ^{2}D (spin 1) is the qutrit. (b) Energy level diagram of ^{13}C-^{2}D qubit-qutrit system is shown. There are six energy levels (numbered from 1-6) labeled with the basis vectors; the populations are given above each energy level ('r' is the ratio of gyromagnetic ratios of ^{13}C and ^{2}D, r=$\frac{\gamma_C}{\gamma_D}$). Spectral line of a qubit under the effect of scalar coupling with a qutrit splits into three lines which is shown by three transitions of qubit (blue line). The qutrit under the effect of scalar coupling and quadrupolar moment, undergoes four transitions shown in purple. (c) Pulse sequence to create the pseudo-pure state $|00'\rangle$ in a hybrid qubit-qutrit system using transition selective pulses, followed by QFT. QFT implementation is carried out with the numerically optimized pulses using GRAPE.

averages to zero ($Q = 0$) in an isotropic medium leading to overlap in the qutrit transitions in frequency space. However the degeneracy in qutrit-transitions can be removed by orienting the qutrit in an anisotropic environment (such as a liquid crystal). An anisotropic environment retains the quadrupolar splitting between the spectral lines. The splitting between the spectral lines of the qutrit (which are otherwise degenerate) is attributed to the amount of anisotropy of the medium which is its 'order parameter'.

The simulation of a qubit-qutrit system with parameters resembling a deutrated Chloroform molecule CDCl$_3$ is shown in Figure 6.1(a), where ^{13}C is a qubit and the spin 1 ^{2}D is a qutrit, together forming a six-level quantum system. This molecule is simulated in NMRSIM software (Topspin 2.1) as per the Hamiltonian given in Equation 6.4. Chemical shift values of ^{13}C (ω_1) and ^{2}D (ω_2) are taken as 77 ppm and 7 ppm respectively and the scalar coupling J_{12} is 32 Hz. The molecule is simulated in an anisotropic environment providing effective value of quadrupolar moment of ^{2}D to be 120Hz. Thermal equilibrium spectrum of this system is shown in Figure 6.3(a).

6.1.1 Qubit-qutrit QFT

Quantum Fourier transform is a unitary transformation, which in its explicit form for a six-level quantum system is given as:

$$QFT = \frac{1}{\sqrt{6}} \begin{pmatrix} 1 & 1 & 1 & 1 & 1 & 1 \\ 1 & \omega & \omega^2 & \omega^3 & \omega^4 & \omega^5 \\ 1 & \omega^2 & \omega^4 & 1 & \omega^2 & \omega^4 \\ 1 & \omega^3 & 1 & \omega^3 & 1 & \omega^3 \\ 1 & \omega^4 & \omega^2 & 1 & \omega^4 & \omega^2 \\ 1 & \omega^5 & \omega^4 & \omega^3 & \omega^2 & \omega \end{pmatrix} \tag{6.5}$$

where $\omega = e^{\frac{-2\pi\iota}{6}}$ is the sixth root of unity. This matrix implements quantum Fourier transform on a six-level quantum system. The decomposition of this QFT matrix in terms of single spin and two-spin rotations are given as: $H_1 R_{12} H_2$. H_1 is the Hadamard gate on first the first spin(qubit), R_{12} is a controlled operation with first spin (qubit) acts as control, and the second spin (qutrit) acts as target. Thus whenever the qubit is in state $|1\rangle$, the target qutrit acquires a phase of $e^{\frac{2\pi\iota k}{6}}$ where $k \in \{0, 1, 2\}$ depending upon whether qutrit is in state $|0'\rangle$ or $|1'\rangle$ or $|2'\rangle$ respectively. Explicit operator representation of this gate is given as:

$$R_{12} = \begin{pmatrix} 1 & 0 & 0 & 0 & 0 & 0 \\ 0 & 1 & 0 & 0 & 0 & 0 \\ 0 & 0 & 1 & 0 & 0 & 0 \\ 0 & 0 & 0 & 1 & 0 & 0 \\ 0 & 0 & 0 & 0 & e^{\frac{2\pi\iota}{6}} & 0 \\ 0 & 0 & 0 & 0 & 0 & e^{\frac{4\pi\iota}{6}} \end{pmatrix} \tag{6.6}$$

Finally H_2 is the Fourier gate which is three dimensional analogue of the Hadamard gate (also known as Chrestenson gate [164]). This is a single qutrit gate given as: $I_{2\times2} \otimes C$ where

$$C = \frac{1}{\sqrt{3}} \begin{pmatrix} 1 & 1 & 1 \\ 1 & e^{\frac{2\pi\iota}{3}} & e^{\frac{4\pi\iota}{3}} \\ 1 & e^{\frac{4\pi\iota}{3}} & e^{\frac{2\pi\iota}{3}} \end{pmatrix} \tag{6.7}$$

The NMR pulse schemes for the implementation of these gates have been worked out in detail in chapter 5. In this chapter a different technique is adopted for the QFT implementation on a hybrid qudit system. QFT implementation is achieved here by numerically optimizing a single pulse corresponding to the explicit QFT matrix given in Equation (6.5).

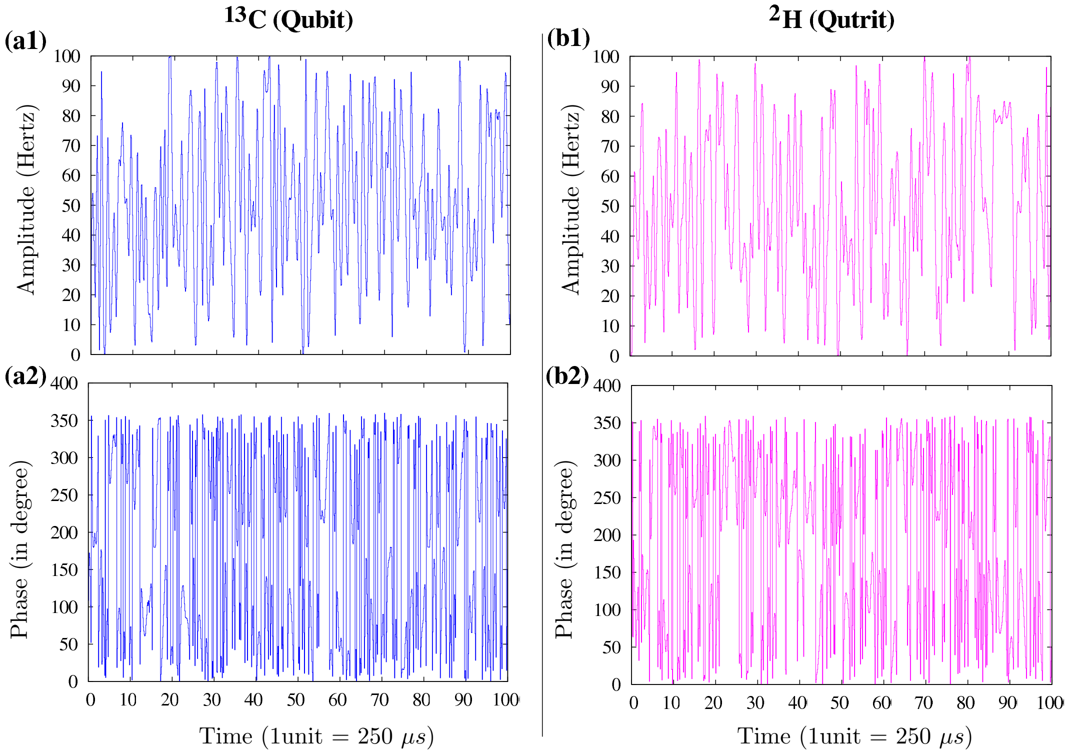

Figure 6.2: Numerical pulse profile optimized for ^{13}C and ^{2}D of CDCl3 molecule, that implements a hybrid quantum Fourier transform. The horizontal axis shows the pulse duration in 100 steps of 280μs each. In (a1) and (b1), vertical axis represents the pulse amplitude normalized to 100. Vertical axis in parts (a2) and (b2) show the phase of the pulse (in degrees).

Here numerically optimized pulses using GRAPE [89] accessed through SIMPSON [90] are used to generate radio frequency pulse profiles for various unitary operators. The explicit QFT= $H_1 R_{12} H_2$ is also a unitary operator and thus RF profile for complete QFT matrix can be optimized numerically. In case of numerical optimization, it is better to decompose the complex operators rather than finding the RF profile for the full operator. However, the QFT for a qubit-qutrit system contains only one controlled operation (R_{12}), therefore it is not difficult to optimize QFT operator as a whole. Operator 'QFT' is optimized with 100 pulse points, duration $t = 28ms$, $\gamma B_{max} = 2459$Hz obtaining a fidelity of 0.99. Figure 6.2 shows the amplitude and phase profile for the deuterium and carbon spins respectively. The RF profile simulating explicit QFT operator was simulated using (a) thermal state and (b) Pseudopure state as initial states of the qubit-qutrit system.

6.1.2 Simulation of a hybrid QFT on a qubit-qutrit system

6.1.2.1 Pseudo pure state preparation

A qubit-qutrit pseudo-pure state, $|00'\rangle$ is prepared using transition selective pulses. Applying a transition selective pulse [40] from levels 'r' to 's' with populations p_r and p_s respectively, shuffles the populations such that the respective final populations are :

$$\begin{aligned} p_r^{'} &= p_r \cos^2\frac{\theta}{2} + p_s \sin^2\frac{\theta}{2} \\ p_s^{'} &= p_s \cos^2\frac{\theta}{2} + p_r \sin^2\frac{\theta}{2} \end{aligned} \tag{6.8}$$

The idea is to find the optimal angle corresponding to the desired final population such that $p_r^{'}, p_s^{'}$ fall in the range $[p_r, p_s]$. The pulse sequence for pseudo-pure state preparation is shown in Figure 6.1(c). Optimized RF profile for QFT is applied to both carbon and deuterium channels simultaneously. Simulated spectra of the final state are shown in Figure 6.3. The pulse sequence for pseudo-pure state formation in the qubit-qutrit system (all the angles are in degrees, the order is effective from left to right) is given by: $(52.37)^1\, G_1\, (53.13)^{2,3}\, (180)^{3,6}\, (137.7)^{2,3}\, (126.87)^{4,5}\, (90)^{2,5} G_2$. The initial state of the system is taken as thermal equilibrium state: $\gamma_C I_z + \gamma_D S_z$. The first pulse of the sequence is a spin-selective pulse acting on ^{13}C (qubit) which is followed by a non-selective z-gradient pulse (G_1). At the end of this pulse, a fraction (=$\frac{\gamma_D}{\gamma_C} \approx 0.61$) of ^{13}C spins are dephased, and hence no more contribute to the net NMR signal. This is followed by several consecutive transition-selective pulses with final populations as per Equation (6.8). The pseudo-pure state $|00'\rangle$ is created at the end of the cleanup gradient G_2 (which cleans up unwanted coherences). Upon detection with a small angle pulse, the resulting pseudo-pure state gives rise to one spectral line corresponding to each of the two spins. The spectrum obtained at the end of pseudo-pure state creation acquired with a 30^0 non-selective detection pulse is shown in parts (c1) and (c2) of Figure 6.3.

6.1.2.2 Qudit QFT Simulation

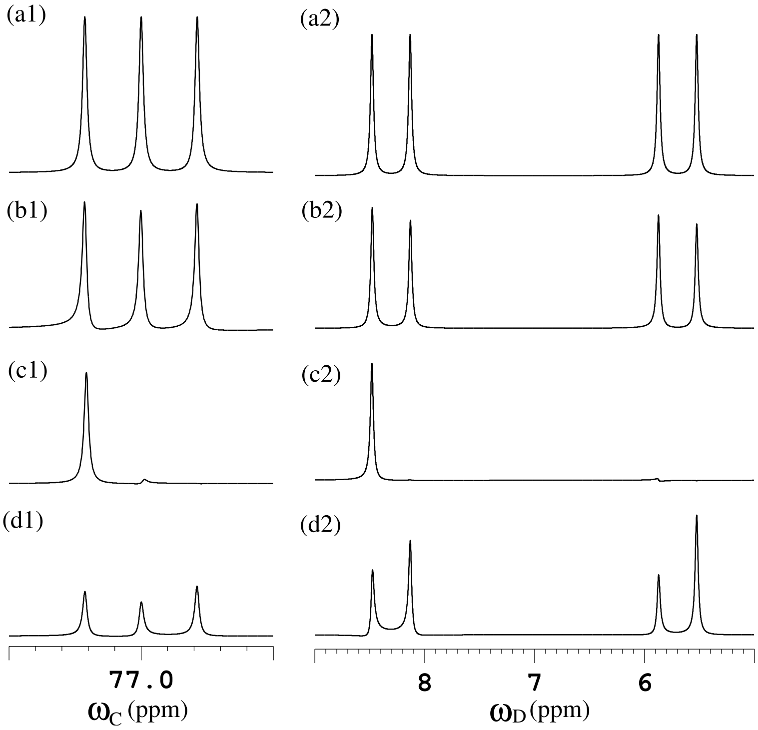

Figure 6.3: Simulated NMR spectra of ^{13}C and ^{2}D of CDCl3 molecule using NMRSIM. The figure shows sequentially NMR spectra of (1) Thermal equilibrium state with small angle detection, (2) QFT simulation on the thermal equilibrium, (3) Pseudopure state with small angle detection and the (4) NMR spectrum obtained by QFT simulation on a qubit-qutrit pseudo-pure state. This is the simulated spectrum of CDCl3 (qubit-qutrit system). Three equispaced lines centered around 77ppm correspond to carbon nucleus(qubit) and four lines centered around 7ppm correspond to Deuterium(qutrit). Part (a) contains the spectra of thermal state for both nuclei, part(b) contains the spectrum obtained after simulation of QFT on the thermal state. Part (c) contains the pseudo-pure state 00' and the final state spectrum resulted from QFT on the pseudo-pure state 00' is given in (d). Pseudopure spectrum is shown with a 30^0 detection pulse. Spectra in (b) and (d) are on the same intensity scale for respective nuclei. Expected reduced intensity is obtained in (d) as compared to (b).

The QFT simulation on thermal as well as pseudo-pure state of the qubit-qutrit system is carried out using the numerically optimized pulse in SIMPSON. A single rf pulse profile has been optimized numerically to implement full QFT operator. The resulting radio frequency pulse consists of separate pulse profiles for the carbon and the deuterium channels. These two pulse profiles are implemented simultaneously in order to perform the desired operation. RF profiles corresponding to each of the nucleus, performing a hybrid QFT are shown in Figure 6.2. This section discusses only the simulation of the QFT in NMRSIM using the pulse sequences as per Figure 6.2. However, the same sequence of operations can be used for experimental implementation of the hybrid QFT on a qubit-qutrit system.

The numerically optimized RF profile is applied on the thermal equilibrium state of a qubit-qutrit system. The resultant state is expected to have seven lines with all the three qubit spectral lines of equal intensities ($=\frac{1}{\sqrt{6}}$) and same phase, and the four qutrit spectral lines are in-phase with same values of intensity ($=\frac{1}{\sqrt{6}}$). However there is a relative phase between the qubit and the qutrit spectra. The resulting spectrum is shown in Figure 6.3(b1,b2). The spectrum corresponding to each spin is corrected for phase, in order to provide a better spectrum.

QFT has also been simulated on $|00'\rangle$ pseudo-pure state of the qubit-qutrit system. The expected spectrum after the QFT simulation possesses all lines with equal intensity and same phase. NMR spectrum of the final state after QFT simulation on the pseudo-pure state of a qubit-qutrit system is shown in Figure 6.3(d1,d2). The spectrum gives in-phase lines with slightly varying intensities.

6.2 Numerically optimized band-selective pulses in SOFAST-HMQC experiments for biomolecular NMR

Hetronuclear correlation experiments in 2D NMR such as HSQC, HMQC, HMBC, HOESY, HETCOR etc are very useful in characterizing the molecular structure, conformation and dynamics [40, 43, 58, 165, 166, 167, 168]. Such standard 2D NMR pulse sequences have been substantially improved over the years [169, 170, 171, 172, 173, 174, 175]. A 2D ^{1}H-X HMQC (Hetronuclear Multiple Quantum Correlation) experiment correlates ^{1}H and X nuclei, and is well known for its simplicity, elegance and usefulness [43]. The basic pulse sequence for 2D HMQC experiment begins with a 90^0 excitation pulse on proton channel (^{1}H) at thermal equilibrium. The coherence thus developed is allowed to evolve under ^{1}H-X scalar coupling strength. This is followed by an INEPT sequence that transfers the ^{1}H polarization to insensitive X nucleus. Finally there is another J(^{1}H-X)-evolution for a fixed period of time ($\frac{1}{2J}$) which is followed by signal acquisition on the proton channel. The next scan can be obtained after a relaxation delay (d_1) during which the magnetization relaxes back to equilibrium. The delay d_1 is the most time consuming part of this sequence. Long experimental times in case of biomolecular NMR experiments can give rise to serious issues like sample degradation. There have been several propositions to mitigate the issue of long experimental times, such as non-uniform sampling in the indirect dimension [66, 176, 177], use of Ernst angle excitation [178], BEST, ASAP and SOFAST type of experiments [57, 59, 60, 62, 63, 179, 180] and several other schemes that obtain the correlations with fewer number of scans [61, 64, 65, 159, 181].

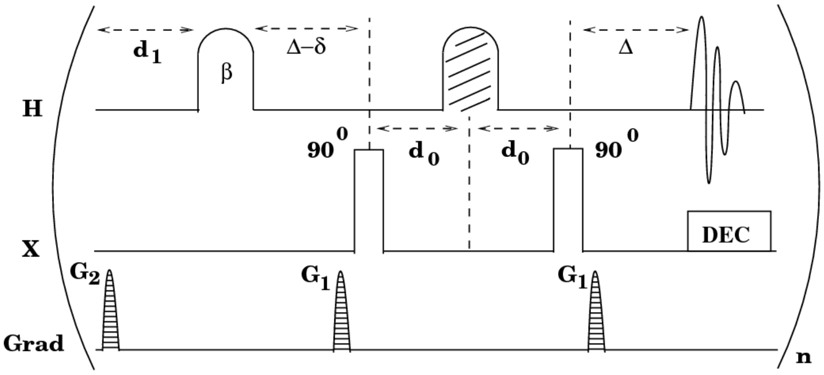

Figure 6.4: SOFAST-HMQC pulse sequence with a dome shaped band-selective excitation pulse with flip angle 'β'. Rectangular pulses are 90^0 hard pulses applied on X nuclei, while the shaded dome- shaped shaded pulse in the middle of the incremental delay is the refocusing pulse applied on ^{1}H channel. The inter-scan delay and the variable delay are represented by d_1 and d_0 respectively, '$\Delta = 1/2J$' is the evolution period, 'δ' is the time period compensating for evolution during the β angle pulse and G1, G2 are the gradient strengths with values 11% and 7% (of the maximum strength) respectively.

The focus of the present part of this chapter is to incorporate the use of numerical pulse in a SOFAST HMQC experiment. SOFAST-HMQC experiments overcome the problem of longer experimental times by using a selectively optimized flip angle of the first excitation pulse on the proton channel. SOFAST-HMQC experiments have been designed that rely on both Ernst angle excitation [178, 181] ($\cos\alpha = \exp[-\frac{aq+d_1}{T_1}]$ where 'α' is the Ernst angle, 'aq' is the total time taken by the pulse sequence (including time for acquisition), 'd_1' is the inter scan delay, 'T_1' is the spin-lattice relaxation time) and longitudinal relaxation optimization. The NMR pulse sequence for a SOFAST-HMQC is given in Figure 6.4 wherein a soft pulse of selectively optimized flip angle for exciting ^{1}H is shown by a shaped pulse of angle β. A β pulse does not transfer whole of the longitudinal equilibrium magnetization to the transverse plane. This brilliant idea keeps retaining a part of the longitudinal magnetization, which keeps on growing throughout the sequence of operation. The value of the angle of excitation is chosen in such a manner that every time one starts off with roughly same amount of magnetization. Thus sensitivity enhancement in SOFAST-HMQC experiments is obtained by modifying the angle of excitation which reduces the inter-scan delay. Hence more number of scans are possible in lesser time, giving higher signal to noise ratio [57, 59].

In conventional SOFAST-HMQC experiments, a band-selective excitation pulse is preferred to perform a β angle excitation. An efficient and robust, conventionally used band-selective excitation pulse is a polychromatic pulse (pc9) composed of nine $sinc$ functions [182]. In this pulse shape, the central lobe of each $sinc$ function has been placed on the first minima of the consecutive sinc function making a train of nine such functions. The use of this pulse with SOFAST-HMQC experiments provides better sensitivity. However replacing this pc9 pulse with a numerically optimized band-selective pulse is capable of providing even better sensitivity and lesser phase distortions. This lack of relative phases inturn result into a better resolution of the correlations in SOFAST-HMQC spectrum.

6.2.1 SOFAST-HMQC experiment with a numerical pulse

A detailed analysis of the SOFAST-HMQC pulse sequence is carried out (Figure 6.4) with an emphasis on the possible sources of distortion in the final signal obtained.

Following set of equations summarize the explicit form of the magnetization components involved and their evolution under various operations.

$$
\begin{array}{ll}
(i) & I_z + S_z \quad \xrightarrow{\beta_x^I} \\
(ii) & \cos\beta I_z - p(\omega)\sin\beta I_y - q(\omega)\sin\beta I_x + S_z \quad \xrightarrow{\frac{1}{2J}} \\
(iii) & \cos\beta I_z + 2p(\omega)\sin\beta I_x S_z - 2q(\omega)\sin\beta I_y S_z + S_z \quad \xrightarrow{90_x^S} \\
(iv) & \cos\beta I_z - 2p(\omega)\sin\beta I_x S_y + 2q(\omega)\sin\beta I_y S_y - S_y \quad \xrightarrow{2\pi\Omega_S S_z} \\
(v) & \cos\beta I_z - 2p(\omega)\sin\beta\cos\theta I_x S_y + 2p(\omega)\sin\beta\sin\theta I_x S_x + 2q(\omega)\sin\beta\cos\theta I_y S_y \\
 & -2q(\omega)\sin\beta\sin\theta I_y S_x - \cos\theta S_y + \sin\theta S_x \quad \xrightarrow{90_x^S} \\
(vi) & \cos\beta I_z - 2p(\omega)\sin\beta\cos\theta I_x S_z + 2p(\omega)\sin\beta\sin\theta I_x S_x + 2q(\omega)\sin\beta\cos\theta I_y S_z \\
 & -2q(\omega)\sin\beta\sin\theta I_y S_x - \cos\theta S_z + \sin\theta S_x \quad \xrightarrow{\frac{1}{2J}} \\
(vii) & \cos\beta I_z - p(\omega)\sin\beta\cos\theta I_y + p(\omega)\sin\beta\sin\theta I_x S_x - q(\omega)\sin\beta\cos\theta I_x \\
 & +q(\omega)\sin\beta\sin\theta I_x S_x - \cos\theta S_z + 2\sin\theta I_z S_y
\end{array}
\tag{6.9}
$$

assuming I_i and S_j ($i, j \in [x, y, z]$) to be the i^{th} and j^{th} components of the magnetization vector corresponding to ^1H and ‘X’ nuclei respectively. Band-selective excitation pulse with angle ‘β’ on first nucleus giving anti-clockwise rotation about x-axis (Figure 6.4) should ideally bring the magnetization vector to yz-plane aligned at angle ‘β’ with the z-axis. However practically, magnetization vectors of spins at different offsets begin to fan-out in the xy-plane instead of ending at the same point. Hence at the end of step (i), one unexpectedly obtains significant magnitude of x-magnetization as well. Symbolically, p(ω) and q(ω) be two functions of offset ‘ω’ representing magnitudes of y, x-components of magnetization respectively. In case both p(ω) and q(ω) are constant functions, spin response can be considered as uniform (here p(ω)=1, q(ω)=0 is the requirement). State after ‘β’ angle excitation is given in step-(ii). At the end of the sequence, final state given in step-(vii) contain detectable in-phase terms which can be either ‘I_x’ or ‘I_y’ depending on the offset frequency (ω).

If ‘β’ angle pulse about x-axis on ^{1}H uniformly flips all the spins in the desired bandwidth, magnetization vector at all the offsets falling in the given bandwidth will rest in the yz plane aligned at angle ‘β’ with +z axis which is an ideal case with p(ω)=1 and q(ω)=0. Hence final state (given in step-(vii)) should ideally contain only one in-phase term ‘Iy’ and thus the final correlation spectrum is purely absorptive (with a global phase). However practically there exists q(ω) also and therefore intensity of ‘x’ and ‘y’ components of magnetization vector in the final state appears as a function of offset. Presence of both absorptive and dispersive peaks at the same time lead to phase distortion along ^{1}H dimension in the final spectrum.

Use of a band-selective numerically optimized pulse for β angle excitation is expected to have a better response in terms of phase in the final spectrum. This expected behaviour can be tested by performing a simulation of the spin response in a desired bandwidth. A shaped pulse is optimized numerically using GRAPE [89] algorithm accessed via SIMPSON [90] simulation tool. The pulse is optimized to excite a bandwidth of 2500 Hz in 2 ms duration by an angle of 120^0 with maximum RF strength γB_{max} =1945.95 Hz. The resulting pulse profile is named as Numerically optimized Band-Selective Excitation pulse II (NBSEP II).

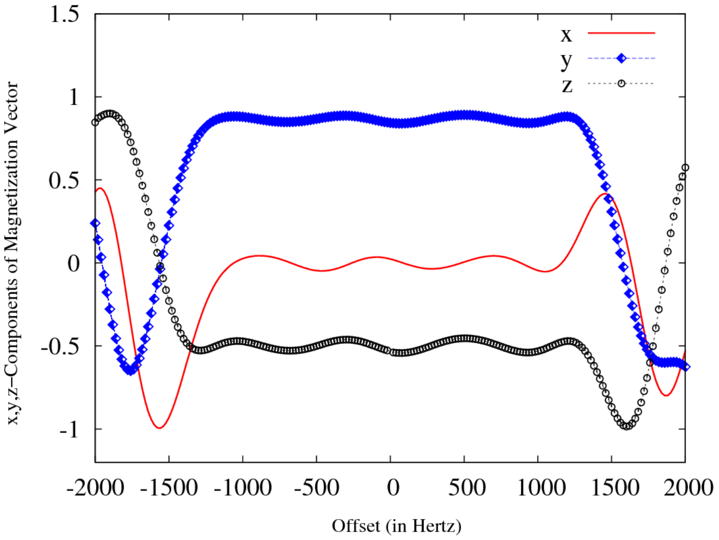

Figure 6.5: Spin response obtained by the implementation of numerically optimized NBSEP-II pulse in a given bandwidth of 2500 Hertz, used for 120 degree excitation starting with initial magnetization along +z axis. x,y and z-components of the magnetization vector are plotted as a function of offset. x,y,z-components of the spin response are shown in red, blue and black colored lines respectively. All three curves clearly show that the response is uniform in the given bandwidth (ranging from -1250 Hz to +1250 Hz).

NBSEP-II pulse is simulated using NMRSIM simulator (Topspin 2.1) assuming a single spin Bloch model. This simulation tool assumes the single spin model and ignores the effect of coupling between spins. Thus simulating the frequency response of a single spin at different offsets successively, is equivalent to simulating several spins at the same time, resonating at different offsets. A band-selective pulse designed to uniformly excite a bandwidth of '$\Delta\omega$' of a given duration should ideally lead to a hat-like spin response. Considering the initial magnetization to be along z-axis, applying the pulse about x-axis (clockwise) takes the state to -0.5 I_z + 0.866 I_y (where I_y and I_z are the components of magnetization vector along 'y' and 'z' axes respectively). As can be seen in Figure 6.5, the x-component of the magnetization vector remains almost zero in the region of interest, however wiggles can be seen beyond desired bandwidth. A similar result is obtained for the y and z components. When confined to the region of interest, the use of numerically optimized pulse gives nearly in-phase spin response. Thus a nearly hat-shaped response of an arbitrary shaped pulse is obtained. Corresponding spin response for the case of ploychromatic Pc9 pulse shape is also obtained (Figure 6.6) As clear from the Figure 6.6 a standard Pc9 pulse gives a varying phase of

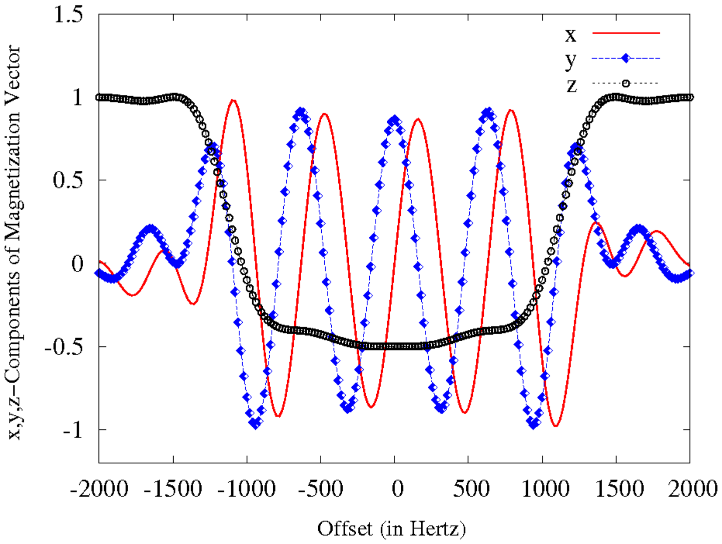

Figure 6.6: Spin response obtained by the implementation of numerically optimized Pc9 pulse in a given bandwidth of 2500 Hertz, used for 120 degree excitation starting with initial magnetization along +z axis. x,y and z-components of the magnetization vector are plotted as a function of offset which are shown in red, blue and black colored lines respectively.

the resulting spectral lines. the x and y components of the magnetization are found to keep oscillating while the amplitude $\sqrt{x^2 + y^2}$ remains constant. The final spectrum obtained in this case does not have the linear combination of x and y magnetization. Comparing the spin response obtained with NBSEP II pulse (Figure 6.5) and the Pc9 pulse (Figure 6.6), one can conclude that the numerical pulse provides an in-phase spectrum as per requirement posed in the set of Equations (6.9).

6.2.2 Experimental details

A set of ^{1}H-^{13}C and ^{1}H-^{15}N SOFAST-HMQC experiments with numerically optimized band-selective pulses is performed on Ubiquitin. The model protein used in this study is ^{13}C, ^{15}N labeled human ubiquitin purchased from Protera (1mM sample in D_2O and NaPi buffer of PH 7.0). Ubiquitin (PDBID 1UBQ) with 76 amino acids forming 3 alpha helices and 7 beta strands, is a regulatory protein serving as a tag that marks specific proteins for degradation and is widely used as an NMR standard. All NMR datasets were recorded at 22^0 C (otherwise specified) on a Bruker Biospin Avance-III 600 MHz spectrometer equipped with a triple resonance (HCN) probehead and actively shielded X,Y,Z-axes gradients. Data processing was performed using Bruker Topspin 2.1.

A $^1H -^{15} N$ SOFAST-HMQC experiment was obtained with 1024 and 128 complex points at spectral widths of 10 and 30 ppm corresponding to acquisition times of 85.3 ms and 35 ms in the t2 and t1 time domains respectively. A relaxation delay of 0.3s was used. 16 transients were collected per stored FID corresponding to a total experimental duration of 14min 25sec for each dataset. Gradient values, G_1 and G_2 are 5.3 and 3.37 G/cm respectively. The experiments were performed with two types of band-selective excitation pulses: a standard polychromatic 'Pc9' (Bruker name $Pc9\_4\_120.1000$) and numerically optimized band-selective excitation pulse NBSEP-II with durations of 3000 μs and 2000 μs respectively. For refocusing, pulses from the 'SNOB' family (Bruker name $Rsnob.1000$) with a duration of 1 ms, were used. The value of the coefficient compensating the chemical shift dispersion and evolutions during the pulse duration (proportional to $\frac{\delta}{\tau}$, where τ is the duration of the selective pulse with flip angle 'β') was fixed at 0.529 for the Pc9 pulse and 0.0055 for the NBSEP-I pulse. These compensatory values are experimentally optimized such that the band-selective shaped pulse followed by an evolutionary delay gives rise to the expected signal. Broadband adiabatic decoupling was achieved with a smoothed 1.5 ms chirp pulse 'Crp32,1.5,20.2' for inversion and a decoupling supercycle given in the Bruker library: 'P5m4sp180' with offset at 115 ppm for ^{15}N.

Numerically optimized band-selective pulses were also optimized and experimentally implemented for relatively smaller bandwidths in case of 2D ^{1}H-^{13}C SOFAST-HMQC experiments. Hetronuclear ^{1}H-^{13}C correlations in organic compounds exist in the aliphatic and the methyl regions of the spectra. Ubiquitin is a 76 residue protein that exhibits a large number of ^{1}H-^{13}C correlations with different intensities. These correlations result in crowded spectral regions, leading to poor resolution. Here regions of smaller bandwidths have been selectively excited to obtain cleaner spectra.

For ^1H-^{13}C SOFAST-HMQC experiments, a bandwidth of 1200 Hz centered around 0.5 ppm is excited by angle of 120^0 in the case of the methyl region. For the aliphatic region (1.5-3.5 ppm, including the methyl peaks), the proton transmitter frequency was kept at 2.5 ppm with all other parameters unchanged. Pulses used were polychromatic 'Pc9', and numerically optimized band-selective excitation pulse NBSEP-I with pulse durations of 6260 μs and 5000 μs respectively. RSNOB pulses were used for refocusing with a duration of 2 ms. The same set of ^1H-^{13}C experiments were also acquired using Reburp (Bruker name $Reburp.1000$) refocusing pulse with duration 2.8 ms corresponding to a bandwidth of 1200 Hz (data not shown as spectra look similar to those acquired using RSNOB refocusing pulses).

6.2.3 ^{1}H-^{15}N SOFAST-HMQC experiment

$^1H-^{15}N$ SOFAST-HMQC spectrum is acquired using a numerically optimized band-selective pulse with angle of excitation $\beta = 120^0$ on given sample of human ubiquitin. The numerically optimized pulse of 120^0 flip angle is of 2000 μs duration, and excites a bandwidth of 2500 Hz. In ^{1}H-^{15}N SOFAST-HMQC experiment, this pulse selectively excites the prescribed bandwidth centered around 8ppm in the ^{1}H dimension. This numerically optimized band-selective excitation pulse is being termed as NBSEP-II in this thesis. 2D NMR spectrum of Ubiquitin resulting from the ^{1}H-^{15}N SOFAST-HMQC experiment is shown in Figure 6.7. Peaks obtained corresponding to various correlations have been labeled from 1-62.

As shown in Figure 6.7 sufficient number of peaks depicting ^{1}H-^{15}N correlations have been numbered for subsequent use during the quantitative analysis. In the quan-

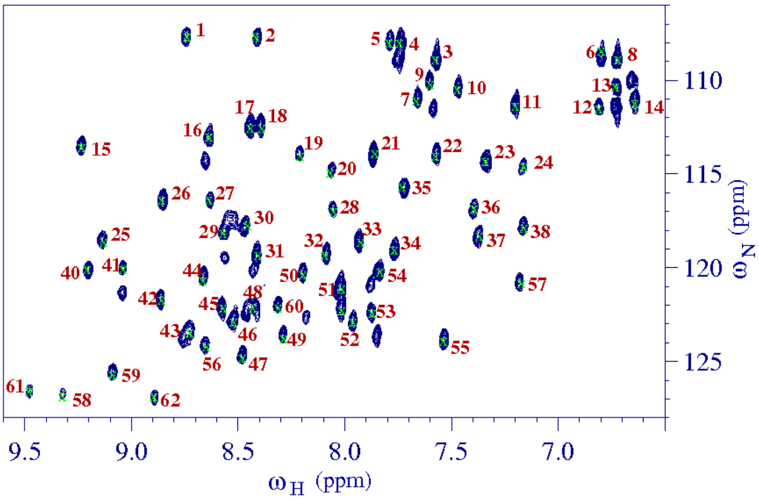

Figure 6.7: NMR spectrum of ^{1}H-^{15}N SOFAST-HMQC experiment where peaks are labeled from 1-62.

titative analysis, peaks are henceforth addressed by their respective labels. As can be seen clearly, using a numerically optimized shaped pulse in ^{1}H-^{15}N SOFAST-HMQC experiment gives rise to a well resolved spectrum, acquired in less time as compared to the experiment performed with conventional pulses.

Keeping the same constraints on acquisition time, bandwidths, flip angle and relaxation delay, ^{1}H-^{15}N SOFAST-HMQC experiment is also acquired with standard pc9 pulse shape. The spectra obtained in this case is compared with that of the ^{1}H-^{15}N SOFAST-HMQC spectrum acquired using NBSEP II pulse. Apart from the β angle pulse shapes (and their corresponding parameters) all other experimental parameters remain same. The spectra acquired in both cases are compared for resolution and sensitivity differences. Insets in Figure 6.8 depict the variation of resolution of peaks with experiments acquired with both the pulse types. One can conclude from the spectra in Figure 6.8 that both the pulse types are quite efficient, however a spectrum acquired with NBSEP II pulse shape leads to better resolution.

6.2.3.1 Quantitative analysis

Quantitative analysis of the ^{1}H-^{15}N SOFAST-HMQC experiment is carried out to compare the spectra as obtained using NBSEP II and polychromatic Pc9 pulses for the β

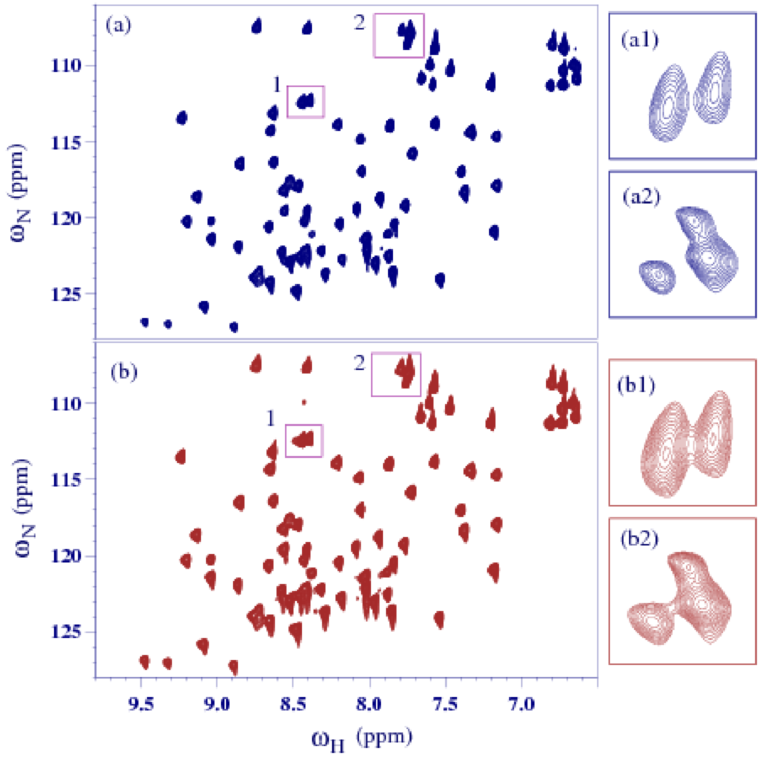

Figure 6.8: ^{1}H-^{15}N SOFAST-HMQC spectra obtained using (a) Numerically optimized pulse band-selective excitation pulse NBSEP-II and (b) Standard polychromatic Pc9 band-selective pulse for 'β' angle excitation are shown. Resolution of specifically marked regions are shown as insets where (a1) and (a2) show the contours of the marked regions 1,2 respectively corresponding to spectrum (a), and insets (b1) and (b2) show contours of the corresponding regions of spectrum (b).

angle selective excitation (Figure 6.4). Signal to noise ratios (S/N) of various peaks as per labels in Figure 6.7 are calculated and compared with that of the corresponding peaks of ^{1}H-^{15}N SOFAST-HMQC experiment acquired using polychromatic Pc9 pulse shape. A higher value of S/N corresponds to the better sensitivity of the peak. S/N of the corresponding peaks of the ^{1}H-^{15}N SOFAST-HMQC spectrum is calculated independently for both the pulse types. Relative difference in S/N ratio is obtained by subtracting the S/N value of respective peaks using Pc9 pulse from that of NBSEP II pulse and then divided by the S/N of same peak corresponding to that of Pc9 pulse. Relative difference in S/N ratios has been calculated for various peaks of the HMQC

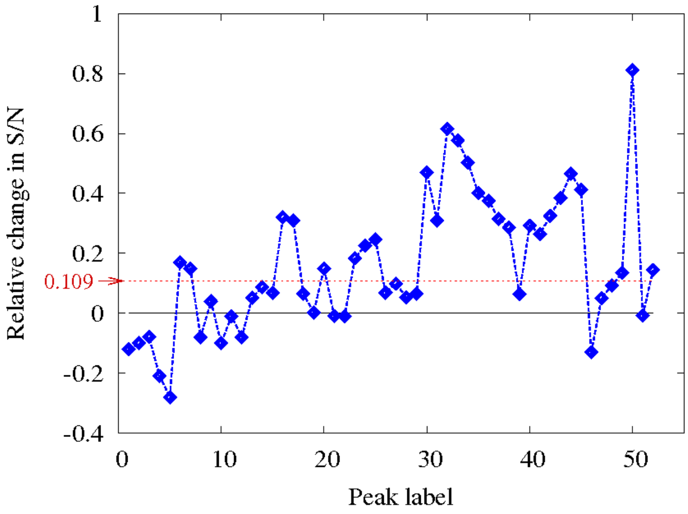

Figure 6.9: Plot showing the relative increase in S/N of respective peaks (as labeled in Figure 6.7) in 1H-15N SOFAST-HMQC experiment. The blue dotted curve with diamonds shows the relative difference in S/N in case of NBSEP-II as compared to that of Pc9. The dotted red line (y= 0.109) is the average value of the relative increase in the S/N ratio for the pulse scheme using numerically optimized pulse shapes.

spectrum. These relative S/N ratios have been plotted against the peak label as shown in Figure 6.9.

The horizontal line (y=0) in Figure 6.9 corresponds to the equal values of S/N of respective peaks in the SOFAST-HMQC spectra with two different pulse types. A positive value of S/N stands for higher sensitivity while negative value signifies lower sensitivity of respective peaks in case of NBSEP II pulse. As can be seen clearly, a positive value of relative S/N value is found to exist for most of the peaks. Average value of this relative S/N values is represented by a horizontal dotted line at y=0.109. Therefore one can say that a 10.9% of improvement in the sensitivity is seen in case of a SOFAST-HMQC experiment with a numerically optimized pulse for selectively optimized flip angle excitation. The explicit values of the relative changes in the S/N ration of each peak is given in Table 6.1.

Table 6.1: Relative variation in signal to noise ratio in ^{1}H-^{15}N SOAFST-HMQC experiment corresponding to peak labels are as per Figure 6.7.

Peak label	Relative S/N $\frac{(NBSEPII-Pc9)}{Pc9}$	Peak label	Relative S/N $\frac{(NBSEPII-Pc9)}{Pc9}$
1	-0.1201	27	0.0991
2	-0.1061	28	0.0535
3	-0.0874	29	0.0646
4	-0.2110	30	0.4703
5	-0.2804	31	0.3094
6	0.1762	32	0.6155
7	0.1539	33	0.5772
8	-0.0869	34	0.5028
9	0.0471	35	0.4017
10	-0.1052	36	0.3756
11	-0.0184	37	0.3144
12	-0.0820	38	0.2858
13	0.0527	39	0.0643
14	0.0876	40	0.2924
15	0.0690	41	0.2650
16	0.3229	42	0.3249
17	0.3167	43	0.3849
18	0.0654	44	0.4653
19	0.0022	45	0.4129
20	0.1498	46	-0.1306
21	-0.0097	47	0.0508
22	-0.0111	48	0.0927
23	0.1840	49	0.1355
24	0.2255	50	0.8108
25	0.2462	51	-0.0081
26	0.0682	52	0.1439

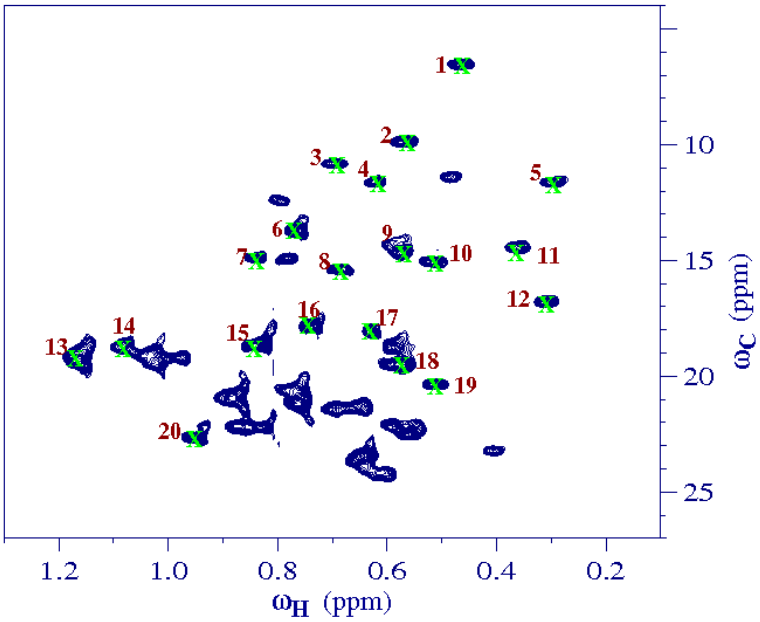

Figure 6.10: 2D NMR spectrum of Ubiquitin is shown corresponding to ^{1}H-^{13}C SOFAST-HMQC experiment acquired using numerically optimized pulse shape NBSEP I.

6.2.4 ^{1}H-^{13}C SOFAST-HMQC experiment

The $^1H -^{13} C$ SOFAST-HMQC spectrum was acquired with numerically optimized band-selective shaped pulse NBSEP I which is designed to excite a bandwidth of 1200Hz. Different parts of the aliphatic region ranging from (-0.5 to 1.5 ppm) and (1.5 to 3.5 ppm) were acquired separately. A ^{1}H-^{13}C SOFAST-HMQC spectrum is shown in Figure 6.10 where the various correlations have been numbered.

Keeping the same constraints on acquisition time, bandwidths, flip angle and relaxation delay, ^{1}H-^{13}C SOFAST-HMQC experiments in the given ranges are also acquired with standard polychromatic Pc9 pulse shape. The spectra obtained in this case is compared with that of the ^{1}H-^{13}C SOFAST-HMQC spectrum acquired using NBSEP I pulse. Apart from the β angle pulse shapes (and their corresponding parameters) all other experimental parameters remain same. The spectra acquired in different ranges in both the cases are compared for resolution and sensitivity differences. Figure 6.11 contains the spectra resulting with both the pulse types. Figure 6.11(a,b) contain the 2D HMQC spectra of Ubiquitin acquired in the ^{1}H spectral ranges of (1.5 to 3.5 ppm) and (-0.5 to 1.5 ppm) respectively. Parts (c, d) of Figure 6.11 contain the correspond-

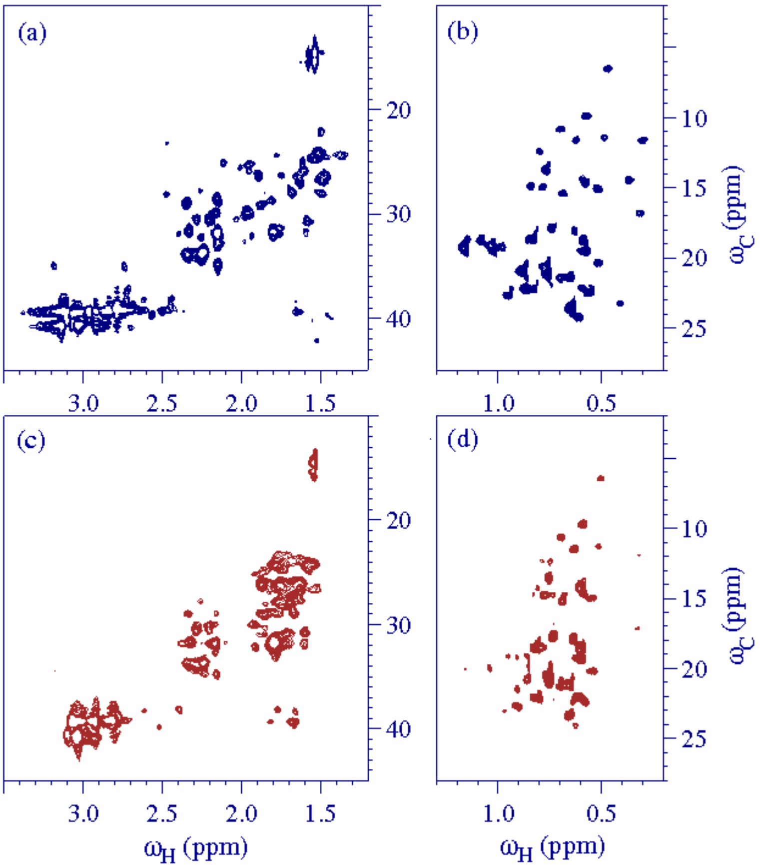

Figure 6.11: ^{1}H-^{13}C SOFAST-HMQC spectra of ubiquitin is shown separately for different portions of the aliphatic region. Spectra in (a,b) correspond to the ^{1}H-^{13}C SOFAST-HMQC experiment using NBSEP I and (c,d) correspond to that of Pc9.

ing NMR spectra obtained as a result of ^{1}H-^{13}C SOFAST-HMQC experiment with a polychromatic Pc9 pulse shape.

It is observed that by using the standard Pc9 pulse shape poorly resolved spectral peaks are obtained, while peaks are much better resolved in case of numerical NBSEP-I pulse. Several peaks in Figure 6.11(c) are found to be missing as compared to Figure 6.11(a). This is due to the poor resolution which gives rise to a lumpy structure instead of distinguishable peaks. A glimpse of Figure 6.11 is enough to conclude that use of NBSEP I pulse in ^{1}H-^{13}C SOFAST-HMQC experiment gives rise to a better resolved spectrum.

6.2.4.1 Quantitive analysis

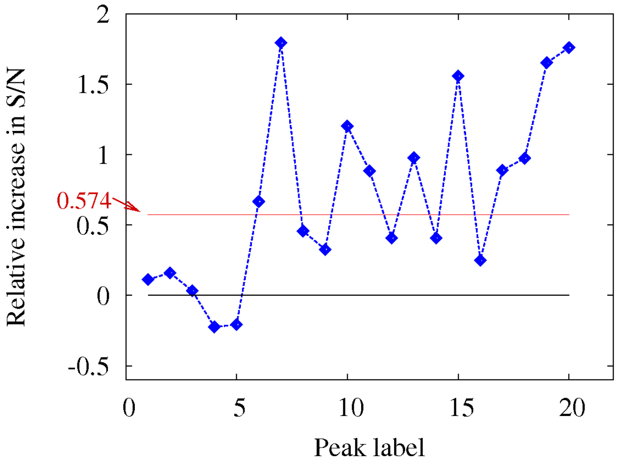

Figure 6.12: Plot showing the relative variation in the S/N ratios of various peaks (as labeled in Figure 6.10) obtained using NBSEP-I as compared to a standard Pc9 pulse in the ^{1}H-^{13}C SOFAST-HMQC experiment. The solid black line (y=0) is the reference, and the solid red line (y= 0.574) is the average value of the relative increase in the S/N ratio in case of numerically optimized pulse shapes.

Quantitative analysis of the ^{1}H-^{13}C SOFAST-HMQC experiment is carried out to compare the spectra as obtained using NBSEP I and polychromatic Pc9 pulses for the β angle selective excitation (Figure 6.4). Signal to noise ratios (S/N) of various peaks as per labels in Figure 6.10 are calculated and compared with that of the corresponding peaks of ^{1}H-^{13}C SOFAST-HMQC experiment acquired using polychromatic Pc9 pulse shape. Relative difference in S/N ratios has been calculated for various peaks of the SOFAST-HMQC spectrum. These relative S/N ratios have been plooted against the peak label as shown in Figure 6.12.

The horizontal line (y=0) in Figure 6.12 corresponds to the equal values of S/N of respective peaks in the SOFAST-HMQC spectra with two different pulse types. A positive value of S/N stands for higher sensitivity while negative value signifies lower sensitivity of respective peaks in case of NBSEP I pulse. As can be seen clearly, a positive value of relative S/N value is found to exist for most of the peaks. Average value of this relative S/N values is represented by a horizontal dotted line at y=0.574. Therefore one can say that a 57.4% of improvement in the sensitivity is seen in case

Table 6.2: Relative variation in signal to noise ratio in ^{1}H-^{13}C SOAFST-HMQC experiment corresponding to peak labels are as per Figure 6.10.

Peak label	Relative S/N $\frac{(NBSEPI-Pc9)}{Pc9}$	Peak label	Relative S/N $\frac{(NBSEPI-Pc9)}{Pc9}$
1	0.1118	11	0.8845
2	0.1599	12	0.4080
3	0.0324	13	0.9780
4	-0.22411	14	0.4074
5	-0.2073	15	1.5581
6	0.6673	16	0.2496
7	1.7936	17	0.8898
8	0.4577	18	0.9742
9	0.3266	19	1.6527
10	1.2028	20	1.7605

of a SOFAST-HMQC experiment with a numerically optimized pulse for selectively optimized flip angle excitation. This huge improvement is mainly attributed to the lack of existence of resolved peaks in case of polychromatic Pc9 pulse shapes. The explicit values of relative change in the S/N values are given in Table 6.2.

6.3 Low Temperature Protein Dynamics

Another example in support of the versatility of a numerically optimized pulse is being presented here. Numerically optimized band-selective pulse (NBSEP II) is used here in the ^{1}H-^{15}N SOFAST-HMQC experiment of human protein ubiquitin at different values of temperatures. With decreasing temperature, various types of molecular motions contributing to the protein dynamics get constrained. The dynamics of a small molecule at lower temperature hence resembles the dynamics of a larger molecule at higher temperature. It is well known that correlation time of a protein [43] at room temperature is directly proportional to its molecular weight. Furthermore due to restricted protein dynamics at lower temperature, the correlation time increases with decreasing temperature. Hence smaller proteins at low temperatures can simulate the room temperature dynamics of larger proteins. In this section, ^{1}H-^{15}N SOFAST-HMQC experiments using NBSEP II are acquired at low temperatures ranging from 278-298 K and hence simulating the dynamics of a bigger protein.

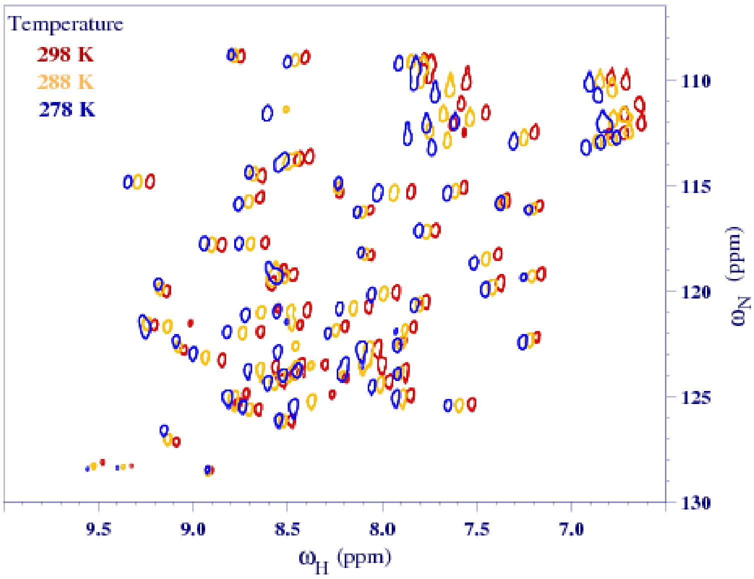

Figure 6.13: ^{1}H-^{15}N SOFAST-HMQC spectrum obtained using NBSEP II at three different temperatures: 298K, 288K and 278K. Expected shift in the resonances is observed with decreasing temperature values.

Due to practical difficulties like resolution and sensitivity, complete characterization of larger protein molecules is a challenge & different ways are adopted to study the dynamics of large proteins [167]. In order to test the efficacy of numerically optimized pulse profiles on large proteins with longer relaxation times, $^1H-^{15}N$ SOFAST-HMQC experiments on the model protein ubiquitin were performed at lower temperatures. Rotational correlation (τ_c) of a molecule with hydrodynamic radius 'r', oriented in a solvent with viscosity 'η' at temperature 'T' time is given as

$$\tau_c = \frac{4\pi\eta r^3}{3kT} \tag{6.10}$$

where 'k' is the Boltzmann constant.

^{1}H-^{15}N SOFAST-HMQC experiment of ubiquitin(^{13}C, ^{15}N) was acquired at five different temperatures: 298 K, 293 K, 288 K, 283 K and 278 K. Spectra obtained at various temperature values were superimposed. Fixing the peak at (8.9ppm, 128.5ppm) as reference (as it does not shift in this temperature range [183]), the expected shifting of all other resonances is observed [183, 184]. Figure 6.13 shows the spectra at three temperatures values: 298K, 288K and 278K. A shift in the peaks towards higher ppm values with decreasing temperature is clearly observed. This observation matches with the known shift with temperature in the single quantum heteronuclear correlation peaks [183]. Even at lower temperatures (and for "larger" simulated proteins), the numerically optimized pulses perform well in terms of good signal-to-noise ratios and uniform excitation over the desired bandwidth. A useful future application of these numerically optimized pulses would hence be in designing correlation experiments for large, multi-domain proteins.

6.4 Conclusions

This chapter mainly deals with NMR methodology development with an emphasis on the numerically optimized shaped pulses optimized using GRAPE. GRAPE optimized numerical pulses have good selectivity and are robust against rf inhomogeneity. In this chapter, numerical pulses of desired angles, duration and bandwidths are optimized using GRAPE, which is accessed via SIMPSON simulation tool. The simulations of the spin response are carried out under the effect of various shaped pulse assuming a single spin Bloch model in NMRSIM simulator. The numerically optimized pulse is found to give a better spin response as compared to that of a conventionally used shaped pulse (Pc9). In this chapter three applications of the numerically optimized shaped pulses are discussed (1) To simulate a QFT on a hybrid qubit-qutrit system. (2) Comparison of the NBSEP I and NBSEP II pulses with a conventionally used band-selective pulse in ^{1}H-^{13}C and ^{1}H-^{15}N SOFAST-HMQC experiments respectively. (3) Simulation of the room temperature protein dynamics of large proteins by smaller proteins at low temperatures. In all the three cases, the numerically optimized pulses perform quite well, as compared to spectra acquired with standard pulse shapes.

Chapter 7

Summary and future outlook

This thesis is focused on the design and implementation of various quantum computing protocols, and the study of the inherent resources that provide power for quantum computational tasks. The experiments were performed on the nuclear spins based quantum computers that harness the intrinsic magnetic properties of the nuclear spins, which are manipulated by specifically tailored radio frequency pulses (quantum gates) to perform the desired computational tasks.

This thesis begins with the study of novel aspects of multipartite entanglement, addressing a fundamental question: “how does a multipartite quantum system store information?". This question is tackled in the context of a three-qubit system. A thorough analysis of the two inequivalent entanglement classes: Greenberger-Horne-Zeilinger (GHZ) and Werner (W) class of states is carried out. Experimental evidence is obtained in support of the theoretical hypotheses that W-states do not have irreducible three-party correlations whereas the three-party non-local correlations exhibited by GHZ states are irreducible. This feature is contradicted by an interesting W-superposition state, which is obtained from maximally entangled GHZ state by SLOCC, but its three-party non-local correlations can be completely and uniquely obtained from the reduced two-party correlations. This is an interesting development that adds to the existing knowledge of multipartite entanglement.

Another major direction followed in the present thesis deals with higher dimensional quantum objects for computation, with a focus on different features of a single-qutrit system. A single-qutrit is the smallest, indivisible quantum system exhibiting quantum features. This makes a qutrit an interesting system to be explored. The study begins with the understanding of Majorana geometrical picture of a single-qutrit in three-dimensional real coordinate space. Single-qutrit dynamics under SO(3) and SU(3) transformations is studied and a correspondence is drawn between the single-qutrit unitary transformations in three-dimensional Hilbert space and the rotations on the Majorana sphere. The insights gained are used to obtain the decompositions of single-qutrit quantum gates. An intuitive geometrical picture of a single-qutrit magnetization vector is also proposed, which provides a physical picture to the continuous spectrum of values in the range [0,1] possessed by the magnitude of the magnetization vector.

NMR experimental implementations of the basic building blocks for single-qutrit quantum computing are implemented on a spin-1 system oriented in a liquid crystal. A single-qutrit is also exploited to experimentally perform a useful computational task, which is of determine the parity of a permutation among three- objects. Though this is a toy algorithm, however it provides confirmation for the existence of the underlying quantum resource in an indivisible system. The speedup in a single-qutrit quantum computation is attributed to contextuality, which is explored in depth. An NMR experimental test is performed that uses a set of nine-observables to reveal the contextuality of almost all single-qutrit states.

Quantum computing protocols for higher dimensional systems are proposed and implemented on a four-qubit quantum emulator. An explicit implementation of the QFT is carried out on a qubit-qubit-qutrit system. The QFT is a key ingredient in several quantum computational algorithms, and hence its implementation is an important step towards hybrid-qudit computing. A part of the study is focused on NMR methodology development with an emphasis on the applications of numerically optimized radio-frequency pulses for biomolecular NMR and quantum gate optimizations.

7.1 Future outlook

In the context of multipartite entanglement, the developments made in case of three-qubit systems can be explored in n-party qubit systems say for the case of four-qubits (which have nine inequivalent entanglement classes). Further, the theoretical propositions regarding reconstruction of three-qubit correlations from reduced two-party correlations can be extended to higher dimensional three-party quantum systems. These future prospects of the problem are non-trivial tasks, however they may lead to some interesting developments in the understanding of multipartite entanglement correlations.

In the context of qutrit computing, this is an area of much recent research and thus there can be several new directions to be followed. Few of these are summarized below:

- In this thesis, Majorana representation of a single-qutrit is studied, which is given by two points on the surface of a unit sphere. It is to be noted that this representation is provided only for pure single qutrit states. Thus one may think of the possible extensions to the geometrical realization of single-qutrit mixed states.
- There are certain theoretical propositions that discuss single-qutrit based quantum gates such as a three-box paradox. One may think of NMR experimental implementations of such algorithms.
- From the NMR point of view, one may develop the analytic set of calculations that explain the spin-1 dynamics. This can be further extended to a complete study of spin-1 relaxation.

Appendix A

Orienting spin-1 in a liquid crystal

A.1 Liquid crystal

Liquid crystal exists in a liquid phase and possess features of a crystal under given circumstances. The molecular components of a liquid crystal have a preferred direction of orientation and thus exhibit anisotropy like a crystal [185]. Depending upon liquid crystalline properties, they can be distinguished as : thermotropic, lyotropic and metallotropic liquid crystals. Thermotropic and lyotropic liquid crystals consist of organic molecules while metallotropic liquid crystals have both organic and inorganic constituents.

Thermotropic liquid crystals show liquid crystalline phase that varies with temperature. Liquid crystalline phase in lyotropic liquid crystals is sensitive to both concentration as well as temperature. Molecules of a liquid crystal may have one or more preferred directions of orientation. The alignment of molecules is signified by a vector 'director' and the anisotropy is quantified by the 'order parameter'. Therefore depending upon number of directions of orientation, liquid crystals may exist in a uniaxial or biaxial phases. Liquid crystalline phases can further be classified as nematic, smectic and chiral phases.

The liquid crystal of our interest is a lyotropic liquid crystal in a biaxial nematic phase [186]. We use a lyotropic liquid crystal that consists of Potassium laurate (25.96%), 1-Decanol (6.24%) and H_2O (67.8%). A microscopic image of this anisotropic liquid crystal at room temperature is obtained via polarization microscope (Fig. A.1).

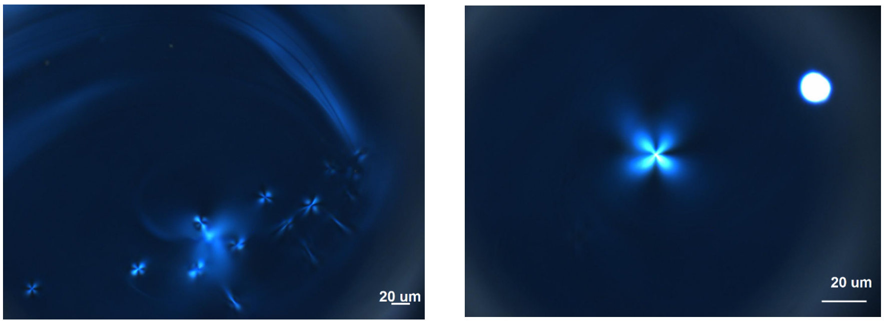

Figure A.1: Microscopic view of the lyotropic liquid crystal.
A polarization microscope image of the lyotropic liquid crystal at room temperature. The presence of Maltese cross clearly indicates the existence of the liquid crystalline phase. The images are acquired at two different resolving powers.

A.2 Details of the sample

Single qutrit used in this work is the deuterium nucleus (^{2}D) of Chloroform-D molecule, oriented in a lyotropic crystal. In order to obtain the lyotropic liquid crystal, the components: Potassium laurate (25.96%), 1-Decanol (6.24%) and H_2O (67.8%) are taken in the prescribed amounts, and mixed together in a veyl. The components are mixed properly to obtain a homogeneous mixture. Obtaining a homogeneous mixture is the most crucial part of the protocol, thus one may consider to centrifuge the mixture back and forth for several hours. This, after transferring to the NMR tube, is allowed to sonicate until a clear solution is obtained. The sonication is done for several hours in steps of 30 minutes each. The temperature of water bath is kept at a value > 40^0C.

In liquid crystalline phase, this solution appears to be a thick liquid with high viscosity and turbid appearance. Once the liquid crystal is ready, 50 μl of $CDCl_3$ (Chloroform-D) is added to 500 μl of the liquid crystal directly into the NMR tube. The liquid crystal provides an anisotropic environment to the chloroform molecule ($CDCl_3$). In order to have a proper alignment, the temperature of the solution is raised to 50^0C so that the liquid crystal exhibits an isotropic phase. Once chloroform is mixed, the solution is brought back to the room temperature. The sample is again kept for sonication keeping in mind that the temperature of the water bath should not exceed the boiling point of chloroform.

Decanol used in this sample is purchased from ‘Sigma-Aldrich’, ‘Deutrated Chloroform' is an NMR solvent, though here is utilized in traces. This is purchased from 'Merck millipore'. 'Potassium Laurate' is the potassium salt of the Lauric acid obtained from 'Viva corporation, Mumbai' (Viva Corporation, India House No 1, Kemps Corner, Bombay 400 026 INDIA.). The microscopic images of the liquid crystal were acquired from the lab of Dr. S. K. Pal (Department of Chemical sciences, IISER Mohali).

A.3 NMR analysis of the liquid crystalline phase

In lyotropic liquid crystals, the liquid crystalline phase depends upon the concentration of the constituents. Further there is a change in the anisotropy with change in temperature. The variation of anisotropy is studied here using deuterium NMR for a given concentration of the liquid crystal.

Here liquid crystalline behaviour is observed by acquiring the NMR signal of small molecule ($CDCl_3$) oriented in the lyotropic liquid crystal. The nucleus of interest here is Deuterium, therefore all the experiments on this sample are performed in the 'unlock' condition of the sample. Manual shimming in the 'gs' mode is performed. The experiments were performed on triple resonance QXI or TXI probeheads and a broad band BBO probehead on a 600 MHz Avance III spectrometer. The temperature control is provided by the BCU unit which is capable of providing temperature of the ranges -50^0 C to +80^0 C. It is advised to leave the sample in the magnet for a few hours before performing the experiments, for stabilization.

The NMR signal of the liquid crystal is observed for a wide range of temperature. The anisotropy of the liquid crystal is reflected in the relative separation between the spectral lines. Fig. A.2 shows the NMR spectra of the Chloroform-D molecule oriented in a lyotropic liquid crystal at different values of temperature.

As shown in Fig. A.2, NMR spectral lines depicting the degenerate single quantum transitions of a qutrit overlap with each other at 313 K, named as 'line 1'. Another line, named 'line 2' corresponds to the isotropic part of $CDCl_3$ that remained unoriented in the liquid crystal. The position of line 2 remains unchanged with change of temperature. As the temperature begins to decrease, line 1 splits into two lines. The difference between these two lines increases with decreasing temperature. Increased separation is the signature of increased anisotropy. A suitable value of temperature is chosen, at which the sample is used to perform quantum computational tasks.

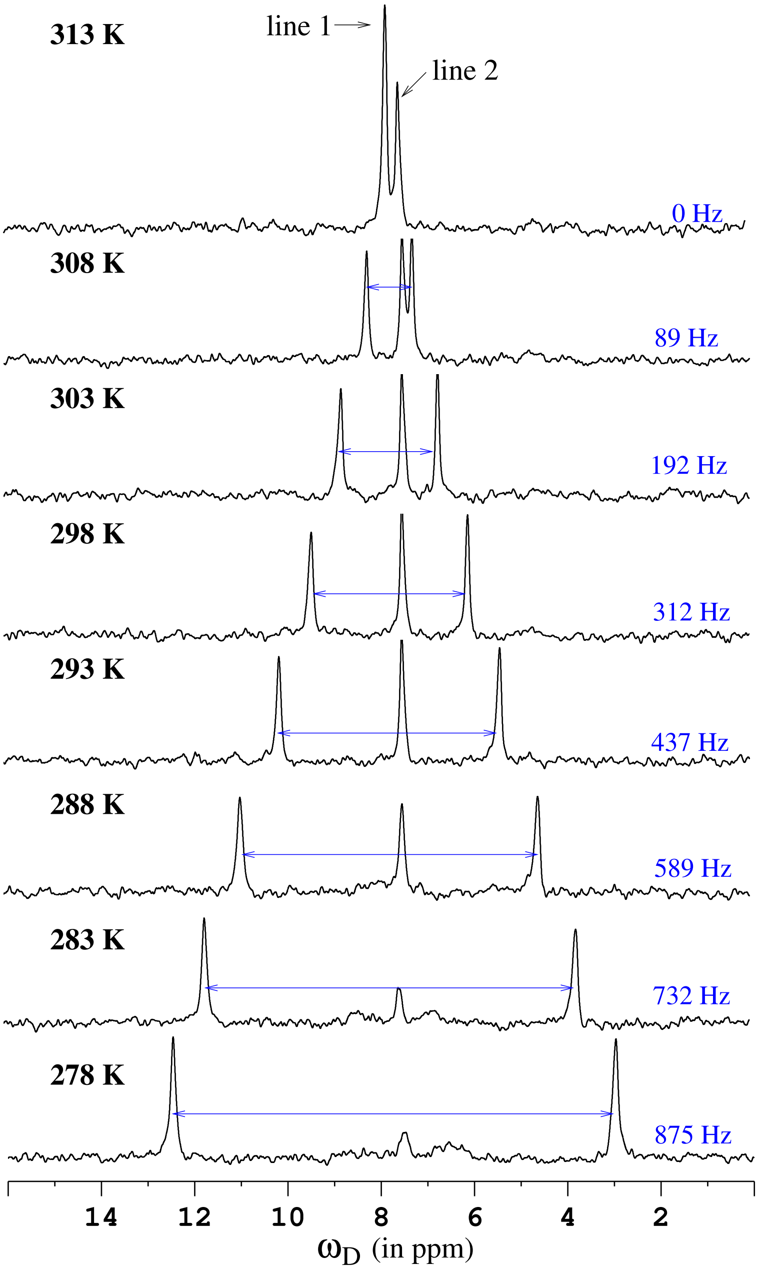

Figure A.2: ^{2}D NMR spectrum of the chloroform molecule oriented in a liquid crystal.

References

[1] M. A. Nielsen and I. L. Chuang, *Quantum Computation and Quantum Information*, Cambridge University Press, Cambridge UK, 2000. 1, 3, 6, 7, 55, 91, 96, 120

[2] A. V. Sergienko, *Quantum Communications and Cryptography*, Taylor & Frncis Group, U.S., 2006. 1

[3] J. Audretsch, *Entangled Systems*, Wiley-VCH, Germany, 2005. 1

[4] J. Stolze and D. Suter, *Quantum computing : a short course from theory to experiment*, Wiley-VCH, 2008., Weinheim, 2008. 1, 2

[5] T. D. Ladd, F. Jelezko, R. Laflamme, Y. Nakamura, C. Monroe, and J. L. O'Brien, Quantum computers, Nature **464**(7285), 45 (2010). 1, 2, 3, 15, 56, 91, 143

[6] I. S. Oliveira, T. J. Bonagamba, R. S. Sarthour, J. C. Freitas, and E. R. deAzevedo, *NMR Quantum Information Processing*, Elsevier, Amsterdam, The Netherlands, 2007. 1, 2

[7] R. P. Feynmann, On quantum physics and computer simulation, Int. J. Quant. Inf. **21**, 7 (1982). 1

[8] D. Deutsch, Quantum computational networks, Proc. R. Soc. London A **425**, 73 (1989). 1, 91

[9] D. Deutsch and R. Jozsa, Rapid solution of problems by quantum computation, Proc. R. Soc. London A **439**, 553 (1992). 1, 91

[10] Arvind and D. Collins, Scaling issues in ensemble implementations of the Deutsch-Jozsa algorithm, Phys. Rev. A **68**, 052301 (2003). 1, 91

[11] K. Dorai, Arvind, and A. Kumar, Implementation of a Deutsch-like quantum algorithm utilizing entanglement at the two-qubit level on an NMR quantum-information processor, Phys. Rev. A **63**, 034101 (2001). 1

[12] D. Collins, K. W. Kim, and W. C. Holton, Deutsch-Jozsa algorithm as a test of quantum computation, Phys. Rev. A **58**, R1633 (1998). 1

[13] Y. S. Weinstein, M. A. Pravia, E. M. Fortunato, S. Lloyd, and D. G. Cory, Implementation of the quantum Fourier transform, Phys. Rev. Lett. **86**, 1889 (2001). 1, 11, 27, 120, 131

[14] Y. Cao, S. G. Peng, C. Zheng, and G. L. Long, Quantum Fourier Transform and Phase Estimation in Qudit System, Commun. Theor. Phys. **55**, 790 (2011). 1, 120

[15] P. W. Shor, Polynomial time algorithms for prime factorization and discrete logarithms on a quantum computer, SIAM J. Comput. **26**, 1484 (1997). 1, 92, 120

[16] L. K. Grover, Quantum Mechanics Helps in Searching for a Needle in a Haystack, Phys. Rev. Lett. **79**, 325 (1997). 1

[17] M. A. Solis-Prosser, O. Jimenez, L. Neves, and A. Delgado, Quantum teleportation via quantum channels with non-maximal Schmidt rank, Physica Scripta , 014058 (2013). 1

[18] V. Veitch, S. A. H. Mousavian, D. Gottesman, and J. Emerson, The resource theory of stabilizer quantum computation, New J. Phys. **16**(1), 013009 (2014). 1

[19] N. Wiebe, D. Braun, and S. Lloyd, Quantum Algorithm for Data Fitting, Phys. Rev. Lett. **109**, 050505 (2012). 1

[20] A. M. Souza, J. Zhang, and R. Laflamme, Experimental magic state distillation for fault-tolerant quantum computing, Nat. Commun. **2**, 169 (2011). 1

[21] M. Howard, J. Wallman, V. Veitch, and J. Emerson, Contextuality supplies the 'magic' for quantum computation, Nature **510**, 351 (2014). 1

[22] I. Bengtsson, K. Blanchfield, E. Campbell, and M. Howard, Order 3 symmetry in the Clifford hierarchy, J. Phys. A **47**(45), 455302 (2014). 2

[23] D. N. Biggerstaff, R. Kaltenbaek, D. R. Hamel, G. Weihs, T. Rudolph, and K. J. Resch, Cluster-State Quantum Computing Enhanced by High-Fidelity Generalized Measurements, Phys. Rev. Lett. **103**, 240504 (2009). 2

[24] T. Tanamoto, Y.-x. Liu, X. Hu, and F. Nori, Efficient Quantum Circuits for One-Way Quantum Computing, Phys. Rev. Lett. **102**, 100501 (2009). 2

[25] C. H. Banett and D. P. DiVincenzo, Quantum information and computation, Nature **404**, 247 (2000). 2

[26] D. Kielpinski, C. Monroe, and D. J. Wineland, Architecture for a large-scale ion-trap quantum computer, Nature **417**, 709 (2013). 2

[27] J. I. Cirac and P. Zoller, Quantum Computations with Cold Trapped Ions, Phys. Rev. Lett. **74**, 4091 (1995). 2

[28] L. Childress and R. Hanson, Diamond NV centers for quantum computing and quantum networks, MRS Bulletin **38**, 134 (2013). 2

[29] K. Inaba, Y. Tokunaga, K. Tamaki, K. Igeta, and M. Yamashita, High-Fidelity Cluster State Generation for Ultracold Atoms in an Optical Lattice, Phys. Rev. Lett. **112**, 110501 (2014). 2

[30] D. Loss and D. P. DiVincenzo, Quantum computation with quantum dots, Phys. Rev. A **57**, 120 (1998). 2

[31] E. Knill and R. Laflamme, Power of One Bit of Quantum Information, Phys. Rev. Lett. **81**, 5672 (1998). 2

[32] B. Criger, G. Passante, D. Park, and R. Laflamme, Recent advances in nuclear magnetic resonance quantum information processing, Phil. Trans. R. Soc. A **370**, 4620 (2012). 2, 143

[33] D. P. DiVincenzo, The Physical Implementation of Quantum Computation, Fortschritte der Physik **48**(9-11), 771 (2000). 2

[34] F. Bloch, W. W. Hansen, and M. Packard, The Nuclear Induction Experiment, Phys. Rev. **70**, 474 (1946). 2

[35] E. M. Purcell, H. C. Torrey, and R. V. Pound, Resonance Absorption by Nuclear Magnetic Moments in a Solid, Phys. Rev. **69**, 37 (1946). 2

[36] W. Gerlach and O. Stern, Uber die Richtungsquantelung im Magnetfeld, Ann. Physik **379**, 673 (1924). 2

[37] I. I. Rabi, J. R. Zacharias, S. Millman, and P. Kusch, A New Method of Measuring Nuclear Magnetic Moment, Phys. Rev. **53**, 318 (1938). 2

[38] R. R. Ernst, Sensitivity Enhancement in Magnetic Resonance, Adv. Mag. Reson. **2**, 1 (1966). 2

[39] M. H. Levitt, *Spin dynamics : Basics of nuclear magnetic resonance*, John Wiley and Sons, Chichester England, 2008. 2, 3, 5, 7, 55, 76, 96, 121, 123

[40] R. R. Ernst, G. Bodenhausen, and A. Wokaun, *Principles of nuclear magnetic resonance in one and two dimensions*, Oxford University Press, New York, 1987. 2, 3, 5, 70, 149, 151

[41] D. W. McRobbie, E. A. Moore, M. J. Graves, and M. R. Prince, *MRI: From Picture to Proton*, Cambridge University Press, New York, 2006. 2, 3

[42] C. P. Slichter, *Principles of Magnetic resonance*, Springer, New York, 1996. 2, 55, 76, 121, 123

[43] J. Cavanaugh, W. J. Fairbrother, A. G. P. III, and N. J. Skelton, *Protein NMR spectroscopy: Principles and practice*, Academic Press Inc., San Diego USA, 1995. 2, 3, 151, 166

[44] J. Natterer and J. Bargon, Parahydrogen induced polarization, Prog. Nuc. Magn. Reson. **31**, 293 (1997). 2

[45] D. Lu, N. Xu, R. Xu, H. Chen, J. Gong, X. Peng, and J. Du, Simulation of Chemical Isomerization Reaction Dynamics on a NMR Quantum Simulator, Phys. Rev. Lett. **107**, 020501 (2011). 3

[46] N. Gogna, M. Krishna, A. M. Oommen, and K. Dorai, Investigating correlations in the altered metabolic profiles of obese and diabetic subjects in a South Indian Asian population using an NMR-based metabolomic approach, Molecular Biosystems **11**, 595 (2015). 3

[47] A. L. Christopher, M. M. Jonathan, and W. J. Peng, Theory and Applications of NMR-Based Screening in Pharmaceutical Research, Chem. Rev. **104**, 3641 (2004). 3

[48] D. E. Bugay, Solid state Nuclear magnetic resonance spectroscopy: Theory and Pharmaceutical applications, Pharmaceutical Research **10** (1993). 3

[49] W. S. Price, *NMR studies of translational motion*, Cambridge University Press, UK, 2009. 3

[50] J. N. Robinson, A. Coy, R. Dykstra, C. D. Eccles, M. W. Hunter, and P. T. Callaghan, Two-dimensional NMR spectroscopy in Earth's magnetic field, J. Magn. Reson. **182**(2), 343 (2006). 3

[51] A. Kumar, R. C. R. Grace, and P. K. Madhu, Cross-correlations in NMR, Prog. Nuc. Magn. Reson. **37**, 191 (2000). 3

[52] H. G. Krojanski and D. Suter, Decoherence in large NMR quantum registers, Phys. Rev. A **74**, 062319 (2006). 3

[53] G. A. Álvarez and D. Suter, NMR Quantum Simulation of Localization Effects Induced by Decoherence, Phys. Rev. Lett. **104**, 230403 (2010). 3

[54] G. Teklemariam, E. M. Fortunato, M. A. Pravia, T. F. Havel, and D. G. Cory, Experimental investigations of decoherence on a quantum information processor, Chaos, Solitons and Fractals **16**, 457 (2003). 3

[55] H. Singh, Arvind, and K. Dorai, Experimental protection against evolution of states in a subspace via a super-Zeno scheme on an NMR quantum information processor, Phys. Rev. A **90**, 052329 (2014). 3

[56] K. Zangger, Pure shift NMR, Prog. Nuc. Magn. Reson. **86**, 1 (2015). 3

[57] P. Schanda and B. Brutscher, Very Fast Two-Dimensional NMR Spectroscopy for Real-Time Investigation of Dynamic Events in Proteins on the Time Scale of Seconds, J. Am. Chem. Soc. **127**, 8014 (2005). 3, 12, 152, 153

[58] I. Noda, Progress in two-dimensional (2D) correlation spectroscopy, J. Mol. Struct. **799**(1-3), 2 (2006). 3, 151

[59] P. Schanda, E. Kupce, and B. Brutscher, SOFAST-HMQC experiments for recording two-dimensional hetronuclear correlation spectra of proteins within a few seconds, J. Bio. NMR **33**, 199 (2005). 3, 12, 152, 153

[60] P. Schanda, H. V. Melckebeke, and B. Brutscher, Speeding Up Three-Dimensional Protein NMR Experiments to a Few Minutes, J. Am. Chem. Soc. **128**, 28 (2006). 3, 152

[61] T. Kern, P. Schanda, and B. Brutscher, Sensitivity-enhanced IPAP-SOFAST-HMQC for fast-pulsing 2D NMR with reduced radiofrequency load, J. Magn. Reson. **190**, 333 (2008). 3, 152

[62] B. B. E. Lescop, P. Schanda, A set of BEST triple-resonance experiments for time-optimized protein resonance assignment, J. Magn. Reson. **187**, 163 (2007). 3, 152

[63] E. Kupce and R. Freeman, Fast multidimensional NMR by polarization sharing, Magn. Reson. Chem. **45**, 2 (2007). 3, 152

[64] E. Kupce and R. Freeman, Projection-reconstruction technique for speeding up multidimensional NMR spectroscopy, J. Am. Chem. Soc. **126**, 6429 (2004). 3, 152

[65] P. Schanda and B. Brutscher, Hadamard frequency-encoded SOFAST-HMQC for ultrafast two-dimensional protein NMR, J. Magn. Reson. **178**, 334 (2006). 3, 152

[66] D. Marion, Combining methods for speeding up multi-dimensional acquisition. Sparse sampling and fast pulsing methods for unfolded proteins, J. Magn. Reson. **206**, 81 (2010). 3, 152

[67] J. A. Jones, Quantum computing with NMR, Prog. Nuc. Magn. Reson. Spec. **59**, 91 (2011). 3, 56

[68] K. Dorai, T. S. Mahesh, Arvind, and A. Kumar, Quantum computation using NMR, Current Science **79**(10), 1447 (2000). 3, 91

[69] A. Abragam, *The principles of nuclear magnetism*, Oxford University Press, UK, 1961. 3, 5

[70] J. Keeler, *Understanding NMR spectroscopy*, Wiley, Cambridge, 2002. 3, 5

[71] J. J. Sakurai, *Modern Quantum Mechanics*, Pearson Education, New Delhi, 2007. 4, 102

[72] W. F. Kieffer, *The mole concept in chemistry*, Chapman & Hall, London, 1965. 6

[73] J. W. Gibbs, *Elementary principles in statistical mechanics*, Charles Scribner's sons, New York, 1902. 7

[74] D. Cory, M. Price, and T. Havel, Nuclear magnetic resonance spectroscopy: An experimentally accessible paradigm for quantum computing, Physica D **120**, 82 (1998). 7, 25

[75] T. S. Mahesh and A. Kumar, Ensemble quantum-information processing by NMR: Spatially averaged logical labeling technique for creating pseudopure states, Phys. Rev. A **64**, 012307 (2001). 8

[76] J. A. Jones, R. Hansen, and M. Mosca, Quantum Logic Gates and Nuclear Magnetic Resonance Pulse Sequences, J. Magn. Reson. **135**, 353 (1998). 9

[77] J. S. Lee and A. K. Khitrin, Projective measurement in nuclear magnetic resonance, App. Phys. Lett. **89**, 074105 (2006). 10

[78] G. M. Leskowitz and L. J. Mueller, State interrogation in nuclear magnetic resonance quantum-information processing, Phys. Rev. A **69**, 052302 (2004). 10, 26, 44

[79] G. Long, H. Yan, and Y. Sun, Analysis of density matrix reconstruction in NMR quantum computing, J. Opt. B **3**, 376 (2001). 10

[80] O. Gühne and G. Töth, Entanglement detection, Physics Reports **474**(1-6), 1 (2009). 11, 16, 31, 33, 37

[81] R. Horodecki, P. Horodecki, M. Horodecki, and K. Horodecki, Quantum entanglement, Rev. Mod. Phys. **81**, 865 (2009). 11, 15, 16, 31, 33, 37

[82] H. Kampermann, D. Bruss, X. Peng, and D. Suter, Experimental generation of pseudo-bound entanglement, Phys. Rev. A **81**, 040304 (2010). 11, 37

[83] A. Acin, A. Andrianov, L. Costa, E. Jane, J. I. Latorre, and R. Tarrach, Generalized Schmidt decomposition and classification of three-quantum-bit states, Phys. Rev. Lett. **85**, 1560 (2000). 11, 17, 37

[84] Sudha, A. R. U. Devi, and A. K. Rajagopal, Monogamy of quantum correlations in three-qubit pure states, Phys. Rev. A **85**, 012103 (2012). 11, 16, 37

[85] E. Specker, Die logik nicht gleichzeitig entscheidbarer aussagen, Dialectica **14**(2-3), 239 (1960). 12, 56, 92

[86] P. Kurzynski and D. Kaszlikowski, Contextuality of almost all qutrit states can be revealed with nine observables, Phys. Rev. A **86**, 042125 (2012). 12, 56, 92, 93, 96, 102

[87] S. Yu and C. H. Oh, State-Independent Proof of Kochen-Specker Theorem with 13 Rays, Phys. Rev. Lett. **108**, 030402 (2012). 12, 56, 92, 93, 96

[88] E. Majorana, Oriented atoms in a variable magnetic field, Nuovo Cimento **9**, 43 (1932). 12, 56

[89] N. Khaneja, T. Reiss, C. Kehlet, T. S. Herbrueggen, and S. J. Glaser, Optimal control of coupled spin dynamics: design of NMR pulse sequences by gradient ascent algorithms, J. Magn. Reson. **172**, 296 (2005). 12, 144, 148, 155

[90] Z. Tosner, T. Vosegaard, C. Kehlet, N. Khaneja, S. J. Glaser, and N. C. Nielsen, Optimal control in NMR spectroscopy: Numerical implementation in SIMPSON, J. Magn. Reson. **197**, 120 (2009). 12, 144, 148, 155

[91] R. Laflamme, E. Knill, W. H. Zurek, P. Catasti, and S. V. S. Mariappan, NMR Greenberger-Horne-Zeilinger states, Phil. T. Roy. Soc. A **356**, 1941 (1998). 15

[92] R. J. Nelson, D. G. Cory, and S. Lloyd, Experimental demonstration of Greenberger-Horne-Zeilinger correlations using nuclear magnetic resonance, Phys. Rev. A **61**, 022106 (2000). 15

[93] G. Teklemariam, E. M. Fortunato, M. A. Pravia, Y. Sharf, T. F. Havel, D. G. Cory, A. Bhattaharyya, and J. Hou, Quantum erasers and probing classifications of entanglement via nuclear magnetic resonance, Phys. Rev. A **66**, 012309 (2002). 15

[94] L. Chen and Y. X. Chen, Classification of GHZ-type, W-type and GHZ-W-type multiqubit entanglement, Phys. Rev. A **74**, 062310 (2006). 15

[95] N. Linden, S. Popescu, and W. K. Wootters, Almost every pure state of three qubits is completely determined by its two-particle reduced density matrices, Phys. Rev. Lett. **89**, 207901 (2002). 16, 41

[96] L. Diosi, Three party pure quantum states are determined by two two-party reduced states, Phys. Rev. A **70**, 010302 (2004). 16, 42

[97] D. Cavalcanti, L. M. Cioletti, and M. O. T. Cunha, Tomographic characterization of three-qubit pure states with only two-qubit detectors, Phys. Rev. A **71**, 014301 (2005). 16

[98] K. Dorai and A. Kumar, Cascades of selective pulses on connected single-quantum transitions leading to the selective excitation of multiple-quantum coherences, J. Magn. Reson. **114 A**, 155 (1995). 18, 21, 81

[99] X. Peng, X. Zhu, X. Fang, M. Feng, K. Gao, X. Yang, and M. Liu, Preparation of pseudo-pure states by line-selective pulses in nuclear magnetic resonance, Chem.Phys.Lett. **340**(5-6), 509 (2001). 18, 21

[100] I. L. Chuang, N. Gershenfeld, M. Kubinec, and D. W. Leung, Bulk quantum computation with nuclear magnetic resonance: Theory and experiment, Phil. T. Roy. Soc. A **454**, 447 (1998). 26

[101] A. R. U. Devi, Sudha, and A. K. Rajagopal, Majorana representation of symmetric multiqubit states, Quantum Information Processing **11**(3), 685 (2012). 37, 56

[102] N. Linden and W. K. Wootters, The parts determine the whole in a generic pure quantum state, Phys. Rev. Lett. **89**, 277906 (2002). 41

[103] N. S. Jones and N. Linden, Parts of quantum states, Phys. Rev. A **71**, 012324 (2005). 41

[104] I. Bengtsson and K. Zyczkowski, *Geometry of Quantum States : An introduction to quantum entanglement*, Cambridge University Press, New York, 2006. 55

[105] Arvind, K. S. Mallesh, and N. Mukunda, A generalized Pancharatnam geometric phase formula for three level quantum systems, J. Phys. A **30**, 2417 (1997). 56, 57, 69

[106] S. K. Goyal, B. N. Simon, R. Singh, and S. Simon, Geometry of the generalized Bloch sphere for qutrit, ArXiv e-prints, quant-ph/1111.4427v1 (2011). 56

[107] S. Ashourisheikhi and S. Sirsi, Local unitary equivalent classes of symmetric N-qubit mixed states., Int. J. Quant. Inf. **11**(8), 1350072 (2013). 56

[108] S. Sen, M. R. Nath, T. K. Dey, and G. Gangopadhyay, Bloch space structure, the qutrit wavefunction and atom-field entanglement in three-level systems, Annals of Physics **327**(2), 224 (2012). 56

[109] M. Planat, On the geometry and invariants of qubits, quartits and octits, Int. J. Geom. Methods Mod. Phys. **8**, 303 (2011). 56

[110] F. Yan, M. Yang, and Z. L. Cao, Optimal reconstruction of states in qutrits system, Phys. Rev. A **82** (2010). 56

[111] H. Mäkelä and A. Messina, Polynomial method to study the entanglement of pure N-qubit states, Phys. Rev. A **81**, 012326 (2010). 56

[112] H. Mäkelä and A. Messina, N -qubit states as points on the Bloch sphere, Physica Scripta **2010**(T140), 014054 (2010). 56

[113] J. H. Hannay, The Berry phase for spin in the Majorana representation, J. Phys. A **31**, L53 (1998). 56

[114] H. D. Liu and L. B. Fu, Representation of Berry Phase by the Trajectories of Majorana Stars, Phys. Rev. Lett. **113**, 240403 (2014). 56

[115] W. Ganczarek, M. Kuses, and K. Z. Zyczkowski, Barycentric measure of quantum entanglement, Phys. Rev. A **85**, 032314 (2012). 56

[116] J. H. Hannay, Chaotic analytic zero points : exact statistics for those of a random spin state., J. Phys. A **29**, L101 (1996). 56

[117] J. H. Hannay, The Majorana representation of polarization, and the Berry phase of light, J. Mod. Opt. **45**(5), 1001 (1998). 56

[118] B. Li, Z.-H. Yu, and S.-M. Fei, Geometry of quantum computation with qutrits, Scientific Reports **3**, 2594 (2013). 56

[119] V. E. Zobov and V. P. Shauro, On time optimal NMR control of states of qutrits represented by quadrupole nuclei with the spin I = 1, J. Exp. Theo. Phys. **113**(2), 181 (2011). 56

[120] C. Akyuz, E. Aydiner, and O. Mustecaplioglu, Thermal entanglement of a two-qutrit Ising system with Dzialoshinski-Moriya interaction, Optics Communications **281**, 5271 (2008). 56

[121] G. Molina-Terriza, A. Vaziri, J. Rehacek, Z. Hradil, and A. Zeilinger, Triggered qutrits for quantum communication protocols, Phys. Rev. Lett. **92**, 167903 (2004). 56

[122] D. Bruß and C. Macchiavello, Optimal eavesdropping in cryptography with three-dimensional quantum states, Phys. Rev. Lett. **88**, 127901 (2002). 56

[123] N. K. Langford, R. B. Dalton, M. D. Harvey, J. L. O'Brien, G. J. Pryde, A. Gilchrist, S. D. Bartlett, and A. G. White, Measuring entangled qutrits and their use for quantum bit commitment, Phys. Rev. Lett. **93**, 053601 (2004). 56

[124] B. P. Lanyon, T. J. Weinhold, N. K. Langford, J. L. O'Brien, K. J. Resch, A. Gilchrist, and A. G. White, Manipulating Biphotonic Qutrits, Phys. Rev. Lett. **100**, 060504 (2008). 56

[125] Z. Gedik, I. A. Silva, B. Cakmak, G. Karpat, E. L. G. Vidoto, D. O. Soares-Pinto, E. R. deAzevedo, and F. F. Fanchini, Computational speed-up with a single qudit, Scientific Reports **5**, 14671 (2015). 56

[126] M. Gell-Mann and Y. Neeman, *The eightfold way*, W.A. Benjamin, Michigan, 1964. 63, 69

[127] Arvind, Quantum entanglement and quantum computational algorithms, Pramana - J. Phys. **56**, 357 (2001). 91

[128] Arvind, G. Kaur, and G. Narang, Optical implementations, oracle equivalence, and the Bernstein-Vazirani algorithm, J. Opt. Soc. Am. B **24**, 221 (2007). 91

[129] D. Deutsch, Quantum theory, the Church-Turing principle and the universal quantum computer, Proc. R. Soc. London A **400**, 97 (1989). 91

[130] D. Collins, Discrimination of unitary transformations in the Deutsch-Jozsa algorithm: Implications for thermal-equilibrium-ensemble implementations, Phys. Rev. A **81**, 052323 (2010). 91

[131] A. Cabello, Proposed experiments of qutrit state-independent contextuality and two-qutrit contextuality-based nonlocality, Phys. Rev. A **85**, 032108 (2012). 92, 93

[132] A. Peres, *Quantum Theory: Concepts and Methods*, Kluwer Academic Publishers, The Netherlands, 1993. 92

[133] S. Kochen and E. P. Specker, The problem hidden variables in quantum mechanics, J. Math. Mech. **17**, 59 (1967). 93, 94

[134] A. Peres, Two simple proofs of the Kochen-Specker theorem, J. Phys. A **24**, L175 (1991). 93

[135] A. A. Klyachko, M. A. Can, S. Binicioğlu, and A. S. Shumovsky, Simple Test for Hidden Variables in Spin-1 Systems, Phys. Rev. Lett. **101**, 020403 (2008). 93

[136] J. Thompson, R. Pisarczyk, P. Kurzynski, and D. Kaszlikowski, An experimental proposal for revealing contextuality in almost all qutrit states, Scientific Reports **3**, 2706 (2013). 93

[137] C. Zu, Y.-X. Wang, D.-L. Deng, X.-Y. Chang, K. Liu, P.-Y. Hou, H.-X. Yang, and L.-M. Duan, State-independent experimental test of quantum contextuality in an indivisible system, Phys. Rev. Lett. **109**, 150401 (2012). 93, 96

[138] O. Moussa, C. A. Ryan, D. G. Cory, and R. Laflamme, Testing contextuality on quantum ensembles with one clean qubit, Phys. Rev. Lett. **104**, 160501 (2010). 93

[139] Z. Gedik, Computational speed-up with a single qutrit, ArXiv e-prints, quant-ph/1406.3579 (2014). 109

[140] A. L. Cauchy, Cauchy's Memoire Sur le Nombre des Valeurs, J. de lEcole polytechnique **10**, 1–28 (1815). 110

[141] R. N. Bracewell, *The Fourier transform and its applications*, McGraw-Hill Book Co, Singapore, 2000. 119, 120

[142] J. Fourier, *The analytical theory of heat*, Cambridge University Press, Cambridge UK, 1878. 119

[143] G. B. Arfken and H. J. Weber, *Mathematical methods for physicists*, Elsevier, Academic Press, MA USA, 2005. 119

[144] J. Daboul, X. Wang, and B. C. Sanders, Quantum gates on hybrid qudits, J. Phys. A **36**, 2525 (2003). 120, 122

[145] A. Muthukrishnan and C. R. Stroud, Quantum fast Fourier transform using multilevel atoms, J. Mod. Opt. **49**, 2115 (2002). 120, 122

[146] R. Cleve, A. Ekert, C. Macchiavello, and M. Mosca, Quantum algorithms revisited, Phil. T. Roy. Soc. A **454**, 339 (1998). 120

[147] D. R. Simon, On the power of quantum computation, SIAM J. Comput. **26**, 1474 (1997). 120

[148] K. Dorai and D. Suter, Efficient implementations of the quantum Fourier transform: An experimental perspective, Int. J. Quant. Inf. **3**, 413 (2005). 120

[149] H.-F. Wang, X.-X. Jiang, S. Zhang, and K.-H. Yeon, Efficient quantum circuit for implementing discrete quantum Fourier transform in solid-state qubits, J. Phys. B **44**, 115502 (2011). 120

[150] A.-S. Obada, H. A. Hessian, A.-B. Mohamed, and A. H. Homid, Implementing discrete quantum Fourier transform via superconducting qubits coupled to a superconducting cavity, J. Opt. Soc. Am. B **30**, 1178 (2013). 120

[151] L. Dong, X.-M. Xiu, H.-Z. Shen, Y.-J. Gao, and X. X. Yi, Quantum Fourier transform of polarization photons mediated by weak cross-Kerr nonlinearity, J. Opt. Soc. Am. B **30**, 2765 (2013). 120

[152] V. E. Zobov and A. S. Ermilov, Pulse sequences for realizing the Quantum Fourier transform on multilevel systems, J. Exp. Theo. Phys. **83**, 467 (2006). 120

[153] Z. Zilic and K. Radecka, Scaling and Better Approximating Quantum Fourier Transform by Higher Radices, IEEE Trans. Comp. **56**(2), 202 (2007). 120

[154] D. Coppersmith, An approximate Fourier Transform useful in Quantum Factoring, IBM Research Report , RC19642 (1994). 122

[155] D. Gottesman, Fault-tolerant quantum computation with higher-dimensional systems, Chaos, Solitons and Fractals **10**, 1749 (1999). 122

[156] A. Muthukrishnan and C. R. Stroud, Multivalued logic gates for quantum computation, Phys. Rev. A **62**, 052309 (2000). 123

[157] N. C. Nielsen, C. Kehlet, S. J. Glaser, and N. Khaneja, *Optimal Control Methods in NMR Spectroscopy*, eMagRes., John Wiley & Sons, Ltd, 2007. 143

[158] J. Neves, B. Heitmann, T. Reiss, H. Schor, N. Khaneja, and S. Glaser, Exploring the limit of polarization transfer efficiency in homonuclear three spin systems, J. Magn. Reson. **181**, 126 (2006). 143

[159] N. Gershenzon, T. Skinner, B. Brutscher, N. Khaneja, M. Nimbalkar, B. Luy, and S. J. Glaser, Linear phase slope in pulse design: Application to coherence transfer, J. Magn. Reson. **192**, 235 (2008). 143, 152

[160] T. Skinner, K. Kobzar, B. Luy, M. Bendall, N. Khaneja, and S. Glaser, Optimal control design of constant amplitude phase-modulated pulses: application to calibration-free broadband excitation, J. Magn. Reson. **179**, 241 (2006). 143

[161] C. A. Ryan, C. Negrevergne, M. Laforest, E. Knill, and R. Laflamme, Liquid-state nuclear magnetic resonance as a testbed for developing quantum control methods, Phys. Rev. A **78**, 012328 (2008). 143

[162] P. Rebentrost, I. Serban, T. Schulte-Herbrüggen, and F. K. Wilhelm, Optimal Control of a Qubit Coupled to a Non-Markovian Environment, Phys. Rev. Lett. **102**, 090401 (2009). 143

[163] R. Freeman, *Spin choreography: basic steps in high resolution NMR*, Delhi University Science Books, New Delhi, 2003. 143

[164] Z. Zilic and K. Radecka, The role of Superfast Transforms in speeding up Quantum Computations, IEEE Trans. Comp. **0195**, 623 (2002). 147

[165] I. Noda, Recent advancement in the field of two-dimensional correlation spectroscopy, J. Mol. Struct. **883**, 2 (2008). 151

[166] A. Brar, A. K. Goyal, and S. Hooda, Structural investigation of poly (methyl acrylate) by 2D HMBC NMR, J. Mol. Struct. **885**(1-3), 15 (2008). 151

[167] R. A. Venters, R. Thompson, and J. Cavanagh, Current approaches for the study of large proteins by NMR, J. Mol. Struct. **602**, 275 (2002). 151, 167

[168] G. Topcu and A. Ulubelen, Structure elucidation of organic compounds from natural sources using 1D and 2D NMR techniques, J. Mol. Struct. **834**, 57 (2007). 151

[169] W. Kozminski, A Pure-Phase Homonuclear J-Modulated HMQC Experiment with Tilted Cross-Peak Patterns for an Accurate Determination of Homonuclear Coupling Constants, J. Magn. Reson. **141**, 185 (1999). 151

[170] W. Kozminski, E. Bednarek, W. Bocian, J. Sitkowski, and L. Kozerski, The new HMQC based technique for the quantitative determination of heteronuclear coupling constants. Application for the measurement of 3J(H3'i,Pi+1) in DNA oligomers, J. Magn. Reson. **160**, 120 (2003). 151

[171] K. Feher, S. Berger, and K. E. Kover, Accurate determination of small one-bond heteronuclear residual dipolar couplings by F1 coupled HSQC modified with a G-BIRD(r) module, J. Magn. Reson. **163**(2), 340 (2003). 151

[172] I. Baskyr, T. Brand, M. Findeisen, and S. Berger, Acquisition Regime for High-Resolution Heteronuclear 2D NMR Spectra, Angwandte Chemie **45**(46), 7821 (2006). 151

[173] B. Baishya, C. Khetrapal, and K. K. Dey, Perfect Echo HMQC: Sensitivity and resolution enhancement by broadband homonuclear decoupling, J. Magn. Reson. **234**, 67 (2013). 151

[174] G. M. Kirwan and M. J. Adams, Peak width issues with generalised 2D correlation NMR spectroscopy, J. Mol. Struct. **892**(1-3), 225 (2008). 151

[175] I. Saka and A. Gencten, Product operator theory of 2D MAXY-HMQC NMR spectroscopy for CDn groups, J. Mol. Struct. **834**, 521 (2007). 151

[176] D. Rovnyak, D. P. Frueh, M. Sastry, Z. Y. J. Sun, A. S. Stern, J. C. Hoch, and G. Wagner, Accelerated acquisition of high resolution triple-resonance spectra using non-uniform sampling and maximum entropy reconstruction, J. Magn. Reson. **170**, 15 (2004). 152

[177] M. Misiak and W. Kozminski, Determination of heteronuclear coupling constants from 3D HSQC-TOCSY experiment with optimized random sampling of evolution time space, Magn. Reson. Chem. **47**, 205 (2009). 152

[178] A. Ross, M. Salzmann, and H. Senn, Fast-HMQC using Ernst angle pulses : An efficient tool for screening of ligand binding to target proteins, J. Bio. NMR **10**, 389 (1997). 152

[179] A. Favier and B. Brutscher, Recovering lost magnetization: polarization enhancement in biomolecular NMR, J. Bio. NMR **49**, 9 (2011). 152

[180] P. Schanda, Fast-pulsing longitudinal relaxation optimized techniques: Enriching the toolbox of fast biomolecular NMR spectroscopy, Prog. Nuc. Magn. Reson. **55**, 238 (2009). 152

[181] B. Brutscher, Combined frequency and time-domain NMR spectroscopy. Application to fast protein resonance assignment, J. Bio. NMR **29**, 57 (2004). 152

[182] E. Kupce and R. Freeman, Polychromatic Selective Pulses, J. Magn. Reson. **102**, 122 (1993). 153

[183] M. K. Cho, S. Xiang, H. Y. Kim, S. Becker, and M. Zweckstetter, Cold-induced changes in the protein ubiquitin, PLoS ONE **7**, 37270 (2012). 168

[184] S.L.Chang and N.Tjandra, Temperature dependence of protein backbone motion from carbonyl ^{13}C and amide ^{15}N NMR relaxation., J. Magn. Reson. **174**, 43 (2005). 168

[185] G. H. Brown, *Advances in Liquid Crystals 6*, Academic Press, New York, 1983. 173

[186] L. J. Yu and A. Saupe, Observation of a biaxial nematic phase in Potassium Laurate-1-Decanol-Water mixtures, Phys. Rev. Lett. **45**(12), 1000 (1980). 173